

**New and innovative approaches for enhancing the
repeatability and thermoelectric performance of Ag_2X ($\text{X} =$
S, Se, and Te) and SnTe**

A thesis

Submitted in partial fulfillment of the requirements of the degree of

Doctor of Philosophy

by:

Navita

Registration ID 20173564



Department of Physics

INDIAN INSTITUTE OF SCIENCE EDUCATION AND RESEARCH

PUNE-411008, India

Certificate

Certified that the work incorporated in the thesis entitled “**New and innovative approaches for enhancing the repeatability and thermoelectric performance of Ag_2X (X = S, Se, and Te) and SnTe**” submitted by **Navita** was carried out by the candidate, under my supervision. The work presented here or any part of it has not been included in any other thesis submitted previously for the award of any degree or diploma from any other university or institution.

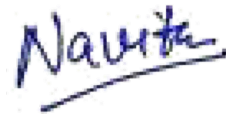


(Supervisor)

Date: October 24, 2023

Declaration

I declare that this written thesis entitled **”New and innovative approaches for enhancing the repeatability and thermoelectric performance of Ag_2X (X = S, Se, and Te) and SnTe”** represents my ideas in my own words and where others’ ideas have been included, I have adequately cited and referenced the original sources. I also declare that I have adhered to all principles of academic honesty and integrity and have not misrepresented or fabricated or falsified any idea/data/fact/source in my submission. I understand that violation of the above will be cause for disciplinary action by the Institute and can also evoke penal action from the sources which have thus not been properly cited or from whom proper permission has not been taken when needed.

A handwritten signature in blue ink that reads "Navita". The signature is written in a cursive style and is underlined with a single horizontal stroke.

(Navita)

Date: October 24, 2023

Acknowledgments

First and foremost, I would like to express my heartfelt gratitude to my thesis supervisor, Dr. Surjeet Singh, for his unwavering support and guidance throughout this work. I have greatly benefited from his wealth of knowledge and meticulous editing. I am deeply grateful to him for accepting me as a research student in his lab and for having faith in me over the years.

I would also like to extend my thanks to my research advisory committee members, Dr. Ajay Singh and Dr. Prasenjit Ghosh, for their interest in my work and valuable inputs during our annual meetings. A special appreciation goes to Dr. Ajay Singh for always being available and traveling from Mumbai to Pune for these meetings. His necessary and valuable inputs in my thesis work, along with his polite and humble nature, have boosted my confidence and motivated me.

In addition, I am sincerely grateful to my collaborators, Dr. Ankita Katre and Neeta Bisht from Pune University, who provided valuable theoretical insights into a significant portion of my work. Their expertise and guidance have been instrumental in shaping my understanding and contributing to the overall success of my project.

Furthermore, I want to express my heartfelt gratitude to Kalyani Thakur for introducing me to chemical synthesis methods and directing me while initiating this thesis work right after I joined the lab. I am truly grateful for the opportunity to learn and grow under her guidance.

I extend my heartfelt thanks to my senior, Kumar Saurabh, for training me during my initial days in the lab. He introduced me to the research work culture of the lab and provided endless support throughout this journey. Together, we explored the field of thermoelectrics through numerous discussions and journal club meetings. As a result, this work represents the second thesis work in thermoelectrics after Dr. Kumar Saurabh.

Furthermore, I want to express my equal respect and appreciation to Dibyata Rout, who shared her early months of research in thermoelectrics before switching to low dimensional magnetism. She is a multi-talented individual, excelling as a researcher, player (badminton, cricket, etc.), guitarist, and sometimes even a chef. Her critical feedback on my work has

always motivated me to think more critically about my observations. I will always remember the IISER Women league 2022 match, where she hit the very first six in the women's team.

I would like to extend very special thanks to my former lab members, Rabindranath Bag, Prachi Telang, Prakash Kumar, Sancheyta, Haritha, and Anupam, for being understanding and supportive lab partners. I am also thankful to my current lab members, Ankit, Nashra, Dinesh, Rupesh, Lalith, Pankaj, and Sagar. Special thanks to Sagar for always being available for all my trekking plans and for patiently listening to my non-stop random chit-chats.

I would like to acknowledge the contributions of the technical and engineering staff, especially Nilesh sir, whose unwavering support was crucial in handling emergency situations related to our instruments. My sincere thanks go to him for his availability and assistance.

In addition, I want to express my heartfelt gratitude to my friends at IISER campus who made this journey enjoyable and fulfilling. I feel blessed to have such wonderful friends who supported me during my difficult days. I extend my sincere thanks to Sarvottam, Bhumika, Anupam, Prakash, Chetna, and Ronit for their unwavering support. Chetna and Ronit are the kindest and most brilliant individuals I have ever known, and I have shared my best times with them. I will always remember their unconditional support during ups and downs over the years, and I am blessed to have countless memories with them.

I would also like to express my heartfelt gratitude to the members of the cricket teams, "Happening XI" and "Kill Bill," as well as the football team and the athletic group. You all have magnified every moment of joy when it comes to enjoying Kreedajung at IISER campus. Your enthusiasm and sportsmanship have inspired me to push my limits and strive for excellence. Thank you for making my experience at IISER Pune so memorable and enjoyable.

Finally, I want to express my deepest gratitude to my family. In particular, I am immensely thankful for my parents, whose unwavering love and support continuously motivate and empower me. Their constant belief in me has played a pivotal role in my achievements. I am especially grateful to my father, who not only encouraged me to pursue my studies but also helped shape the person I am today. It is truly remarkable that despite never having at-

tended college himself, he wholeheartedly believed in his daughter's potential and supported my desire to study anywhere in the world, even when it meant going against the opinions of other family members. I hold the utmost respect and gratitude for him, as I realize that no matter how hard I try, I can never fully repay his efforts and unconditional love. Equally deserving of my gratitude is my mother, who has showered me with unconditional love, blessings, and unwavering support.

Moreover, I want to extend my deepest thanks to my siblings, Navneet and Davit, who serve as the other two pillars of my life's tripod. They keep me grounded, remind me of what truly matters in life, and offer unwavering support in all my endeavors. I consider myself incredibly fortunate to have such a loving and supportive family, and I firmly believe that their presence has made me the luckiest person on Earth.

A handwritten signature in blue ink that reads "Navita" with a horizontal line underneath.

(Navita)

Date: October 24, 2023

This thesis is dedicated to my father

Abstract

Chalcogenide thermoelectric materials have gained significant attention in recent years due to their potential for high-performance thermoelectric energy conversion applications. While enhancing their thermoelectric performance has remained a core area of research, significant current interest has been shifting to address other important issues, including improving the reproducibility and reducing the toxicity of these materials. Chalcogenides offer numerous advantages over other classes of thermoelectric materials. These advantages include the fabrication of both n-type and p-type thermoelectric legs, often from the same parent material, through doping, low thermal conductivity, and high thermoelectric performance across a wide temperature range. For instance, Bi-based alloys exhibit high thermoelectric performance at room temperature; PbTe-based TE materials often reach their peak TE performance in mid-temperature range; and, Cu-based superionic compounds show excellent performance at high temperatures. However, it is important to note that sample stability under applied current and temperature gradients over several thermal cycles is an essential requirement for practical applications. This stability is crucial for achieving reproducibility and ultimately ensuring the success of thermoelectric devices. By successfully developing and implementing an efficient and optimized synthesis method, researchers can achieve a breakthrough in resolving the stability concerns of chalcogenide-based TE devices. This advancement would not only enable enhanced reproducibility but also pave the way for achieving superior TE performance in practical applications. This thesis addresses the issue of irreproducibility in the electronic transport properties of superionic thermoelectric materials of the Ag_2X family ($\text{X} = \text{S}, \text{Se}, \text{and Te}$), and the multivalent alloys derived from SnTe. Ag_2Te has long been recognized as a superionic compound with a decent figure of merit (zT) spanning from room temperature to the mid-temperature range. However, the sample-dependent transport properties of Ag_2Te have hindered its potential as a thermoelectric (TE) material for practical applications. In Chapter 3 of this thesis, we investigate this issue in great details. We show that the primary reason for the observed irreproducibility is Ag metal ion migration during furnace/hot press or spark-plasma sintering at high temperatures. Above superionic transi-

tion, the Ag ions tend to migrate if the temperature or voltage gradient the material is subject to exceeds a temperature dependent threshold value. We then propose a novel synthesis method that operates at room temperature, resulting in the fabrication of highly dense and reproducible samples. This newly method also offers the advantage of controlling the formation hierarchy in particle size. As a result, the thermoelectric performance of the n-type Ag_2Te is significantly enhanced by reducing the lattice thermal conductivity below its superionic limit. Thus, a high zT of 1.2 in n-type Ag_2Te and close to 0.7 in p-type Ag_2Te is obtained at 570 K. Through our research, we have also show that 570 K is a safe temperature limit for Ag_2Te , below which reproducible properties can be obtained as the Ag metal ion migration under the applied voltage and temperature gradient remains local.

Chapter 4 explores the thermoelectric properties of Ag_2Se , which suffers large variations in transport properties for similar composition samples due to sample inhomogeneity and meta-stable phase formation. Such irreproducible behavior is reported in high temperature processed samples. In this chapter, our all-room-temperature synthesis approach, described in detail in chapter 3, is utilized to achieve high thermoelectric performance with excellent reproducibility and homogeneity. The role of Se excess in enhancing the zT is studied, revealing the suppression of Ag interstitial defects and reduction in carrier concentration, leading to improved thermoelectric properties compared to pristine Ag_2Se . A high and reproducible zT value of 0.9 at 370 K is obtained without any extrinsic doping.

In chapter 5, we employed our all room temperature synthesis technique to fabricate high density, nanostructured pellets of Ag_2S . The thermal conductivity of our Ag_2S sample is significantly suppressed compared to the ingot sample due to grain boundary scattering. By synthesizing anion excess samples, the thermal conductivity is further decreased, and a significantly improved zT value of around 0.9 at 670 K is obtained. The underlying reason of such reduction in thermal conductivity due to anion excess is studied via detailed differential scanning calorimetry (DSC) and temperature dependent electrical resistivity.

In Chapter 6, the thermoelectric properties of SnTe are investigated, considering its low Seebeck coefficient and high thermal conductivity caused by Sn vacancies. A novel furnace

sintering method is employed to fabricate nanostructured SnTe samples with significantly reduced thermal conductivity. We show that during the furnace sintering of a cold-pressed pellet, the nanoparticles of SnTe precipitates at the grain boundaries, leading to a nanostructured pellet which further enhances the thermoelectric properties. Band engineering with Ag doping is also explored, resulting in improved power factor and thermoelectric performance due to both valence band convergence and an increase in the band gap.

Overall, this thesis successfully resolves the issue of irreproducibility in the electronic transport properties of Ag_2Te and Ag_2Se . High TE figure of merit is obtained in Ag_2Te , Ag_2Se , Ag_2S superionics and SnTe metavalent compounds through innovative synthesis methods, including grain-size reduction, and hence nanostructuring, and band engineering techniques. The reproducibility of the observed properties is solidly established. The findings contribute to the understanding and development of thermoelectric materials with enhanced reproducibility and improved performance.

List of publications

- *Synergistic Approach Toward a Reproducible High zT in n-Type and p-Type Superionic Thermoelectric Ag_2Te* ; **Navita Jakhar**, Neeta Bisht, Ankita Katre and Surjeet Singh, ACS Applied Materials and Interfaces 2022 14 (48), 53916-53927.
- *Reproducible high thermoelectric figure of merit in Ag_2Se* ; **Navita Jakhar**, Dinesh Kumar Kedia, Ankit Kumar, Kumar Saurabh and Surjeet Singh, Appl. Phys. Lett. 122, 163901 (2023).
- *Grain boundary engineering in metavalent $SnTe$: A simplified approach*, **Navita Jakhar**, Dinesh kumar kedia, Ankit Kumar, and Surjeet Singh, Appl. Phys. Lett. 123, 173901 (2023).
- *A facile room temperature synthesis method to prepare an inorganic ductile superionic sulphide with high figure of merit*, **Navita Jakhar**, Dinesh Kumar Kedia and Surjeet Singh (to be submitted).
- *Thermoelectric and Photovoltaic Properties of Mn-Doped Kesterite $Cu_2Zn_{1-x}Mn_xSnSe_4$* ; Gaurav Jamwal, Mohd Warish, Saravanan Muthiah, Shruti Chakravarty, **Navita Jakhar**, Asokan Kandasami, and Asad Niazi, Inorg. Chem. 2022, 61, 16390-16404
- *Signature of superconducting onset in presence of large magnetoresistance in type-II Dirac semimetal candidate Ir_2In_8S* , Pallavi Malavi, Prakash Kumar, **Navita Jakhar**, Surjeet Singh and S. Karmakar, Pallavi Malavi et al 2022 New J. Phys. 24, 102002.

List of Figures

1.1	Global energy consumption spectrum for year 2022. <i>Figure regenerated from Ref [1].</i>	2
1.2	Pie diagram showing development in TE materials from 1950 to 2017 [2]. .	4
1.3	Schematic diagram for (a) thermoelectric effect, (b) thermoelectric generator, and (c) thermoelectric refrigerator.	4
1.4	Schematic diagram for Seebeck effect.	5
1.5	TEG efficiency variation with ZT_{ave} for different cold end temperatures while hot end kept at 700 K, <i>adapted from Ref [3].</i>	8
1.6	Relationship between S , σ , $S^2\sigma$, κ_e and κ_l with carrier concentration, <i>adapted from Ref [4].</i>	9
1.7	Schematic showing heavy hole valence band (Σ , with band degeneracy of 12) and light hole valence band (L, with band degeneracy of 4) getting converged with increasing Pb alloying in SnTe, <i>figure adapted from Ref [5].</i>	13
1.8	Schematic representation of (a) resonant impurity states and (b) charge carrier filtering via Pb nano-precipitates in PbTe matrix.	15
1.9	Illustration of thermal conductivity in terms of heat flow per unit time (\dot{Q}) and temperature gradient $T_1 - T_2$ across thickness (w) of a specimen of cross sectional area A	17

1.10	Schematic illustration of all-scale hierarchical nanostructuring (ASHN) for scattering of different mean free path lengths phonons. <i>Figure regenerated from Ref [6].</i>	21
1.11	Part-liquid and part-solid hybrid crystal structure in a superionic material. .	26
1.12	Electronic band calculations for (a) rigid phase, and (b) superionic phase of Cu ₂ Se. Reproduced from Ref[[7]]	26
1.13	(a) Temperature variation of κ_l of superionic compounds and compared with the state of the art materials, and (b) shows the zT of superionic compounds reported in the literature. <i>Figure regenerated from Ref [8].</i>	27
1.14	Ion migration and metal deposition in superionic materials (a) Metallic Cu deposition on the surface of Cu ₂ S induced by high current density, and (b to f) are schematics showing, (b) energy profile associated with ions, (c) random ionic motion in the absence of any external force resulting net zero ion flux, (d) oriented ionic motion under applied directional field due to which superionic materials either reach, (e) steady state without metal deposition, or (f) deposits metal (Cu), if local Cu concentration reaches a critical value determined for the stability of superionic material. <i>Figure adepted from Ref [9].</i>	30
1.15	Material degradation in superionic compounds (a) is the FESEM image of sintered Ag ₂ S pellet at 773 K showing Ag migration at the edges of pellet (from our study), (b) is the FESEM image of Zn _{12.8} Sb ₁₀ sample showing Zn migration after current flow experiment when a high current density of 68.8 A cm ⁻² was applied for continuous 26 minutes while keeping T _{hot} at 473 K, and (c, and d) shows the photographs of top view and whole sample view of Zn _{12.8} Sb ₁₀ degraded samples when exposed to high current density experiment taken from <i>Ref [10].</i>	32
1.16	Recent progress in SnTe thermoelectrics. <i>Figure adepted from Ref [11].</i> . .	33

2.1	(a) Ball Mill used for mechanical alloying synthesis, (b) Ag_2X powder obtained after milling, and (c) low-magnification image showing formation of in our synthesized Ag_2X samples.	39
2.2	Gradual color change from gray (a) to black (c) during the synthesis of Ag_2S . Panel (b) shows the color during an intermediate stage.	40
2.3	Image of cold-pressed pellet, the vacuum sealed cold-pressed pellets and the furnace used for sintering.	41
2.4	Few representative pictures of ingot samples obtained from solid-state melting method.	43
2.5	Samples (left panel: ingot and right panel: pellet) for electronic and thermal transport property measurements obtained after cutting and polishing process.	44
2.6	(a) Schematic diagram for x-ray diffraction from crystalline material, (b) schematic diagram for Bragg-Brentano geometry used in our PXRD analysis	46
2.7	(a) Various emergent signals from the specimen in scanning electron microscope (b) schematic diagram for field emission scanning electron microscope.	50
2.8	Representative FESEM images showing morphology of Ag_2Te for (a) cold-pressed, and (b) sintered pellets on freshly fractured surfaces taken at 3 kV.	51
2.9	Schematic diagram of transmission electron microscope (TEM).	53
2.10	(a) Copper grid coated with amorphous carbon, (b) TEM image lower resolution showing nanoparticle distribution, (c) high resolution TEM image, and (d) electron diffraction taken on our synthesized Ag_2S nanoparticle. . .	55
2.11	STA 449 F1 Jupiter from Netzsch used for TG-DSC analysis, schematic is adapted from Ref [12] where number denotes different component of the set up such as 1 furnace thermocouple, 2 heating element, 3 sample carrier, 4 protective tube, 5 radiation shield, 6 evacuation system inlet, 7 balance system, 8 gas outlet valve, 9 hoisting device, 10 purge 1 gas inlet, 11 purge 2 gas inlet, 12 protective gas inlet.	57

2.12	Experimental data showing mass loss (TGA) and phase transition (DSC) measured simultaneously for our Ag_2Te sample under N_2 atmosphere using STA 449 F1 Jupiter from Netzsch.	58
2.13	Estimation of C_p using DSC7020 differential scanning calorimeter for Ag_2Se sample (a) shows the variation of DSC curves with time, and (b) depicts the temperature dependent C_p variation of Ag_2Se pellet.	59
2.14	Schematic diagram for measuring Seebeck coefficient and resistivity in LSR-3. (Figure adapted from Linseis LSR-3 digital manual)	60
2.15	Temperature dependent (a) resistivity, and (b) Seebeck coefficient of standard sample (constantan: an alloy of 55% Cu and 45% Ni) measured simultaneously using LSR 3 set-up.	61
2.16	Schematic diagram of Hall effect in a semiconducting bar.	62
2.17	Home build automated high temperature Hall effect measurement setup.	62
2.18	(a) Shows the schematic diagrams of front side of sample holder, and (b) is the picture of sample holder.	65
2.19	Schematic diagram for laser flash technique for thermal diffusivity measurement.	66
2.20	(a) Voltage vs time experimental curve and, (b) fitted experimental data with different correction models in LFA 1000 setup.	67
2.21	Temperature dependent thermal diffusivity (α) of standard sample, graphite, measured using LFA 1000 set-up.	68
3.1	(a) x-ray powder diffraction patterns for sintered and SSM samples, and (b) for cold-pressed Ag_2Te sample; (c) Crystal structure of room-temperature monoclinic $\beta\text{-Ag}_2\text{Te}$, and (d) Crystal structure of the high temperature cubic α -phase.	79
3.2	Morphology at $1 \mu\text{m}$ length scale of freshly fractured bulk pellets of few representative Ag_2Te samples synthesized BS, HS and CP methods.	80

3.3	(a) Thermogravimetric analysis (TGA), and (b) differential scanning calorimetry (DSC) of BS1, BS2 and BS4 samples.	81
3.4	High temperature XRD of Ag ₂ Te.	81
3.5	TEM analysis of the Ball-milled powders (a) a low resolution TEM image showing Ag ₂ Te nanoparticles. Inset shows the particle-size distribution, (b - f) high-resolution TEM images showing different morphologies and degree of crystalline order in the Ag ₂ Te nanoparticles in (a), (g) FFT of nanoparticle in (g) showing the polycrystalline-like diffraction pattern on a single Ag ₂ Te nanoparticle in (f), (h) a zoomed-in image on the bordered area (in white) in (f). The dashed lines showing the grain boundaries are drawn as a guide to eye.	84
3.6	Temperature dependence of electrical conductivity, thermopower, and power factor for our samples. (a - c) BS and HS samples, (d - f) stoichiometric CP samples prepared for different milling durations, (g - i) CP samples prepared with different Ag/Te molar ratio (see text for details).	86
3.7	Temperature dependent Hall carrier concentration measured from 300 K to 506 K.	87
3.8	Temperature dependent (a) electrical conductivity, (b) Seebeck coefficient, (c) power factor, and (d) thermal conductivity for two n-type Ag ₂ Te samples synthesized by ball-milling for 500 minutes.	90
3.9	Composition analysis of LSR bars after measuring the electronic transport properties upto 570 K and 610 K (showing Ag migration).	92
3.10	(a) Electrical resistivity measured for 140 minutes at different current densities, and (b) relative change in sample resistivity with respect to the resistivity value for lowest current density.	93
3.11	Electronic band calculation of (a) pristine (left panel) and 6.5 % Ag deficient (right panel) Ag ₂ Te for room temperature monoclinic phase and (b) Fermi surface calculations with different percentage Ag vacancy.	94

3.12	Electronic band calculation of (a) pristine (left panel) and 6.5 % Ag deficient (right panel) Ag_2Te for high temperature cubic phase, (b) shows the Fermi surfaces in pristine and 6.5% Ag deficient phases.	95
3.13	Thermal cycling effect to test the sample stability (a) electrical conductivity (b) thermopower (c) PF and, (d)thermal conductivity of CP4 sample.	96
3.14	(a) Temperature dependent κ of CP samples prepared with different milling durations, (b) Temperature dependent κ of CP samples prepared with different Ag/Te molar ratio, (c) κ_l extracted from the measured κ using the SKB model for a few samples, (d) Calculate phonon dispersion for $\beta\text{-Ag}_2\text{Te}$, (e) Theoretically calculated thermal conductivity showing effect of anharmonicity, grain-size and Ag-vacancies/Te-interstitials, (f) a representative high-resolution TEM image of a CP Ag_2Te sample after several thermal cycling. In (a), thermal conductivity of our ingot sample is also included for comparison.	97
3.15	Temperature dependent (a) thermal conductivity and, (b) zT of BS and HS samples.	98
3.16	Calculated results for (a) Grüniessen parameter and, (b) relaxation time with frequency of phonons.	102
3.17	Morphology of freshly broken surface of CP4 sample of as cold pressed and sintered pellet at 550 K (a) low magnification image of cold pressed pallet (b) is for sintered pellet (c) image at 200 nm for cold pressed and (d) image at 200 nm for the sintered pellet.	103
3.18	Few representative TEM amd HRTEM images of ball billed powder samples.	103

3.19	HRTEM images of CP samples after multiple runs of transport property measurements (a) HRTEM at 5 nm showing highly crystalline nanoparticle (b) IFFT image on rectangular area marked as 1 in (a), (c) IFFT image on rectangular area marked as 2 in (a) where green lines are showing the line defects, (d) HRTEM image at 10 nm showing large number of nanometer sized grains oriented in different directions (e) HRTEM image of single nanoparticle containing multiple orientation of planes and, (f) HRTEM image at 10 nm showing two grains and insets are their respective FFT on the marked red and green regions.	104
3.20	Temperature dependent zT variation for (a) stoichiometric CP samples prepared with different milling times (SSM sample and literature data from J. Capps et al. study are included for comparison), and (b) different Ag/Te molar ratio receptively.	105
4.1	Powder x-ray diffraction patterns for samples AS1, AS2, ..., AS6. Data for a SSM sample is also shown. The simulated pattern for the space group $P2_12_12_1$ is shown at the bottom. Inset (right) shows the crystal structure of Ag_2Se . Inset (left) shows a zoomed-in view of the diffraction pattern for 1%Ag excess sample.	111
4.2	The Rietveld refinement for a representative sample AS1.	112
4.3	Chemical mapping of Ag_2Se samples studied in this chapter.	113
4.4	Morphology of bulk (a) ball-milled, cold pressed sample, the grain size distribution is shown in the inset, and (b) solid-state melted sample (c) shows the high resolution TEM image at 5 nm and inset is showing the FFT taken over marked rectangular area, (d) IFFT image of rectangular area marked in (c) showing [112] planes.	115
4.5	Morphology of AS1 sample before and after the LSR measurements.	115
4.6	DSC measurements for all synthesized samples.	116

4.7	Temperature variation of (a) electrical conductivity (σ), (b) Hall carrier concentration (n_H), and (c) Hall mobility (μ_H), and (d) Seebeck coefficient (S) for the Ag_2Se samples studied in this paper.	117
4.8	Temperature dependent electrical conductivity for two representative cold-pressed samples AS1 and AS3 from 77 K to 300 K.	119
4.9	Pisarenko plots showing experimental S versus n_H data from our study and several previous reported data [13–16]. The solid lines are calculated within the single parabolic band approximation for carrier effective mass $0.18m_e$, $0.20m_e$ and $0.23m_e$	121
4.10	Temperature dependent power factor (PF) for Ag_2Se samples.	122
4.11	Temperature dependence of (a) thermal conductivity (κ), (b) lattice thermal conductivity (κ_l), and (c) figure-of-merit (zT). In (d) zT from literature [i] Li et al. [17], [ii] Huang et al. [18], [iii] Mi et al. [13], [iv] Chen et al. [14], [v] Yang et al. [19], [vi] Jin et al. [20], [vii] Jood et al. [16], [viii] Wang et al. [15] are plotted along with the zT of our 2.5% Se-excess sample.	123
4.12	Temperature dependent electronic thermal conductivity estimated using Weidemann Franz law $\kappa_e = LT\sigma$ where L calculated using single kane band (SKB) model.	124
4.13	Temperature dependence of electrical conductivity and thermopower in two successive cycles.	125
5.1	Crystal structure of Ag_2S , (a) monoclinic also known acanthite (or β -phase) stable below 450 K, (b) superionic BCC (or α -phase) phase also known as argentite stable below 859 K, and (c) superionic FCC stable above 860 K. In both β and α phases, the S atoms are arranged on a body centered cubic lattice. While in β -phase Ag atoms form a regular lattice, in α -phase the four Ag atoms are randomly distributed on the 42 crystallographic positions. . .	129
5.2	Powder x-ray diffraction of Ag_2S at different synthesis stages in ambient condition.	131

5.3	(a) Powder x-ray diffraction at room temperature, (b) (12-2) and (022) peaks showing negligible peak shift with S excess for the monoclinic phase, (c) shows the powder x-ray diffraction of the BCC superionic phase, and (d) shows a zoomed-in view of the (200) peak in different samples.	133
5.4	Retvield Refinement of Ag_2S (a) by using theoretical model proposed by Blanton et al. [21], and (b) using structure parameters reported by Frueh et al. [22].	135
5.5	TEM analysis of Ag_2S powder sample where (a, and b) showing the TEM image at 100 nm with different nano-particle size (inset in (a) is the histogram showing particle size distribution), (c, and d) are HRTEM image at 10 nm showing two nano-particles having single crystalline and polycrystalline morphology respectively.	136
5.6	(a) HRTEM image a nanoparticle comprising of two different phases, insets shows the FFT of green and yellow marked rectangular boxes, and (b) Differential scanning calorimetry (DSC) of Ag_2S sample showing two transitions while heating (H_1 and H_2) as well as in cooling (C_1 and C_2).	137
5.7	HRTEM analysis of Ag_2S powder sample where (a) shows rod like nanoparticle composed of two family of planes (-121) and (-123) forming coherent boundary (inset shows the FFT of particle), (b, and c) are the FFT of red and yellow marked rectangular areas in (a).	138
5.8	(a, and b) Shows the effect of thermal cycling on DSC of Ag_2S , and $\text{Ag}_2\text{S}_{1.01}$ cold-pressed pellet samples respectively.	140
5.9	(a) Temperature dependent resistivity with three consecutive runs, (b) a zoomed-in view of the resistivity vs temperature plots around the $\beta \alpha$ transition, (c) variation of resistivity with temperature during run 3, and (d) DSC runs with three heating and cooling cycles.	141
5.10	Temperature dependent electrical conductivity of Ag_2S with multiple heating and cooling cycles.	142

5.11	Thermal cycling effect on temperature dependent (a) electrical conductivity (σ), and (b) Seebeck coefficient (S) of Ag_2S ingot sample.	143
5.12	Morphology of freshly fractured piece from ingot and cold pressed pallets in back scattered electron detector mode.	144
5.13	Chemical mapping of $\text{Ag}_2\text{S}_{1.02}$ CP pellet.	144
5.14	Temperature dependent (a) electrical conductivity (σ), (b) Seebeck coefficient (S), (c) power factor (PF), and (d) total thermal conductivity (κ_T). . .	145
5.15	Temperature dependent carrier concentration of Ag_2S ingot sample.	146
5.16	Effect of thermal cycling on thermal conductivity (κ_T) of $\text{Ag}_2\text{S}_{1.02}$ sample. .	148
5.17	(a) HRTEM image at 10 nm and insets are showing the FFT taken over red and green marked rectangular areas, (b) shows the selected area electron diffraction (SAED) of HRTEM image shown (a) depicting presence of twinning in nanoparticle, (c) is IFFT image of red rectangular area marked in (a) and (d) shows the IFFT image on green marked rectangular area of (a). . . .	149
5.18	(a) Temperature dependent zT of $\text{Ag}_2\text{S}_{1+\delta}$ samples, and (b) comparison of zT of our outperforming Ag_2S sample and some reported n and p-type sulfides in previous studies by He et al. [23], Qin et al. [24] and Xiao et al. [25]. . .	150
5.19	Electrical resistivity under 1 A cm^{-2} current density measured for continuous 200 minutes.	150
6.1	(a) Crystal structure of SnTe/PbTe, (b) Brillouin zone for cubic SnTe or PbTe showing 8 half hole pockets at low symmetry L point resulting 4-fold band degeneracy and 12 hole pockets along Σ direction giving rise to 12-fold band degeneracy (adapted from Ref [26]), (c) electronic band structure of PbTe and SnTe (adapted from Ref. [27]).	154
6.2	(a) Powder x-ray diffraction patterns for $\text{Sn}_{1.03}\text{Te}$ I, HPS and FS samples, (b) shows the broadening of 200 peak after sintering the ingot powder using HPS at 773 K and furnace at 973 K, and (c) shows the morphology variation at 200 nm for three I, HPS and FS $\text{Sn}_{1.03}\text{Te}$ samples.	160

6.3	Microstructure comparison of sintered pellet and ingot $\text{Sn}_{1.03}\text{Te}$ sample. . .	161
6.4	EDX analysis for determining the chemical composition of nanoparticles and bigger micrometer grains in $\text{Sn}_{1.03}\text{Te}$ FS sample.	162
6.5	(a) Powder x-ray diffraction patterns for $\text{Sn}_{1.03}\text{Te}$ ingot and sintered pellet samples, (b) the chemical mapping	163
6.6	(a) Powder x-ray diffraction patterns for ingots, and (b) for sintered pellets (c, and d) represents the variation of full width at half maxima (FWHM) and lattice parameters of $\text{Sn}_{1.03-x}\text{Ag}_x\text{Te}$ ($x = 0, 0.03, 0.06$ and 0.09) ingot and sintered pellet samples.	164
6.7	Morphology of freshly broken surfaces from $\text{Sn}_{1.03-x}\text{Ag}_x\text{Te}$ ($x = 0, 0.03, 0.06$ and 0.09) ingot samples.	165
6.8	Morphology of freshly broken surfaces from $\text{Sn}_{1.03-x}\text{Ag}_x\text{Te}$ ($x = 0, 0.03, 0.06$ and 0.09) sintered pellet samples.	166
6.9	Chemical mapping of $\text{Sn}_{0.97}\text{Ag}_{0.06}\text{Te}$ sample.	167
6.10	TE properties of $\text{Sn}_{1.03}\text{Te}$ I, FS @ 973 K and HPS @ 773 K, (a, and b) represents the temperature dependent σ and S, (c) shows the hole carrier concentration and mobility in different samples, (d,e, and f) represents the temperature dependent PF, total thermal conductivity (κ_T) and zT. Inset in (f) shows the zT_{max} and zT_{avg} obtained in three different samples.	169
6.11	(a) κ_e and κ_l at 340 K, (b) shows zT_{max} and zT_{avg} for $\text{Sn}_{1.03}\text{Te}$ I, HPS, and FS samples from this work compared with their values from Ref [28]. . . .	170
6.12	Temperature dependent (a) Hall carrier concentration, and (b) mobility variation of $\text{Sn}_{1.03}\text{Te}$ I, HPS, and FS samples.	171

6.13	(a) Temperature dependent σ , (b) hall carrier concentration and mobility variation with Ag doping, (c) temperature dependent S, and (d) S vs n Pisarenko lines computed by using two valence band model with varying ΔE_V (heavy hole band: SPB model with $m_H^* = 0.35m_e$ and light hole band: SKB model and $m_L^* = 0.16 m_e$ and $0.24 m_e$). Literature data is also included for comparison [29–32].	173
6.14	<i>Ab-initio</i> electronic band calculations for $\text{Sn}_{27}\text{Te}_{27}$, $\text{Sn}_{26}\text{AgTe}_{27}$, $\text{Sn}_{25}\text{Ag}_2\text{Te}_{27}$ and $\text{Sn}_{27}\text{Ag}_3\text{Te}_{27}$ compositions.	174
6.15	Schematic representing the electronic band structure modifications after Ag doping	175
6.16	Temperature dependent (a) power factor (PF), (b) total thermal conductivity (κ_T), (c) lattice thermal conductivity (κ_l) at 340 K, and (d)zT for $\text{Sn}_{1.03-x}\text{Ag}_x\text{Te}$ ($x = 0, 0.03, 0.06$ and 0.09) samples.	176
6.17	High resolution transmission electron microscopy analysis of sintered $\text{SnAg}_{0.03}\text{Te}$, (a) represents the multiple nano-size grain boundaries (b), and (c) shows the presence of semi-coherent and coherent grain boundaries, (d) shows incoherent grain boundary formed between (220) and (200) planes, (e, and f) denotes a IFFT image showing dislocation defects along (220) and (422) planes. . .	178
6.18	Comparison of (a) thermal diffusivity (D), (b) total thermal conductivity κ_T , and (c) zT of $\text{SnAg}_{0.03}\text{Te}$ sample from our study with the literature data from Xu et al. [33], Pathak et al. [28], Sarkar et al. [31], Lee et al. [34]	179
6.19	$\text{SnAg}_{0.03}\text{Te}$ sample's comparison from our study with the literature, temperature dependent (a) thermal diffusivity (D), (b) total thermal conductivity κ_T , and (c) zT.	180
6.20	$\text{SnAg}_{0.03}\text{Te}$ sample's comparison from our study with the literature, temperature dependent (a) thermal diffusivity (D), (b) total thermal conductivity κ_T , and (c) zT.	181

- A.1 Temperature dependent (a) σ , (b) Seebeck coefficient (S), (c) power factor (PF), and (d) total thermal conductivity (κ_T) for ingot $\text{Sn}_{1.03-x}\text{Ag}_x\text{Te}$ samples. 190
- A.2 Temperature dependent figure-of-merit (zT) for ingot $\text{Sn}_{1.03-x}\text{Ag}_x\text{Te}$ samples. 191

List of Tables

1.1	Typical values for transport properties, Seebeck coefficient (S), electrical conductivity (σ) and thermal conductivity (κ) in insulators, semiconductors, and metals at room temperature	10
1.2	Crystal structure of superionic compounds	25
2.1	Technical details of LFA 1000	68
3.1	The details of various Ag_2Te samples used in this study are given here. The sample name is given in the first column. Here, BS represents samples prepared by ball-milling followed by sintering of the cold-pressed pellets at 673 K for 24 h; HS represents samples prepared by hand-milling and sintering as in the BS series; CP represents samples prepared by ball-milling followed by cold-pressing (no sintering); and SSM represents an ingot sample prepared by solid-state melting. The second column (τ_m) gives the milling duration where applicable. The nominal stoichiometry of the starting Ag and Te powders in each case appears in the third column, and the last column (ρ_m) gives the density of the pellets on which the thermoelectric measurements are done.	77
3.2	Lattice parameters of all the samples and compared with reported values by Lee et al. [35]	82

3.3	Room temperature carrier concentration (n), electrical conductivity (σ), hall mobility (μ), thermopower (S) and power factor (PF).	88
4.1	Details of $\text{Ag}_2\text{Se}_{1+\delta}$ samples studied in this work.	109
4.2	Lattice parameters of all the samples and compared with reported values by J. Yu et al. [36]	114
5.1	Room temperature crystal structure (Monoclinic, $P2_1/c$) details obtained from Rietveld refinement analysis using two different previously reported models. [21,22]	134
6.1	Synthesis details and sample density (ρ_{exp})/ ρ_{th}	158

Contents

Declaration	v
Acknowledgments	vii
Abstract	xiii
List of publications	xvii
List of figures	xix
List of tables	xxxiii
1 Introduction	1
1.1 Motivation	1
1.2 Thermoelectricity	3
1.2.1 Seebeck Effect	5
1.2.2 Peltier Effect	6
1.2.3 Thomson Effect	6
1.3 Thermoelectric Efficiency	7
1.4 Transport properties	10
1.4.1 Electronic Transport Properties	10

1.4.2	Thermal Transport Properties	16
1.5	State of the Art	21
1.5.1	Heusler Alloys	21
1.5.2	Oxides	22
1.5.3	Clathrates and Skutterudites	22
1.5.4	Chalcogenides	23
1.6	Synopsis of this thesis work	34
2	Experimental Methods	37
2.1	Sample Synthesis	37
2.1.1	Mechanical Alloying	38
2.1.2	Solid-State Melting Method	41
2.1.3	Sample Processing For Transport Property Measurements	43
2.2	Characterization Techniques	44
2.2.1	Powder X-ray diffraction	44
2.2.2	Rietveld refinement	47
2.2.3	Electron Microscopy	48
2.2.4	Thermogravimetric analysis and Differential Scanning calorimetry (TGA and DSC)	56
2.3	Transport Property Measurement Techniques	59
2.3.1	Resistivity and Seebeck measurement set up (LSR-3)	59
2.3.2	Hall Carrier Concentration	61
2.3.3	Laser Flash Analyzer (LFA)	65
2.4	Electronic band calculations	69
2.4.1	Ag ₂ Te	69
2.4.2	SnTe	70
3	Synergistic approach towards a reproducible high zT in n-type and p-type superionic thermoelectric Ag₂Te	73

3.1	Introduction	73
3.2	Sample Synthesis and Nomenclature	75
3.3	Characterization and transport property measurement	78
3.4	Results and Discussion	79
3.4.1	Sample Characterization	79
3.4.2	Electrical conductivity and Thermopower	84
3.4.3	Estimation of critical temperature and critical current density in Ag_2Te	92
3.4.4	Power Factor	93
3.4.5	Electronic band structure	93
3.4.6	Effect of thermal cycling in Ag_2Te cold-pressed samples	95
3.4.7	Thermal transport	96
3.4.8	Thermoelectric figure-of-merit zT	104
3.5	Summary and conclusions	106
4	Reproducible high thermoelectric figure of merit in Ag_2Se	107
4.1	Introduction and Motivation	107
4.2	Sample Synthesis and Nomenclature	108
4.3	Characterization and Measurement Details	110
4.4	Results and Discussion	110
4.5	Thermoelectric Properties	114
4.6	Summary and Conclusion	125
5	A facile room temperature synthesis method to prepare an inorganic ductile superionic sulphide with high figure of merit	127
5.1	Introduction and Motivation	127
5.2	Experimental Details	130
5.2.1	Sample Synthesis Using Hand Grinding and cold pressing (HCP)	130
5.2.2	Sample Synthesis Using Melting Method	131
5.2.3	Characterization Techniques	132

5.3	Results and Discussion	132
5.4	Transport properties	145
5.5	Summary and Conclusion	151
6	Development of nanostructured bulk SnTe with enhanced thermoelectric prop- erties	153
6.1	Introduction and Motivation	153
6.2	Experimental Details	157
6.3	Results and Discussion	159
6.3.1	Characterization	159
6.3.2	TE properties of Sn _{1.03} Te	166
6.3.3	Electronic Transport Properties of Sn _{1.03-x} Ag _x Te (x = 0, 0.03, 0.06, and 0.09)	171
6.3.4	Thermal Transport and Figure of Merit of Sn _{1.03-x} Ag _x Te (x = 0, 0.03, 0.06, and 0.09)	175
6.4	Summary and Conclusion	182
7	Summary and Conclusion	183
A	Thermoelectric Properties Of Sn_{1.03-x}Ag_xTe Ingot Samples	189
A.1	189
B	Computational Details and Two Valence Band Model	193
B.1	Computational Details	193
B.2	Two Valence Band Model	193
	Bibliography	197

Chapter 1

Introduction

1.1 Motivation

One of the greatest challenges facing humanity in the 21st century is to meet the world's increasing energy requirements while reducing greenhouse gas emission [37]. Therefore, it is important to discover efficient renewable energy methods to reduce reliance on fossil fuels. The most recent global energy consumption spectrum is shown in Figure 1.1 [1]. It indicates that in 2022, 84.3% of our energy requirements are met through natural reserves: oil, coal, and natural gas which have limited availability on earth and may get exhausted in another 100 years or so. Hence, increasing focus on renewable energy research is also urgent, which is currently limited to hydropower, nuclear, wind energy, solar, bio-fuels etc. Other than the limited amount of energy supply from current energy resources, significant losses in the form of heat occurs throughout the energy supply chain, which further reduces the overall efficiency of both devices and energy sources.

The production of useful energy from omnipresent or lost energy is called "energy harvesting" (EH) and has gained significant attention to fulfill energy requirements of the world. As a consequence, the increased scientific interest in this field led the discovery of wearable devices, portable medical kits, flexible electronics, etc. Thermoelectric (TE) energy harvesting is currently rising in popularity in the scientific community. The TE devices produce

useful electrical energy from waste heat [38]. Interestingly, by supplying an external electric current the same device can also work as a refrigerator [39]. According to U.S. energy flow record [40], about 65% of energy gets wasted in the form of heat. Even if the 10% of it can be harvested to produce clean electricity that would make the whole energy system more efficient and save the environment from increasing temperature. TE finds applications in heat recovery from automobiles, utilities (burning coals and natural gas) and chemical plants. Several advantages of TE energy harvesting technique include their compact design, robustness, zero gas emission, noiseless and maintenance free operation. This makes the TE devices a more attractive renewable energy source. NASA has been using the TE generators for their deep space projects which use Radioisotope Thermoelectric Generators (RTGs) that produce nearly 300 W power and has been running uninterrupted for the last 40 years. [41]. Lack of any moving parts and hence their vibrationless operation attracts their application as cooling units in sensitive scientific instruments like laser systems, etc [42, 43].

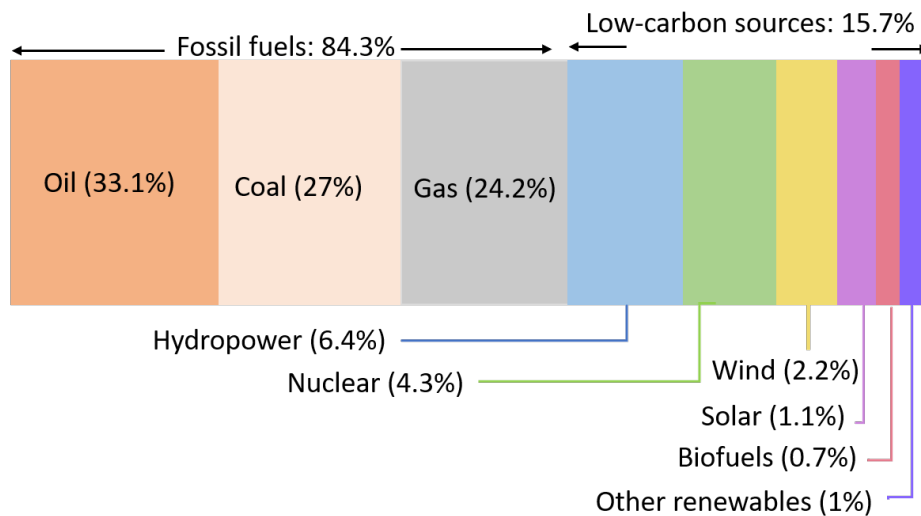


Figure 1.1: Global energy consumption spectrum for year 2022. *Figure regenerated from Ref [1].*

However, due to their low efficiency, the current state-of-the-art thermoelectric generators (TEGs) are only used in some niche applications, such as deep space missions, [2] high-end automobiles for climate control car seats, etc. This motivates the TE research community to work for further development of the field. Recently, the hybrid photovoltaic

(PV)-thermoelectric generator (TEG) has gained attention due to the improved efficiency of PVs resulting from the heating control provided by TEGs [44]. Hence, TE research has been growing very fast in the last decade, where many new TE materials have been discovered with efficiencies comparable to or little less to the commercial PVs [45–48]. Figure 1.2 shows the advancement in TE material research from 1950 to 2017, where chalcogenides are among the most studied TE materials; these include metavalent (PbTe, GeTe, SnTe, etc) [49], superionic (Cu_2X and Ag_2X , $\text{X} \equiv \text{Chalcogen}$) [8], Bi_2X_3 based alloys [50], etc., with around 10% experimental and 16% theoretical conversion efficiencies. But the lead toxicity, use of high cost elements like Ge, and sample instability and hence the irreproducible TE properties are additional challenges besides increasing the TE energy conversion efficiency. Since there is no upper limit on the TE figure of merit (see section 1.3), the working efficiency of TE materials can be enhanced further, which will bring down the fabrication cost, making TE devices more affordable for day-to-day use.

In this thesis, we studied two classes of chalcogenide TE materials: superionic and metavalent, with major focus on attaining reproducibility, improving the TE properties, and avoiding toxic materials, e.g., finding an alternative for Pb containing TEs based on PbTe. This chapter deals with some necessary concepts required for understanding the current research in TE materials, and ways to improve the TE efficiency.

1.2 Thermoelectricity

Thermoelectricity refers to the reversible conversion of heat into electricity. It was discovered by Thomas Johann Seebeck in 1821. When two dissimilar metal wires are joined at their ends to form junctions; and one of the junctions is heated with respect to the other, a current flows through the circuit, as shown in Figure 1.3(a), signifying conversion of heat into electricity. This effect can be used to generate electricity when the two dissimilar metal wires are replaced by n- and p-type semiconducting blocks or legs, such that the resulting voltage is significant enough to power a load connected in series, as shown in Figure 1.3(b). This device is called a thermoelectric generator (TEG). A single TEG consisting of a pair

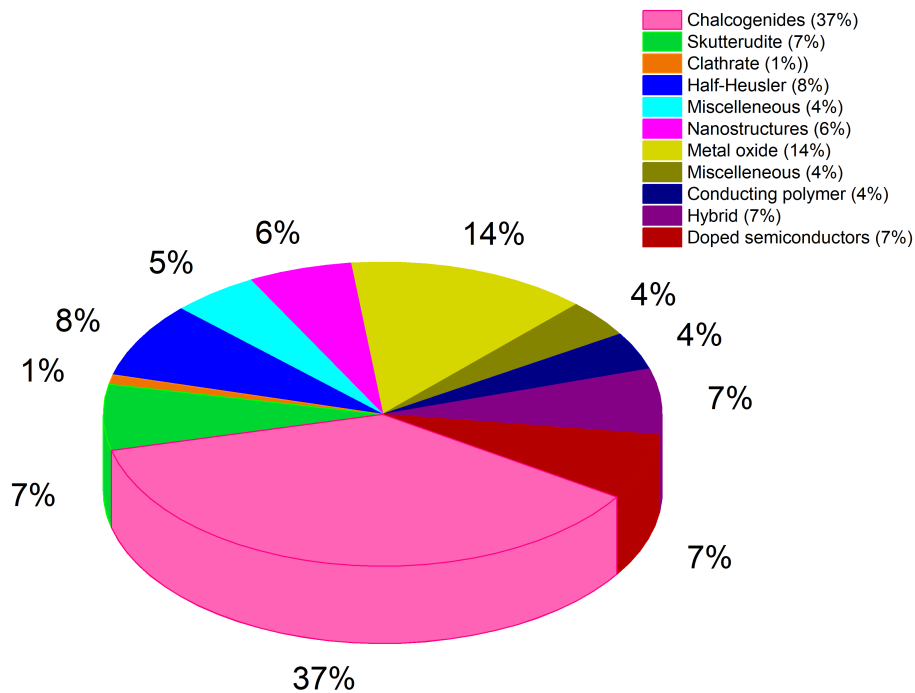


Figure 1.2: Pie diagram showing development in TE materials from 1950 to 2017 [2].

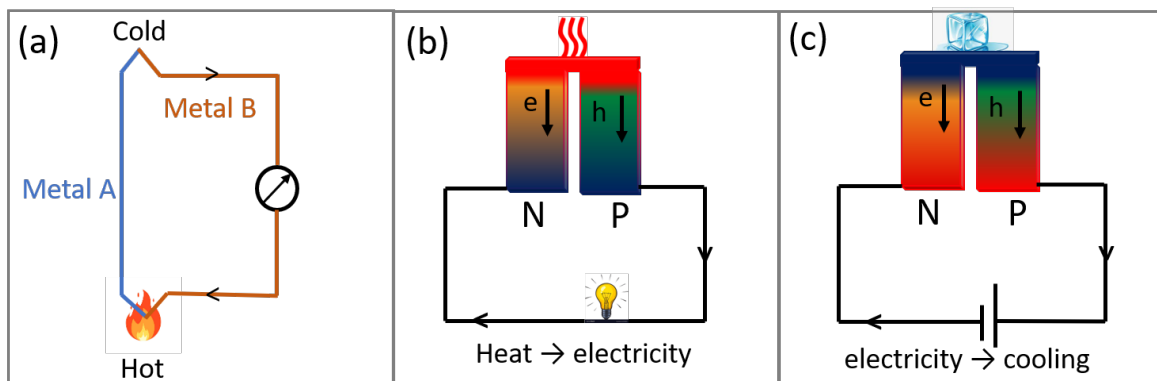


Figure 1.3: Schematic diagram for (a) thermoelectric effect, (b) thermoelectric generator, and (c) thermoelectric refrigerator.

of n-type and p-type legs can generate power up to 125 W [38]. However, for practical applications, an array of n- and p-type legs are connected electrically in series and thermally in parallel to generate electrical power output up to 5 kW. Conversely, passing an external electric current in the circuit produces cooling at one of the junctions with respect to the

other. This is known as the Peltier effect and it can be used in designing Peltier coolers or refrigerators, a schematic of the same is shown in Figure 1.3(c).

1.2.1 Seebeck Effect

The Seebeck effect is the underlying mechanism on which the thermoelectric generators are (TEGs) based [51]. The Seebeck effect refers to the appearance of a voltage in the presence of a temperature gradient across the ends of a metallic or semiconducting block as shown in Figure 1.4. The voltage generated is directly proportional to the temperature gradient and the constant of proportionality is known as Seebeck coefficient. Thus, the Seebeck coefficient, $S = \Delta V / \Delta T$, where ΔV is the voltage obtained when a ΔT temperature difference is applied. Sometimes, S is also called the thermopower, depicting the relationship between temperature (thermo) and electricity (power).

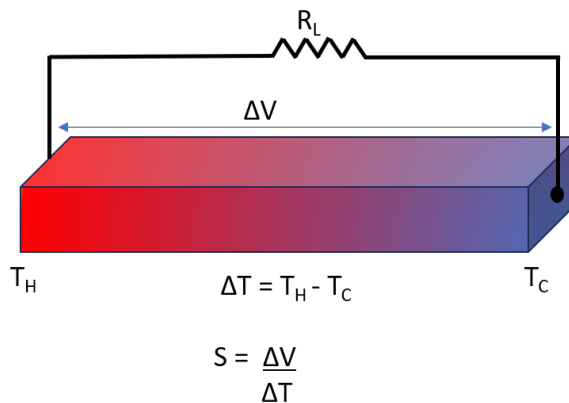


Figure 1.4: Schematic diagram for Seebeck effect.

The Seebeck voltage appears as a consequence of the diffusion of charge carriers from the hot end to the cold end of a material. Hence, the sign of S depends on the type of majority charge carriers present in the material. For p-type materials (holes as majority charge carriers), the Seebeck voltage is positive, and similarly for n-type materials (electrons as majority charge carriers), the Seebeck voltage is negative. However, the negative (positive) sign of the Seebeck coefficient does not necessarily mean the carriers are electrons (holes). For example, in a multiband semiconductor where both types of charge carriers are present, the

sign of the Seebeck coefficient depends on other factors as well including the relative carrier concentrations, of the two types of carriers, band curvatures and the band degeneracies.

1.2.2 Peltier Effect

The Peltier effect is the underlying mechanism of a thermoelectric refrigerator. When a finite current is passed across the n- and p-type semiconductors connected electrically in series, cooling is produced at one of the junctions with respect to the other, as shown in Figure 1.3 (c). At a microscopic level, one can understand this as follows: the application of a potential difference causes the charge carriers to drift. These moving charge carriers carry heat with them, producing a cooling effect at the starting end. This effect was discovered in 1834 by J.C. Athanase Peltier. For a single conductor, the heat absorbed per unit time at its end is defined as,

$$\dot{Q} = \Pi I \quad (1.1)$$

Here, Π represents the Peltier coefficient of the material, and I represents the current passing through it. Similar to the Seebeck coefficient, the Peltier coefficient for a p-type semiconductor is generally positive, while for an n-type semiconductor negative. There is a direct correlation between the Seebeck coefficient and the Peltier coefficient, given by $\Pi = TS$. The heat flow rate (\dot{Q}) may also be affected by Joule heating or a temperature gradient, as discussed below.

1.2.3 Thomson Effect

The Thomson effect was discovered by Sir Lord Kelvin in 1851. Under the conditions of simultaneous temperature gradient ΔT and current density (J) in the conductor, the heat absorbed or rejected per unit volume, after neglecting the Joule heating, can be defined by the relation:

$$\dot{q} = -\Lambda J \Delta T \quad (1.2)$$

Here Λ is the Thomson coefficient. Its relation with Seebeck and Peltier coefficients given by equation,

$$\Lambda = \frac{d\Pi}{dT} - S \quad (1.3)$$

1.3 Thermoelectric Efficiency

A thermoelectric generator (TEG) is equivalent to a heat engine where the charge carriers act as the fluid that carries the heat. We first consider a single-leg TEG which basically consists of a single n-type or p-type element whose end are at maintained at temperatures T_h and T_c , leading to a temperature gradient ΔT due to which the resulting Seebeck voltage drives a current through an external load R_L (see, Figure 1.4). However, due to the finite electrical resistance of the thermoelectric material, the voltage across the load will be less than the open-circuit voltage ($V = IR_L$) by an amount equal to the voltage drop in the internal resistance. The maximum efficiency in this scenario is obtained when the load resistance is equal to the internal resistance, known as load matching condition. If one assumes ΔT to be small and the physical properties of the material to be constant across the length, the thermoelectric conversion efficiency (η) can be expressed as [38]:

$$\eta_{\max} = \frac{\Delta T}{T} \frac{\sqrt{1 + z\bar{T}} - 1}{\sqrt{1 + z\bar{T}} + \frac{T_c}{T_h}} \approx \frac{\Delta T}{T} \frac{\sqrt{1 + z\bar{T}} - 1}{\sqrt{1 + z\bar{T}} + 1} \quad (1.4)$$

Here, $\Delta T/T$ is the Carnot efficiency (η_{\max}) and η remains a small fraction of η_{\max} unless the dimensionless quantity zT in eq. (1.4), called the thermoelectric figure-of-merit of the material, becomes sufficiently large ($\eta \rightarrow \eta_{\max}$ as $zT \rightarrow \infty$). The approximate variation of η with zT for various values of ΔT is shown in Figure 1.5 where $T_{ave} = (T_h + T_c)/2$ is the average temperature. However, zT depends of the contra-related properties, namely, electrical conductivity (σ), Seebeck coefficient (S) and thermal conductivity (κ) of the material and is given by the equation:

$$zT = \frac{\sigma S^2 T}{\kappa} \quad (1.5)$$

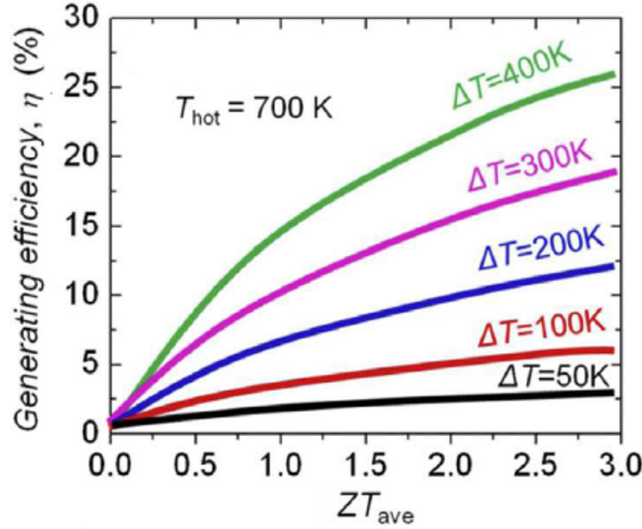


Figure 1.5: TEG efficiency variation with ZT_{ave} for different cold end temperatures while hot end kept at 700 K, adapted from Ref [3].

As is evident from eq. (1.5), for a high value of zT , the material should be a simultaneously good conductor of electricity (high σ) and a poor conductor of heat (low κ). But this is counterintuitive since at any temperature T , the electrical conductivity and the electronic component of κ (designated as κ_e) are directly related via the Wiedemann-Franz law:

$$\kappa_e = LT\sigma \quad (1.6)$$

where L is a constant called the Lorentz number whose numeric value is $2.44 \times 10^{-8} \text{ V}^2 \text{ K}^{-2}$ for metals. Similarly, high σ prohibits a high Seebeck value, the two having opposite tendencies: while Seebeck effect creates a voltage gradient, high σ tends to nullify it. This is nicely exemplified in Figure 1.6 where σ , S , σS^2 (called the power factor and designated as PF), and κ are plotted as a function of carrier concentration (n) using the Single Parabolic Band (SPB) mode approximation. Within the simplified SPB model, S is given by:

$$S = \frac{8\pi^2 k_B^2 m^*}{3eh^2} \left(\frac{\pi}{3n} \right)^{\frac{2}{3}} \quad (1.7)$$

$$\sigma = ne\mu \quad (1.8)$$

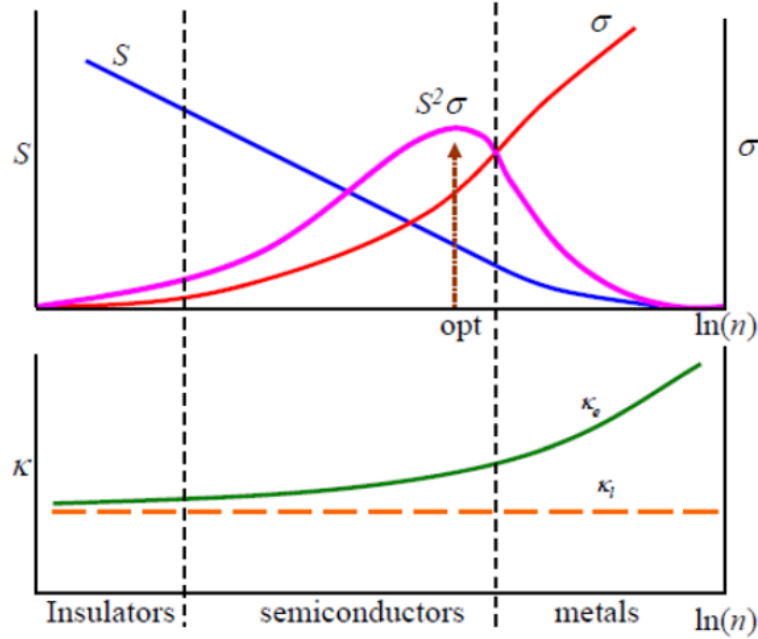


Figure 1.6: Relationship between S , σ , $S^2\sigma$, κ_e and κ_l with carrier concentration, adapted from Ref [4].

Here k_B is the Boltzmann constant, m^* is density of state effective mass, e is the electronic charge, h is Planck constant, n denotes the carrier concentration, and L is Lorentz number. For small n (bad insulators), S is very high but σ is very low and consequently the PF is also very low. In the other extreme of high values of n (a metal), σ is very high but S is very low, and, once again, the resulting PF is low. In the intermediate range of values of n , which extends from 10^{18} to 10^{20} cm^{-3} depending on the material under consideration, the PF attains its peak value. This is the optimum window over which high PF can be expected. Hence, the first step in the process of improving the PF of any new thermoelectric material is to find the optimal carrier concentration.

Eq. (1.4) can also be used for the TEG shown in Figure 1.3(b) where both n-type and p-type elements are connected in series electrically; however, in this case zT replaced by the effective figure-of merit of the device, which is given by the expression [52, 53]:

$$Z = \frac{S_{np}^2}{\left[\left(\frac{\kappa_n}{\sigma_n}\right)^{0.5} + \left(\frac{\kappa_p}{\sigma_p}\right)^{0.5}\right]^2} \quad (1.9)$$

where S_{np} is the thermopower of the whole module, and $\kappa_{n/p}$ and $\sigma_{n/p}$ are the thermal and electrical conductivities of the individual legs. Thus, high zT of the individual legs is the starting point in the search of a good TE material.

1.4 Transport properties

Transport properties can be categorized into two parts, electronic and thermal. Apart from a few exceptions, the average values of the three primary transport quantities for insulators, semiconductors and metal are listed in table 1.1.

Table 1.1: Typical values for transport properties, Seebeck coefficient (S), electrical conductivity (σ) and thermal conductivity (κ) in insulators, semiconductors, and metals at room temperature

Transport property	Insulators	Semiconductors	Metals
$ S $ (μVK^{-1})	~ 1000	~ 200	~ 5
σ (S cm^{-1})	$\sim 10^{-16}$	$\sim 10^3$	$\sim 10^5$
κ ($\text{W m}^{-1} \text{K}^{-1}$)	≤ 1	≤ 100	≥ 300

We will separately discuss these transport properties in great details in the following.

1.4.1 Electronic Transport Properties

Electrical Conductivity

Electrical conductivity (σ) is a measure of the ability of a material to conduct electric current. The easier the passage of electricity, the higher the electrical conductivity. For example, metals such as silver, aluminum, etc, are good conductors of electricity. As mentioned in the previous section, σ can be expressed using equation (1.8), where n denotes the charge carrier concentration, e represents the electronic charge, and μ represents the carrier mobility. For a given value of μ , the variation of σ with n is shown in Figure 1.6. n is negligible for insulators, which is why they show extremely low σ . Metals have larger n (10^{22} cm^{-3}), resulting in their very high electrical conductivity. In semiconductors, n varies from 10^{14} cm^{-3} (intrinsic semiconductors) to 10^{20} cm^{-3} (highly doped or degenerate semiconductors).

Carrier mobility μ determines the ability of charge carriers to conduct, which depends

upon their effective mass (m^*) and relaxation time (τ) via the relation $\mu = e\tau/m^*$. Theoretically, m^* can be calculated from the curvature of the electronic band near the Fermi energy using the expression:

$$m^* = \frac{d^2E}{\hbar^2 dk^2} \quad (1.10)$$

where E is the energy and k is the wave vector associated with the Bloch electrons.

Bands with steep dispersion near the Fermi energy signify low carrier effective mass, and hence, high carrier mobility. High mobility materials are desirable for TE applications. However, with increasing temperature, depending on the scattering mechanism involved, mobility decreases following a $T^{-\alpha}$ dependence. For example, for the alloy scattering and electron-phonon (lattice) scattering α takes values 1/2 and 3/2, respectively. The impurity or defect scattering, on the other hand, weakens upon heating, resulting in a negative value of α which can be shown to be equal to -3/2.

Using the Matthiessen's rule given by equation (1.11), the effective temperature dependence of mobility can be estimated when different scattering mechanisms are simultaneously present [54].

$$\frac{1}{\mu} = \frac{1}{\mu_{impurities}} + \frac{1}{\mu_{alloy}} + \frac{1}{\mu_{lattice}} + \dots \quad (1.11)$$

In thermoelectrics, the quantity μ is one of the key parameters for maximizing the TE performance of a material. For example, in p-type Bi_2Te_3 semiconductor, the zT has been enhanced to values as high as 1.8 by maintaining a high mobility value of $280 \text{ cm}^2 \text{ V}^{-1} \text{ s}^{-1}$ in the melt-spun samples with poor thermal conductivity [55]. Similarly, a zT of 2.5 was attained in p-type PbTe by maintaining a reasonably high mobility value of $80 \text{ cm}^2 \text{ V}^{-1} \text{ s}^{-1}$ despite alloying with SrTe [56]. In conclusion, the optimum value of carrier concentration and high mobility results in a high value of σ , which often leads to high PF values. We shall now look at the strategies for enhancing or maintaining high μ and hence σ .

Strategies for increasing the electrical conductivity

One way to enhance the power factor of a thermoelectric material is to increase its σ to reasonably high values without having a significant adverse effect on the Seebeck coefficient.

The highest σ can be achieved in single-crystalline materials, but they also exhibit very high lattice thermal conductivity, making them less desirable for TE applications. Therefore, polycrystalline TE materials are generally preferred.

In a polycrystalline material, the electrical conductivity can be increased by simultaneously increasing the carrier concentration (n) and carrier mobility (μ). Aliovalent doping can be employed to increase n , while creating coherent grain boundaries can enhance μ . Coherent grain boundaries offer negligible resistance to the flow of electrons. For example, Kim et al. reported that Bi_2Te_3 bulk polycrystalline samples, with coherent and semi-coherent grain boundaries, exhibit very high carrier mobility of $280 \text{ cm}^2 \text{ V}^{-1} \text{ s}^{-1}$ compared to a polycrystalline samples where incoherent grain boundaries lowers the value of μ to $190 \text{ cm}^2 \text{ V}^{-1} \text{ s}^{-1}$ [55].

Seebeck Coefficient

The Seebeck coefficient S is defined in Figure 1.4. Physically, S in a material can be understood as the entropy transfer per unit charge. Since zT is directly proportional to the square of the Seebeck coefficient, understanding the factors that affect the Seebeck coefficient of a material is important to design high zT thermoelectrics. This motivates researchers to find appropriate thermoelectric materials that can provide maximum output emf or voltage. For a semiconductor, Mott defined S as [57],

$$S = \frac{\pi^2 k_B^2 T}{2e} \left(\frac{1}{\mu} \frac{d\mu}{dE} + \frac{1}{n} \frac{dn}{dE} \right)_{E_F} \quad (1.12)$$

here k_B , e , μ , E , and n are, respectively, the Boltzmann constant, electronic charge, carrier mobility, energy and carrier concentration. We can see that, like σ , S also depends on n and μ , but with different functional forms. If a material shows a larger $\frac{d\mu}{dE}$ (carrier filtering) or $\frac{dn}{dE}$ (resonant states), then high S can be obtained. Under the SPB model approximation with electron-phonon scattering mechanism, S in equation (1.12) reduces to equation (1.6), which is often referred to as the Pisarenko relation. From equation (1.6), one can see S is directly proportional to density of state (DOS) effective mass, m_d^* and, T but inversely proportional

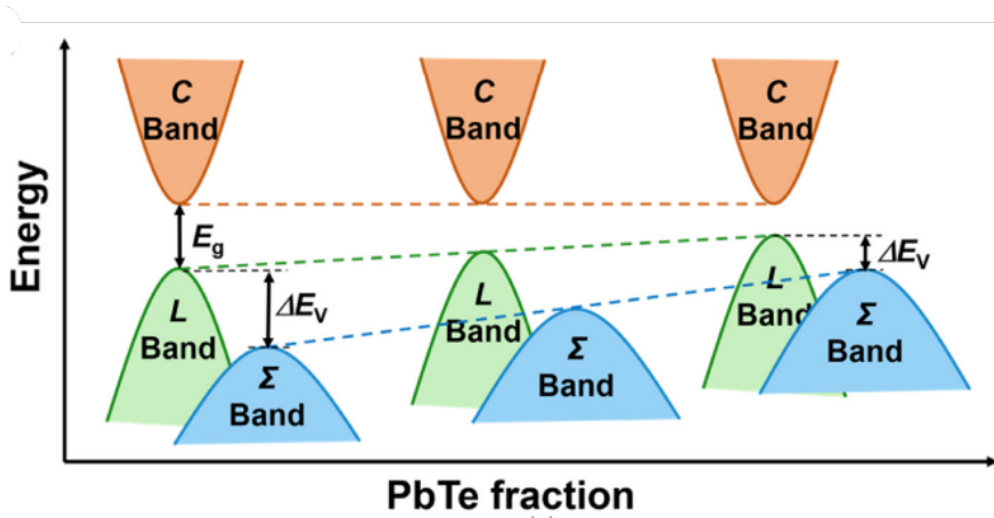


Figure 1.7: Schematic showing heavy hole valence band (Σ , with band degeneracy of 12) and light hole valence band (L, with band degeneracy of 4) getting converged with increasing Pb alloying in SnTe, figure adapted from Ref [5].

to the carrier concentration, n . The m_d^* can be expressed in terms of band effective mass, m^* as [49],

$$m_d^* = N_v^{2/3} m^* \quad (1.13)$$

where N_v is the valley degeneracy. A schematic diagram for understanding the band curvature and band degeneracy is shown in Figure 1.7.

Strategies for increasing the Seebeck coefficient

For high PF it is desirable to have a high Seebeck coefficient (S). There are several strategies reported for increasing S , and we discuss these briefly in this section.

1. Optimizing carrier concentration

Equation (1.6) implies that S can be increased by decreasing the carrier concentration through defect manipulation or chemical doping. The variation of S as a function of n is shown in Figure 1.6. However, in order to obtain a high value of PF, both σ and S should be high. This means that the carrier concentration cannot be reduced beyond an optimal value. The optimal carrier concentration varies across different materials, but it can be controlled through doping level and defect optimization. Optimizing the carrier concentration is the most common

approach to enhance the Seebeck coefficient and hence the PF value [58].

2. Resonant impurity states

Resonant impurity states, which are sharp distortions created in the density of states (DOS) by elemental doping in the host material (see Figure 1.8(a)), are known to significantly affect electronic transport when they appear near the Fermi level of the host material [59]. The introduction of resonant impurity states results in an additional, less dispersive band near the Fermi level of the host material. This induced flat band or sharp DOS significantly increase the overall S of the host material according to Mott equation (1.12) [57]. Along with the significant enhancement in S , the electrical conductivity of the material also remain high as it was for the host material resulting in high values of PF. Typically, the best results for achieving high PF due to increased S through resonant doping were reported for very dilute doping concentrations ($< 1\%$). Overall, resonant impurity states can have a significant impact on the electronic transport properties of a material, and their introduction can be used to tailor the Seebeck coefficient and power factor values of the host material.

3. Band Degeneracy

Band degeneracy (N_v), also known as valley degeneracy, is another way of enhancing S without compromising the high σ of a material when intervalley scattering is negligible. As is evident from equation (1.13), increasing m_d^* via N_v can increase S . N_v increases when multiple bands appear within a small energy range of a few $k_B T$. Materials that have a more symmetric crystal structure but possess carrier pockets at low symmetric points (for example, L-point and, Σ -point as in metavalent class of materials such as PbTe, SnTe, and GeTe) tend to have high band degeneracy [49]. For example, in SnTe, the Σ band with $N_v = 12$ lies within 0.35 eV below the valence band maxima at L-point. These bands can be easily made to converge by appropriate dopants, resulting in increased band degeneracy, see Figure 1.7. For example chemical doping in PbTe with Mg, Na, and other elements results in band convergence [60]. Schematic diagram in Figure 1.7 depicts the band degeneracy between light hole and heavy hole valence bands due to Pb doping in SnTe.

4. Energy Filtering Effect

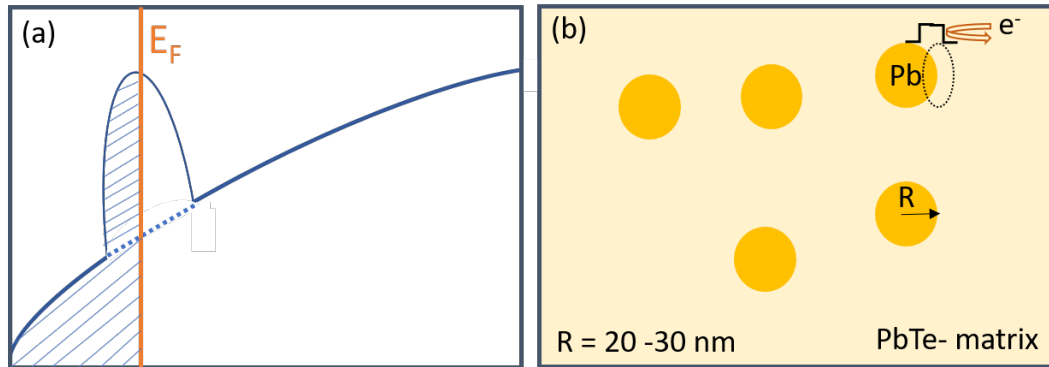


Figure 1.8: Schematic representation of (a) resonant impurity states and (b) charge carrier filtering via Pb nano-precipitates in PbTe matrix.

In the energy filtering (EF) effect, low energy charge carriers and minority carriers are selectively filtered, resulting in an overall enhancement of the Seebeck coefficient with negligible deterioration of electrical conductivity. It has been reported that materials with nanograined core-shell heterostructures enable, the selective scattering of low energy charge carriers by the potential barriers at the interface works as a carrier filter [61]. Heremans reported an enhanced Seebeck coefficient due to energy filtering using $\approx 30 \text{ nm}$ Pb nano-inclusions in PbTe bulk samples [62]. Similarly, grain boundaries in semiconductors become electrically active due to charge trapping in the gaped states localized at the interface and create a potential barrier (see Figure 1.8(b)). Now depending on the strength of the potential barrier, charge carriers can be reflected back and filtered out, allowing only the propagation of high-energy carriers. Additionally, these potential barriers can be utilized to control the flow of charge carriers in nanoscale devices, making energy filtering an important concept in the development of advanced electronic and thermoelectric devices.

The net result of the filtering process is that the average kinetic energy of electrons increases, which, in turn, enhances the Seebeck value. As the Seebeck coefficient (S) is a measure of the entropy carried per charge carrier, the increase in the average kinetic energy of electrons due to energy filtering, leads to an increase in the entropy carried per charge carrier, which, in turn, enhances the Seebeck coefficient.

1.4.2 Thermal Transport Properties

Thermal Conductivity

According to the Fourier's law of heat conduction, the rate of heat transfer per unit time is proportional to the negative of temperature gradient and area through which the heat flows. The constant of proportionality is known as the thermal conductivity of the specimen. Fourier's equation can be expressed as:

$$\dot{Q} = -\kappa A \frac{dT}{dx} \quad (1.14)$$

Here \dot{Q} is the heat flow measured in Watts (W). dT/dx denotes the temperature gradient across the positive x-axis; A is the cross section area normal to the heat flow, and κ refers to thermal conductivity. The negative sign in equation (1.14) signify that the temperature decreases along sample thickness. A schematic illustration of κ is shown in Figure 1.9 where T_1 and T_2 ($T_1 > T_2$) are the temperatures of the left and right ends of the sample of cross-sectional area and width w .

The most commonly used method for determining the thermal conductivity (κ) of thermoelectrics is through the measurement of thermal diffusivity (D) in steady state. The thermal conductivity can then be estimated using the formula $\kappa = D\rho_m C_p$, where ρ_m represents the mass density of the sample and C_p is its specific heat. For most semiconducting materials, C_p above room temperature tends to a constant value given by the Dulong-Petit limit. However, some materials with very high Debye temperature may have their C_p still increasing with temperature even above room temperature.

κ comprises two parts: thermal conductivity due to the lattice, called κ_l , and thermal conductivity due to the charge carriers, called κ_e . Due to high κ_e , metals conduct heat very quickly, while insulators are the opposite unless their lattice thermal conductivity is high as for example in the case of diamond. The high κ_e value of metals is due to their significantly higher electrical conductivity (σ) compared to the insulators. The σ and κ_e in a metal are related through the Weidemann Franz law given by equation (1.7).

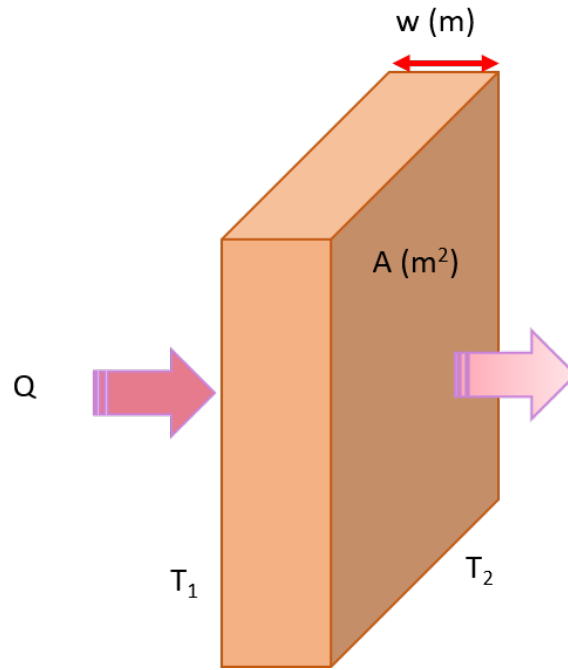


Figure 1.9: Illustration of thermal conductivity in terms of heat flow per unit time (\dot{Q}) and temperature gradient $T_1 - T_2$ across thickness (w) of a specimen of cross sectional area A .

For TE applications, most of the materials used are semiconductors having electron-phonon scattering as the dominant scattering mechanism. For such materials, the Lorenz number differ considerably from its ideal value of $2.44 \times 10^{-8} \text{ V}^2 \text{ K}^{-2}$ which is generally valid for metal. In semiconductors L is typically estimated by simulating the temperature dependent Seebeck coefficient under single parabolic band approximation, using the expression:

$$S = \frac{k_B}{e} \left(\frac{2F_1(\eta)}{F_0(\eta)} - \eta \right) \quad (1.15)$$

Here $F_j(\eta)$ is Fermi integral, defined as, $F_j(\eta) = \int_0^\infty \frac{\epsilon^j d\epsilon}{1 + \exp(\epsilon - \eta)}$ where ϵ denotes the reduced energy ($\frac{E}{k_B T}$) and η represents the reduced Fermi energy ($\frac{E_F}{k_B T}$). After finding η vs temperature from above equation, $L(T)$ can be easily determined by using expression,

$$L = \left(\frac{k_B}{e} \right)^2 \frac{3F_0(\eta)F_2(\eta) - 4F_1^2(\eta)}{F_0^2(\eta)} \quad (1.16)$$

Furthermore, the SKB model can be utilized to estimate $L(T)$ for semiconductors with non-parabolic bands, taking into account the band non-parabolicity factor [63]. The determination of κ_e using the Weidemann Franz law enables the estimation of κ_l , which is obtained by subtracting κ_e from the total thermal conductivity κ .

In addition, Slack's model predicts the thermal conductivity of any insulator by considering the fact that only acoustic phonons transport heat. Slack's equation can be used to theoretically calculate the minimum κ_l limit for a material having n atoms per unit cell [64].

$$\kappa_l = A \cdot \frac{\overline{M}\theta^3\delta}{\gamma^2 T n^{2/3}} \quad (1.17)$$

In this equation, \overline{M} represents the average atomic mass, θ is the Debye temperature, δ is the cubic root of the average volume per atom in angstroms, and γ denotes the Grüneisen parameter. The Grüneisen parameter measures the departure from harmonicity in a crystal and is experimentally determined from thermal expansion data. Even for a perfect crystal the thermal conductivity does not become infinitely large due to unavoidable anharmonicity associated with it. Notably, SnSe has been reported to exhibit strong anharmonicity along its a -crystallographic axis, resulting in an extremely high value of γ around 4.1. This anharmonicity contributes to the ultra-low thermal conductivity along the a -axis [65]. It is also evident from equation (1.17) that κ_l decreases with increasing temperature. This decreasing behavior is attributed to the anharmonic umklapp scattering processes of phonons [66] in crystalline materials.

In addition to lattice thermal conductivity, some small band gap semiconducting TE materials such as Bi_2Te_3 [55], PbTe [67], NbCoSb [68], among others, have a third thermal contribution arising from bipolar diffusion due to minority charge carriers. Separating the bipolar thermal conductivity from the total thermal conductivity can be a challenging task. For a comprehensive explanation of bipolar thermal diffusion, details can be found in an article by Wang et al. [69].

Strategies for decreasing thermal conductivity

The thermal conductivity of a material is influenced by the independent contributions of charge carriers, phonons, and bipolar diffusion. The contribution of charge carriers is optimized via n , similar to σ , whereas the contribution of bipolar diffusion in small band gap semiconductors is controlled by increasing n and/or widening the band gap through chemical doping. The contribution of phonons or lattice component can be obtained from equation (1.19).

$$\kappa_l = \frac{1}{3} c_v v_g \bar{l}_p \quad (1.18)$$

The specific heat, denoted by c_v , and the phonon group velocity, denoted by v_g ($v_g = \sqrt{F/M}$, F denotes bonding strength and M is the atomic mass), as well as the mean free path of phonons, denoted by \bar{l}_p ($v_g \tau_p$), are important parameters that contribute to the lattice thermal conductivity of a material.

In order to reduce the thermal conductivity due to phonons (κ_l), there exist many material engineering strategies, which are described as follows.

1. Nanostructuring

Researchers have investigated the TE performance of several nanostructured materials, such as nano-composites and superlattices, and have found that they outperform their bulk counterparts. This is because nanostructures strongly scatter heat-carrying phonons that have a mean free path length comparable to their size. For example, endotaxially embedded nanocrystals of alkaline earth telluride (5% CaTe) decreased the κ_l of the PbTe-1%Na₂Te system from 1.2 W m⁻¹ K⁻¹ to 0.43 W m⁻¹ K⁻¹ [70]. In addition, Venkatasubramanian et al. achieved a zT of 2.4 in a superlattice device of Bi₂Te₃/Sb₂Te₃ [71]. Roychowdhury et al. reported a huge improvement in the zT of 2.6 in a nano-structured bulk AgSbTe₂ [47]. More recently, zT of Ag₂Te have also been increased from 0.9 to 1.2 by reducing the lattice thermal conductivity to 0.32 W m⁻¹ K⁻¹ due to nanostructuring [72]. Therefore, nanostructuring has proved to be a very efficient strategy for lowering κ_l .

2. Alloying and point defect scattering

Alloying or doping with a small concentration of any element can efficiently reduce the lattice thermal conductivity of a host material. This reduction occurs as a result of mass fluctuations and induced local strains in the matrix of host material. When heavy elements are doped in place of lighter ones, the phonon group velocity decreases via $\sqrt{F/M}$, leading to a reduced κ_l . For example, in PbTe, the κ_l value reduced from $2.25 \text{ W m}^{-1} \text{ K}^{-1}$ to $1.25 \text{ W m}^{-1} \text{ K}^{-1}$ at room temperature by 2.5% Se doping due to mass fluctuation [60]. A significant reduction in κ_l due to alloying was also achieved in half-Heusler alloys by doping the massive Hf element [73]. With a higher doping percentage of foreign elements, nano or micro-precipitation may occur, which subsequently scatters more phonons of comparable mean free path. In a class of materials known as (TAGS-x), which includes $(\text{GeTe})_x(\text{AgSbTe}_2)_{1-x}$, ultra-low thermal conductivity is achieved due to point defect scattering in addition to scattering from nano-precipitates [74].

3. All-scale hierarchical nanostructuring (ASHN)

It combines the effect of point defects, nanostructures and grain boundary scattering effect all together to reduce the lattice thermal conductivity significantly. The local strains induced due to point defects and dislocations, nano-inclusions and mesoscale interface scatters the small, mid and long mean free path (\bar{l}_p) phonon, respectively. Great enhancement in zT of PbTe was achieved by Zhao et al. via all-scale hierarchical nanostructuring by Mg alloying and more than 100% decrement was obtained [75]. This concept is vastly used for every class of materials like chalcogenides [47, 72], half-Heusler alloys [76], skutterudites [77] and oxide [78]. The schematic representation of ASHN effect in scattering different range of mean free path phonon lengths is shown in Figure 1.10

There exist some materials which inherently possess very low lattice thermal conductivity due to their unique crystal structure, for e.g. Clathrates [79] and superionic compounds [80]. We will discuss about different class of TE materials in the subsequent section.

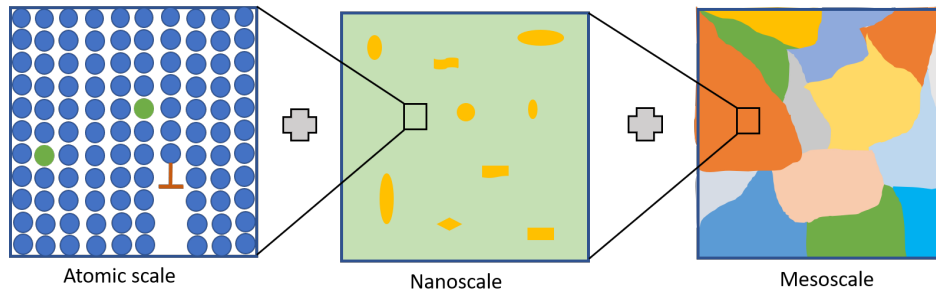


Figure 1.10: Schematic illustration of all-scale hierarchical nanostructuring (ASHN) for scattering of different mean free path lengths phonons. *Figure regenerated from Ref [6].*

1.5 State of the Art

There is a vast verity of TE materials with interesting properties. In this section we will discuss a few of state of the art class of materials.

1.5.1 Heusler Alloys

Heusler compounds crystallize in the face-centered cubic (FCC) phase with the chemical formula XYZ (half Heusler) and X_2YZ (full Heusler), where X and Y are transition metal elements and Z is a p-block element. This class of materials possesses great mechanical strength and excellent sample stability at high temperatures (above 1000 K). Moreover, moderately high electrical conductivity and their highly symmetric structure results in high band degeneracy, making these intermetallics potential candidates for high-temperature TE applications [81]. However, due to the presence of strong covalent bonding, their thermal conductivity is also typically high, making them difficult to use for TE applications unless κ_l is somehow reduced. However, by using some of strategies for reducing the lattice thermal conductivity, discussed in the previous section, one can improve the zT of these materials significantly. Indeed, in some half-Heuslers high zT value of exceeding 1 has been achieved , as in $(\text{Nb}_{0.6}\text{Ta}_{0.4})_{0.8}\text{Ti}_{0.2}$, where, by FeSb after introducing the defects like cation vacancies and appropriate doping, a peak zT of 1.6 at 1200 K has been reported [73].

1.5.2 Oxides

Oxide thermoelectrics have gained significant attention due to their various advantageous features such as low cost, environment-friendly nature, and structural stability at high temperatures. However, despite these benefits, zT of these materials is difficult to enhance due to their low electrical conductivity and high thermal conductivity [82]. The most promising oxide thermoelectric materials to date are n-type ZnO, SrTiO₃, and CaMnO₃ [83], as well as p-type Ca₃Co₄O₉ [84]. Bi-doped Ca₃Co₄O₉ single crystals have achieved a high zT of 0.9 at 973 K [85]. Polycrystalline NaCo₂O₄ with Cu doping at Co site resulted zT value of 0.5 at 573 K for Na(Co_{1-x}Cu_x)₂O₄ composition [86]. In addition, Al-doped nanocrystals have exhibited a significant enhancement in zT up to 0.44 at 1000 K for n-type ZnO [87]. Overall, oxide thermoelectric materials exhibit great potential as thermoelectric candidates due to their structural robustness and environmentally friendly nature.

1.5.3 Clathrates and Skutterudites

There are inorganic materials that have open crystal structure frameworks in which a guest atom can reside [88]. The foreign guest atom is loosely bound to the host and rattles inside the oversized voids in their crystal structure. This rattling gives rise to low energy optical phonon modes, which interact with the heat-carrying long-wavelength acoustic phonons of the host material, resulting in an increased phonon scattering and, therefore, a low thermal conductivity. However, electronic transport occurs through the covalently bonded frameworks of the host matrix, providing an uninterrupted electronic motion. As a result, these materials are also known as phonon glass electron crystals (PGEC) [88], a term first introduced by Slack [89]. Examples of such materials include clathrate Ba₈Ga₁₆Ge₃₀ [90] and filled skutterudite Ba_{0.08}La_{0.05}Yb_{0.04}Co₄Sb₁₂ [91], which show high zT values of 1.35 at 900 K and 1.8 at 800 K, respectively.

1.5.4 Chalcogenides

This class of compounds offers a variety of crystal structures. For example, at room temperature, PbTe and SnTe stabilize in cubic, while GeTe and SnSe stabilizes in rhombohedral and orthorhombic forms, respectively. These compounds are very interesting and find applications in phase change materials [92], topological insulators [93], and thermoelectric energy conversion [94]. In fact, this is the most studied class of compounds in the thermoelectric research for low and mid-temperature range applications. The name "chalcogenides" originates from the three chalcogen atoms S, Se, and Te. Starting from their elemental forms, such as Te (a p-type semiconductor), they exhibit superior thermoelectric performance with $zT \approx 1$ [95–97]. Many studies have achieved $zT \approx 2$ in their binary compound forms, such as PbTe, PbSe, Cu₂Se, SnSe, and Bi₂Te₃ [55, 75, 80, 98, 99]. Moreover, in ternary chalcogenides, such as AgSbTe₂, Roychowdhury et al. reported a very high zT of 2.6 at 573 K [47]. It is advantageous to work with chalcogenides due to the sample stability and ease of tuning to obtain n-type and p-type behavior with appropriate doping. Chalcogenides TEs usually consist of heavy elements, large anharmonicity and soft chemical bonding, which are responsible for their low thermal conductivity [49].

In the chalcogenide class of compounds, there are two categories which are studied in this thesis work: superionic materials and metavalent compounds. Within this subset of materials, we will focus on two specific types: silver chalcogenides (Ag₂X, where X = S, Se and Te) in the superionic category, and SnTe in the metavalent category.

Superionic Compounds

After Slack's concept of PGEC where one obtains a glass-like thermal conductivity, it was discovered in 2012 that thermal conductivity beyond the glass limit can be realized in superionic materials [100]. As a result, this class of materials are called phonon-liquid electron-crystal (PLEC). The PLEC class includes materials such as copper chalcogenides Cu_{2- δ} X (X = S, Se, Te) [80, 101], silver chalcogenides Ag_{2- δ} X (X = S, Se, Te) [19, 20, 72, 102, 103], Ag-Agyrodites [104], Cu-Agyrodites [105], and AgCrSe₂ [106].

The common feature of superionic compounds is their anomalously high ionic conductivity compared to other solid materials. Superionic compounds are also known as mixed ion conductors. Ionic conductivity of a good superionic conductor falls in the range of $\sigma_i \approx 10^{-1}$ to 10^0 S cm⁻¹. [107] For comparison, the electronic conductivity of metals varies from $\sigma_e \approx 10^4$ to 10^6 S cm⁻¹. [107] The origin of the high ionic conductivity of these materials is related to the migration of one type of sublattice inside the framework formed by the rigid sublattice. Due to the availability of a large number of vacant sites in the rigid framework compared to the number of ionic entities in the composition, this leads to unimpeded ion migration via hopping from one vacant site to another. [8, 107]

At low temperatures, both the cations and anions occupy fixed lattice sites in the crystal structure and stabilize in a low-symmetry phase, such as monoclinic or orthorhombic. However, as the temperature increases, they undergo a structural transition to a more symmetric phase, usually a cubic space group. The details of the crystal structures of a few superionic compounds are shown in table [1.2].

The superionic transition is also called as diffuse transition or Faraday transition [108]. In the superionic phase, while the anions form a rigid sublattice, the cations become liquid-like [100], as shown in Figure 1.11. The liquid-like flow of cations occurs via hopping over the interstitial sites or voids in the anionic sublattice [8]. These compounds have gained significant attention recently due to their high zT. In these compounds, high zT value of up to 2 has been reported [47, 56, 98].

The unique, part-liquid part-solid, hybrid behavior of superionic compounds

The hybrid state of mixed liquid-like and crystalline species in superionic compounds significantly affects their thermal and electronic properties. The mobile sublattice is weakly bonded to the rigid sublattice, resulting in high disorder and enhanced phonon scattering, which lowers the lattice thermal conductivity (κ_l). Due to melting of one of the sublattices, the specific heat of superionic materials lowers below the Dulong-Petit limit per formula unit, as reported for Cu₂Se [100], Cu₂S [23], and Ag₉GaSe₆ [109]. As a consequence of increased phonon scattering due to the mobile sublattice, these materials exhibit exceptionally

Table 1.2: Crystal structure of superionic compounds

Compounds	Normal phase at RT	Superionic phase
Ag ₂ Te	Monoclinic P2 ₁ /c	$\xrightarrow{420\text{ K}}$ FCC Fm-3m
Ag ₂ Se	Orthorhombic P2 ₁ 2 ₁ 2 ₁	$\xrightarrow{406\text{ K}}$ BCC Im-3m
Ag ₂ S	Monoclinic P2 ₁ /c	$\xrightarrow{450\text{ K}}$ BCC $\xrightarrow{860\text{ K}}$ FCC Im-3m Fm-3m
Cu ₂ Te	α -Hexagonal and Rhombohedral P6/mmm and P3m1 $\xrightarrow{\alpha-\beta\ 454\text{ K}}$ β -Hexagonal, $\xrightarrow{\beta-\gamma\ 597\text{ K}}$ γ -Orthogonal, $\xrightarrow{\gamma-\delta\ 627\text{ K}}$ δ -Hexagonal	$\xrightarrow{\delta-\epsilon\ 848\text{ K}}$ ϵ -FCC Fm-3m $\xrightarrow{\delta-\epsilon\ 848\text{ K}}$ ϵ -FCC Fm-3m
Cu ₂ Se	Monoclinic C2/c	$\xrightarrow{400\text{ K}}$ FCC Fm-3m
Cu ₂ S	Monoclinic P2 ₁ /c	$\xrightarrow{400\text{ K}}$ FCC Fm-3m
Argyrodites	Orthorhombic P2na ₁	$\xrightarrow{310\text{ K}}$ FCC F43m

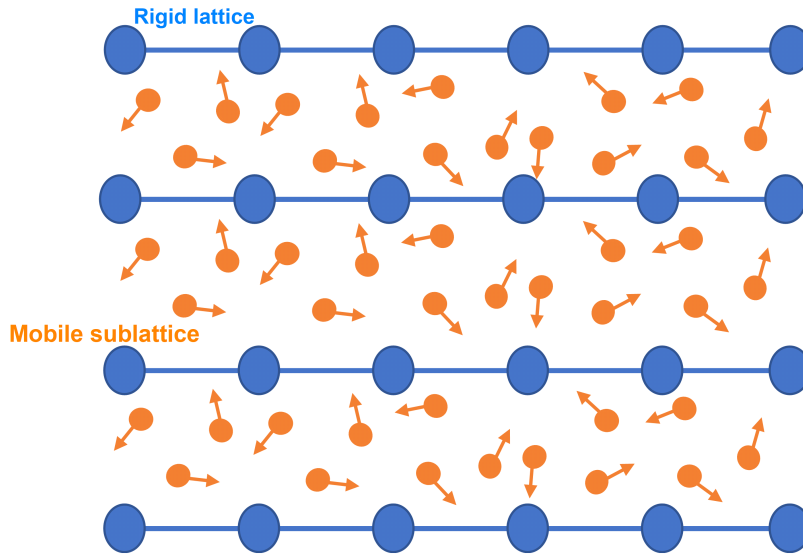


Figure 1.11: Part-liquid and part-solid hybrid crystal structure in a superionic material.

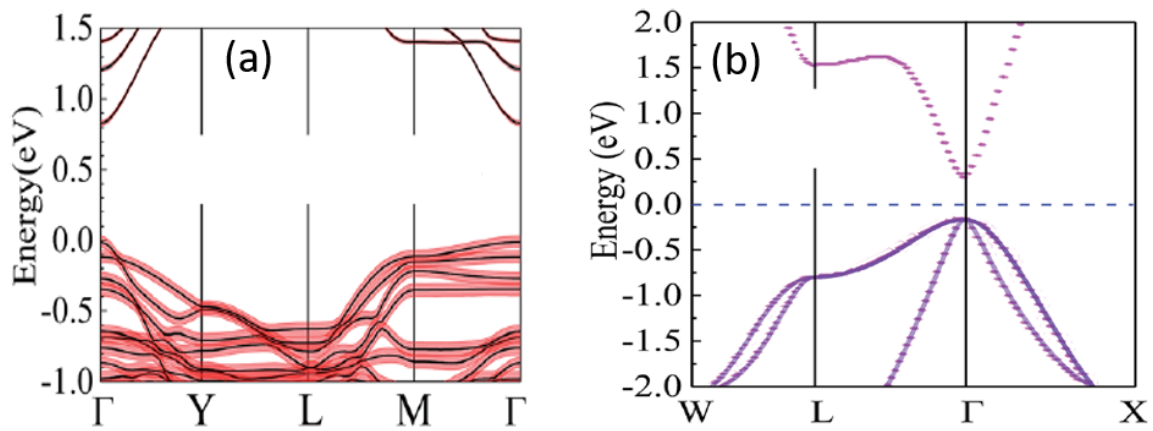


Figure 1.12: Electronic band calculations for (a) rigid phase, and (b) superionic phase of Cu_2Se . Reproduced from Ref[[7]]

ultra-low thermal conductivity of $0.2 \text{ W m}^{-1}\text{K}^{-1}$ - $0.7 \text{ W m}^{-1} \text{K}^{-1}$, which is lower than that of various state-of-the-art materials ($>0.8 \text{ W m}^{-1} \text{K}^{-1}$), see Figure 1.13(a).

On the other hand, the electrical transport in superionic compounds is governed by the crystalline rigid sublattice, which provides pathways for the charge flow. Band calculations have also shown that the bands residing near the Fermi level are from the rigid sublattice; for

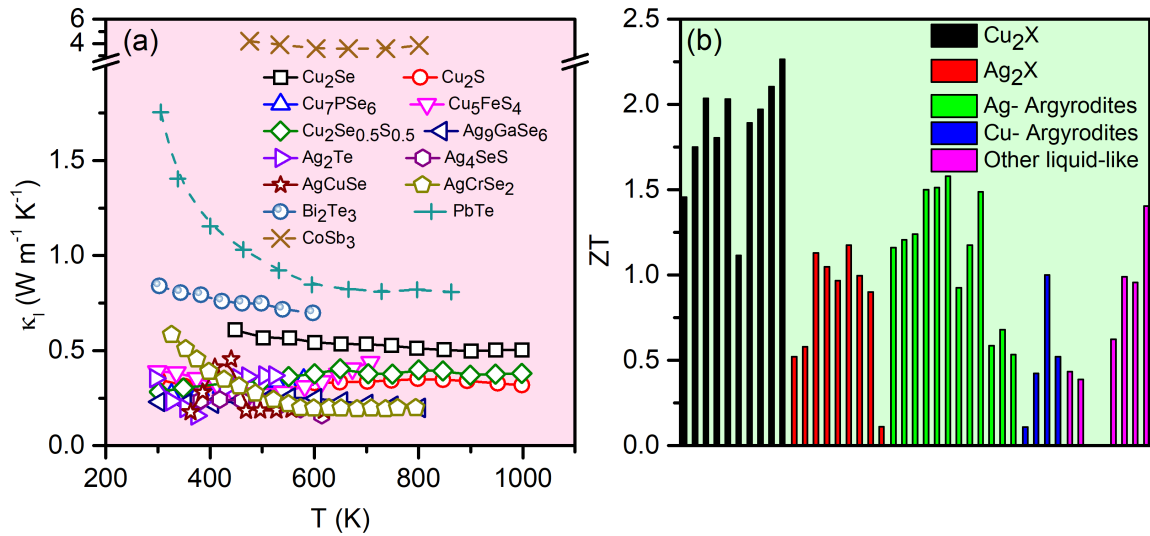


Figure 1.13: (a) Temperature variation of κ_l of superionic compounds and compared with the state of the art materials, and (b) shows the zT of superionic compounds reported in the literature. *Figure regenerated from Ref [8].*

example, from Se in Cu_2Se [7]. Sun et al. reported *ab initio* calculations using the Projector Augmented Wave (PAW) method in the Vienna *Ab initio* Simulation Package (VASP) to calculate the band structure of both the rigid phase and superionic phase of Cu_2Se . In the band calculations, they utilized the Perdew – Burke – Ernzerhof (PBE) type Generalized Gradient Approximation (GGA) as the exchange–correlation functional. [110] The triclinic structure (space group, P-1) was employed for the room temperature phase, while the cubic antiferroite structure was used for the high superionic phases in the calculation of their band structure, as shown in Figure 1.12. [7] From the band structure and the calculated electronic transport properties, it has been found that the mobile sublattice has negligible effects on electronic transport and only impedes the heat carrying phonons.

Hence, it can be seen that the existence of two types of sublattices favors superionic materials as suitable candidates for thermoelectrics.

Progress on TE properties of superionic materials

Cu_2X : The binary Cu_2X superionic compounds are extensively investigated systems. They exhibit very complex crystal structures at room temperature. For example, there are controversies regarding the room temperature phase of Cu_2Se , which has been reported to stabilize

in monoclinic [111], orthorhombic [112], and trigonal phases [113]. These materials undergo simultaneous structural and superionic phase transitions at elevated temperatures. Cu_2S undergoes two phase transitions at 373 K and 700 K, while Cu_2Se undergoes one structural transition at 400 K [113]. Cu_2Te possesses five successive phase transitions between 300 K and 900 K [8]. Due to the presence of unavoidable Cu vacancies, which occur in different concentrations depending on the bonding strength in Cu_2X , these materials form as p-type semiconductors with different ranges of hole carrier concentration. In 2012, Liu et al. reported the exceptional high zT of 1.5 at 1000 K in $\text{Cu}_{1-\delta}\text{Se}$ superionic material [100]. With further material processing, such as nanostructuring and chemical doping, zT of $\text{Cu}_{1-\delta}\text{Se}$ has been improved to 2.6 at 1030 K [114]. In 2014, He et al. reported the high zT of 1.7 at 1000 K in $\text{Cu}_{1.97}\text{S}$ [23]. For undoped Cu_2Te , zT of 1.1 at 1000 K has also been reported by He et al [115]. Furthermore, zT values above 2 has been reported for solid solutions of Cu_2X [116, 117].

Ag_2X : Silver chalcogenides, Ag_2X , exhibit similar superionic transitions as Cu_2X materials. However, their room temperature crystal structures are well known to be either monoclinic (Ag_2S or Ag_2Te) [118, 119] and orthorhombic (Ag_2Se) [36]. In the superionic phase, Ag_2S shows two structural transitions at 450 K and 800 K to BCC and FCC superionic phases, respectively [120]. In contrast, Ag_2Se and Ag_2Te transform to BCC and FCC around 400 K and 450 K, respectively [120].

Ag_2X materials are n-type semiconductors [19, 103, 121] in their room temperature phases, but Ag-deficient Ag_2Te exhibits p-type behavior in the superionic phase [122]. The band gap of the room temperature phase of Ag_2S is 1.1 eV, with a low carrier concentration of 10^{14} cm^{-3} , resulting in a very low zT value (<1), despite having ultra-low thermal conductivity [123]. However, in its superionic BCC phase, the band gap reduces to 0.42 eV, and the carrier concentration increases by orders of magnitude to 10^{19} cm^{-3} due to increased Ag interstitial defects, along with low thermal conductivity, resulting in a zT value of 0.55 at 575 K without any doping [123].

Unlike Ag_2S , Ag_2Se and Ag_2Te exhibit reasonably high values of zT in their regular structure (orthorhombic and monoclinic, respectively), below the superionic phase transition with zT values reaching as high as 1 in Ag_2Se [16, 19] and 0.6 in Ag_2Te [72]. In the superionic phase, Ag_2Se becomes metallic, and the Seebeck coefficient decreases significantly, resulting in a deteriorated zT value to <0.2 [13]. In contrast, Ag_2Te becomes a semiconductor with increased band gap (E_g) compared to rigid phase and shows enhanced thermoelectric performance in the superionic phase, with a zT value of around 1 at 550 K, obtained with the help of Pb alloying [121]. The high zT values in Ag_2Se and Ag_2Te at temperatures much lower compared to Cu_2X materials has been attributed to their high carrier mobility ($3000 \text{ cm}^2 \text{ V}^{-1} \text{ s}^{-1}$ [16, 124]) and comparatively low thermal conductivity, as shown in Figure 1.13.

Argyrodites: Argyrodites have complex crystal structure that displays superionic or liquid-like behavior. These materials have a chemical formula of the form $\text{A}_{12-n}^+ \text{B}^{n+} \text{X}_6^{2-}$, where A^+ is Li^+ , Cu^+ , or Ag^+ , B^{n+} is Al^{3+} , Ba^{3+} , Sn^{4+} , Si^{4+} , or Ge^{4+} , and X^{2-} is S^{2-} , Se^{2-} , or Te^{2-} [125]. They crystallize in orthorhombic, monoclinic, or cubic phases at room temperature, and undergo a structural transition to more symmetric hexagonal or cubic phase at higher temperatures [125]. In the liquid-like high-temperature phase, A cations become delocalized and disordered inside the rigid sublattice formed by B cations and Q anions. Argyrodites have a very complex and heavy unit cell, as well as a part-liquid sublattice, which results in an ultra-low thermal conductivity varying between $0.2 \text{ W m}^{-1} \text{ K}^{-1}$ to $0.4 \text{ W m}^{-1} \text{ K}^{-1}$ [104, 126–128]. It is worth noting that Cu-based Argyrodites exhibit p-type conductivity, while Ag-based Argyrodites show n-type conduction with higher mobility. This feature of n-type and p-type conduction is reminiscent of copper/silver binary chalcogenides discussed above. In p-type Argyrodites, a high zT value of above 1 at 800 K is reported for $\text{Cu}_{7.6}\text{Ag}_{0.4}\text{GeSe}_{5.1}\text{Te}_{0.9}$ [129]. In n-type Argyrodites, a zT value of 1.5 at 850 K is reported for Ag_9GaSe_6 [130].

Challenges associated with superionic materials

Despite very high TE figure-of-merit in some superionic materials, their practical utility is

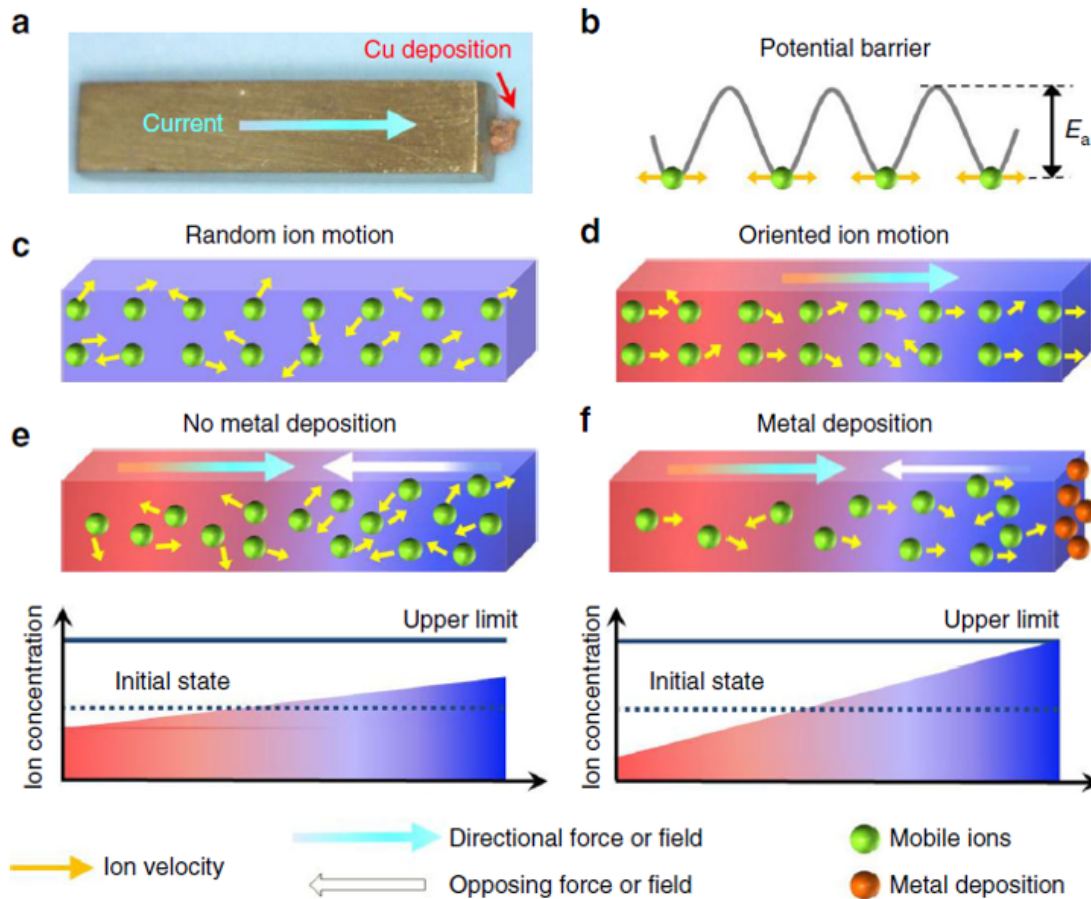


Figure 1.14: Ion migration and metal deposition in superionic materials (a) Metallic Cu deposition on the surface of Cu_2S induced by high current density, and (b to f) are schematics showing, (b) energy profile associated with ions, (c) random ionic motion in the absence of any external force resulting net zero ion flux, (d) oriented ionic motion under applied directional field due to which superionic materials either reach, (e) steady state without metal deposition, or (f) deposits metal (Cu), if local Cu concentration reaches a critical value determined for the stability of superionic material. *Figure adapted from Ref [9].*

limited due to sample degradation issue, which arises due to liquid-like flow of cations in the presence of applied external electric field or temperature gradient, see Figure 1.15. Dennler et al. discussed in their review about the sample degradation of Cu_2X family of superionic compounds at high temperatures and under high current density (J) values [80]. Under a thermal or electric field gradient, the cations diffuse to the colder end or to the positive electrode and once their concentration exceeds the solubility limit, they are extruded out from the sample in the form of flakes or wires as shown in Figure 1.15 for the specific case of Ag_2S and $\text{Zn}_{12.8}\text{Sb}_{10}$. The schematic shown in Figure 1.14, explains the mechanism of ion migration in superionic materials.

The phase stability at a given temperature in the superionic phase is determined by threshold voltage V_C . That is, if the applied voltage exceeds V_C ($V > V_C$) then the metal-ion expulsion is observed. Of course, the higher the operating temperature the lower the V_C . This sets an upper temperature limit beyond which the material becomes unusable. Since most superionic materials possess high zT values at very high temperatures, far above the superionic transition temperature where the metal-ions are relatively easy to flow or migrate under a temperature or voltage gradient and hence leak out of the sample. A detailed mechanism of ion migration and discussion on strategies for its suppression are explained in the review article by Qiu et al [9]. An alternative way to avoid ion migration due to external applied field in superionic materials is by obtaining high zT at low temperatures (i.e. a temperature not too high above the superionic transition). V_C is also found to be a function of sample's chemical composition and is higher for cation vacancy samples which explains the reason behind the better thermal stability of $\text{Cu}_{1.97}\text{S}$ compared to Cu_2S [9].

Metavalent compound SnTe

A subgroup of chalcogenides that includes IV-VI compounds, such as PbTe , GeTe , and SnTe , possess a unique bonding mechanism known as metavalent bonding, which refers to a type of bonding with mixed ionic, covalent and metallic character. Mostly these materials are composed of heavy constituent elements and have soft chemical bonding, resulting in their low lattice thermal conductivity [131, 132]. Due to their highly symmetric crystal structure, they

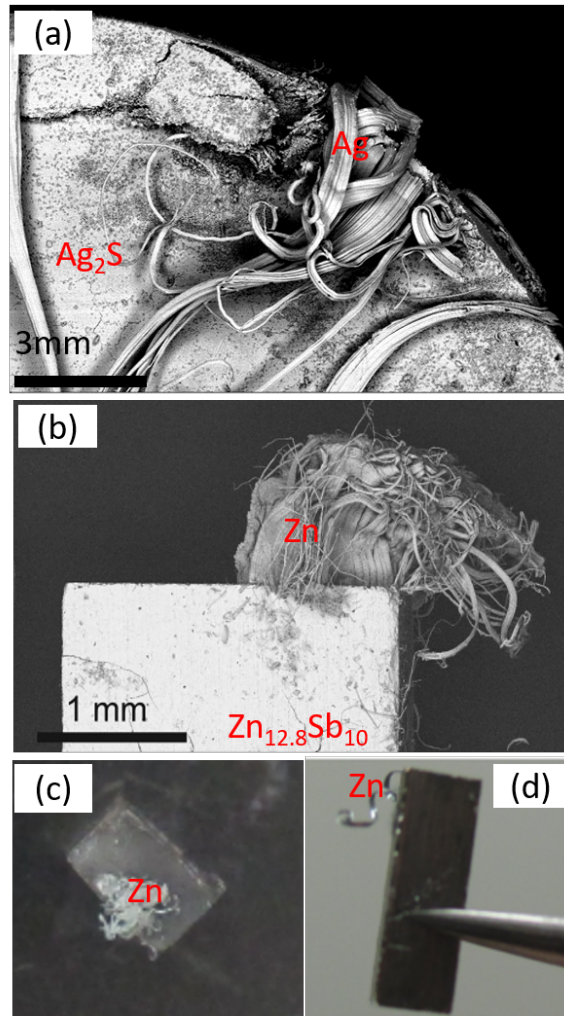


Figure 1.15: Material degradation in superionic compounds (a) is the FESEM image of sintered Ag_2S pellet at 773 K showing Ag migration at the edges of pellet (from our study), (b) is the FESEM image of $\text{Zn}_{12.8}\text{Sb}_{10}$ sample showing Zn migration after current flow experiment when a high current density of 68.8 A cm^{-2} was applied for continuous 26 minutes while keeping T_{hot} at 473 K, and (c, and d) shows the photographs of top view and whole sample view of $\text{Zn}_{12.8}\text{Sb}_{10}$ degraded samples when exposed to high current density experiment taken from *Ref [10]*.

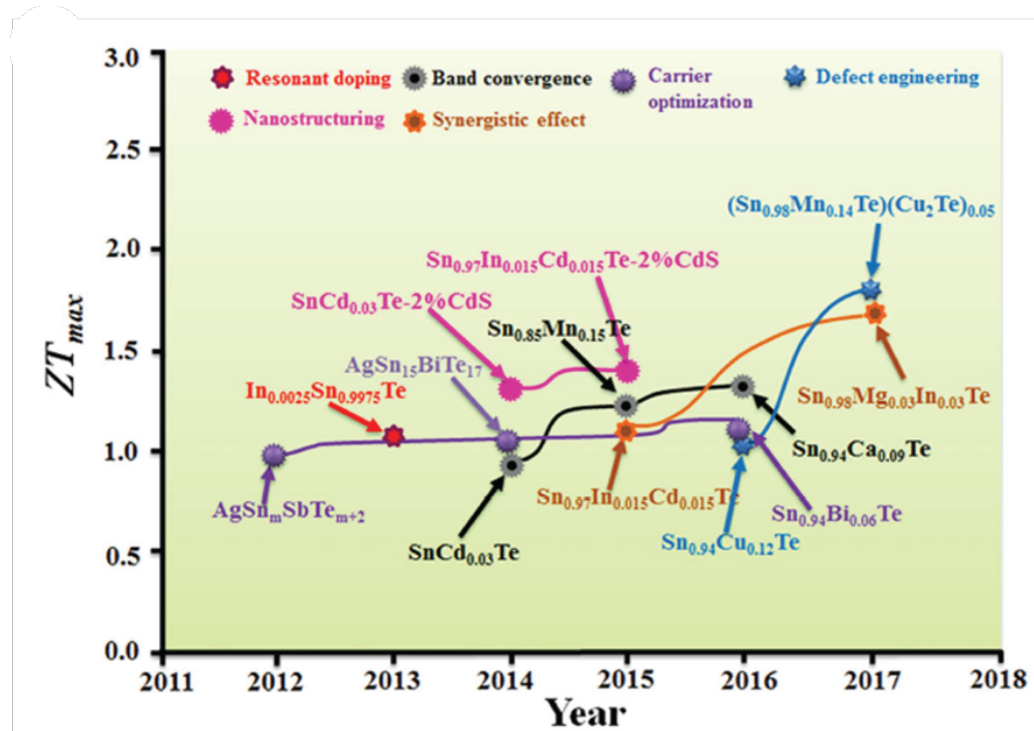


Figure 1.16: Recent progress in SnTe thermoelectrics. Figure adapted from Ref [11].

possess a unique band structure that results in high band degeneracy (N_v) [49]. As a result, single crystals of n-type obtained via Br doping in SnSe and p-type SnSe, show very high zT values of 2.8 and 2.6 at 773 K and 923 K, respectively [133, 134]. p-type $Ge_{0.9-y}Pb_{0.1}Bi_yTe$ show a zT value of 2.4 at 600 K [135], and p-type $Na_{0.03}Eu_{0.03}Sn_{0.02}Pb_{0.92}Te$ outperformed with a maximum zT of 2.6 at 850 K [136]. SnTe is a promising material for thermoelectric applications due to its high thermoelectric performance, relative abundance, and low toxicity [11]. The thermoelectric performance of SnTe is due to its unique crystal structure, similar to that of the champion material PbTe, which features a layered arrangement of Sn and Te atoms and dual valence bands, namely at L and Σ point of the Brillouin zone, with nearby energies [30]. Recent research has focused on improving the thermoelectric properties of SnTe by doping it with various impurities, which reduces the difference between the two valence bands [11]. Theoretical first-principle calculations revealed that the energy difference between L and Σ ($\Delta E_{L\Sigma}$) is 0.35 eV, which reduces to 0.22 eV with 2% Sn va-

cancies [137]. Further doping elements, such as Mg, Mn, Cd, and Hg, decreases the $\Delta E_{L\Sigma}$ to 0.13 eV, 0.13 eV, 0.067 eV, and 0.028 eV, respectively, and enhances the Seebeck coefficient significantly [137]. At higher temperatures, Mn doping results in the highest S value of $270 \mu\text{V K}^{-1}$ at 870 K compared to other doping elements [138]. The Indium doping results in resonant impurity level near Fermi level which in turn increases the S to $80 \mu\text{V K}^{-1}$ near room temperature [139]. Single metal elemental doping increased the zT of SnTe from 0.4 to 0.7 at 873 K [140]. However, co-doping of Mn and Sb has significantly improved the zT to 1.8 at 873 K as a consequence of synergistic improvement in PF and lowered κ_l [141]. The lowest κ_l of $0.4 \text{ W m}^{-1}\text{K}^{-1}$ has been achieved via Cu doping, resulting in a zT value of 1.6 at 873 K in Mn and Cu co-doped SnTe [142]. Therefore, monovalent cation doping has shown significant improvement in TE properties of SnTe, making it comparable to the best Pb-based compounds, motivating further investigation.

1.6 Synopsis of this thesis work

This thesis focuses on the study of the thermoelectric properties of several chalcogenides belonging to the superionic family and the family of metavalently bonded materials. In the first chapter, we introduce the TE research field, including the challenges involved and the materials landscape in TE research. Chapter 2 details the experimental techniques and methods used for the synthesis, structural and thermoelectric characterizations of the materials investigated in this thesis. In chapters 3, 4, 5, and 6, we present and discuss the work carried out during this thesis on superionic Ag_2Te , Ag_2Se , Ag_2S , and metavalent SnTe compounds, respectively.

In chapter 3, we investigate the TE properties of Ag_2Te compound and address the problems of irreproducibility and sample stability. We present a new method for synthesizing both n- and p-type Ag_2Te samples via precise compositional tuning and nanostructuring, achieving an enhanced zT value of 1.2 at 570 K, which is the highest ever reported value for any n-type Ag_2Te sample. We demonstrate the sample reproducibility, thermal stability, and electrical sample stability at a higher current density value of above 15 A cm^{-2} in

the superionic phase at 570 K. Our synthesis method can easily be scaled-up for large scale production, making it promising for industrial-level application.

In chapter 4, we investigate the TE properties of Ag_2Se and address the issue of sample-dependent TE properties reported in previous literature due to compositional inhomogeneity arising due to metal-ion migration during high temperature sintering . By using an all-room temperature synthesis method discovered by us in the context of Ag_2Te as discussed in chapter 3, we resolve the irreproducibility issue associated with Ag_2Se samples and obtain a comparable high zT value as reported in previous studies. Additionally, we shed light on the role of slight anion excess in Ag_2Se responsible for its high zT value near room temperature.

In chapter 5, we study the TE properties of an environmentally friendly sulfide material, Ag_2S . We investigate the effect of anion excess on the TE properties of Ag_2S and show that a mere 1% S excess sample shows an ultra-low thermal conductivity resulting in a high ZT value of 0.83 at 670 K. For n-type Ag_2S , this is the highest reported value for any sulfide material in the temperature range of 450-670 K.

In chapter 6, we investigate the TE properties of metavalent compound SnTe . We show for the first time that upon furnace sintering a cold-pressed pellet, nanoparticles of SnTe precipitate in the grain boundary region, resulting in bulk nanostructuring via grain boundary engineering. Previously, grain boundary engineering was reported using complex and sophisticated procedure of coating the SnTe grains with CdTe layers; compared to this our method is simple, unsophisticated, and economical and does not involve the of toxic Cd. We report a 67% enhancement in zT compared to the ingot SnTe sample. We also performed band engineering by doping Ag to enhance the Seebeck coefficient, confirmed via DFT calculations, and obtained a zT value of 0.92 at 820 K.

Finally, in chapter 7 we summarize the results obtained in Chapters 3-6 and give an outlook on the future research direction on these materials.

Chapter 2

Experimental Methods

The properties of most TE materials are often highly sensitive to the stoichiometry and presence of interstitial defects, both of which results in self-doping, changing the carrier concentration and hence the basic properties such as electrical conductivity (σ) and Seebeck coefficient (S) on which thermoelectric (TE) figure of merit depends. Therefore, the synthesis techniques used, unambiguous structural and physical characterizations of TE materials is very important. In this chapter we give details of the synthesis methods used in this thesis. The structural characterization techniques used are discussed in details. And, finally the experimental techniques employed in this thesis work for thermoelectric characterization, including electrical resistivity, Seebeck coefficient, thermal diffusivity and Hall effect etc are presented.

2.1 Sample Synthesis

One of the major challenges in thermoelectric is to obtain reproducible results. To obtain reproducible properties it is important to optimize the sample synthesis method. In this section we describe the synthesis methods used during this thesis work.

2.1.1 Mechanical Alloying

Ball Milling

A top-down synthesis approach is employed for fabricating nanoparticles in this study. The ball milling technique is utilized to prepare samples with low enthalpy of formation using elemental powder precursors. This technique, initially developed by Benjamin and coworkers in 1960, is commonly known as mechanical alloying. It is known to produce a uniform distribution of oxide particles, such as Al_2O_3 in nickel-base superalloys [143].

The ball milling process involves the use of hard-material balls, typically stainless steel (SS), silicon carbide, agate or tungsten carbide, within a stainless steel jar, which can also have a lining of a suitable material. During milling the balls cold weld with the powder, reducing the particle size down to nanometer. The planetary mills or horizontal ball mills are commonly used for this purpose. We used a locally procured low-frequency (2 Hz) mill, with a stainless steel milling jar of $\Phi = 19$ mm (and volume = 12000 mm³) and $\Phi = 4$ mm SS balls. In this set-up, the SS jar is placed inside an aluminum jacket, which vibrates back and forth about its mean position, as indicated by the double-sided orange arrow in Figure 2.1. In order to prevent oxidation of the precursor material, the jar was loaded and sealed in an argon filled glove-box.

In this study, Ag_2X (X = S, Se, and Te) powder samples are synthesized under an Ar atmosphere by ball milling Ag and X elemental powders in the desired proportions. The ball milling process results in the formation of Ag_2X nanoparticles as shown in Figure 2.1(c) where a low-resolution transmission electron image is shown. To investigate the transport properties of the ball-milled samples, the powder is consolidated by cold-pressing it into $\Phi = 8$ mm diameter pellets, achieving nearly 100% pellet density. Ag_2X materials, though semiconducting exhibit a metal-like ductile behavior because of which a mere cold-pressing allows us to achieve 100% dense pellets (i.e. the measured density is nearly the same as the theoretical density). These pellets are then cut into the desired shapes for measurement purposes. The transport properties of a few sintered pellets were also examined for comparison.

The details of the sintering process will be described later in this section.

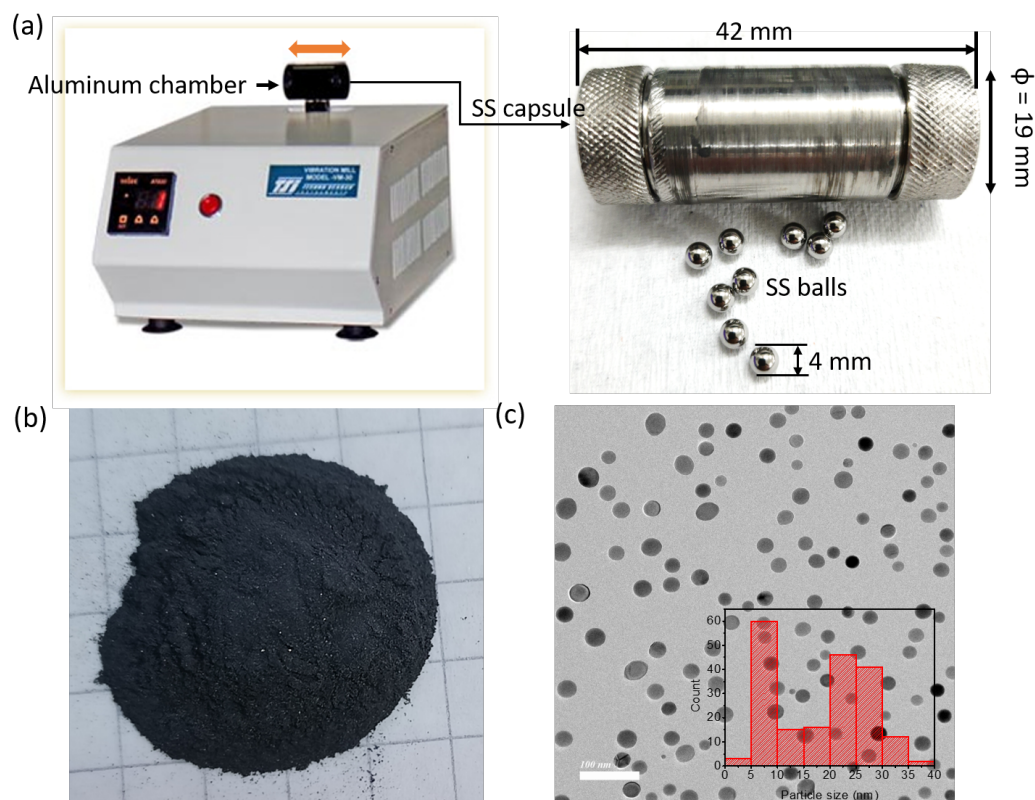


Figure 2.1: (a) Ball Mill used for mechanical alloying synthesis, (b) Ag_2X powder obtained after milling, and (c) low-magnification image showing formation of in our synthesized Ag_2X samples.

Hand Grinding

We also synthesized phase pure Ag_2X samples simply by hand grinding the elemental powders of Ag and X (either, S, Se or Te) using agate mortar-pestle. The clear evidence of Ag_2X phase formation can be observed by the change of color from gray to black, as the reaction proceeds, see Figure 2.2. The detailed reaction mechanism for the formation of pure Ag_2X phase is given by Yang et al. [19] The time required for phase pure Ag_2Te sample (2 g) by hand grinding is approximately 1 h; where as for Ag_2Se (2 g) the time required is more than 1 h. On the other hand, to form phase pure Ag_2S sample it requires about 2 h of grinding after which it should left for 24 h for any unreacted Ag and S to react completely. The hand grinded powders were also consolidated by cold-pressing as discussed previously for

the ball-milled powders.

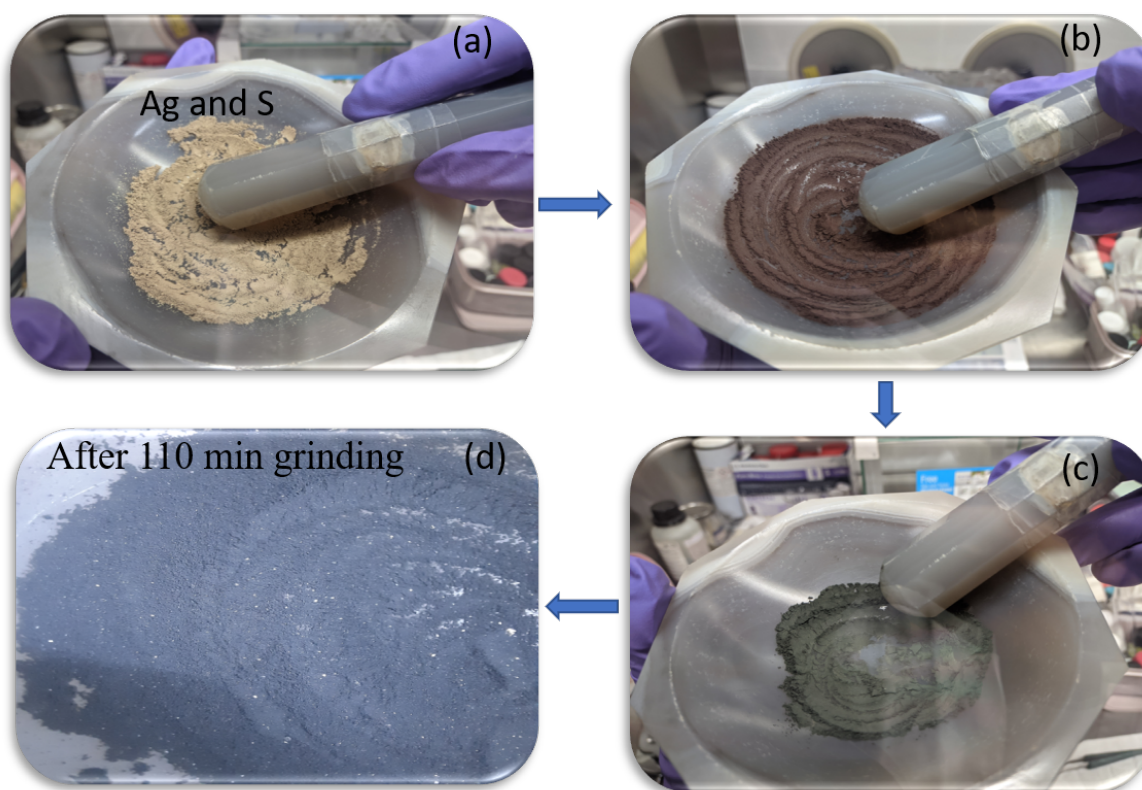


Figure 2.2: Gradual color change from gray (a) to black (c) during the synthesis of Ag_2S . Panel (b) shows the color during an intermediate stage.

Sintering Process

A few of the CP pellets (both, ball milled and hand grinded) were sintered at high temperature using Nabertherm box furnace. For this purpose, the pellets were vacuum sealed in preheated quartz tubes under 10^{-5} Torr pressure and then sintered at 673 K for 24 h. In order to avoid any temperature gradient the tubes were placed at the center of the box furnace. The cold-pressed pellet, sealed quartz tubes and furnace used for sintering are shown in Figure 2.3

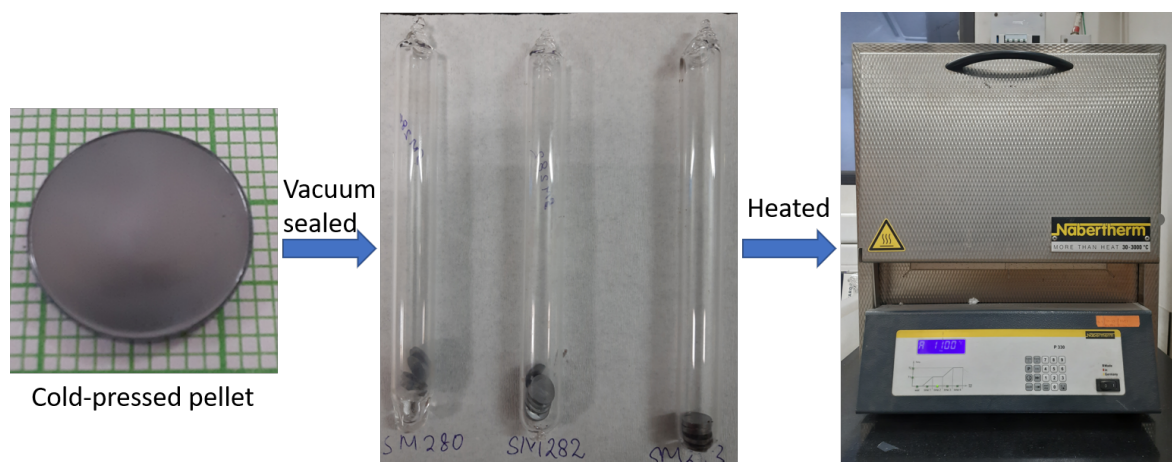


Figure 2.3: Image of cold-pressed pellet, the vacuum sealed cold-pressed pellets and the furnace used for sintering.

2.1.2 Solid-State Melting Method

We have used the solid-state melting method to prepare the ingots of Ag_2S , Ag_2Se , Ag_2Te and SnTe samples. In the solid state melting synthesis method, precursors were vacuum sealed in silica tubes (ampoules) as described above and melted in a box furnace in the temperature range 1173 K to 1273 K depending on X in Ag_2X and SnTe samples. Few representative pictures of the synthesized ingots are shown in Figure 2.4. Depending upon the desired compositions, details are given as follows:

Ag_2S : Ag powder (> 99.9%) and S flakes (99.999%) were filled in a quartz ampule that was preheated overnight at 1173 K to remove any moisture adhered to its walls. The precursor were filled in an Ar-filled glove box to avoid oxidation of elemental precursors. The quartz ampule was then evacuated to 10^{-5} Torr pressure and sealed. This ampule was placed in a box furnace and heated to 1173 K at the rate of 50 K h^{-1} where it kept for 24 h. At the end of this the furnace was turned off to allow the ampule to cool down to the room temperature.

Ag_2Se : Elemental powders of Ag (>99.9%) and Se (99.999%) were taken in 2:1 ratio in the preheated quartz ampule and vacuum sealed by following exactly the similar procedure as described for Ag_2S above. The ampule was heated to 623 K with a rate of 50 K h^{-1} where it was kept for 10 h before heating again to 1193 K with a heating rate of 100 K h^{-1} and

dwelled there for 24 h. Ampule was then cooled to room temperature at a cooling rate of 100 K h^{-1} . We also synthesized an Ag_2Se ingot by following a temperature profile recently reported by Jood et al. [16].

Ag₂Te: Elemental Ag (>99.9%) powder and Te (99.999%) pieces were taken in the desired composition of 2:1 ratio filled inside a preheated quartz ampule and then vacuum sealed in same manner as described above. The ampule was then heated to 1273 K at a heating rate of 100 K h^{-1} where it dwelled for 24 h. After that the ampule was cooled to 873 K at a cooling rate of 50 K h^{-1} and stayed at this temperature for 24 h before quenching it in ice water. We also synthesized an Ag_2Te ingot using the temperature profile similar to that reported by Capps et al. [144].

SnTe: To synthesize the pristine and doped SnTe samples we have used the preheated quartz ampules containing alumina crucible. Sn (99.9%), Te (99.999%) and Ag (>99.9%) elemental powders were taken in the desired proportions to synthesize the $\text{Sn}_{1.03}\text{Te}$, $\text{SnAg}_{0.03}\text{Te}$, $\text{Sn}_{0.97}\text{Ag}_{0.06}\text{Te}$ and $\text{Sn}_{0.94}\text{Ag}_{0.09}\text{Te}$. The synthesis was carried out in vacuum sealed ampules that were heated to 1173 K in 7 h. After staying at this temperature for 12 h, furnace was cooled to room temperature at a cooling rate of 70 K h^{-1} . A few representative images of ingots obtained by solid-state melting method are shown in Figure 2.4.

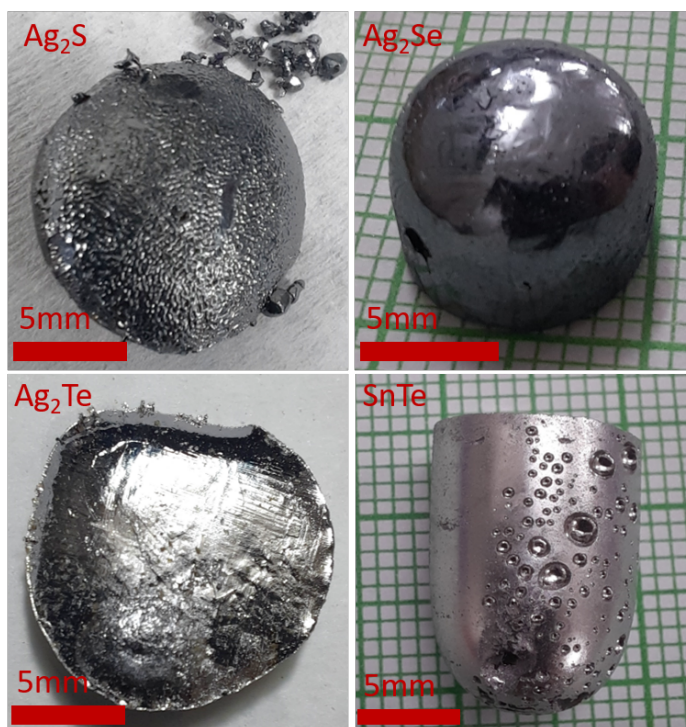


Figure 2.4: Few representative pictures of ingot samples obtained from solid-state melting method.

2.1.3 Sample Processing For Transport Property Measurements

For bulk property measurements like electric and thermal transport, samples with different geometries are required. To shape the pellets (cold-pressed or sintered) or the ingots into desired form, we need to cut and polish them. Rectangular bar shaped samples are used for the electronic transport measurements, and polished 6×6 mm² square or 8 mm disc shaped samples are used for thermal transport measurements. Cutting and polishing procedures are explained below.

Cutting and Polishing

Pellets and ingots were cut into rectangular bar shapes using a low-speed cutting machine (South Bay, USA) loaded with a diamond-coated disc-shaped blade. A few representative images of the rectangular shaped specimen obtained after cutting is shown in Figure 2.5. Such samples were used to perform electronic transport measurements such as resistivity

and Hall carrier concentration. Furthermore, for thermal diffusivity measurements, a square sample measuring $6 \times 6 \text{ mm}^2$ obtained after cutting the ingot or an 8 mm diameter pellet, polished using SiC polishing paper with a 1000 grit size to prepare a sample of constant and uniform thickness. The large flat faces were coated with graphite layer prior to the measurement.

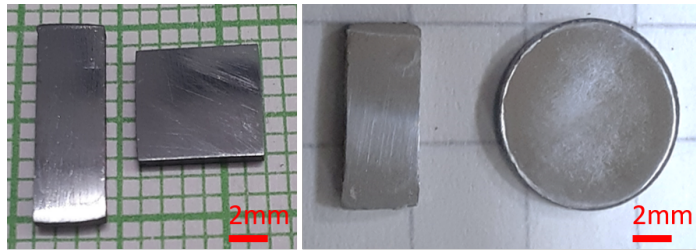


Figure 2.5: Samples (left panel: ingot and right panel: pellet) for electronic and thermal transport property measurements obtained after cutting and polishing process.

2.2 Characterization Techniques

After synthesizing the samples by using any one of the earlier discussed synthesis procedures, structural characterizations were done to confirm the phase purity, composition, micro-structure and presence/absence of defects etc. In this section we will explain the characterization techniques used.

2.2.1 Powder X-ray diffraction

X-ray diffraction was discovered by Max von Laue in 1912 and later in 1914 he was awarded with the Noble prize for his discovery. X-ray powder diffraction (XRD) is a primarily analytic technique used for phase identification of a crystalline material and provide the information about the atomic arrangement in lattice. For X-ray powder analysis, material must be homogeneous and finely ground.

Working principle of X-ray powder diffraction: It works on the principle of constructive interference. Due to the comparable length scale of interatomic spacing with X-ray wavelength, the atomic arrangement can diffract X-rays because of the periodic arrangement of atoms in a crystalline material acting as a 3D grating, which diffracts the incident monochro-

matic X-rays, see Figure 2.6(a). The interaction of X-rays with the crystalline material forms constructive interference when the Bragg's equation in (2.1) is satisfied. Atoms diffract incident X-rays primarily through interaction with their electrons, which is elastic scattering and hence sensitive to the atomic number of the element present in the crystal structure. The diffracted X-ray beam is then detected and counted by scanning the sample over any 2θ range. Depending on its constituent atoms and their arrangement in the lattice, each crystalline material results in a unique diffraction pattern.

$$2d\sin\theta = n\lambda \quad (2.1)$$

Powder X-ray diffraction instrument: The instrument majorly consists of three elements, X-ray source, sample holder and a detector, and it is used in two different geometries depending upon the rotation and fixed positions of its three constituent elements. The two geometries are (1) Bragg-Brentano (BB) and (2) parallel beam (PB). In this thesis, Bruker D8 Advance diffractometer was used for carrying out the crystal structure analysis of powder samples in the BB geometry. The schematic for the same has shown in Figure 2.6(b).

X-ray source: X-rays are produced in a cathode ray tube by heating a filament to generate electrons which are accelerated by an applied voltage and bombarded on a target. Usually, the target used are of elemental metals like Cu, Mo, Cr etc. The incident high energy electron beam knock out the core-shell electrons from the target metal. The vacant site of knock out electron is filled by the outer shell electrons and this transition emits the X-ray of energy or wavelength corresponding to the energy difference between the atomic shells. K_α is produced for the transition of electron from L-shell to the K-shell. In case of Cu target, K_α consists of $K_{\alpha 1}$ and $K_{\alpha 2}$. $K_{\alpha 1}$ has slightly lower wavelength but significantly closer to $K_{\alpha 2}$ (1.54059 Å and 1.54432 Å). The produced monochromatic x-rays are collimated and incidence on the sample.

Sample: For powder XRD, sample should be finely grounded which can avoid any preferred

orientation present in powder samples. A thin layer of amorphous oil (paraffin oil in our case) applied with the help of an earbud at the center of a microscope slide is used on which the finely grounded powder is sprinkled as a thin layer. This slide then fits into the aluminum sample holder provided with a spring arrangement in Bruker D8 Advance instrument. This thin layer of powder sample gives sufficiently good statistics of diffracted counts for strongly diffracting crystalline samples to analyze the data such as using the Rietveld refinement analysis.

Detector: In Bruker D8 Advance, LYNXEYE, a semiconductor 1-D detector based on the silicon strip technology is used. This technology allows count detection operation at much higher rate compared to a scintillation detector while maintaining all the benefits. The 192 silicon strips act as individual 192 0-D detectors. Optimum tuning of silicon strip sensor to the requirements of X-ray energy from 6 keV to 15 keV is provided which is factory optimized for our Cu-K α X-ray detection. More benefits of using silicon based detector is the absence of gas, water cooling or liquid nitrogen cooling making it very compact, robust and maintenance free.

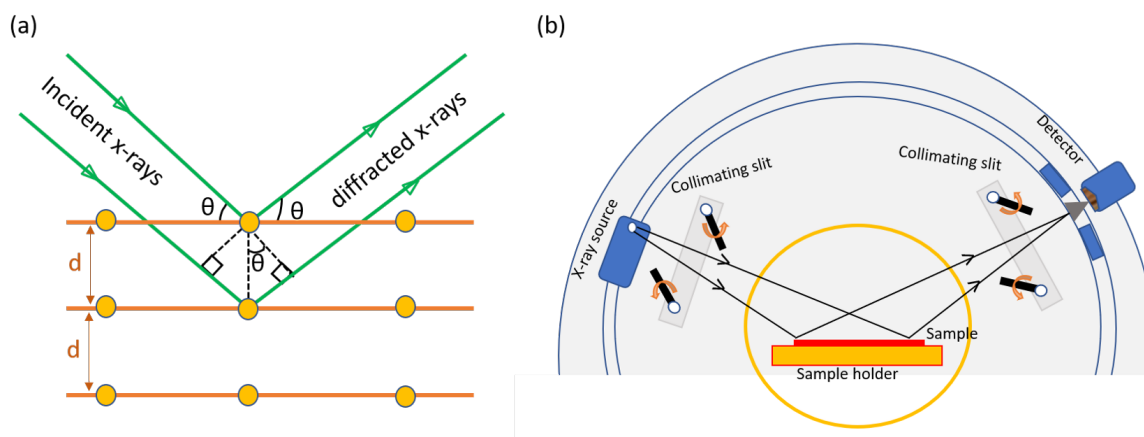


Figure 2.6: (a) Schematic diagram for x-ray diffraction from crystalline material, (b) schematic diagram for Bragg-Brentano geometry used in our PXRD analysis

The experimental geometry of the instrument is shown in Figure 2.6(b). The sample holder rotation of 15 rps were used while collecting diffraction data to minimize the effect of preferred orientation on the observed intensity. Rietveld refinement analysis technique was

used for fitting the experimental diffraction pattern with their theoretical model to precisely estimate the lattice parameters of the crystalline powder sample.

How to interpret the data: The X-ray diffraction generate peaks on various 2θ values along with background. Any X-ray diffraction pattern can provide the following information about the sample:

1. 2θ positions corresponds to certain d-spacings of the atomic planes.
2. Peak intensity signifies the number of atoms or molecules present in a plane.
3. Width of the diffraction peaks provide information about the crystallite size and strain present in the sample. The sharper the peak, bigger and strain free the crystallites.
4. Diffraction background indicates the degree of amorphous component associated with the crystalline material which usually give broad hump in the background along with sharp diffraction peaks.
5. The diffraction pattern for an unknown compound can be compared with the literature to verify the crystalline structure, matching both the location, width, and relative heights of the diffraction patterns.

2.2.2 Rietveld refinement

Rietveld refinement technique is used to analyze the X-ray diffraction data by fitting it with theoretical model. It works on the principle of one-to-one correspondence between the experimental pattern and theoretical pattern. FullProf Suit is the software used to perform the Rietveld refinement analysis for finding the lattice parameters, atomic positions and their occupancy. Since, refinement is about finding the best fit between theoretical and experimental pattern, it is necessary then to quantify the quality of fit. The goodness of fit is determined by three parameters in the refinement process, χ^2 , R_{wp} , and R_{exp} . If $y_{O,i}$ is the intensity observed at $2\theta_{O,i}$ with an uncertainty of $\sigma[y_{O,i}] = \sqrt{\langle (y_{O,i} - \langle y_{O,i} \rangle)^2 \rangle}$. Similarly, $y_{C,i}$ is the calculated intensity at $2\theta_{C,i}$. Then the goodness of fit parameters obtained from the refinement are given by equations (2.2), (2.3), and (2.4).

$$\chi^2 = \frac{1}{N} \frac{\sum_i w_i (y_{C,i} - y_{O,i})^2}{\sigma^2[y_{O,i}]} \quad (2.2)$$

$$R_{wp} = \frac{\sum_i w_i (y_{C,i} - y_{O,i})^2}{\sum_i w_i (y_{O,i})^2} \quad (2.3)$$

and,

$$R_{exp} = \frac{N}{\sum_i w_i (y_{O,i})^2} \quad (2.4)$$

where w_i is given by $\frac{1}{\sigma^2[y_{O,i}]}$.

χ^2 can also be written as $\frac{R_{wp}}{R_{exp}}$. And a χ^2 value of ≈ 1 is usually considered to be best quality fit. But the best to confirm the fitting quality of experimental is by visual analysis of fit by plotting the experimental and calculated pattern on the same scale. In that case, even higher values of χ^2 , 4-5 are acceptable for correctly analyzing the crystal structure.

2.2.3 Electron Microscopy

Electron microscopy works on the principle of electron waves diffraction from the sample of interest. Electron microscope (EM) are used to study the structure of organic, inorganic and biological samples including polymers, alloys, large molecules, cells etc. EM are widely used for sample imaging because they produces high resolution images compared to optical microscope. When high energy electron beam of known wavelength comparable to inter-atomic distance, interact with the crystalline material, they interfere with electronic cloud associated with atoms. The emergent electron beam from the sample contains information about the morphology, elemental constituents, atomic arrangement and defects etc. The scanning electron microscope (SEM) and transmission electron microscope (TEM) techniques are used to study the electron diffraction response from crystalline materials.

Steps involved in EMs

1. Stream of high energy electrons generated by heating filament or field emission cathode are accelerated in vacuum towards the sample of interest with the positive electric potential.
2. The electron beam is focused by using metal aperture and magnetic lens to form a thin,

focused and monochromatic beam.

3. The incident beam interacts with the specimen and

4. Scattered electrons are then detected by different types of detectors to construct the image and extract other atomic information.

Now, we will discuss two electron microscopes, SEM and TEM in detail.

Scanning electron microscope (SEM): Electron beam generated from the electron gun are focused on sample by means of a lens system. The selected area of the sample scanned under the control of current across the scan coil in final focusing lens. Highly magnified images of 200 KX can be possible with SEM. The sample preparation technique is very simple for conducting samples but a thin gold layer coating is required for insulating samples. A tiny sample quantity is mounted on an aluminum stub with the help of carbon adhesive tape. The incident electrons interact with the sample and produce various signals containing information about the sample topography and chemical composition. The various emerging electrons from the specimen and complete schematic diagram of a field emission scanning microscope is shown in Figure 2.7(a and b).

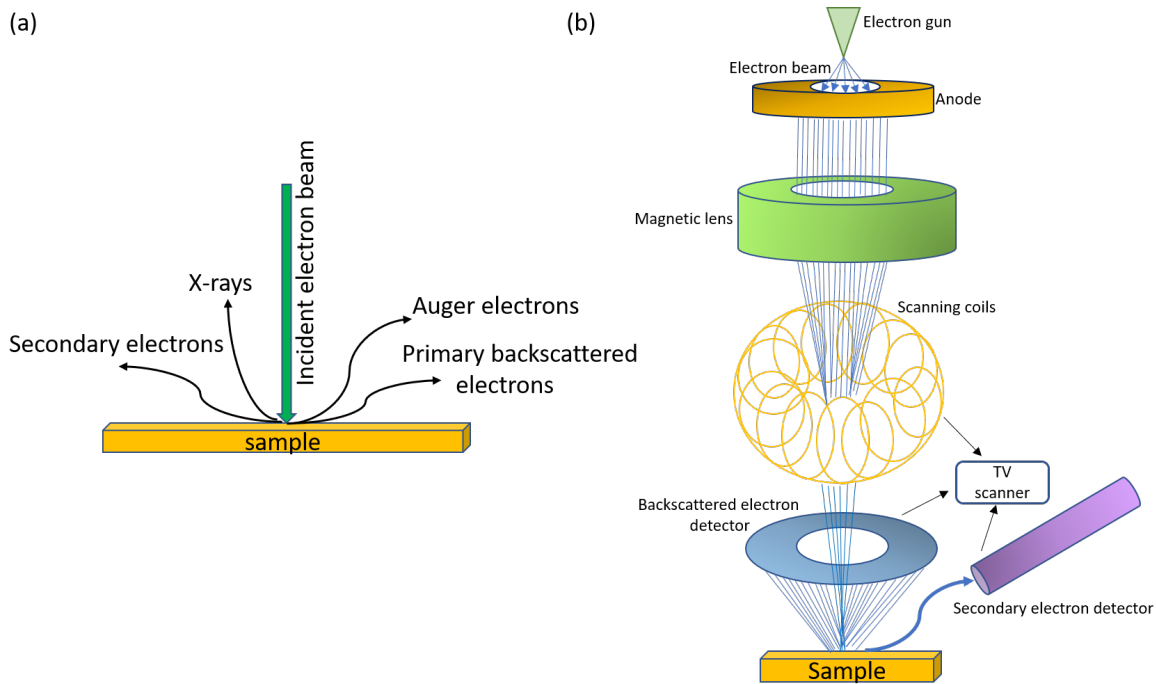


Figure 2.7: (a) Various emergent signals from the specimen in scanning electron microscope (b) schematic diagram for field emission scanning electron microscope.

Various types of electrons produced when electron beam interacts with specimen such as, secondary electrons (SEs), back scattered or reflected electrons (BSEs), X-rays, Auger electrons and photons etc. Most of the SEM systems are equipped with the secondary electron and back scattered electron detectors and the X-ray detector equipped externally to the microscope. SEs and BSEs are used for imaging the sample surface and X-ray signal used to analyze the chemical composition. SEs emerge from the topmost few layers of sample thickness nearly 20 nm and localize at the point of primary incident electrons and hence able to provide sample morphology information. SEs usually have low energy (50 eV) and can produce 1 nm resolution image. On the other hand, BSEs produced by elastic scattering emerge from more deeper depths in the sample. Since, the BSEs are produced by elastic scattering from atoms, their intensity depends upon the Z value of elements present in the specimen and can create the contrast image of the samples having different elemental distribution over the space. Auger electrons are emitted when incident electron beam creates electron holes

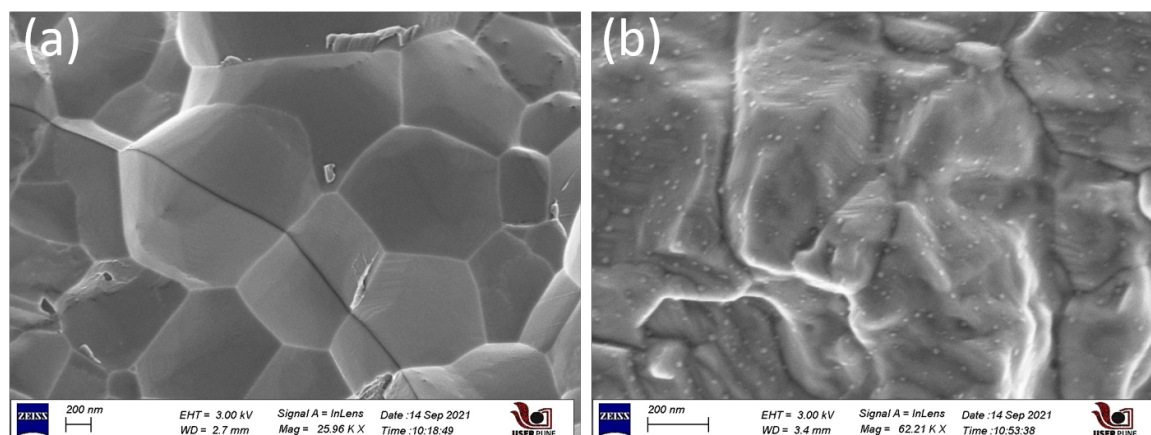


Figure 2.8: Representative FESEM images showing morphology of Ag_2Te for (a) cold-pressed, and (b) sintered pellets on freshly fractured surfaces taken at 3 kV.

in innermost shells, K, L, M etc. which is filled by outermost shell electrons. During this transition, the produced X-ray energy is transferred to another electron which is then emitted. This is the auger electron. These are used for auger electron microscopy for analyzing thin film and coatings. The final useful signal is X-ray produced from the depth of specimen when incident electron beam dislodge the innermost shell electrons, whose vacancy then filled by outer shell electrons results in the production of characteristic X-ray signal. These characteristic X-rays can be measured by Wavelength-dispersive X-ray spectroscopy (WDS) or Energy-dispersive X-ray spectroscopy (EDS) to analyze the elemental composition.

In this work we have used the Ultra Ziess Plus microscope equipped with Oxford Inca EDX detector. We have used the 20 keV incident energy electron beam for finding the chemical compositions of our samples and both low (3 keV) and high incident energies (20 keV) for morphology analysis. Few of the representative images accessed from SEM are shown in Figure 2.8

Transmission electron microscope (TEM): The transmission electron microscope works on similar principle of an optical microscope. Additionally it produce high resolution images as a result of much lower wavelength associated with electrons as compared to optical wavelength. Since electrons are very small entities and can easily be scattered by hydrocarbons or air molecules, very high vacuum medium is required for transmission electron microscopy.

Hence, a series of vacuum pumps are required to achieve the ultra-high vacuum column for the transmission of electron beam. Rotary pump used first in the column to lower down the pressure to 0.0001 Pa. This stage of vacuum is also called low or roughing vacuum. Rotary pump sets enough low pressure for the usage of turbo molecular or diffusion pump to reach the vacuum level of 10^{-8} Pa in the column. For ultra-high TEMs, vacuum level of 10^{-9} Pa is required near the cathode to prevent an electric arc. The schematic diagram of TEM is shown in Figure 2.9. TEM has four components namely, electron source, electromagnetic lenses, lens aperture and the data collection.

Electron Source: It consists of three components: a filament, Wehnelt cap and an anode. Electrons can be pumped from the filament by connecting it to the negative voltage. Wehnelt cylinder connected to higher negative voltage than the filament, providing the emergent electron beam in converging pattern. Further, electron beam pumped into the column via anode.

Electromagnetic lenses: Electromagnetic (EM) lenses serves the same purpose as the optical lens, to converge electron beam at their focal point. TEM uses electromagnetic coils made up of iron, iron-cobalt or perm-alloy etc. to make convex lens. Focal point of lens can be controlled by altering the current passing thorough coils. There are five EM lenses used in the TEM, first and second condenser lens, objective lens near the specimen, intermediate lens and projector lens for image collection.

Lens aperture: Annular metallic thick discs are used to block the excessive electron beam and passes only axial electrons. Aperture filter-out the unwanted electrons scattered from lens defects at higher angles. At the same time it also reduces the beam intensity, as it removes some electrons from the beam.

Imaging: The exiting electrons from the sample form the image after passing through three lens assembly. Depending upon the intensity and phase of electrons, it possess information about the sample and the beam itself. TEM has two operation modes namely, imaging mode and diffraction mode collected from two types of exiting electrons, unscattered and scattered. For imaging mode, objective aperture is placed at the back focal plane of objective lens. When objective aperture made selective for the unscattered electrons only and block

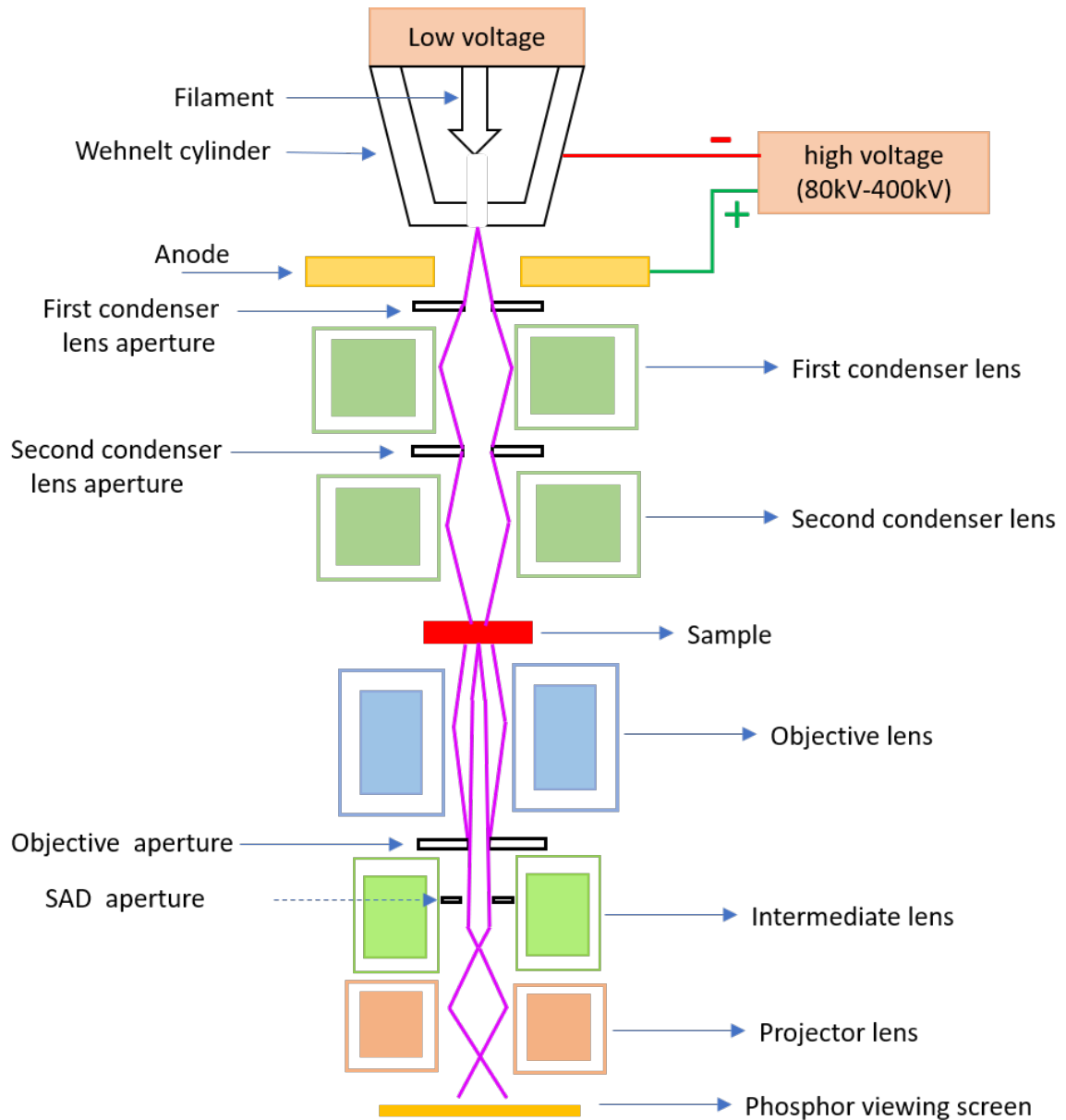


Figure 2.9: Schematic diagram of transmission electron microscope (TEM).

other diffracted electron, then the obtained image is called bright field image. And if only scattered electrons are allowed and axial electrons are blocked then the dark field image formed. The selected electron beam magnified and projected on the viewing screen with the help of intermediate lens. Abbe criteria is measure of resolution d , of any microscope, given as:

$$d = 0.61 \frac{\lambda}{n \sin \alpha} \quad (2.5)$$

where λ is the wavelength of incident electron beam which depends upon the accelerating voltage. Here, n is refractive index of the medium and α is cone angle of the exiting beam from specimen and $n \sin \alpha$ is called numerical aperture which is 0.01 for electron microscope and 1 for optical microscope. For diffraction mode of TEM, the scattered electrons projected on the viewing screen by changing the current through intermediate lens.

Sample preparation: In our study we have used the drop-cast method to prepare TEM specimen. Amorphous carbon coated copper grid of 300 mesh size was used for holding the drop-cast sample. We have performed the TEM analysis on powder samples dispersed in any organic solvent like, acetone or ethanol. Very thin sample of around 100 nm is required for the transmission of electron beam in TEM imaging. The TEM grid and few representative TEM images are shown in Figure 2.10

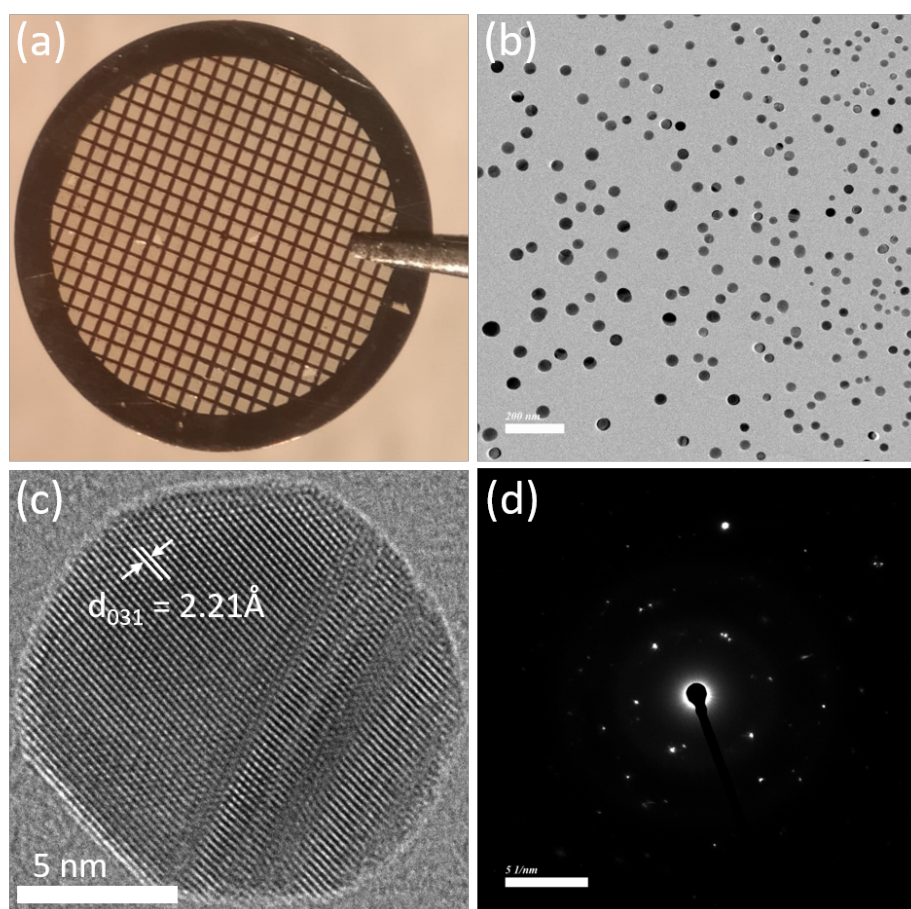


Figure 2.10: (a) Copper grid coated with amorphous carbon, (b) TEM image lower resolution showing nanoparticle distribution, (c) high resolution TEM image, and (d) electron diffraction taken on our synthesized Ag_2S nanoparticle.

Scanning transmission electron microscope (STEM): TEM can be modified to STEM by reversing the point of source and point of observation with respect to the direction of electron beam. A convergent electron beam raster the sample surface and image is formed when combined with suitable detector. In STEM various detectors on different collection angles are used to capture the diffracted electrons of interest. However, we have not used STEM in this thesis work.

In this thesis, we have used the JEOL JEM 2200FS transmission electron microscope working at 200 kV electron beam energy. Few representative images accessed from our TEM set-up are shown in Figure 2.10.

Information obtained from the TEM: There are many advantages of using TEM in material science and few of them are listed as:

1. It provides the highest possible resolution images for organic or inorganic samples.
2. TEM provides the information about crystal structure and the atomic arrangement in a crystalline material.
3. One can analyze strain, defects, voids, grain boundary features in materials.
4. In-situ TEM is a powerful tool for monitoring chemical reactions and phase transition phenomenon in crystalline materials.

2.2.4 Thermogravimetric analysis and Differential Scanning calorimetry (TGA and DSC)

TGA and DSC are thermal analysis techniques. TGA measures the sample weight change over time with increasing temperature and DSC is a measure of heat rejected from the sample or absorbed by the sample depending upon the exothermic or endothermic processes involved. In TGA, sample weight can change due to several reasons like, oxidation, reduction, decomposition, evaporation etc. It tells about the sample thermal stability. There are three types of thermogravimetry.

- **Isothermal or static TGA:** sample weight is measured over time at constant temperature.
- **Quasistatic TGA:** when sample temperature is increased in steps followed by isotherms and weight is recorded at each isotherm.
- **Dynamic TGA:** sample weight is measured over time when temperature increases linearly.

In DSC, heat rejected or heat absorbed is recorded with increasing temperature or time. It is a powerful technique for evaluating glass transition temperature, melting, crystallization, structural transition etc. STA 449 F1 Jupiter allows simultaneous measurement of TGA and high performance Heat Flux DSC with nanogram resolution thermobalance. It is advantageous of measuring both the thermal analysis, TGA and DSC in identical environment. For measurements, a small amount of powder (10-15 mg) was taken in Al_2O_3 crucible and kept

under temperature controlled heating sequence for data acquisition under an appropriate gas environment. A second empty Al_2O_3 crucible used as a reference. Weight change and heat flow was measured across the sample crucible in a controlled steady state of heating/cooling thermal cycles. STA 449 F1 offers the highest resolution of 25 ng in TGA signal and $<1 \mu\text{W}$ in DSC signal. We have evaluated the phase transition temperature of our samples using the DSC signals. The schematic diagram of STA 449 F1 Jupiter is shown in Figure 2.11 and the experimental data obtained for one of our sample is shown in Figure 2.12.

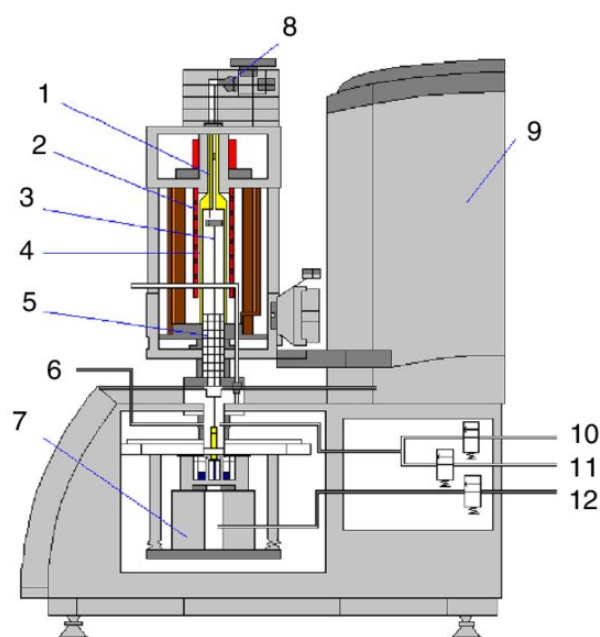


Figure 2.11: STA 449 F1 Jupiter from Netzsch used for TG-DSC analysis, schematic is adapted from Ref [12] where number denotes different component of the set up such as 1 furnace thermocouple, 2 heating element, 3 sample carrier, 4 protective tube, 5 radiation shield, 6 evacuation system inlet, 7 balance system, 8 gas outlet valve, 9 hoisting device, 10 purge 1 gas inlet, 11 purge 2 gas inlet, 12 protective gas inlet.

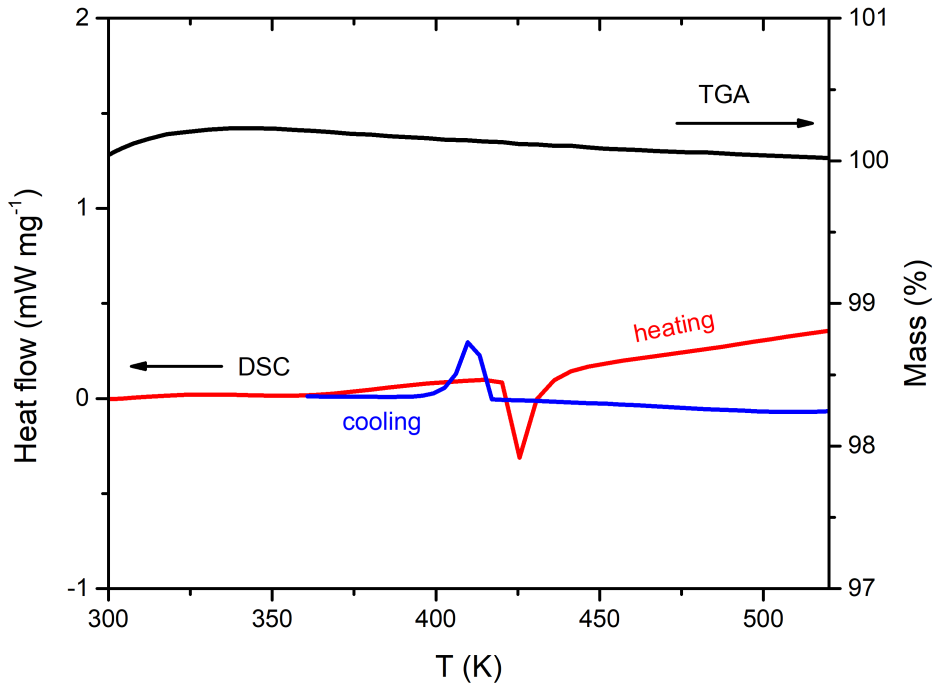


Figure 2.12: Experimental data showing mass loss (TGA) and phase transition (DSC) measured simultaneously for our Ag_2Te sample under N_2 atmosphere using STA 449 F1 Jupiter from Netzsch.

• Differential Scanning Calorimeter DSC7000 Series

We have used the DSC7000 Hitachi setup to conduct DSC and heat capacity measurements on few of our samples at temperatures above room temperature (specifically Ag_2S compounds). It is a heat flux DSC setup and operates within an inert N_2 atmosphere, covering a temperature range from room temperature to 700°C . To ensure accurate estimation of specific heat, it is crucial to achieve uniform heating across the sample. This requires the use of a metallic furnace and metallic crucible. In the case of the DSC7000, an aluminum crucible is employed, and uniform heating is maintained through a heat sink connected to a resistance heater. Furthermore, we employ a standard sapphire sample for C_p calculations.

C_p calculation method

To estimate specific heat using DSC, three different measurement data are required which include, empty pans data, data from known standard specimen (Sapphire in our case) and

sample data for which C_p is required. The following formula can be used to calculate specific heat.

$$C_{ps} = \frac{Y_s}{Y_r} \times \frac{M_r}{M_s} \times C_{pr} \quad (2.6)$$

C_{ps} : Specific heat of sample

C_{pr} : Specific heat of known standard sample

Y_s : DSC curve difference between empty pan and sample

Y_r : DSC curve difference between empty pan and standard sample

M_r : Weight of standard substance

M_s : Weight of sample

The experimental results of C_p measurement of one of our sample is shown in Figure 2.13.

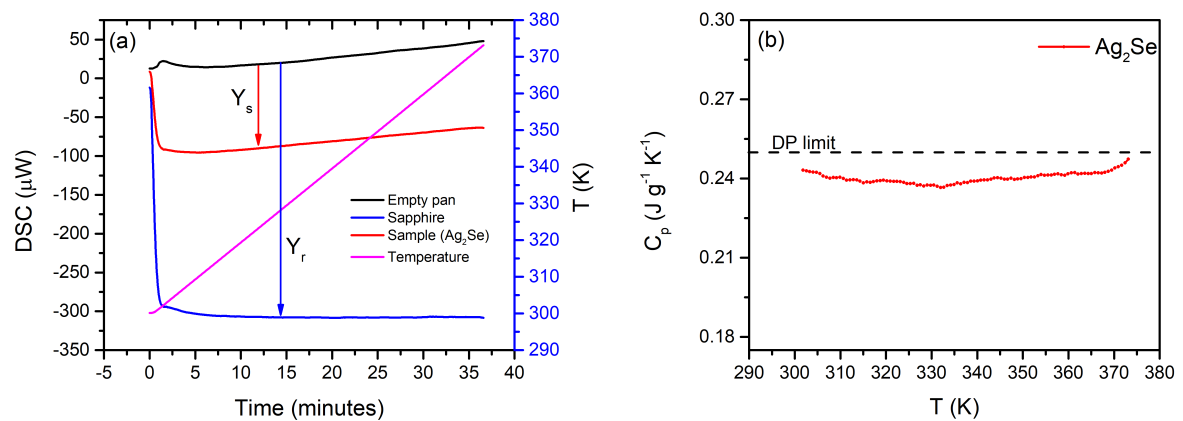


Figure 2.13: Estimation of C_p using DSC7020 differential scanning calorimeter for Ag₂Se sample (a) shows the variation of DSC curves with time, and (b) depicts the temperature dependent C_p variation of Ag₂Se pellet.

2.3 Transport Property Measurement Techniques

2.3.1 Resistivity and Seebeck measurement set up (LSR-3)

Using LSR-3, Seebeck-coefficient and resistivity can be measured simultaneously up to a maximum temperature of 1000°C. Water cooling unit is required for high temperature furnace. Measurements were performed under partial positive He pressure of 0.2 bar.

Principle of Seebeck coefficient measurement: Seebeck coefficient is a measure of potential difference generated as a result of applied temperature gradient to a material. The schematic of measuring S is shown in Figure 2.14

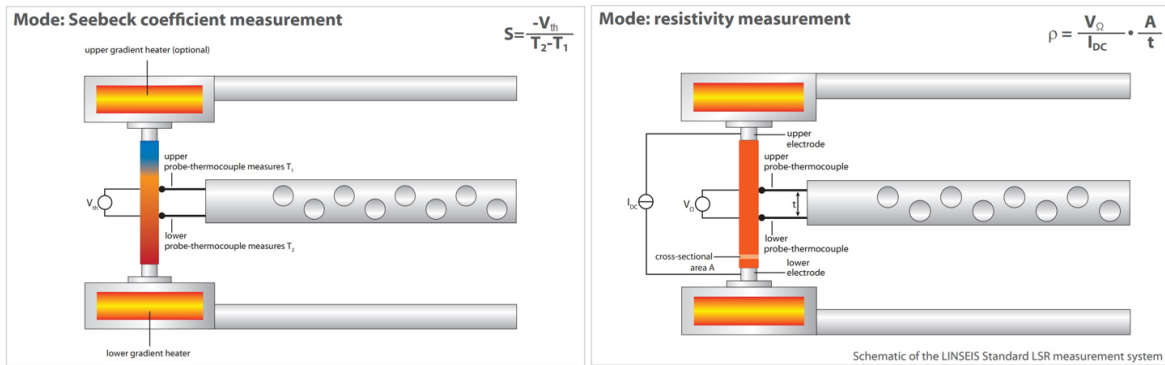


Figure 2.14: Schematic diagram for measuring Seebeck coefficient and resistivity in LSR-3. (Figure adapted from Linseis LSR-3 digital manual)

Rectangular bar or cylindrical shaped sample having cross section dimensions $< 4 \times 4 \text{ mm}^2$ is mounted between two Pt electrodes. Lower electrode contains a heating coil for secondary heater which maintain the controlled temperature gradient across the sample. The overall sample temperature is controlled by uniformly heating filament heater enclosing the entire sample and electrode assembly shown in the schematic. There are two thermocouples namely, upper and lower probe TC of S-type making pressure contacts near the center of the sample. The quality of contact between the sample and probe's TC is controlled by spring adjustment. The probe TC measures the temperature as well as voltage at the point of contacts. Here S can be measured as $V_{th}/(T_1 - T_2)$, where V_{th} is the voltage difference between upper probe (TC1) and lower probe (TC2).

Principle of resistivity measurement: DC four probe configuration is used to measure the electrical resistivity of the sample. While measurement, a constant DC current (I_{DC}) is passed by means of two electrodes in both the directions. In steady state of sample when $\Delta T = 0$, the voltage drop across the sample (V_{Ω}) is measured by probes TC1 and TC2 separated by a distance t . Depending upon the sample length, distance between the probes can be adjusted in LSR-3 set up from 3.1 mm to 4 mm. Based on measured voltage, applied

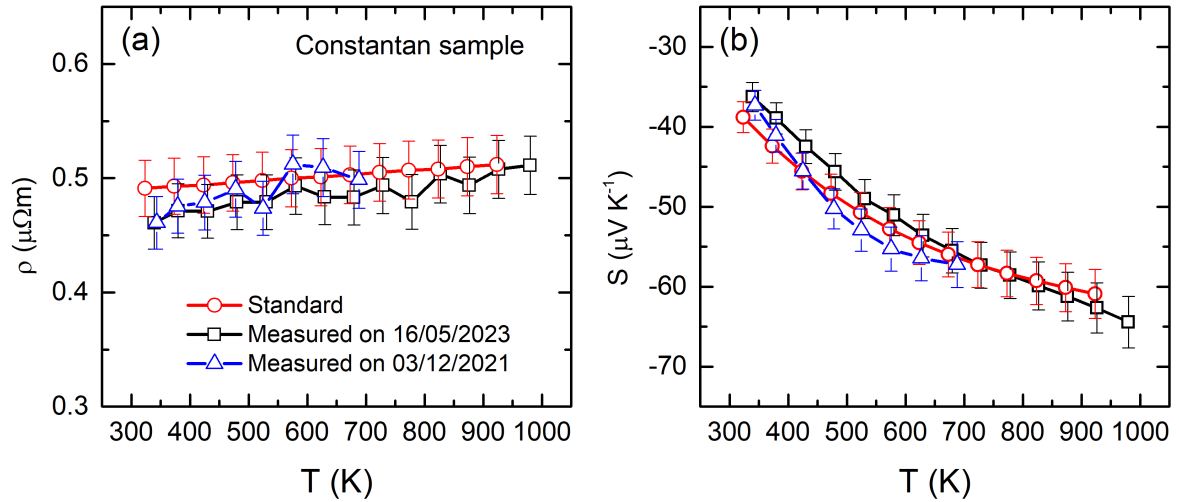


Figure 2.15: Temperature dependent (a) resistivity, and (b) Seebeck coefficient of standard sample (constantan: an alloy of 55% Cu and 45% Ni) measured simultaneously using LSR 3 set-up.

current, cross section area of sample and inter probe distance, resistivity can be estimated as $\rho = \frac{V_{\Omega}A}{I_{DC}}$. Schematic diagram of resistivity measurement in LSR-3 is shown in Figure 2.14.

LSR 3 set up can measure Seebeck value from 1 to 2500 μVK^{-1} with a maximum uncertainty of $\pm 7\%$ in a repeatability error limit of $\pm 3\%$. It can measure electrical conductivity values from 0.01 S cm^{-1} to $2 \times 10^5 \text{ S cm}^{-1}$ within $\pm 5 - 8\%$ uncertainty. Applied DC current passing through sample could take values from 0.1 to 160 mA. Linseis company provided a standard sample of constantan, which is an alloy of copper and nickel, for testing purposes. This sample serves as a benchmark to validate the accuracy of the measured data for any unknown sample that the user is interested in. The measured data for the standard sample is depicted in Figure 2.15, demonstrating a close agreement within the measurement error limit of the experimental setup.

2.3.2 Hall Carrier Concentration

When a current carrying conductor or semiconductor is placed under magnetic field perpendicular to current direction, then voltage is developed perpendicular to the current and magnetic field direction. Measurement of this induced voltage is called Hall effect. It is discovered by Edwin Herbert Hall in 1879. Sign of measured voltage provide information

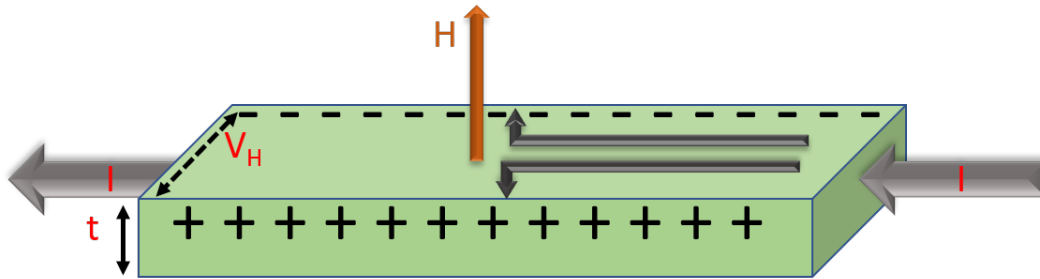


Figure 2.16: Schematic diagram of Hall effect in a semiconducting bar.

about the type of majority charge carrier (electrons or holes) present in any semiconductor. Schematic of Hall bar is shown in Figure 2.16

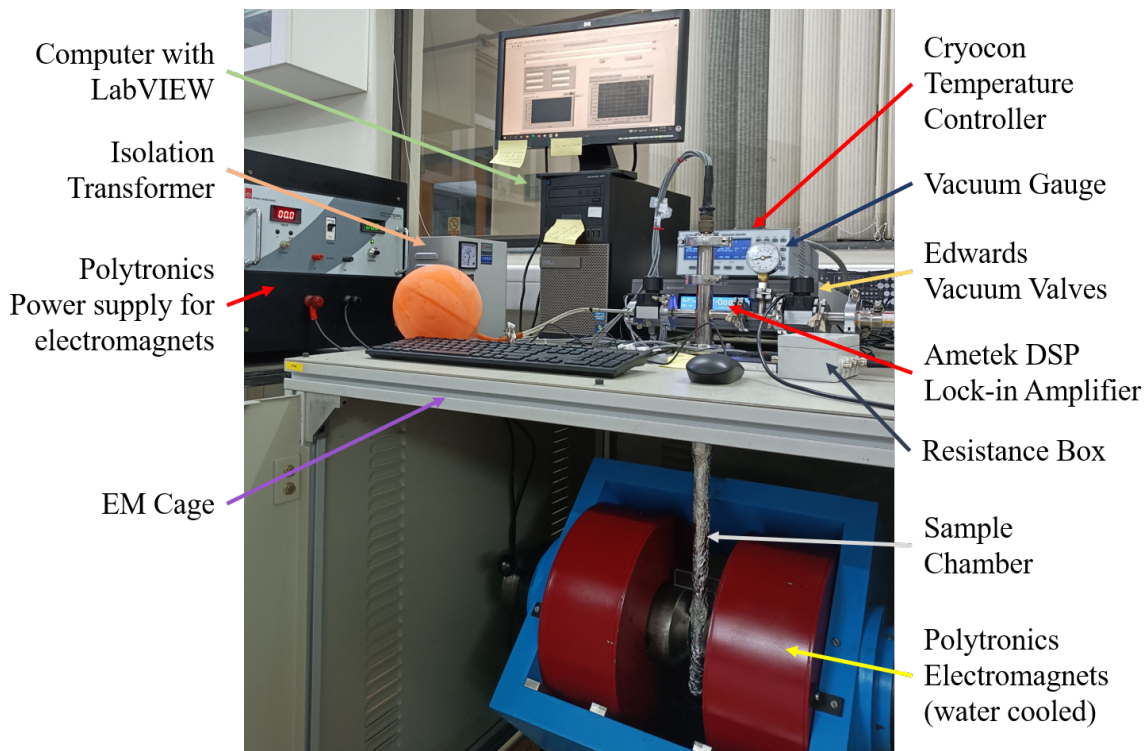


Figure 2.17: Home build automated high temperature Hall effect measurement setup.

For a semiconducting bar carrying current I and of thickness t , V_H is the hall voltage induced when subjected to a perpendicular magnetic field of magnitude H . V_H can be defined

as,

$$V_H = \frac{IH}{net} \quad (2.7)$$

We have measured the charge carrier concentration at room temperature and at higher temperatures using home made set up shown in Figure 2.17. Building this set-up is my collaborative work done with Dinesh Kumar Kedia where I was involved in the initial phase of designing, assembling and calibration process.

Hall set up components:

- Polytronics water cooled electromagnet is used to generate 1 T uniform magnetic field value in 25 mm space between the poles.
- Electromagnetic cage is used for fixing and isolating the electromagnet from environment to avoid any disturbance in magnetic field exerted on sample.
- Sample chamber is made of high quality quartz tube enclosing the sample holder and supporting alumina rod.
- For powering the electromagnets, polytronics power supply is used. It can provide maximum 30 A current to produce 1 T magnetic field.
- Ametek DSP lock-in amplifier is used for supplying constant ac voltage and for measuring output ac signal. The voltage sensitivity is as low as 2 nV and high as 1 V, full scale. It provides highly stable ac signal in a wide frequency range from 0.001 Hz to 250 kHz.
- Resistance box is used to convert the constant ac signal of lock-in amplifier to constant ac current signal. We have used carbon resistors of 250 Ω , 1 K Ω , 10 K Ω , 100 K Ω , 1000 K Ω in the resistance box. Depending upon the ac voltage signal of lock-in, which is from 1 μ V to 5 V, current can be generated according to the requirement by using an appropriate resistance value. In our hall measurements we have used the 5 V ac input signal and 1 K Ω resistance but the range of current can be varied depending upon the requirement.
- Isolation transformer is used to isolate the lock-in amplifier grounding from rest of the components of hall setup for noise cancellation.
- Two Edwards vacuum valves are connected to create vacuum and an inert gas atmosphere inside the sample chamber and vacuum gauge is used for monitoring the pressure inside the

sample chamber.

- For high temperature hall measurements, cryocon temperature controller is used for controlling the current passing through heater and for temperature sensing (Pt 100 resistance sensor is used in our set up, details can be found below in sample holder section).
- The electromagnet, lock-in amplifier and temperature controller are simultaneously controlled by computer through Labview program.
- **Sample Holder:** Sample holder is made from stainless-steel (SS) and shown in Figure 2.18(a). The schematic diagram showing the two color lines, dark black corresponds to components made from stainless steel and light color denotes the alumina components, rod and spacers. Alumina rod holds the entire SS sample holder along with several equally spaced SS radiation shield along its length. Connections are separated from the SS base by using alumina spacers. Cylindrical Pt 100 resistance sensors is mounted in grooved hole of holder. Voltage and current connections (points, 1, 2, 3 and 4) are made up of thin sharp notched SS strips. Thin copper wires of diameter, $100\ \mu\text{m}$ covered with high temperature sleeves are used for extending the connection from sample holder to amphenol connector. The entire assembly is enclosed in a quartz tube where vacuum and inert gas atmosphere can be maintained.

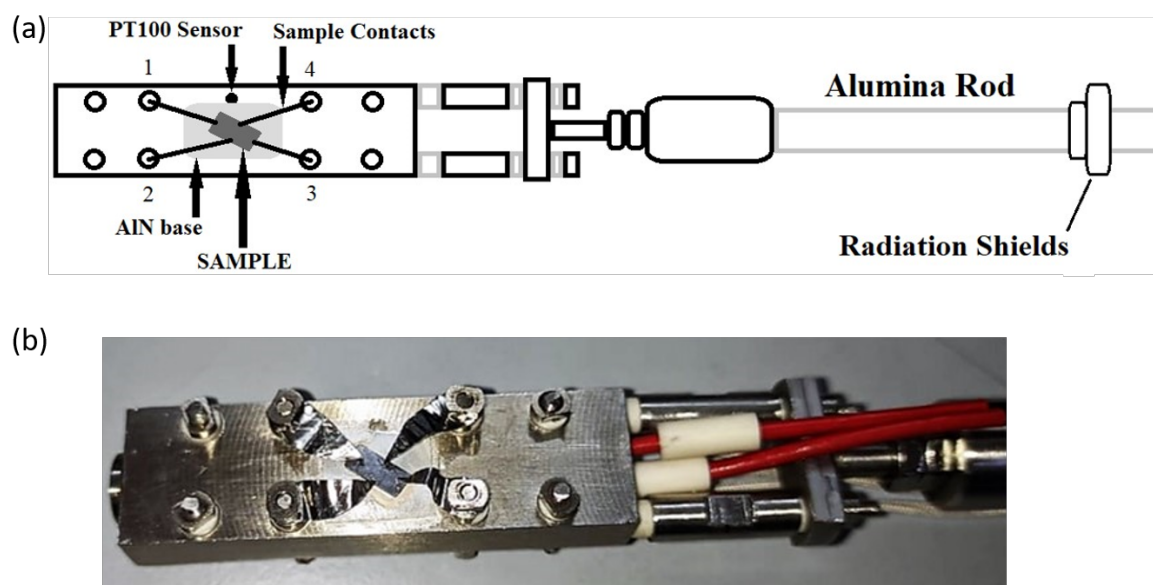


Figure 2.18: (a) Shows the schematic diagrams of front side of sample holder, and (b) is the picture of sample holder.

Our home setup is calibrated by using Ge n-type standard sample at room temperature. And the temperature sensitivity was confirmed with temperature dependent hall measurements of a phase change material, Ag_2Te where transition temperature was previously determined by using DCS and HTXRD. We have measured the temperature dependent hall carrier concentration of our samples under vacuum, using SS pressure contacts.

2.3.3 Laser Flash Analyzer (LFA)

Over past few decades, flash technique has become more versatile for measuring thermal diffusivity and specific heat of various kinds of solids, powders and liquids.

Working principle of LFA: Sample held on a predetermined temperature, back side of sample is irradiated by an infrared laser which homogeneously rise the sample temperature. The laser radiation at the rear end of the sample is collimated by a lens called Irish before going for detection. The resulting rise in temperature gets detected at the rear end of the sample by a semiconducting IR detector. Both thermal diffusivity and specific heat can be estimated from temperature vs time data. The working principle of LFA is also elaborated in

the schematic shown in Figure 2.19.

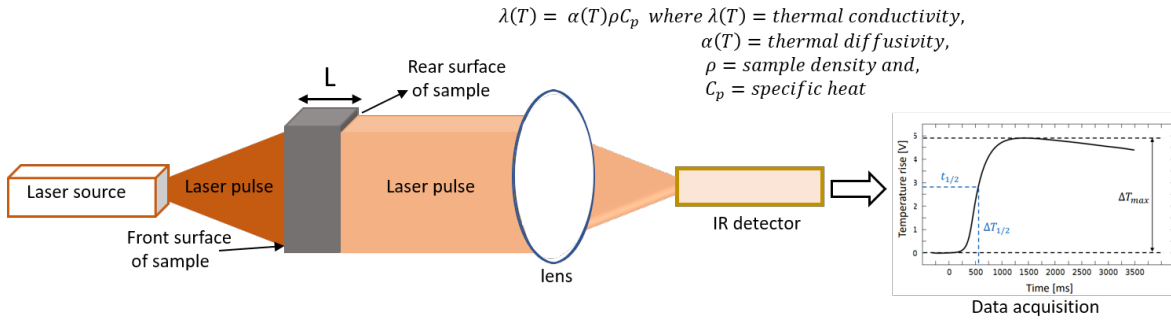


Figure 2.19: Schematic diagram for laser flash technique for thermal diffusivity measurement.

Heat is diffused through thickness L , gives rise to increase in temperature at rear end following the curve shown in schematic. Thermal diffusivity (α) of a sample depends upon half time ($t_{1/2}$) where t is the time for reaching maximum temperature at rear end of the sample. The expression for finding α under adiabatic condition can be expressed as:

$$\alpha = 0.13879 \frac{L^2}{t_{1/2}} \quad (2.8)$$

In ideal cases, temperature of the rear end of sample should increase with time and attains a maximum value under adiabatic conditions, denoted by dotted line in data acquisition shown in schematic diagram. But, as a consequence of heat losses, temperature starts dropping down after achieving a maxima. The time dependent temperature rise at rear end of the sample can be theoretically analyzed by using different models like, Cowan [145], finite pulse correction, heat loss correction, baseline correction, radiation and combined model [146]. However, combined model is the one which takes care of all the corrections including, finite pulse, heat losses etc. Radiation model includes the correction from the direct laser pulse also called ballistic transport in case of porous or cracked samples. But the modified combined model also incorporate the correction of radiation model. Hence, the combined model is a universal model to fit voltage vs time experimental data taken under adiabatic condition of sample. Here, the output signal is voltage obtained from the semiconductor

detector after converting temperature at rear end to voltage. The obtained experimental curve and its theoretical fitted curves are shown in Figure 2.20.

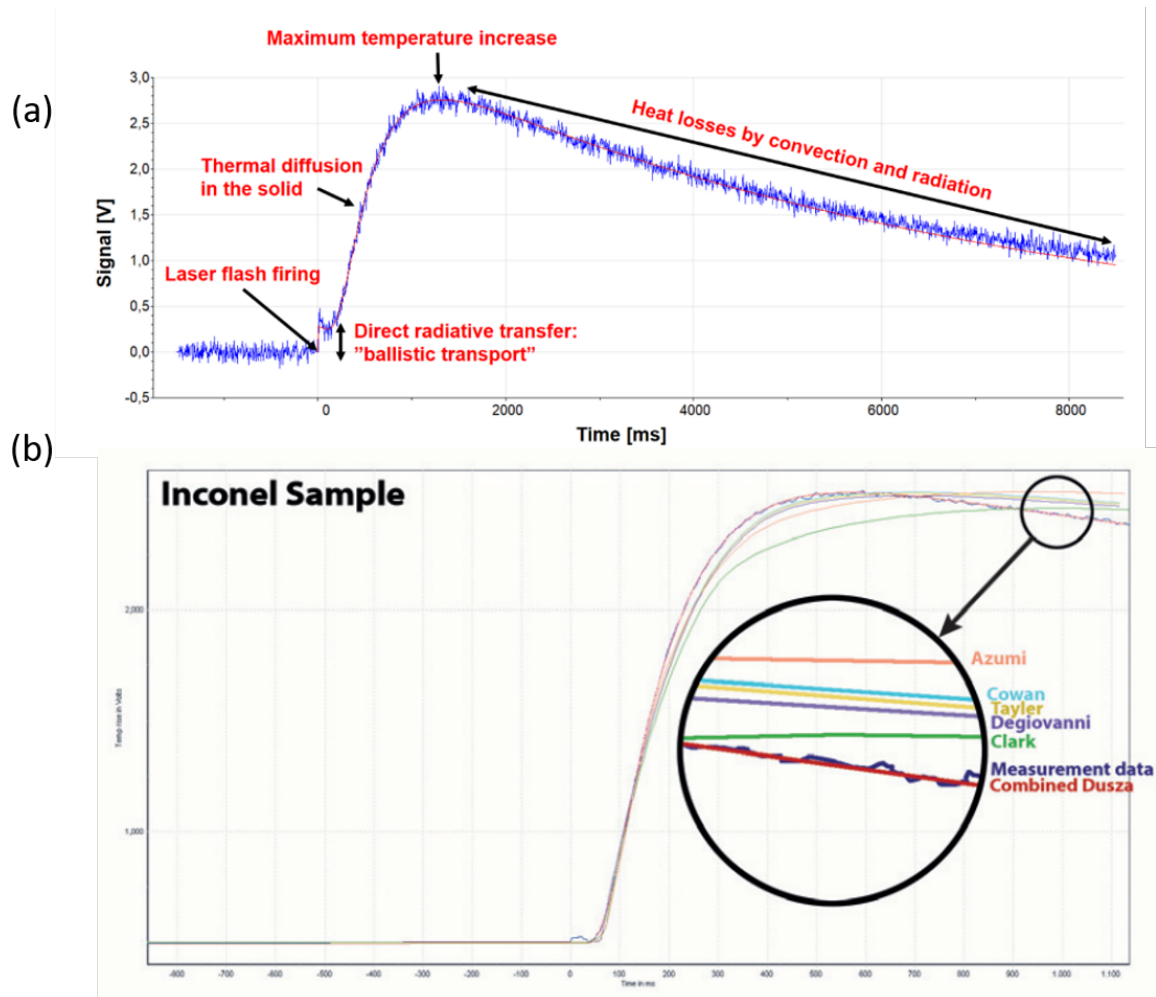


Figure 2.20: (a) Voltage vs time experimental curve and, (b) fitted experimental data with different correction models in LFA 1000 setup.

In LFA, thermal diffusivity is dependent on square of the sample thickness, hence samples should be well polished to attain the uniform thickness. For materials with low thermal conductivity like glass, small sample thickness up to 0.5 mm is required but for highly thermal conducting materials like graphite, it may vary from 1 mm to 3 mm. The experimental data of thermal diffusivity of standard sample graphite, provided by Linseis company for LFA 1000 set-up is shown in Figure 2.21.

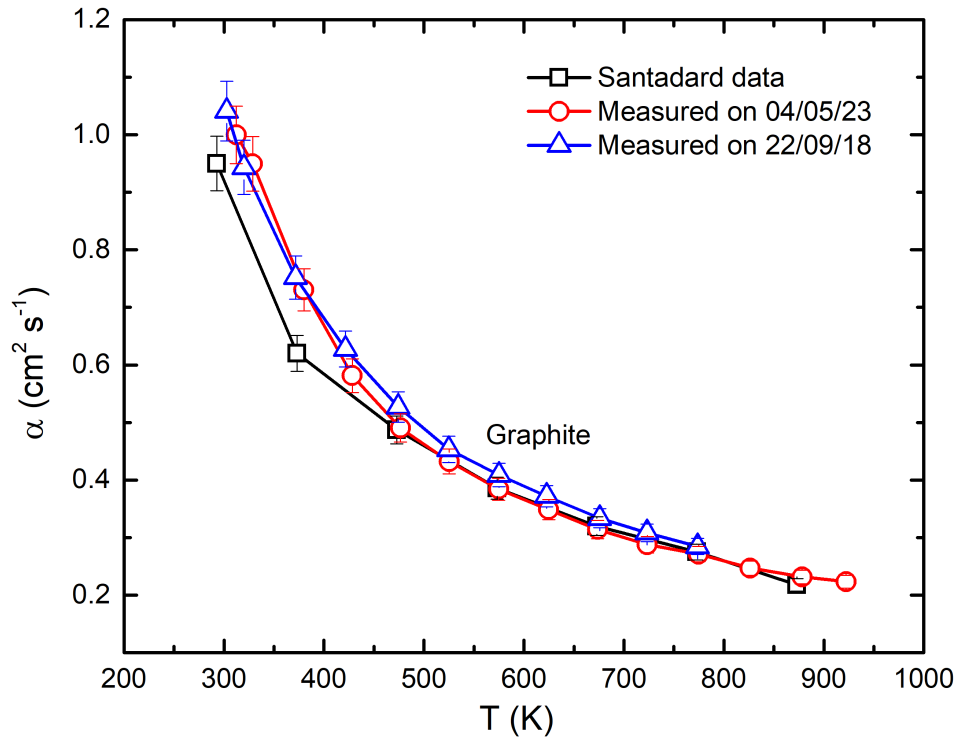


Figure 2.21: Temperature dependent thermal diffusivity (α) of standard sample, graphite, measured using LFA 1000 set-up.

Table 2.1: Technical details of LFA 1000

	LFA 1000
Temperature	RT to 1250°C
Heating rate	0.01 to 20°C
Thermal diffusivity	0.01 to 2000 mm ² sec ⁻¹
Thermal conductivity	0.1 to 4000 Wm ⁻¹ K ⁻¹
Thermal diffusivity accuracy	±2.4%
Repeatability	±1.9%
Flash source	laser Nd-YAG, 25J, Pulse, software controlled
Vision control	Pulse width = 0.05 to 5 msec
IR detector	InSb: RT to 1250°C, liquid N ₂ cooled
Atmosphere	inert, oxidizing and vacuum with S-type thermocouple
Vacuum	up to 10 ⁻⁵ mbar
Gas control	Manual
Sample holders	round (6 mm, 8 mm, 10 mm, 12.7 mm and 25.4 mm) and square (6 mm)
Sample numbers	up to 6 samples

After obtaining the thermal diffusivity of bulk sample using LFA, thermal conductivity can be calculated by using formula, $\kappa = \alpha\rho C_p$. Where sample density ρ was calculated by taking weight and volume of the measured sample and Dulong Petit limit, $C_p = 3nR$, value was taken for specific heat. Since, we have only measured the thermal diffusivity using LFA 1000 then our thermal conductivity have 2.4% data accuracy along with an additional error associated with measuring sample density.

2.4 Electronic band calculations

We collaborated with Dr. Ankita Katre and Neeta Bisht from Pune University for Ag_2Te theoretical calculations. Kumar Ankit from IISER Pune performed the SnTe calculations.

2.4.1 Ag_2Te

The first principles DFT calculations were performed using the Quantum Espresso code (QE) [147]. The exchange correlation energy is represented by a generalized gradient approximation (GGA) functional proposed by Perdew, Burke and Ernzerhof (PBE) [110]. The mesh cut-off for the plane wave was kept as 50 Ry for the ground state calculations. The crystal structure of $\beta\text{-Ag}_2\text{Te}$ is monoclinic with 4 fu per unit cell. The Brillouin zone is sampled using a Monkhorst-Pack scheme, a $12 \times 24 \times 12$ and $20 \times 20 \times 20$ mesh of k-point is used for the geometry optimization. Density of states (DOS) and band structure calculations were performed using a more denser grid of $12 \times 24 \times 12$ and $26 \times 26 \times 26$. The structure is relaxed until the force and energy convergence criteria of 10^{-6} eV and 10^{-7} eV \AA^{-1} , respectively, are achieved. The lattice parameter chosen for β phase are, $a = 8.30 \text{ \AA}$, $b = 4.47 \text{ \AA}$, $c = 7.53 \text{ \AA}$ and $a = 6.70 \text{ \AA}$ for cubic α -phase. These geometrical parameters are in reasonable agreement with the theoretically reported values [148]. The band structures in both the phases were also calculated for 6.5% Ag vacancy. For this we considered a $1 \times 2 \times 1$ and $2 \times 2 \times 2$ supercell of Ag_2Te for β and α phase. The DOS calculations for supercell are performed using a k-mesh of $12 \times 12 \times 12$ and $10 \times 10 \times 10$ for the β and α phase. The thermal transport properties of $\beta\text{-Ag}_2\text{Te}$ are calculated within ab initio framework from

complete phonon description. The normal modes of phonons are calculated using finite displacement approach for $2 \times 4 \times 2$ supercell to avoid periodic boundary effects on calculated atomic forces. LO-TO splitting is accounted by including non-analytical term correction, for which the dielectric tensor and Born effective charges (BEC) are required. These properties along with the atomic forces for each supercell with displacement are calculated using QE package, whereas the dynamical matrix extraction and diagonalization is performed using Phonopy [149]. Anharmonicity is considered within Quasi harmonic approximation (QHA) that required phonon calculations on $\pm 3\%$ of relaxed cell volume. GGA(PBE) and LDA (PZ) [110] exchange-correlation functions, both are tested for computing phonon frequencies and LDA results are further used to determine different phonon scattering rate (τ) contributions and the lattice thermal conductivity κ_l .

2.4.2 SnTe

The first-principles calculations were performed using the QUANTUM ESPRESSO software [147, 150], which implements density functional theory (DFT) using a plane wave basis. Ultrasoft pseudopotentials were employed to describe the electron-ion interactions [151]. For Sn, Te, and Ag, the valence configurations used were $4d^{10} 5s^2 5p^2$, $4d^{10} 5s^2 5p^4$, and $4d^9 5s^2$, respectively. The electron-electron exchange and correlation interactions were described using the Perdew-Burke-Ernzerhof parametrization of the generalized gradient approximation (GGA-PBE) [110]. The electronic wave functions were expanded in a plane wave basis with a kinetic energy cutoff of 60 Ry for all the compounds. To expand the charge density, a kinetic energy cutoff ten times that used for the wave function was employed. Ag doping was incorporated into a $3 \times 3 \times 3$ supercell, which consisted of 27 atoms of Sn and Te each, by replacing Sn with Ag for 3.7%, 7.4% and 11.1% of doping. For Brillouin zone integrations a $4 \times 4 \times 4$ Monkhorst-Pack k-point mesh was utilized [152]. To accelerate convergence Marzari-Vanderbilt smearing with a smearing width of 0.005 Ry was used. The experimental lattice parameters were used as input for structure optimization. Our band structure calculation for pristine SnTe resulted in a very small band gap of around 0.06 eV, which was lower

than the expected value of 0.3 eV [153]. This discrepancy can be attributed to the limitations of DFT which tends to underestimate the small band gaps in semiconductors using GGA-PBE exchange correlations. With Ag doping, the band gap increased and the energy difference between the light hole and heavy hole bands decreased. Additionally, the effective mass of the light hole band (m_L^*) increased from 0.14 m_e for $x = 0$ to 0.45 m_e for $x = 0.074$, as shown in Figure 6.14. This led to a decrease in the carrier mobility with increasing Ag doping. At the same time, the energy difference $\Delta E_{L\Sigma}$ between the light hole and heavy hole bands decreased from 0.35 eV to 0.14 eV ($x = 7.4\%$).

Chapter 3

Synergistic approach towards a reproducible high zT in n-type and p-type superionic thermoelectric Ag_2Te

3.1 Introduction

Here, we investigate the TE properties of superionic Ag_2Te which belongs to a technologically important class of semiconducting/superionic materials Ag_2X ($\text{X} = \text{S}, \text{Se}, \text{or Te}$). Upon heating, Ag_2Te undergoes a superionic transition near $T_t = 420 \text{ K}$. In the room-temperature phase, it has an intrinsically low thermal conductivity of $1.2 \text{ W m}^{-1} \text{ K}^{-1}$ which decreases further to values as small as $\sim 0.7 \text{ W m}^{-1} \text{ K}^{-1}$ in the superionic phase [122, 144]. The carrier mobility in Ag_2Te is high $\sim 10^3 \text{ cm}^2 \text{ V}^{-1}\text{s}^{-1}$ [144], and the carriers mobility ratio (μ_e/μ_h) is around 6 [154]. The Seebeck coefficient at room-temperature is negative and has a reasonably high value of $-100 \mu\text{V K}^{-1}$ despite minority carrier excitations due to a small bandgap E_g of $< 0.1 \text{ eV}$ [119, 144]. These characteristics make Ag_2Te a very promising thermoelectric material. Indeed, in Ag_2Te ingots prepared by solid state melting, a zT of 0.64 at 575 K was previously reported [144]. This was further enhanced to $zT = 1$ at 575 K by PbTe doping through bandgap engineering [121]. These studies suggest that by further opti-

mization, higher zT values can be achieved at temperatures not too high above the superionic transition.

However, despite these remarkable properties Ag_2Te has remained at the backseat in this class of materials. The dark side of Ag_2Te relates to its extreme sample dependence. While in some reports Ag_2Te is shown to undergo a sharp and reversible change in the sign of thermopower (n to p while heating) across T_t [155–158], in some other reports the thermopower is shown to remain negative, featuring only a step-like jump at T_t [121, 144, 154, 155, 158–161]. It is believed that the n-type or p-type behavior in the superionic phase above T_t arises due to very small Ag off-stoichiometry: n-type for a slight Ag excess and p-type for Ag deficient samples. Hereafter, samples that undergo n-to-p transition at T_t will be referred to as p-type, and the samples that undergo n-to-n transition as n-type. Interestingly, within the n-type samples also, the electrical conductivity in the room temperature phase exhibits a significant dispersion varying from 2650 S cm^{-1} in Ag_2Te ingots [162] to 800 S cm^{-1} or even less in hot-pressed Ag_2Te nanopowders [155]. It is therefore evident that the thermoelectric properties of Ag_2Te are extremely sensitive to the exact Ag/Te molar ratio, which varies unpredictably depending on the synthesis conditions.

We mitigate this issue by using an all-room-temperature method of fabricating 100% dense Ag_2Te samples showing reproducible thermoelectric properties. We then go beyond the PLEC limit by adopting a hierarchical nanostructuring approach spanning length scales ranging from nm to μm . This is achieved by using a low frequency vibratory ball-mill which produces a broad particle-size distribution along with a rich variety of particle shapes displaying varying degree of crystallinity with dislocations present over length scale as small as a few nm. The ball-milled nanopowders were directly cold-pressed to achieve densities close to 100% of the theoretical density. This completely precludes the need for high-temperature sintering or spark-plasma sintering, the primary reason for Ag offstoichiometry or inhomogeneity leading to unpredictability and the sample dependence discussed earlier. The realization that Ag_2X materials are ductile in nature played a crucial role in this innovation [163]. Further, by increasing the milling duration, the lattice thermal conductivity is systematically

reduced. We thus obtain a very high zT of 1.2 at 570 K in our n-type samples and 0.64 at 570 K in the p-type samples. The zT values in our study not only supersede the best zT for the undoped samples but even the doped samples previously reported. The highest *average* zT of 0.99 in our n-type Ag_2Te is also comparable to that of doped Bi_2Te_3 , in the temperature range of 300 K to 570 K [164]. The density functional theory (DFT) based electronic structure and thermal transport calculations are also performed to understand the n-type to p-type transition, and the origin of intrinsically low thermal conductivity and its further suppression by nanostructuring.

3.2 Sample Synthesis and Nomenclature

Several Ag_2Te samples were prepared during this study using various methods, including (a) solid-state melting (SSM), (b) Ball-milling followed by cold-pressing (CP) (no sintering), (c) Ball-milling followed by high-temperature sintering (BS) of the cold-pressed pellet, (d) Hand-milling followed by high-temperature sintering (HS) of the cold-pressed pellets.

A summary of all the samples reported here along with their short names is given in Table 3.1. The short names are derived from the fabrication method used. For example, CP1, CP2, etc., correspond to the Ag_2Te samples with $\text{Ag} : \text{Te} \equiv 2 : 1$ obtained by ball-milling followed by cold-pressing. For Ag excess (deficient) samples, the same nomenclature has been used but with an extension $+x$ ($-x$) where x depicts the percentage of Ag excess (+) or Ag deficiency (−). For example, CP+1 corresponds to a sample of the CP series but with starting composition $\text{Ag} : \text{Te} \equiv 2.02 : 1$ (i.e., 1% excess Ag). Similarly, CP-1 corresponds to a starting stoichiometry of $\text{Ag} : \text{Te} \equiv 1.98 : 1$. The relative density ($\rho_m = \rho_{\text{exp}}/\rho_{\text{th}} \times 100$, where ρ_{exp} and ρ_{th} are respectively the experimental and theoretical density) of the pellets used for thermoelectric investigations is also given in Table 3.1. ρ_{exp} was obtained by measuring the mass (M) and volume (V) of the pellet as $\rho_{\text{exp}} = M/V$. This was further cross-checked by measuring the density of several samples using the Archimedes method. The details of CP, BS, HS and SSM methods are given as follows:

In all synthesis experiments, Ag powders from Sigma Aldrich (purity 99.98%) and Te pow-

der from Alfa Aesar (purity 99.999%) were used. The purity and source of precursors was maintained to avoid any variations among the synthesized samples due to unknown factors.

Ball-Milling (BM): For the synthesis of ball-milled Ag_2Te powders, the elemental powders were weighed in the molar ratio according to the desired stoichiometry ($Ag/Te \equiv 2$ for stoichiometric and $2 \pm \delta$ for the off-stoichiometric samples) and transferred into the stainless steel (SS) cylindrical vessel of the milling apparatus along with the SS balls. The vessel was then closed with a lid having a teflon gasket to preserve sample atmosphere during ball-milling. This step was carried out in an Ar-filled glove-box (Mbraun) to avoid any oxidation. The loaded vessel was then removed from the glove-box and loaded in a vibratory ball mill. The volume of the vessel is 6 cm^3 . The SS beads used were of diameter 0.4 cm. The charge (Ag and Te powders) to balls mass ratio was kept around 1 : 2.5. The vessel was made to oscillate along the arc of circle. The vibration frequency was 120 rpm, and amplitude of vibration around $\pm 10^\circ$ about the mean vertical position. At the end it results powder of the desired Ag_2Te phase.

CP: The ball-milled powders were cold pressed in a in KBr press die set to get the CP series of samples.

BS: For the BS series, the cold-pressed pellets were sealed in quartz ampoules under a dynamic vacuum and sintered at 673 K for 24 hours in a muffle furnace with heating elements on the two sides (which is the potential source of temperature gradient leading to Ag migration).

HS: The HS samples were prepared by hand-grinding the Ag and Te powders for 180 minutes inside an Ar-filled glove box. The samples were subsequently cold-pressed in a KBr die-set and sintered in evacuated quartz ampoules as described above.

SSM: The SSM sample was prepared directly melting Ag and Te powder in an evacuated quartz ampule. The ampoule was loaded in a muffle furnace and heated to 1000°C in 10 hours, kept there for 5 hours and then cooled down to 500°C at a rate of 10°C h^{-1} . The furnace was then turned-off to allow cooling down to the room temperature.

Table 3.1: The details of various Ag_2Te samples used in this study are given here. The sample name is given in the first column. Here, BS represents samples prepared by ball-milling followed by sintering of the cold-pressed pellets at 673 K for 24 h; HS represents samples prepared by hand-milling and sintering as in the BS series; CP represents samples prepared by ball-milling followed by cold-pressing (no sintering); and SSM represents an ingot sample prepared by solid-state melting. The second column (τ_m) gives the milling duration where applicable. The nominal stoichiometry of the starting Ag and Te powders in each case appears in the third column, and the last column (ρ_m) gives the density of the pellets on which the thermoelectric measurements are done.

Name	τ_m	Ag : Te	ρ_m
Ball-milled & Sintered			
BS1	300	2 : 1	90
BS2	300	2 : 1	93
BS3	300	2 : 1	92
BS4	300	2 : 1	89
Hand-milled & Sintered			
HS1	300	2 : 1	96
HS2	300	2 : 1	98
HS3	300	2 : 1	97
Ball-milled & Cold-pressed			
CP1	200	2 : 1	100
CP2	400	2 : 1	100
CP3	500	2 : 1	100
CP4	600	2 : 1	100
Off-stoichiometric: Ball-milled & Cold-pressed			
CP+1	500	2.02 : 1	100
CP+0.5	500	2.01 : 1	100
CP-0.5	300	1.99 : 1	100
CP-1	300	1.98 : 1	100
SSM	—	2 : 1	100

3.3 Characterization and transport property measurement

The phase purity of our samples was assessed using the x-ray powder diffraction technique (Bruker, D8 Advance). The lattice parameters were estimated by performing the Rietveld refinement using the Fullprof Suite. The microstructure was assessed using the Field Effect Scanning Electron Microscopy (FESEM) (Ultra Zeiss plus) equipped with an Energy Dispersive x-ray (EDX) analysis attachment (Oxford Instruments). The high-resolution transmission electron microscopy (JEOL JEM 2200FS 200 keV) was done on ball-milled powder as well as powders obtained by crushing a small piece of the sample that has undergone thermal cycling between room temperature and 570 K. The ball-milled or finely ground powder was mixed with ethanol in a vial. This was then centrifuged and the smaller particles from the top of the vial were dropcasted onto a Cu-grid that was subsequently loaded on the TEM sample stage and plasma cleaned at 250 eV. The GMS-3 software package was used for further FFT and IFFT analysis. The electrical resistivity and thermopower were measured simultaneously using Linseis LSR-3 set-up. The thermal diffusivity was measured on disc shaped samples ($\phi = 8$ mm) using Laser Flash Analyzer (Linseis LFA 1000). The thermal conductivity is obtained by using the formula, $\kappa = C_p \rho_m D$ where C_p is the specific heat at constant pressure, ρ_m is sample density and D is the measured thermal diffusivity. The Dulong - Petit limit ($C_p = 3nR$) was directly used. This, of course, is incorrect around the phase transition. For this reason, the temperature range around T_t ($T_t \pm 100$ K) is excluded from the analysis of zT. Sample density was estimated by measuring the mass and dimensions of the disc shaped samples. The measured values were cross-checked using the Archimedes method for several samples and the two methods agreed with $\pm 5\%$. Room temperature (RT) Hall carrier concentration was measured using a Physical Property Measurement System (Quantum Design). The longitudinal contribution was eliminated by measuring V_{xy} in positive and negative fields ($V_{Hall} = (1/2)(V_{xy}(H) - V_{xy}(-H))$), which removes any symmetric contribution.

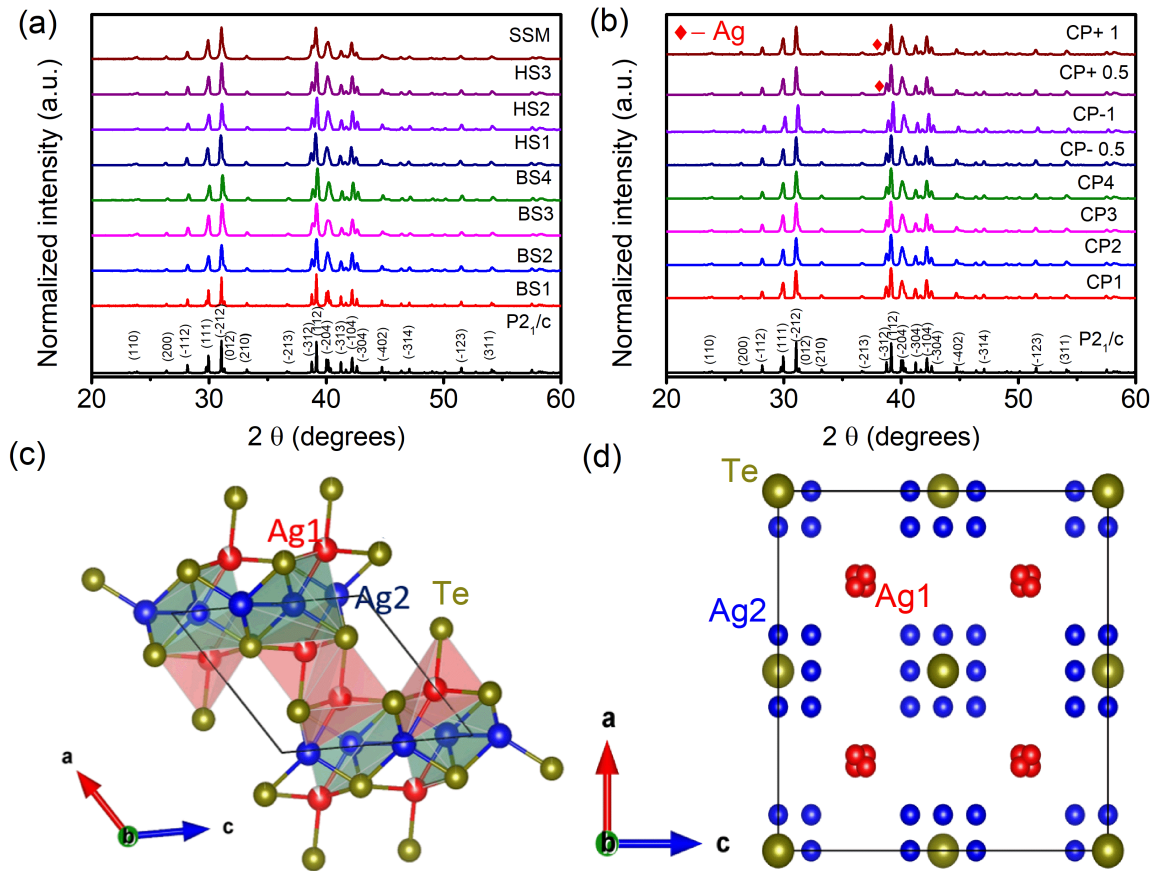


Figure 3.1: (a) x-ray powder diffraction patterns for sintered and SSM samples, and (b) for cold-pressed Ag_2Te sample; (c) Crystal structure of room-temperature monoclinic $\beta\text{-Ag}_2\text{Te}$, and (d) Crystal structure of the high temperature cubic α -phase.

3.4 Results and Discussion

3.4.1 Sample Characterization

The phase purity of our samples was checked using the x-ray powder diffraction (XRPD) method at room-temperature. For all synthesized samples results are shown in Fig. 3.1 (a, and b). The observed XRPD patterns can be satisfactorily indexed on the basis of the monoclinic ($P2_1/c$) symmetry with no extra peaks. The only exception to this are the samples prepared with excess Ag where a small extra peak due to unreacted Ag metal is seen as shown in Fig. 3.1 (b). The crystal structure of room temperature monoclinic and superionic phase are

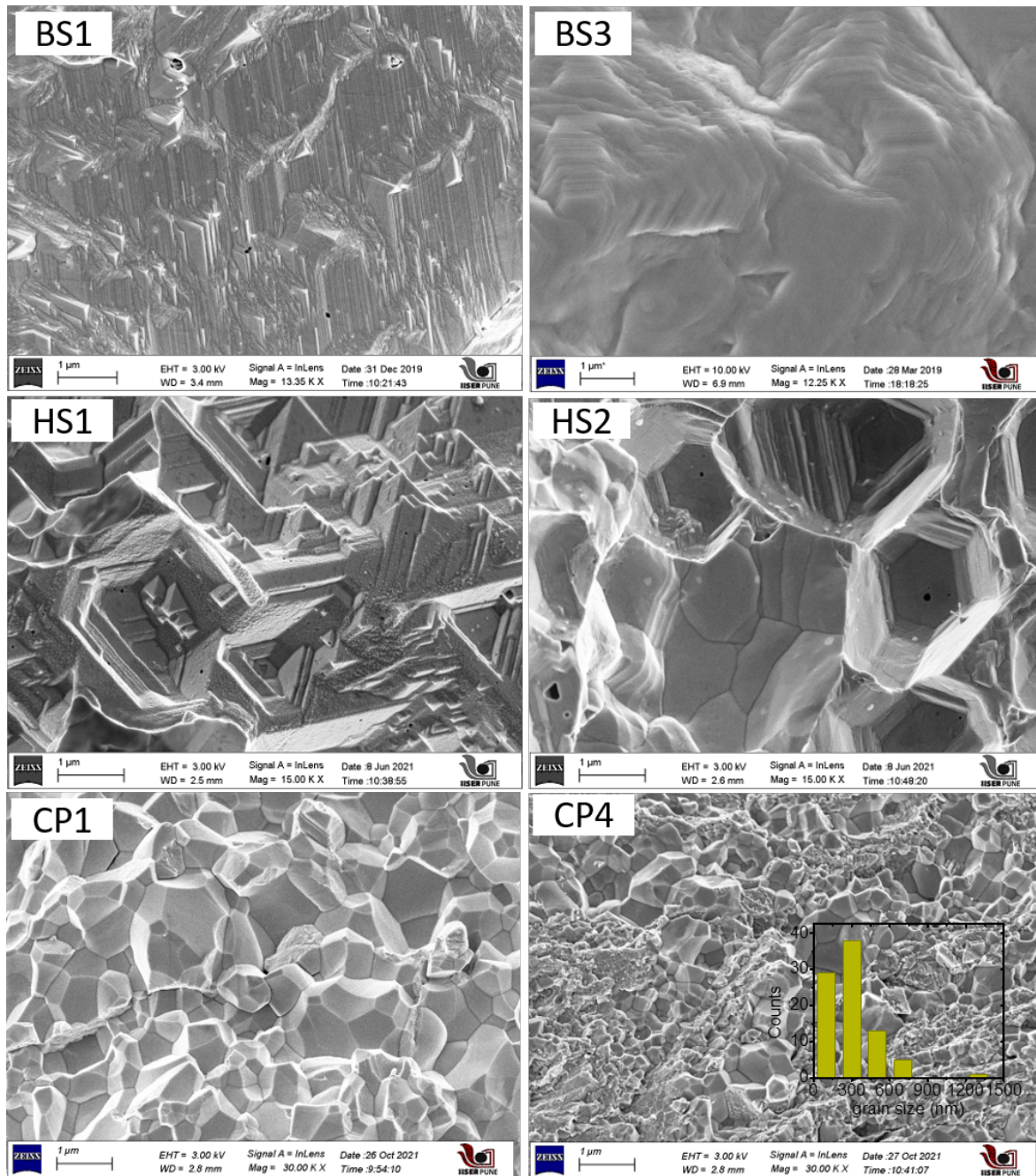


Figure 3.2: Morphology at $1 \mu m$ length scale of freshly fractured bulk pellets of few representative Ag_2Te samples synthesized BS, HS and CP methods.

shown in Fig. 3.1 (c, and d) respectively. For few representative samples, morphology of freshly fractured bulk pellets is shown in Fig. 6.3. Sintered samples have shown the layered

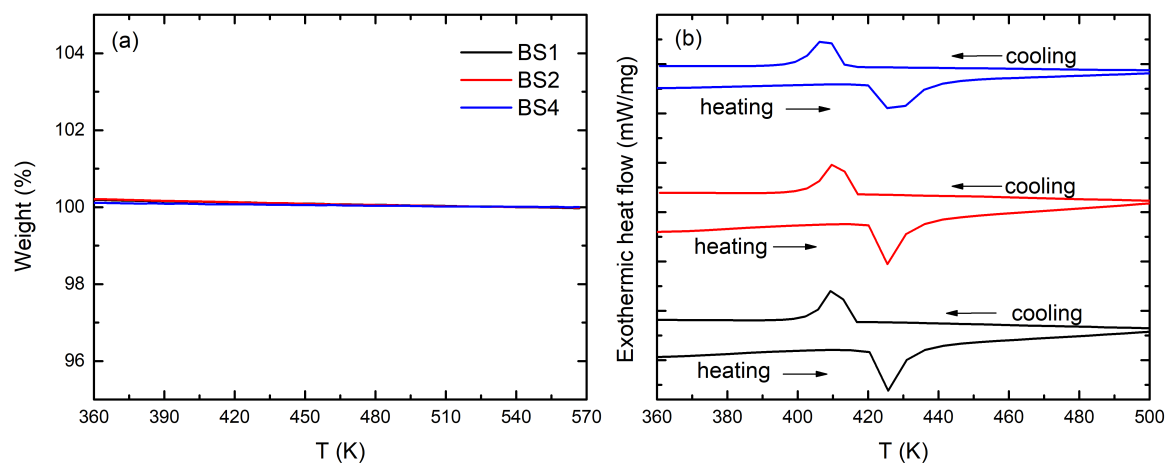


Figure 3.3: (a) Thermogravimetric analysis (TGA), and (b) differential scanning calorimetry (DSC) of BS1, BS2 and BS4 samples.

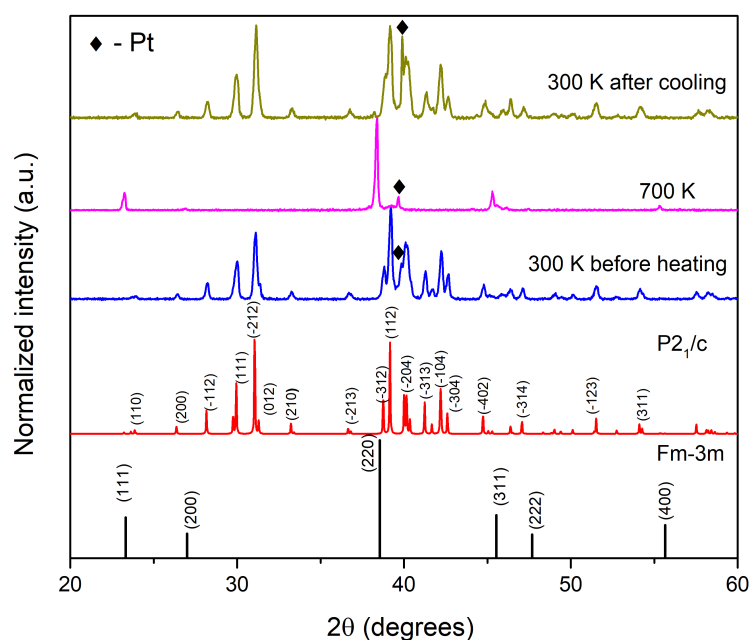


Figure 3.4: High temperature XRD of Ag₂Te.

texture and CP bulk pellets contains large number of grains with varying sizes from few hundreds of nanometers to micrometers. Thermal stability and the presence of structural phase transition at T_t was confirmed using the Differential Scanning Calorimetry shown in Fig. 5.6 and there was no weight loss observed till 570 K. While heating the samples showed structural and superionic transition at 425 K and at 410 K while cooling indicating the first order transition. The cubic $Fm\bar{3}m$ symmetry in the superionic phase was confirmed using the high-temperature XRPD shown in Fig. 3.4. Hereafter, we shall refer to the monoclinic phase below T_t as β -Ag₂Te, and the cubic phase above T_t as α -Ag₂Te. The crystal structure of β -Ag₂Te is layered comprising Ag(1) and Ag(2)-Te layers as shown in Fig. 3.1 (c), where Ag(1) and Ag(2) are inequivalent Ag sites having different Te coordinations. In the high-temperature phase shown in Fig. 3.1 (d), the Te ions form a rigid *fcc* network and the Ag ions hop between various interstitial sites. The lattice constants obtained from the Rietveld refinement are given in Table 3.4.1. A good agreement with the reported lattice parameters is found for all our samples [35].

Table 3.2: Lattice parameters of all the samples and compared with reported values by Lee et al. [35]

Samples	Nominal composition	a(Å)	b(Å)	c(Å)	β (deg)
BS1	Ag ₂ Te	8.17	4.47	8.98	124.12
BS2	Ag ₂ Te	8.17	4.47	8.98	124.13
BS3	Ag ₂ Te	8.16	4.47	8.97	124.04
BS4	Ag ₂ Te	8.16	4.47	8.98	124.12
HS1	Ag ₂ Te	8.16	4.47	8.98	124.12
HS2	Ag ₂ Te	8.17	4.47	8.98	124.14
HS3	Ag ₂ Te	8.16	4.47	8.98	124.12
CP1	Ag ₂ Te	8.17	4.47	8.98	124.15
CP2	Ag ₂ Te	8.17	4.47	8.98	124.13
CP3	Ag ₂ Te	8.16	4.47	8.98	124.10
CP4	Ag ₂ Te	8.16	4.47	8.98	124.11
CP-1	Ag _{1.98} Te	8.17	4.47	8.98	124.15
CP-0.5	Ag _{1.99} Te	8.17	4.47	8.98	124.15
CP+0.5	Ag _{2.01} Te	8.16	4.47	8.98	124.10
CP+1	Ag _{2.02} Te	8.16	4.47	8.98	124.08
Lee et al.	Ag ₂ Te	8.16	4.47	8.98	124.16

A few representative HRTEM images of the ball-milled Ag₂Te nanoparticles are shown

in Fig. 3.5. The HRTEM samples were prepared by centrifuging the ball-milled powder in an ethanol medium. This makes the heavier (and bigger) particles to settle down in the centrifuged vial, allowing only the smaller particles to be picked for examination. The image in panel (a) is a low-resolution TEM image showing the particle-size distribution in our samples. The ball-milled nanoparticles show a surprisingly rich diversity in their shapes and the degree of crystallinity. The image in panel (b), for example, shows a spherical particle showing a high degree of crystallinity with nicely lined-up lattice planes. On the other hand, the particle in (c) shows a hexagonal shape with lattice planes near the top and bottom aligned parallel to the edges of the grain; the alignment is horizontal close to the left and right edges, and vertical around the center of the particle. Similarly, in panel (d) a pentagonal shaped particle, and in (e) a rectangular shaped particle with spatially varying crystalline orientation over nanometer length-scale are shown. To demonstrate this diversity further, a high-resolution HRTEM image of a nearly spherical nanoparticle of diameter 20 nm is shown in panel (f).

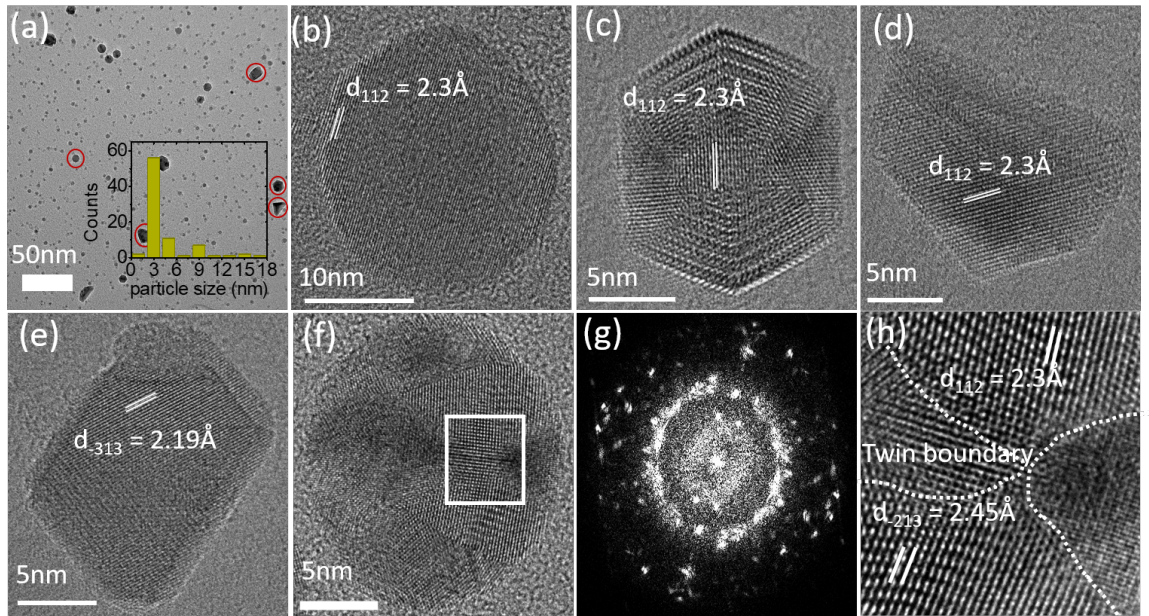


Figure 3.5: TEM analysis of the Ball-milled powders (a) a low resolution TEM image showing Ag₂Te nanoparticles. Inset shows the particle-size distribution, (b - f) high-resolution TEM images showing different morphologies and degree of crystalline order in the Ag₂Te nanoparticles in (a), (g) FFT of nanoparticle in (f) showing the polycrystalline-like diffraction pattern on a single Ag₂Te nanoparticle in (f), (h) a zoomed-in image on the bordered area (in white) in (f). The dashed lines showing the grain boundaries are drawn as a guide to eye.

Unlike the spherical particle in (b), the particle in panel (f) shows a spatially varying crystalline order akin to the other less symmetric particles in other panels. A zoomed-in image of the region in the white box in (f) is shown in (h). It shows four differently oriented grains over an area of 5 nm by 5 nm. In panel (g) we show the FFT of the nanoparticle shown in (f). It reveals the polycrystalline-like electron diffraction pattern due to the presence of nano-domains.

3.4.2 Electrical conductivity and Thermopower

Ag₂Te sintered samples: BS and HS series

The temperature dependence of σ of samples of the BS series, namely, BS_x ($x = 1, 2, 3$ and 4) is shown in Fig. 3.6 (a). The sample BS3 has the highest electrical conductivity of 1805 S cm⁻¹ near 300 K. For this sample, σ increases upon heating above 300 K, exhibits a

maximum around 330 K and drops precipitously thereafter due to the onset of the superionic transition. In the superionic phase, σ continues to decrease steadily showing a $T^{-\alpha}$ temperature dependence with $\alpha \approx 1.2$. Since the carrier concentration (n) is a temperature dependent quantity with $dn/dT > 0$ (see, Figure 3.7), the actual scattering mechanisms seems to be more complex than the simple acoustic-phonon scattering for which a $T^{-3/2}$ behavior is expected. In the superionic phase, among other factor, the mobile Ag-ions would act as an additional source of scattering leading to departure from the $T^{-3/2}$ dependence. On the other hand, in BS1, BS2 and BS4, σ near 300 K has reduced to 1200 S cm^{-1} , 900 S cm^{-1} and 340 S cm^{-1} , respectively. The large reduction for sample BS4 is particularly striking given that all four samples were prepared under identical conditions and with the same starting stoichiometry. The magnitude of σ at 300 K correlates nicely with the carrier concentration (n) at 300 K shown in Table 3.3, which is highest for BS3 ($2.4 \times 10^{18} \text{ cm}^{-3}$) and lowest for BS4 ($0.7 \times 10^{18} \text{ cm}^{-3}$). All the samples exhibit high Hall mobilities: $\sim 5000 \text{ cm}^2 \text{ V}^{-1} \text{ s}^{-1}$ for BSx ($x = 1, 2$ and 3) and $\sim 3000 \text{ cm}^2 \text{ V}^{-1} \text{ s}^{-1}$ for BS4. These mobility values far exceed those of some better known state-of-the-art n-type thermoelectric materials. For example, the carrier mobility in Bi_2Te_3 alloys is $\sim 200 \text{ cm}^2 \text{ V}^{-1} \text{ s}^{-1}$ [165] or that in Mg_3Sb_2 alloys is $\sim 100 \text{ cm}^2 \text{ V}^{-1} \text{ s}^{-1}$ [166]. However, the significant dispersion in the magnitude and temperature dependence of σ of the sintered Ag_2Te samples is what makes them less favorable. This unpredictability is even more vividly revealed in the temperature variation of S shown in Fig. 3.6 (b). While samples BS1, BS2 and BS3 show a n-type behavior, a p-type behavior is observed for BS4. A similar sample dependence is found in the HS samples also. σ and S for three representative HS samples are plotted in Fig. 3.6 (a, b).

The observed unpredictability or sample dependence in our sintered samples is in line with several previous reports where both n-type and p-type behaviors are found for the sintered or hot-pressed Ag_2Te samples. The underlying reason for this unpredictability is related to the Ag-migration during high temperature sintering or spark-plasma sintering. It is known from previous works that in the superionic phase at temperature $T > T_t$, the liquid-like Ag ions form a steady concentration gradient inside the material without any metal deposition

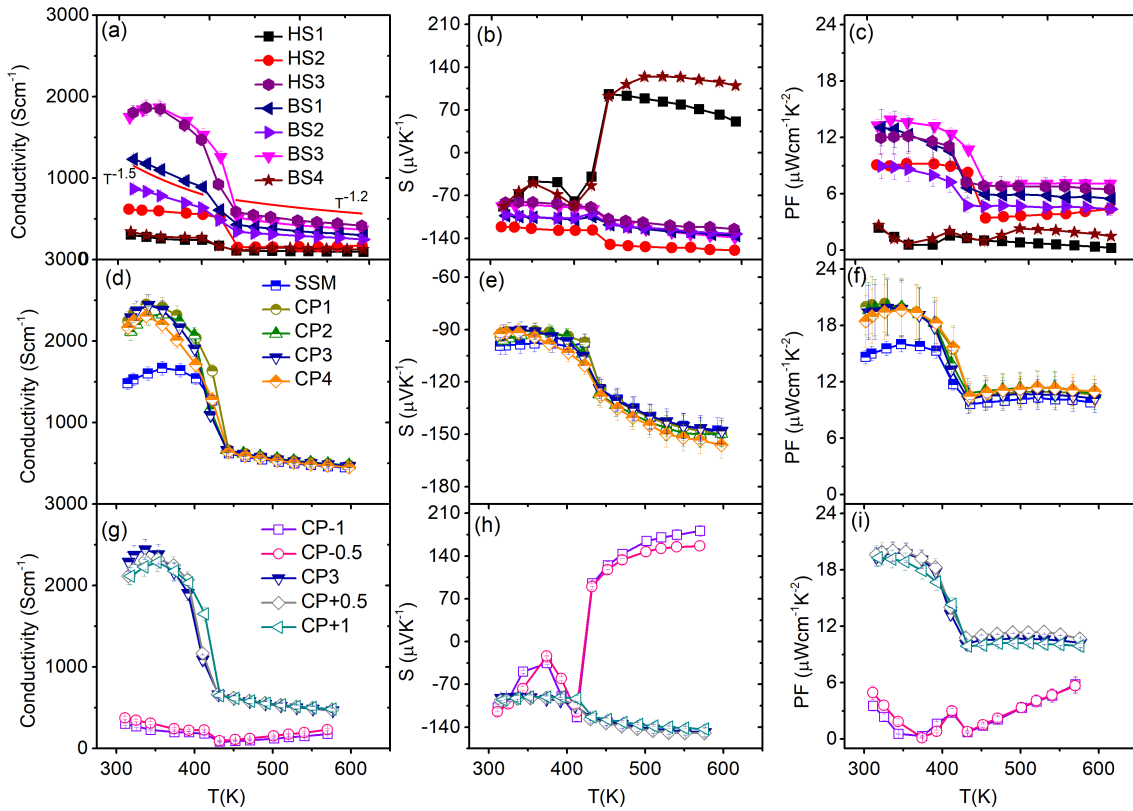


Figure 3.6: Temperature dependence of electrical conductivity, thermopower, and power factor for our samples. (a - c) BS and HS samples, (d - f) stoichiometric CP samples prepared for different milling durations, (g - i) CP samples prepared with different Ag/Te molar ratio (see text for details).

unless the applied voltage (or the electric current density) exceeds a critical value [167,168]. The Ag migration can also get activated in the presence of a temperature gradient. How high a temperature/voltage gradient a given superionic material can withstand without metal-ion migration leading to deposition depends on temperature T above the superionic transition temperature [169]. In Ag₂Te, the current density at 570 K exceeds 15 A cm⁻², and the temperature gradient that the sample can withstand at 570 K is of the order of 20 K, see Figures 3.10 and 3.9.

Ag₂Te cold-pressed samples: CP series

Typically, the high-temperature sintering or spark-plasma sintering (SPS) is done to get high-density nanostructured pellets. However, the Ag₂X family of materials exhibit an extraor-

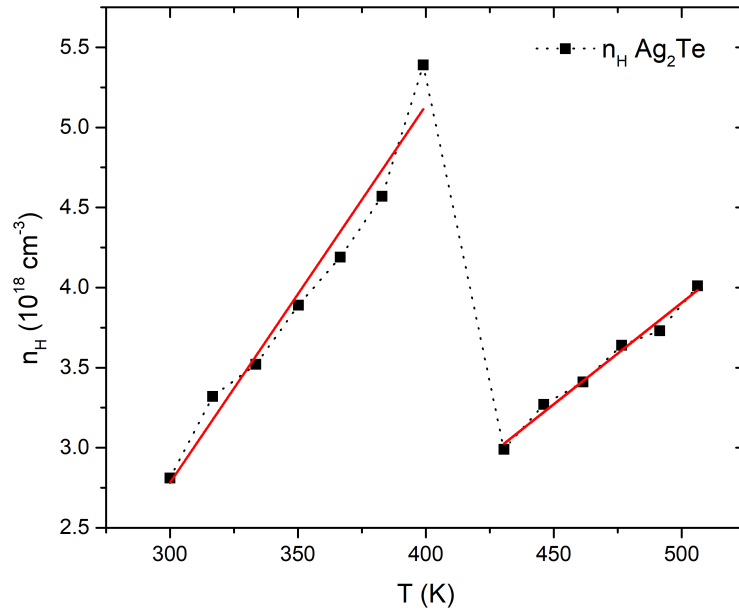


Figure 3.7: Temperature dependent Hall carrier concentration measured from 300 K to 506 K.

dinary metal-like ductility with a large plastic deformation strain [163]. This metal-like ductility can be exploited to obtain high density pellets directly by cold-pressing. Indeed, the cold-pressed pellets of Ag_2Te exhibit mass densities lying within $\pm 5\%$ of the theoretical density. This property is lacking in the Cu_2X family, as similar cold-pressed powders of Cu_2X resulted in densities in the range $70 \pm 5\%$ of the theoretical density as opposed to 100% for the Ag_2X compounds. This eliminates completely the need for high-temperature sintering or SPS. Equipped with this knowledge, we fabricated a series of Ag_2Te samples by ball milling followed by cold-pressing and measured their thermoelectric properties between 300 K and 570 K. Samples CP1, CP2, CP3, and CP4 in Table 3.1 all have the same starting stoichiometry (molar ratio $\text{Ag}/\text{Te} \equiv 2$); however, the ball-milling duration has been varied to influence the average particle-size for reducing the thermal conductivity, discussed later.

The temperature variation of σ and S for these samples is shown in Fig. 3.6 (d, e). They all exhibit a n-type behavior and their thermopower and electrical conductivity plots also overlap showing no sample dependence. The measurements are limited to the highest temperature

Table 3.3: Room temperature carrier concentration (n), electrical conductivity (σ), hall mobility (μ), thermopower (S) and power factor (PF).

Samples	n (10^{18} cm^{-3})	σ (S cm^{-1})	μ ($\text{cm}^2 \text{ V}^{-1} \text{ s}^{-1}$)	S ($\mu\text{V K}^{-1}$)	PF ($\mu\text{W cm}^{-2} \text{ K}^{-1}$)	S at T_t
Ball-milled & Sintered						
BS1	1.45	1233	5315	-103	13	n-n
BS2	1	868	5425	-103	8.9	n-n
BS3	2.4	1805	4700	-85	14.7	n-n
BS4	0.7	345	3080	-87	2.6	n-p
Hand-milled & Sintered						
HS1	2	306	956	-88	2.4	n-p
HS2	1.2	618	3219	-121	9.2	n-n
HS3	4.8	1728	2700	-88	12	n-n
Ball-milled & Cold-pressed						
CP1	3.3	2247	4256	-94	20	n-n
CP2	3.3	2118	4013	-96	19.6	n-n
CP3	3.5	2291	4091	-92	19.4	n-n
CP4	3.5	2167	3869	-92	18.5	n-n
Off-stoichiometric, Ball-milled & Cold-pressed						
CP-1	0.74	803	2550	-108	3.5	n-p
CP-0.5	1	375	2344	-115	5	n-p
CP+0.5	3.1	2118	4270	-97	19.6	n-n
CP+1	3.2	2118	4137	-95	19.3	n-n

of 570 K above which the Ag migration becomes non-local under the temperature gradient applied during the thermopower measurements, see Fig. 3.9. For comparison σ and S for the SSM sample are also shown. The milling duration (or the average particle-size) has apparently no measurable effect on σ and S . These n-type CP samples exhibit high electrical conductivity: $\sigma \approx 2300 \text{ S cm}^{-1}$ near 300 K. This is higher than the electrical conductivity of our SSM sample ($\approx 1500 \text{ S cm}^{-1}$) and comparable to the best ingot samples reported previously in literature [144] (Fig. 3.6 (d)). The carrier concentration in all these samples is around $3.4 \pm 0.1 \times 10^{18} \text{ cm}^{-3}$, independent of the sample (see Table 3.3). This shows that the Ag/Te stoichiometry remains intact in the CP series of samples leading to a highly reproducible behavior.

Additionally, the reproducibility was further confirmed by synthesizing the two Ag_2Te samples with the same milling time of 500 minutes. The thermoelectric properties of these two samples are depicted in Fig. 3.8.

Off-stoichiometric $\text{Ag}_{2\pm\delta}\text{Te}$ cold-pressed samples: $\text{CP}\pm x$ series

Having established that cold-pressing (without sintering) and limiting the highest temperature to 570 K results in highly reproducible results, we now proceed to investigate the effect of Ag-off stoichiometry in the cold-pressed samples. For this purpose, we synthesized Ag-excess and Ag-deficient samples, namely: CP-0.5, CP-1 (0.5% and 1% Ag deficient), CP+0.5, CP+1 (0.5% and 1% Ag excess). The temperature variation of σ and S for these samples is shown in Fig. 3.6 (g, h). The Ag-excess samples show a n-type behavior and their σ and S are comparable to the stoichiometric samples over the whole temperature range. In stark contrast to this, the Ag-deficient samples exhibit a p-type behavior in the superionic phase and for these samples σ has also been significantly suppressed. Not only that, even the qualitative temperature dependence of $\sigma(T)$ for the Ag-deficient samples has changed both below and above T_t . In the superionic α -phase, these samples exhibit an increasing behavior ($d\sigma/dT > 0$), whereas for the n-type samples $d\sigma/dT < 0$. The carrier concentration (n) in our off-stoichiometric samples at 300 K is shown in Table 3.3. In the Ag-excess samples, $n = 3.1 \pm 0.1 \times 10^{18} \text{ cm}^{-3}$ is nearly the same as the carrier concentration in the stoichio-

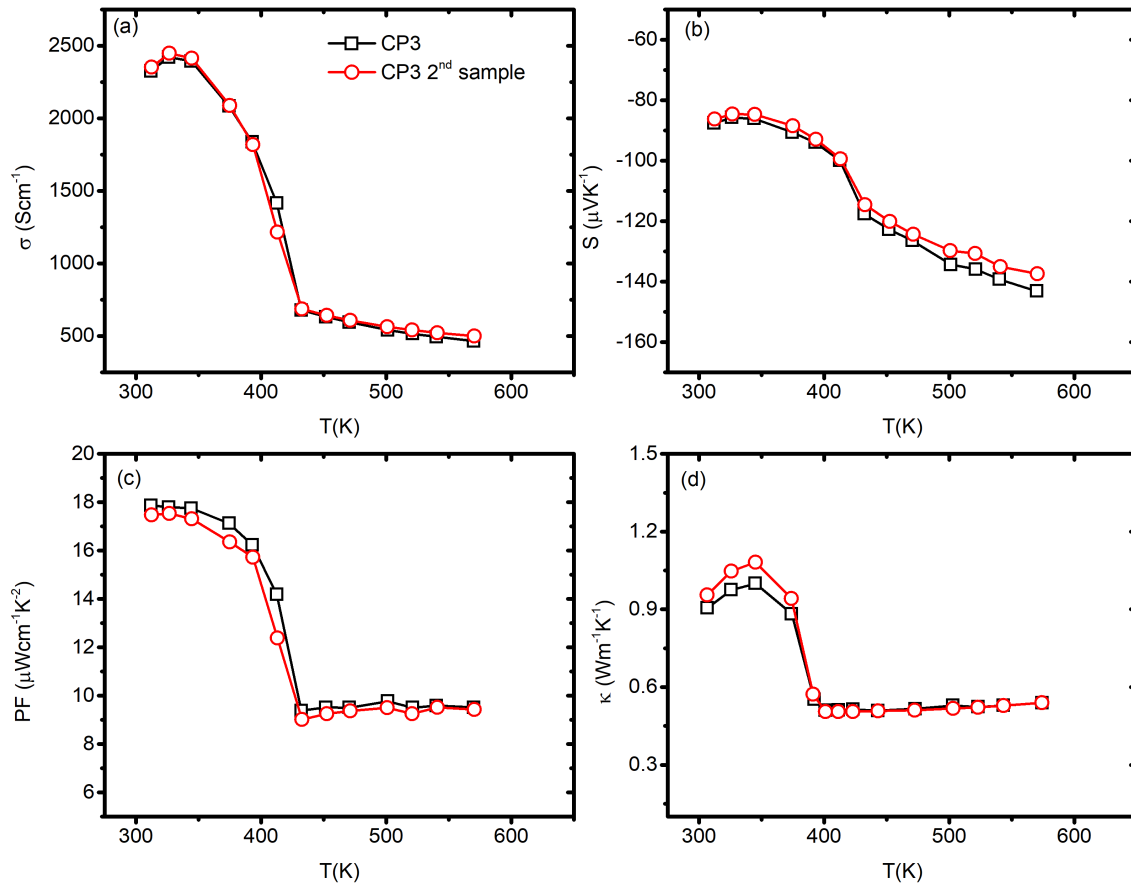


Figure 3.8: Temperature dependent (a) electrical conductivity, (b) Seebeck coefficient, (c) power factor, and (d) thermal conductivity for two n-type Ag_2Te samples synthesized by ball-milling for 500 minutes.

metric samples. In the Ag-deficient samples, however, n decreases to $1.0 \pm 0.1 \times 10^{18} \text{ cm}^{-3}$ for 0.5% and $0.7 \pm 0.1 \times 10^{18} \text{ cm}^{-3}$ for the 1% Ag vacancies. To understand why Ag-excess sample behave more like the stoichiometric samples we recall that the XRPD of these samples showed Ag metal peaks indicating that only a very tiny amount of excess Ag can be incorporated in the structure by mechanical milling at room-temperature. Previously, Taylor and Wood [154] also reported the presence of unreacted silver in their Ag-excess samples prepared by solid-state melting. Notably, the CP-0.5 and CP-1 samples exhibit a peak in their thermopower near 350 K. No phase transition could be detected at this temperature in our TGA/DSC or high temperature powder x-ray diffraction data. The reason behind the appearance of this mysterious peak in the Seebeck coefficient is as yet unclear to us. However, we notice that only those samples that show a n-to-p transition at T_t exhibits this peak. For example, not only CP-1 and CP-0.5 but also HS1 and BS4 show a peak in S near 350 K. What is common between these four samples is that they all exhibit a very low electrical conductivity (of the order of 500 Scm^{-1}). In previous literature also, a peak near 350 K can be seen in Ag_2Te samples showing n-to-p transition. [122, 162] Further detailed and more focused studies to shed light on the origin of this peak are required.

3.4.3 Estimation of critical temperature and critical current density in Ag_2Te

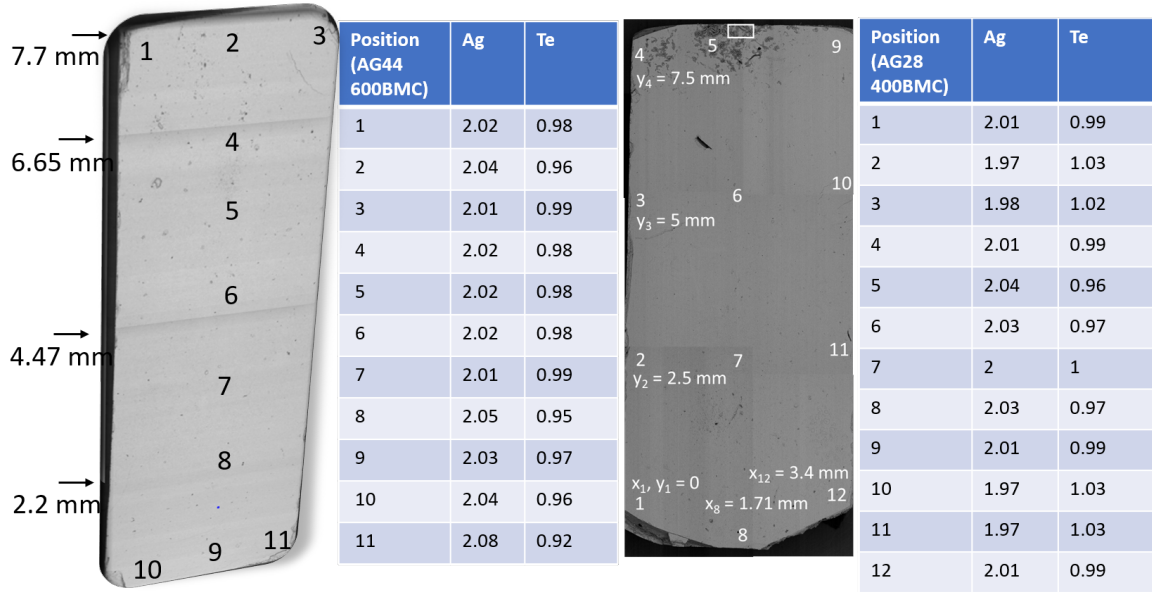


Figure 3.9: Composition analysis of LSR bars after measuring the electronic transport properties upto 570 K and 610 K (showing Ag migration).

We estimated the highest temperature up to which the Ag diffusion remained local in our samples. For this two bar-shaped cold-pressed bars were heated at 570 K (sample 1) and 610 K (sample 2) under a 20 K gradient and with a small DC current flow of $\approx 5 \text{ A cm}^{-2}$. The FESEM images of these samples after the experiment are shown in Fig. 3.9. While in sample 2 some Ag aggregation can be seen at its colder end (see white rectangular box), sample 1 shows no such deposition. Thus, within the superionic phase, the Ag migration becomes non-local only at high temperatures, exceeding $\approx 150 \text{ K}$ above T_t . Based on this, we limited the highest temperature in our experiments to 570 K. In order to estimate the critical current density, the sample resistivity was measured under a DC current at 570 K continuously for 140 minutes for different values of current densities ranging from 3 A cm^{-2} to 15 A cm^{-2} as shown in Fig. 3.10. No perceptible change in the sample resistivity could be

observed up to 15 A cm^{-2} . This suggests that at 570 K the critical current density in Ag_2Te is higher than 15 A cm^{-2} .

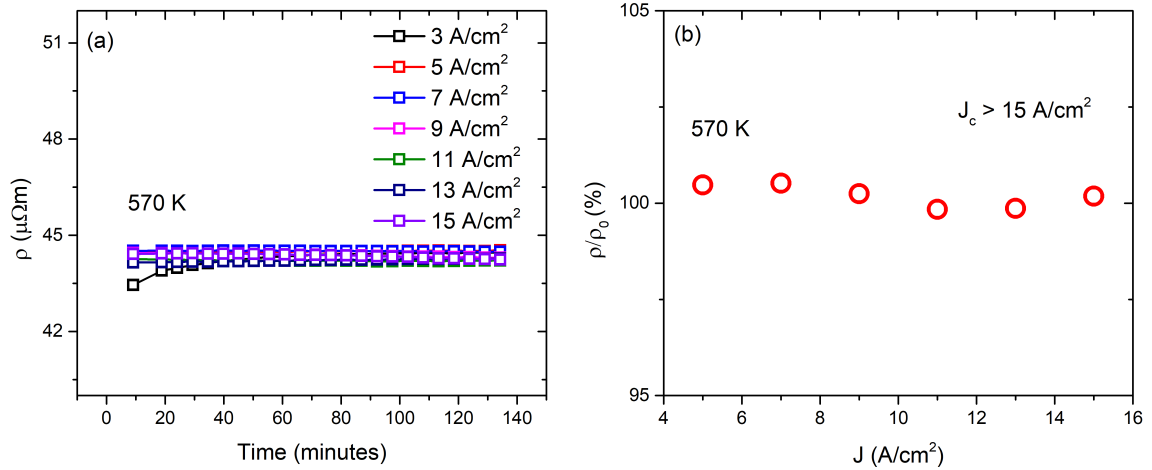


Figure 3.10: (a) Electrical resistivity measured for 140 minutes at different current densities, and (b) relative change in sample resistivity with respect to the resistivity value for lowest current density.

3.4.4 Power Factor

The temperature dependence of PF for our samples is shown in Fig. 3.6(c, f, i). As shown in Fig. 3.6f, the PF for all our n-type CP samples ($\approx 20 \mu\text{W cm}^{-1}\text{K}^{-2}$ at 300 K) overlap over the whole temperature range. In contrast, in the sintered BS or HS samples (Fig. 3.6c), the PF is not only low ($< 12 \mu\text{W cm}^{-1}\text{K}^{-2}$ at 300 K) but the PF for these samples also varies from one sample to other. This underpins the strength of the sample fabrication technique reported here. In our n-type CP samples, the maximum PF obtained is close to $20 \mu\text{W cm}^{-1}\text{K}^{-2}$ in the β -phase and $11 \mu\text{W cm}^{-1}\text{K}^{-2}$ in the superionic phase where it shows a weak temperature dependence. In the p-type CP samples (CP-0.5 and CP-1) the PF shows a linearly increasing behavior in the superionic phase attaining a value of $6 \mu\text{W cm}^{-1}\text{K}^{-2}$ at 570 K (Fig. 3.6i).

3.4.5 Electronic band structure

To gain a qualitative understanding of the charge transport properties in Ag_2Te samples, we turn now to the electronic band structure calculations (done in collaboration with Dr. Ankita

katre and Neeta Bisht from Pune University). The band structure for $\beta\text{-Ag}_2\text{Te}$ is shown in Fig. 3.11a (left panel) where an indirect bandgap of 0.07 eV has been observed upon incorporating the spin-orbit coupling in good agreement with previous reports [119, 148].

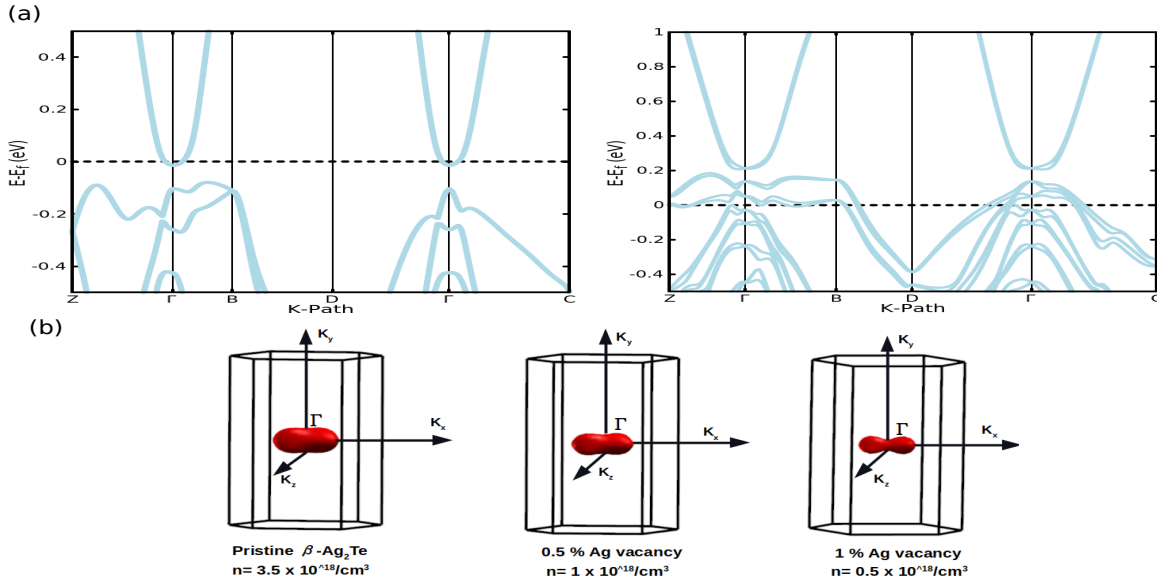


Figure 3.11: Electronic band calculation of (a) pristine (left panel) and 6.5 % Ag deficient (right panel) Ag_2Te for room temperature monoclinic phase and (b) Fermi surface calculations with different percentage Ag vacancy.

The small band gap suggests that both types of charge carriers contribute to the transport. However, since the carrier mobility ratio μ_e/μ_h in the β -phase is about 6 [154], the sign of S is negative. The band structure for $\beta\text{-Ag}_2\text{Te}$ with 6.5% Ag vacancies is also shown in Fig. 3.11(a) (right panel). Due to Ag vacancies the Fermi level has been pushed down into the valence band. This should have resulted in a positive Seebeck coefficient; however, the amount of Ag vacancies in our samples is less than or equal to 1%, which is not high enough to make S positive. This is depicted with the help of Fermi surface plots corresponding to the experimental carrier concentrations. The electronic band structure for $\alpha\text{-Ag}_2\text{Te}$ is shown in Fig. 3.12(a), which agrees favorably with previous literature [148]. The Fermi surface in this case consists of a small hole-pocket centered at the Γ -point and six equivalent electron pockets around the L-point. This is expected to give rise to n-type behavior for stoichiometric

α -Ag₂Te as is indeed seen experimentally. In the 6.5% Ag-deficient sample, the Fermi level goes deeper into the valence band resulting in a large hole-Fermi surface centered around the Γ -point as shown in Fig. 3.12(b) which is expected to result in p-type behavior as is indeed seen experimentally in the α -phase of Ag-deficient samples.

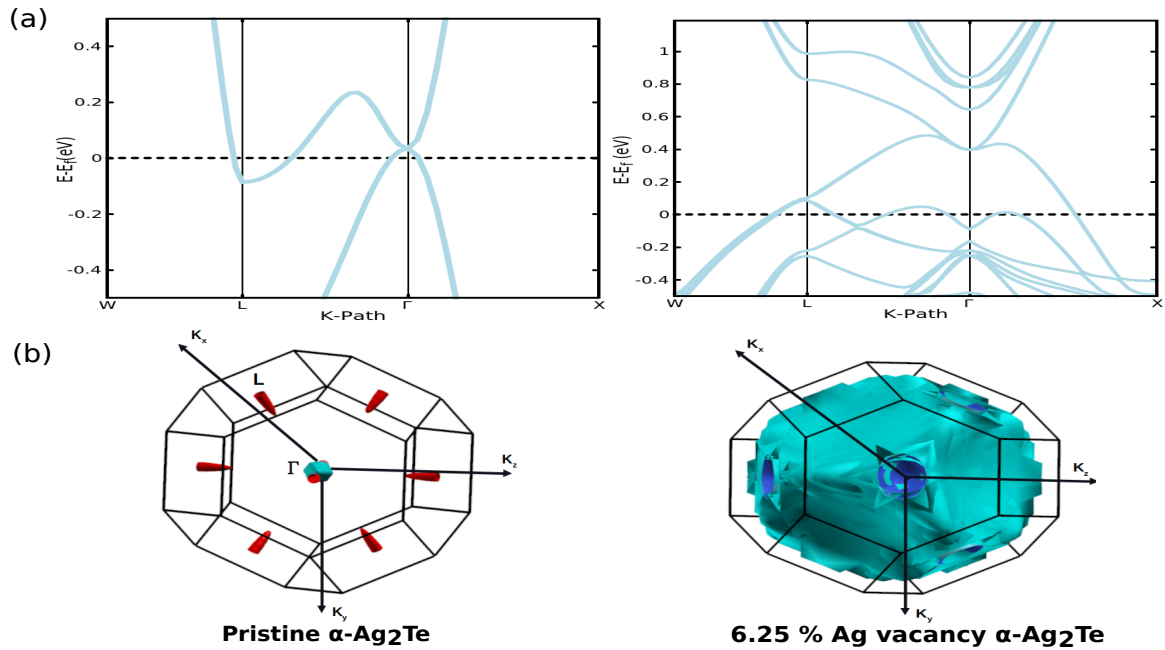


Figure 3.12: Electronic band calculation of (a) pristine (left panel) and 6.5 % Ag deficient (right panel) Ag₂Te for high temperature cubic phase, (b) shows the Fermi surfaces in pristine and 6.5% Ag deficient phases.

3.4.6 Effect of thermal cycling in Ag₂Te cold-pressed samples

The effect of thermal cycling between 300 K and 570 K on σ and S has been checked thoroughly. The results of thermal cycling are shown in Fig. 3.13. With the exception of the first heating run in the β -phase, all the subsequent runs for the 3 measurement cycles overlap within the error bars of our measurements. In fact, in the superionic phase, even the data taken during the first heating run overlaps the cooling data and also the data taken in the subsequent runs. The hysteresis in the first run in the β phase is not understood as yet. Due to the ductile nature of Ag₂Te, during cold-pressing the grains are mechanically deformed at their boundaries in order to fill the space, leaving no pores, and yielding a 100% dense sample.

We believe that during the first heating run, the mechanical strain at the grain boundaries is gradually relieved as the sample is slowly heated. In the subsequent runs, the changes in the grain boundary region may not be significant enough to result in different properties. This could be a part of the reason why our samples exhibit higher resistivity in the first heating run.

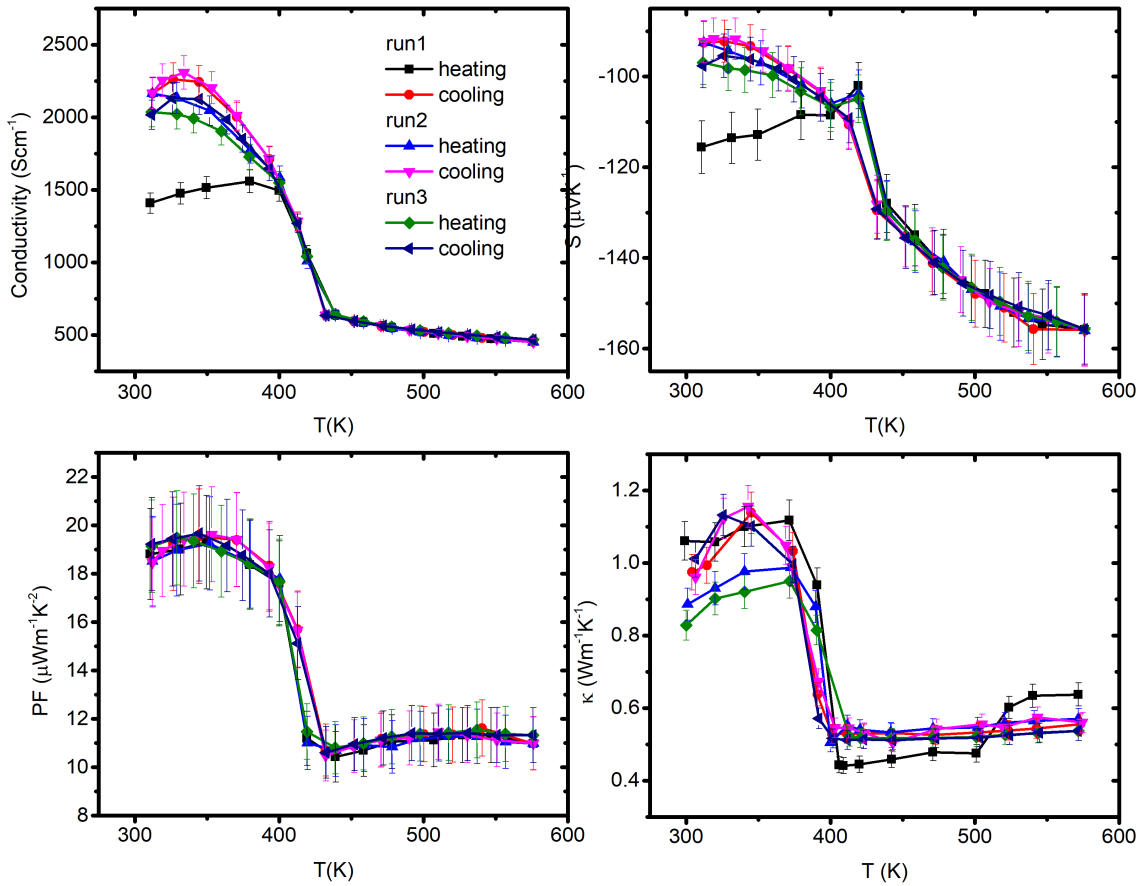


Figure 3.13: Thermal cycling effect to test the sample stability (a) electrical conductivity (b) thermopower (c) PF and, (d) thermal conductivity of CP4 sample.

3.4.7 Thermal transport

The thermal conductivity (κ) of our CP samples (CP1, CP2, CP3, and CP4) is shown in Fig. 6.11(a, b). The data for SSM sample is also included as a reference. κ for remaining samples is shown in Fig. 3.15a. Since σ for stoichiometric CP samples overlap over the

whole temperature range, the κ_e contribution is expected to be the same for these samples.

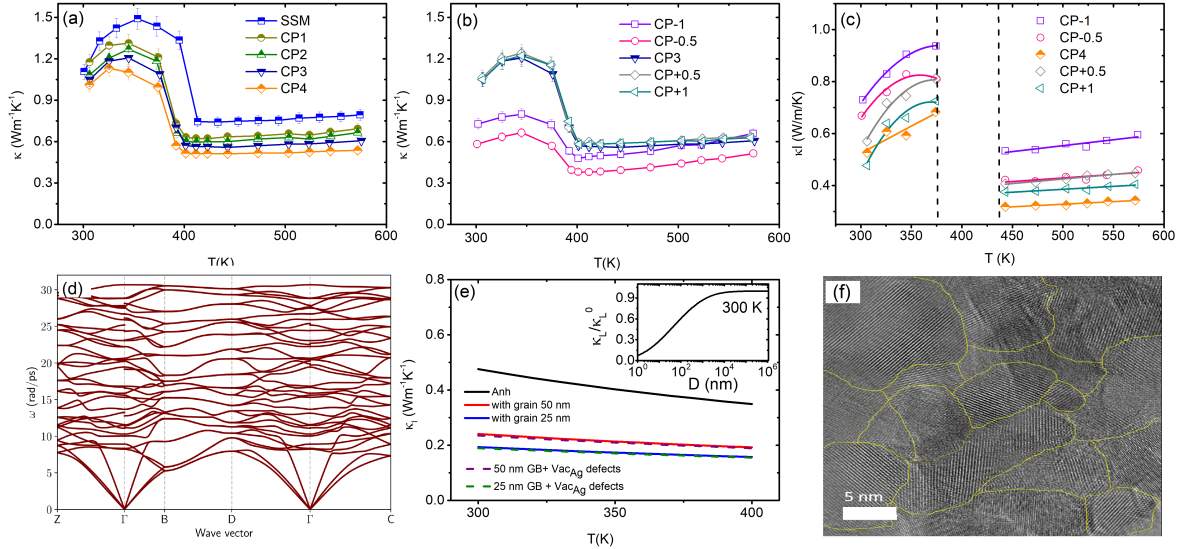


Figure 3.14: (a) Temperature dependent κ of CP samples prepared with different milling durations, (b) Temperature dependent κ of CP samples prepared with different Ag/Te molar ratio, (c) κ_l extracted from the measured κ using the SKB model for a few samples, (d) Calculate phonon dispersion for β -Ag₂Te, (e) Theoretically calculated thermal conductivity showing effect of anharmonicity, grain-size and Ag-vacancies/Te-interstitials, (f) a representative high-resolution TEM image of a CP Ag₂Te sample after several thermal cycling. In (a), thermal conductivity of our ingot sample is also included for comparison.

Hence, the effect of milling time (τ_m) can be readily understood by comparing the total measured thermal conductivity. κ for these (and for n-type samples in general) shows the same qualitative behavior characterized by a broad peak centered around 340 K, followed by a precipitous drop across T_t and a gradually increasing trend ($d\kappa/dT > 0$) upon heating up to the highest temperature in the superionic phase.

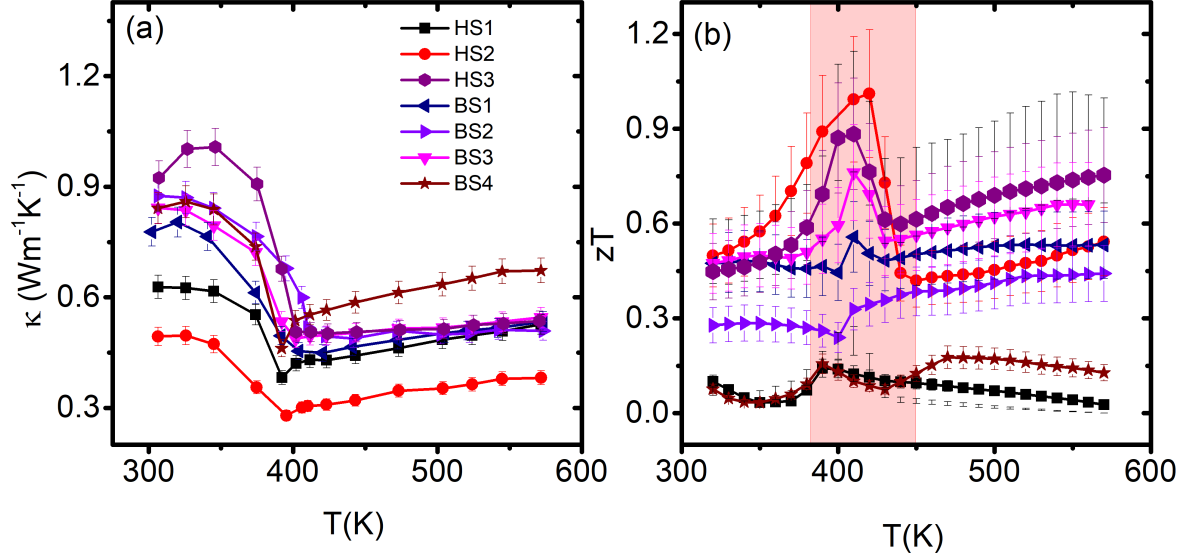


Figure 3.15: Temperature dependent (a) thermal conductivity and, (b) zT of BS and HS samples.

The fact that κ in our SSM sample is significantly higher compared to κ for any of the CP samples despite having a much lower electrical conductivity, 1500 S cm^{-1} near 300 K in SSM against 2300 S cm^{-1} near 300 K in CP, Fig. 3.6(d) clearly brings out the role of grain boundary scattering in suppressing the lattice thermal conductivity. With increasing milling duration, κ decreases further in a systematic manner showing the effect of nanostructuring in suppressing the lattice thermal conductivity of Ag_2Te drastically. The lowest κ is observed for the sample that was milled for the longest duration (600 min). For this sample CP4, Fig. 3.14(a), the maximum and minimum values of κ are, respectively, $1.1 \text{ W m}^{-1} \text{ K}^{-1}$ (at 350 K) and $0.51 \text{ W m}^{-1} \text{ K}^{-1}$ (at 460 K). The corresponding values for our SSM sample are $1.5 \text{ W m}^{-1} \text{ K}^{-1}$ and $0.79 \text{ W m}^{-1} \text{ K}^{-1}$, respectively.

The gradually increasing trend observed in the superionic phase ($d\kappa/dT > 0$) for all the samples is contrary to the decreasing behavior shown by σ ($d\sigma/dT < 0$) over the same temperature range. This anomalous temperature dependence of κ has recently attracted significant attention. It is believed that the heat transport in PLEC class of materials cannot be described by lattice vibrations alone. Wu et al., argued that this anomalous increasing trend

may be associated with the convective heat channel due to mobile Ag ions, which is present in addition to the conductive heat channel due to lattice vibrations associated with the Te sublattice [170].

The effect of Ag off-stoichiometry is shown in Fig. 3.14b. κ in a pristine (CP3) and Ag excess samples (CP+0.5) and (CP+1) nearly overlaps. This is consistent with the fact that excess Ag taken in the beginning of the reaction is not incorporated in the structure. Compared to these samples, the thermal conductivity of 0.5% and 1% Ag deficient samples has decreased which is mainly due to their very low electrical conductivity (Fig. 3.6g). It was previously reported that estimating κ_e in these intrinsically low κ materials often yield unsatisfactory results [171]. Nonetheless, to make a rough estimate of κ_e we used the SKB model as done previously for PbTe-doped n-type Ag_2Te samples. The details are as follows: **Electronic and Lattice thermal conductivity:** To estimate the κ_e using Weideman Frenz law, $\kappa_e = LT\sigma$ where L is the Lorenz number and for its estimation we have used the SKB model which was previously used by Pei et al. [121]. The Lorentz number can be estimated by simulating the temperature dependent thermopower data using following equation,

$$S = \frac{k_B}{e} \left[\frac{{}^1F_{-2}^1(\eta)}{{}^0F_{-2}^1(\eta)} - \eta \right]$$

$$L = \left(\frac{k_B}{e} \right)^2 \left[\frac{{}^2F_{-2}^1(\eta)}{{}^0F_{-2}^1(\eta)} - \left(\frac{{}^1F_{-2}^1(\eta)}{{}^0F_{-2}^1(\eta)} \right)^2 \right]$$

where, ${}^nF_k^m(\eta, \alpha)$ is the Fermi-Dirac integral which includes nonparabolicity in SKB model given by equation,

$${}^nF_k^m(\eta, \alpha) = \int_0^\infty \left(-\frac{\partial f}{\partial \epsilon} \right) \epsilon^n (\epsilon + \alpha\epsilon^2)^m (1 + 2\alpha\epsilon)^k d\epsilon$$

where α is known as band nonparabolicity which depends upon the band gap of the material $\left(\frac{kT}{E_g} \right)$. The n, m, and k are indices of the integral whose values depend on the transport property and charge carrier scattering mechanism. The energy dependence of the relaxation time

(τ) is given by the equation $\tau = \tau_0 \epsilon^{\lambda-1/2}$ where λ depends upon the scattering mechanism. For electron phonon scattering mechanism λ is zero which we have used in our analysis.

In Fig. 3.14c, we show $\kappa_l = \kappa - \kappa_e$ for these samples. The temperature range over which the phase transition occurs has been excluded due to large uncertainty associated with the specific heat, which cannot be approximated by a constant $3nR$ value over this range. For comparison, κ_l for the stoichiometric sample CP4 is also included. The value of κ_l at 300 K is very low in the normal phase itself, ranging from 0.52 W m⁻¹ K⁻¹ (CP4) to 0.7 W m⁻¹ K⁻¹ in (CP-1) at 300 K. It decreases further and becomes ultralow in the high-temperature superionic phase, where it ranges from 0.32 W m⁻¹ K⁻¹ (CP4) to 0.5 W m⁻¹ K⁻¹ in (CP-1) at 440 K. Unexpectedly, the highest lattice thermal conductivity is shown by the 1% Ag-deficient sample (CP-1). This shows that the atomic defects are not the main characters in determining the heat flow mechanism of Ag₂Te. In both the structural phases α and β , the sign of $d\kappa_l/dT$ is positive. As in the superionic phase, the total measured κ itself exhibits an increasing behavior (despite $d\sigma/dT < 0$), we cannot attribute the observed increasing trend in κ_l to any error in the estimation of κ_e . These observations point to a complex heat conduction mechanism in these materials, which is beginning to attract attention from the theorists recently [170].

To understand the origin of the intrinsically low thermal conductivity in the β -phase of Ag₂Te, we studied the effect of anharmonicity, grain boundary and point-defects scattering theoretically. The phonon dispersion in β -Ag₂Te is shown in Fig. 3.14d. There are 36 phonon branches at each q-point, spanning a small energy range from 0 to 30 rad/ps. This is due to the large average molecular mass of Ag₂Te (114 amu). The low lying optical phonons are prominently seen without an acoustic-optic phonon gap due to nearly similar atomic masses of Ag and Te ($m_{\text{Ag}}/m_{\text{Te}} = 0.85$). Both these factors contribute to a high intrinsic anharmonic phonon-phonon scattering in Ag₂Te. Furthermore, less dispersive phonon branches indicate low phonon group velocities. Thus, a combined effect of these is expected to result in an inherently low κ_l in this material.

To get further insight, different phonon scattering contributions in β -Ag₂Te are calcu-

lated. The anharmonic scattering rate (τ_{anh}^{-1}) is calculated using the method in Ref. [172]. The calculated Grüneisen parameter γ_λ are shown in Fig. 3.16a. As anticipated from the phonon dispersion, the anharmonic scattering in Ag_2Te is high, which is evident in Fig. 3.16b. The grain boundary scattering is included as $\tau_{\text{GB}}^{-1} = v_g/D$ where v_g is the phonon group velocity and D is the grain size. The effects of Ag vacancy (Vac_{Ag}) is included using the T-matrix description as discussed in Ref. [173]. The defect scattering rates, τ_{def}^{-1} , are seemingly the least dominant among all the contributions and could be anticipated to have less impact on calculated κ_l . A full ab-initio treatment of phonon-defect interactions, taking into account the bond perturbations also, may somewhat strengthen τ_{def}^{-1} , however, its final effect on κ_l may still remain less pronounced due to already very high anharmonic and grain boundary scattering shown in Fig. 3.16b. The total scattering rate (τ^{-1}) is calculated from full phonon dispersion and mode Grüneisen parameters using the Matheissen rule: $\tau^{-1} = \tau_{\text{anh}}^{-1} + \tau_{\text{GB}}^{-1} + \tau_{\text{def}}^{-1}$. Fig. 6.11e shows the calculated κ_l for Ag_2Te including all the phonon scattering contributions. The calculated κ_l for Ag_2Te (Fig. 3.14e, considering only the anharmonicity to begin with, is already very low ($\sim 0.45 \text{ W m}^{-1} \text{ K}^{-1}$ at 300 K). Including the grain boundary scattering, taking grain-size $D = 50 \text{ nm}$ and 25 nm , reduces κ_l further by more than 50%, which is consistent with the observed low thermal conductivity of our nanostructured Ag_2Te samples. The effect of small concentrations of Ag vacancies on κ is relatively very weak. This is consistent with the experiments where the Ag-deficiency has not contributed to any further decrease in thermal conductivity.

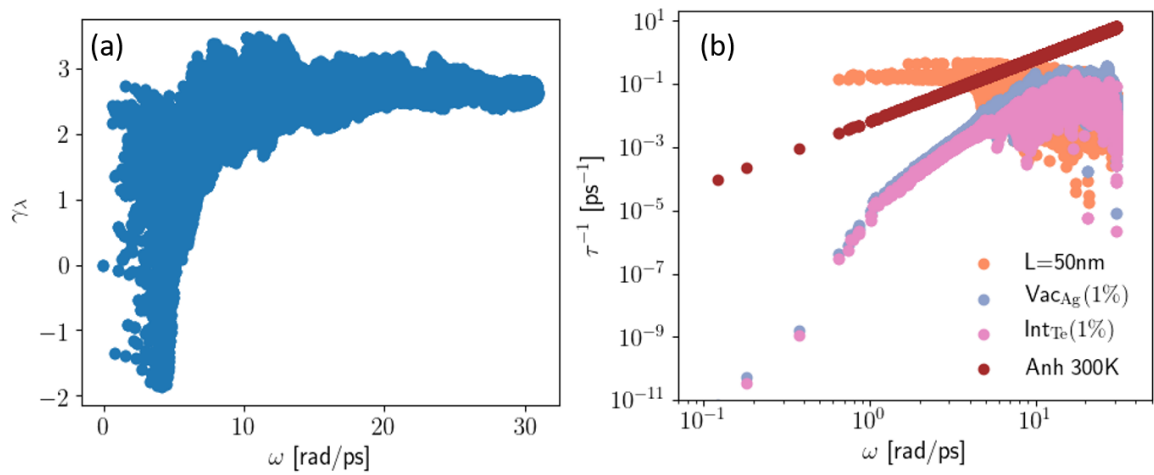


Figure 3.16: Calculated results for (a) Grüneisen parameter and, (b) relaxation time with frequency of phonons.

A more detailed view of the normalised κ_l at room-temperature varying with the grain size is shown in the inset of Fig. 3.14e. This shows that grains, sizing below 1 μm , contribute to the suppression of κ and the smaller grains are most effective in scattering the mid- and long-wavelength phonons. As elucidated in Fig. 3.17c and Fig. 3.18, our samples consists of grains that vary in size from 1 μm down to the less than 100 nm. These grains, however, are themselves composed of nm sized particles of Ag₂Te shown in Fig. 3.5 which cannot be seen in the SEM micrograph. We therefore did extensive HRTEM investigations on our CP samples before and after the thermoelectric measurements. A representative HRTEM image collected after the thermoelectric measurements is shown in Fig. 3.14f (a few more TEM images are shown in Fig. 3.18 & Fig. 3.19). One can clearly see the presence of a large number of nm-sized grains oriented randomly. The grain boundaries are drawn as lines as a guide to eye. These boundaries are not very sharp everywhere, neither do all grains show high-crystallinity, acting thereof as potential scatterers that impede the heat flow. It is well recognized that a wide size distribution and morphology of nanoparticles is more effective in scattering different phonon modes and reduce thermal conductivity significantly. The presence of grains of varying size with a broad distribution in our cold-pressed pellets thus scatter phonons at all length scales leading to their much reduced thermal conductivity

compared to an ingot sample.

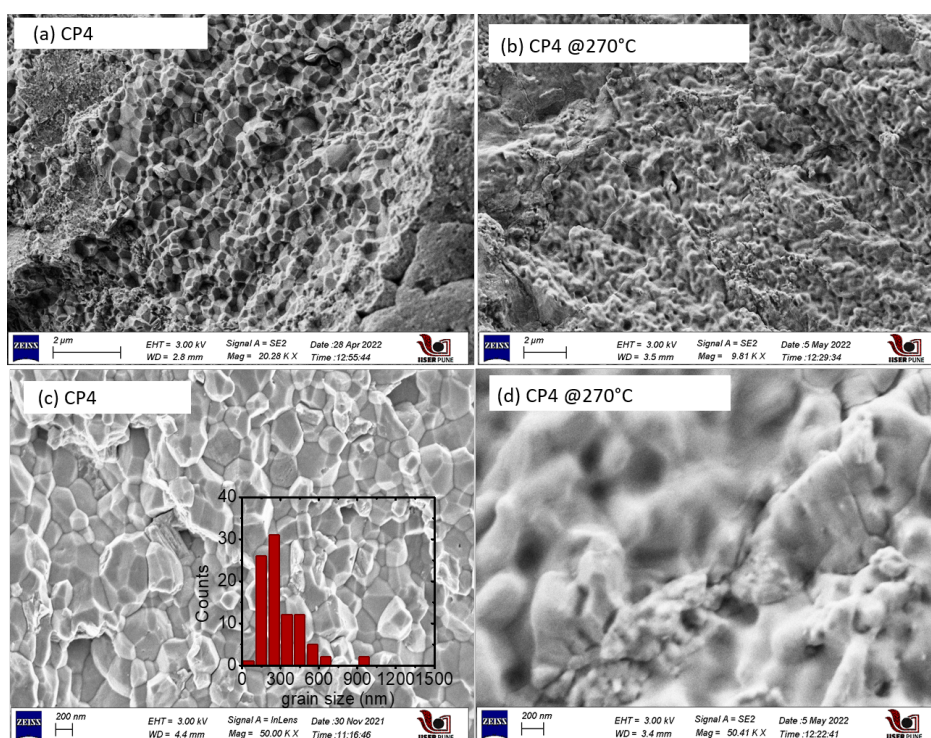


Figure 3.17: Morphology of freshly broken surface of CP4 sample of as cold pressed and sintered pellet at 550 K (a) low magnification image of cold pressed pallet (b) is for sintered pellet (c) image at 200 nm for cold pressed and (d) image at 200 nm for the sintered pellet.

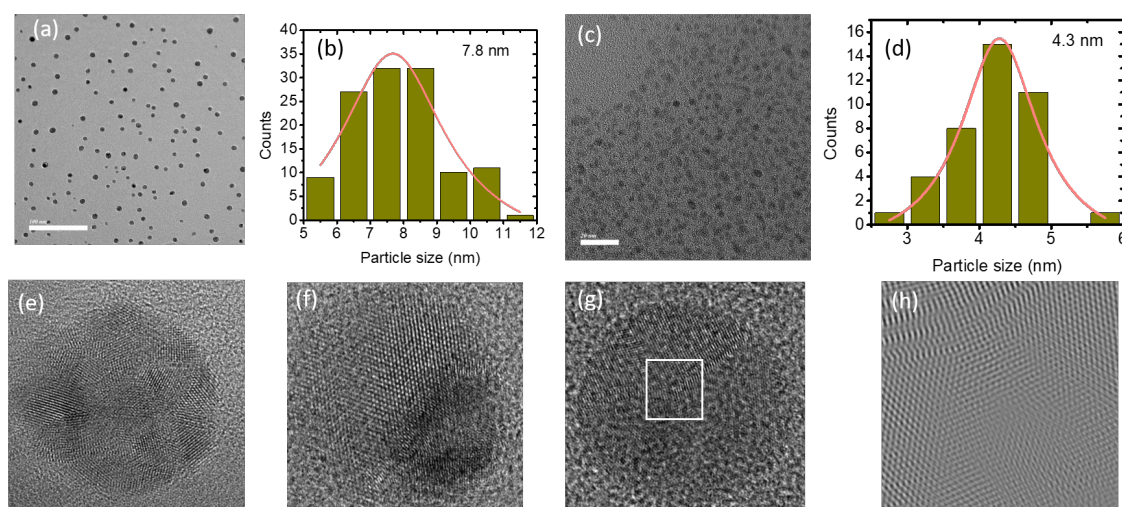


Figure 3.18: Few representative TEM and HRTEM images of ball milled powder samples.

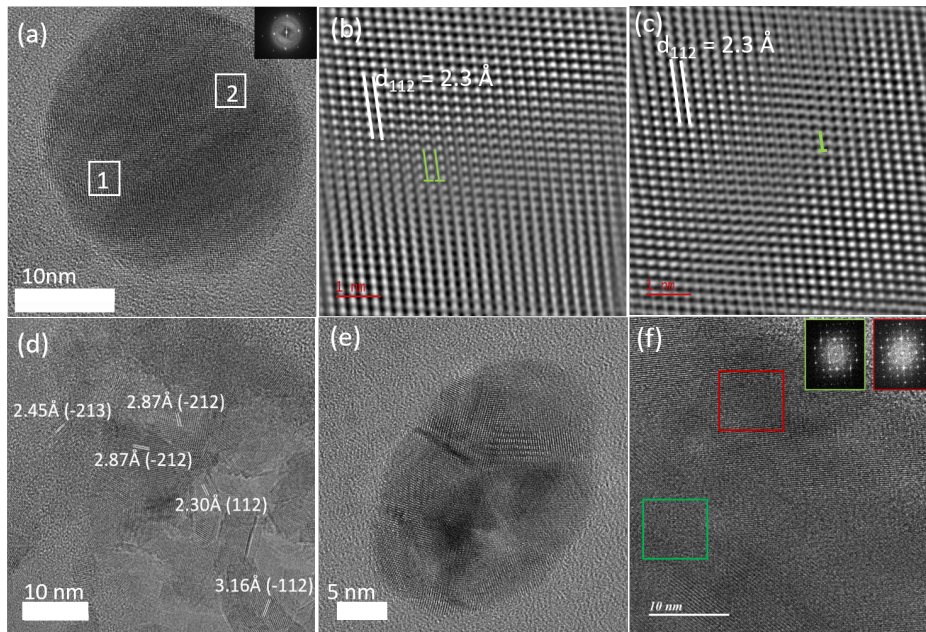


Figure 3.19: HRTEM images of CP samples after multiple runs of transport property measurements (a) HRTEM at 5 nm showing highly crystalline nanoparticle (b) IFFT image on rectangular area marked as 1 in (a), (c) IFFT image on rectangular area marked as 2 in (a) where green lines are showing the line defects, (d) HRTEM image at 10 nm showing large number of nanometer sized grains oriented in different directions (e) HRTEM image of single nanoparticle containing multiple orientation of planes and, (f) HRTEM image at 10 nm showing two grains and insets are their respective FFT on the marked red and green regions.

3.4.8 Thermoelectric figure-of-merit zT

The zT of our stoichiometric CP samples (CP1, CP2, CP3, and CP4) is plotted as a function of temperature in Fig. 3.20(a). The zT of the SSM sample is also included as a reference. For the BS and HS series of samples, zT is shown in Fig. 3.15b. Since the specific heat near the phase transition at T_t is expected to show an anomaly, we exclude the zT in the range $T_t \pm 100$ K (the shaded region) from further discussion. In our stoichiometric CP samples (and for n-type Ag₂Te samples in general), zT shows an increasing trend over the whole temperature range. In BS or HS samples, the zT at 570 K is 0.85.

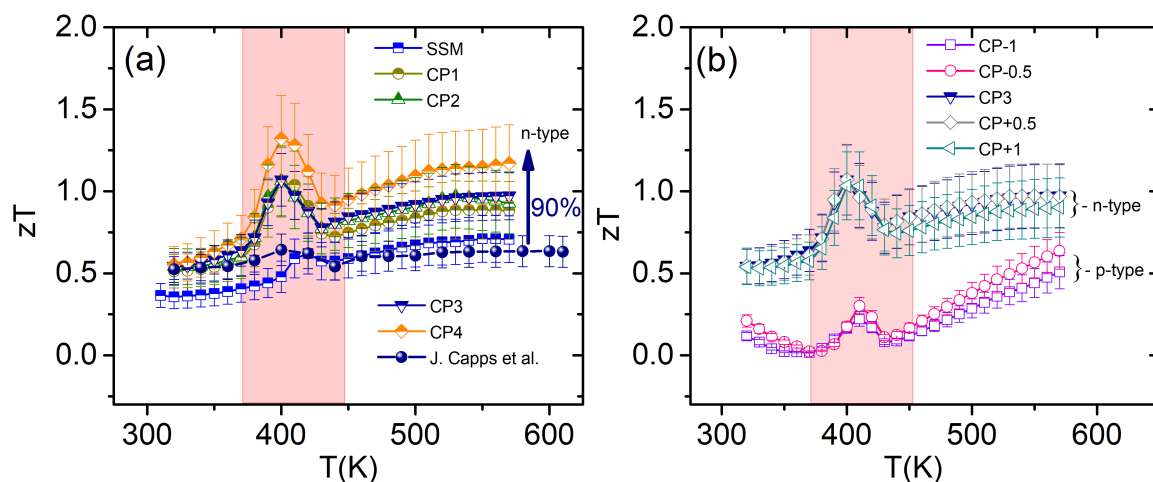


Figure 3.20: Temperature dependent zT variation for (a) stoichiometric CP samples prepared with different milling times (SSM sample and literature data from J. Capps et al. study are included for comparison), and (b) different Ag/Te molar ratio receptively.

In contrast, in our CP samples the zT at 570 K is higher, reaching values as high as 1.2 in CP4 (the sample with the lowest thermal conductivity). Within the CP series, zT shows a systematic increase with decrease in the thermal conductivity due to increasing milling time. Since ball-milling affects the particle-size and their morphologies, the observed suppression reflects the effect of nanostructuring in these materials. Interestingly, the ball-milling has no significant effect on the electrical conductivity and thermopower. This makes Ag_2Te a rather interesting material where the power factor and phonon transport are intrinsically decoupled, providing thereby a huge scope for further improvement. In contrast, the zT of SSM sample is only 0.68 at 570 K. This low value is mainly due to its fairly high thermal conductivity compared to the CP samples.

The effect of Ag/Te molar ratio on zT of our cold-pressed samples is shown in Fig. 3.20b. In the Ag-excess samples (CP+0.5 and CP+1), the zT nearly coincides with the zT for their stoichiometric counterpart CP3. However, in the Ag-deficient, p-type CP samples (CP-0.5 and CP-1), zT shows a decreasing behavior below room-temperature but an increasing behavior in the superionic phase with zT reaching values as high as 0.64 at 570 K (Fig. 3.20b). On the other hand, in the p-type sintered samples, zT is very small (< 0.15 at 570 K) and

it also shows a decreasing behavior in the superionic phase (Fig. 3.15b) as opposed to the increasing behavior observed for our cold-pressed p-type samples.

3.5 Summary and conclusions

The thermoelectric properties of Ag₂Te samples, synthesized using four different methods, namely, BS, HS, CP and SSM were investigated in detail. The sintered BS or HS samples prepared under identical conditions and with the same starting stoichiometry (Ag : Te ≡ 2 : 1) show highly unpredictable behavior with respect to the sign of S and the magnitude of σ . The leading reason for this extreme sample dependence is related to the Ag-ion diffusion during high-temperature sintering. To overcome this issue and to maximize the zT of pristine Ag₂Te, we developed a novel, all-room-temperature, fabrication technique that involves vibratory ball milling followed by cold-pressing. The cold pressed pellets were highly dense (within $\pm 5\%$ of the theoretical density). We demonstrate excellent reproducibility of the thermoelectric properties from one sample to another. To improve the zT of Ag₂Te beyond the phonon-liquid electron-crystal value of about 0.64 at 575 K in the ingot samples, we adopted a hierarchical nanostructuring technique, wherein nanoparticles with diverse morphology and crystallinity (nanoscale) along with larger grains (mesoscale) act together to effectively suppress the thermal conductivity in our samples drastically leading to a significant improvement in the zT values for both n-type and p-type Ag₂Te: 1.2 in n-type and 0.64 in p-type at 570 K. This temperature is much lower than the temperature where the Cu-based superionic materials attain their peak zT. In future, charge carrier optimization by doping in Ag₂Te using the fabrication technique described here can be considered to achieve higher zT, and to suppress Ag-migration up to even higher temperatures than 570 K shown here for the pristine Ag₂Te. As our fabrication technique for obtaining 100% dense pellets does not involve high-temperature sintering or spark-plasma sintering, it can readily be scaled-up for higher yields.

Chapter 4

Reproducible high thermoelectric figure of merit in Ag_2Se

4.1 Introduction and Motivation

The compound Ag_2Se is a narrow band gap *n*-type semiconductor, offering a combination of high carrier mobility ($\sim 10^3 \text{ cm}^2 \text{ V}^{-1} \text{ s}^{-1}$) and Seebeck coefficient ($\sim -140 \mu\text{V K}^{-1}$), and an intrinsically low thermal conductivity ($\sim 1 \text{ W m}^{-1} \text{ K}^{-1}$). The *zT* in $\text{Ag}_2\text{Se}_{1+\delta}$ materials has been occasionally reported to be as high as ~ 1 , making them a potential alternative to replace the thermoelectric materials derived from Bi_2Te_3 [14–16, 18–20]. Along with promising thermoelectric properties, Ag_2Se also exhibits colossal, non-saturating linear magnetoresistance up to very high fields [174, 175]. Upon heating above $\sim 407 \text{ K}$, Ag_2Se becomes superionic. In the superionic phase, the Se ions form a rigid *bcc* lattice and the Ag ions become mobile or liquid-like. Ag_2Se owes its *n*-type behavior to the presence of Ag interstitials (Ag^*), that easily ionize ($E_d \approx 2 \text{ meV}$) to add $1 e^-/\text{Ag}^*$ to the conduction band [176]. Controlling the density of Ag-interstitials via anion excess helps optimize the carrier concentration, and hence in obtaining high *zT* (~ 1), as has been shown in several recent studies [13, 15, 16, 19].

The recent study by Huang et al. however, shows that Ag_2Se samples prepared by spark-

plasma-sintering (SPS) or solid-state melting (SSM) exhibit significant compositional variations over small length scales. Consequently, the samples examined from different parts of the *same* spark-plasma-sintered (SPS) pellets show variations up to $\sim 20\%$ in their thermoelectric properties [18]. In a superionic material, high temperature processing (temperatures exceeding the superionic transition temperature) results in metal-ion migration leading to the observed compositional inhomogeneities [8, 9, 72, 168, 169, 177]. In the case of Ag_2Se , this problem is further compounded by the evaporation of volatile Se at high temperatures during sintering. There is no guarantee then that two different samples prepared identically using these commonly employed technique involving high temperatures will have identical properties too. This is apparent from a review of the previous literature where wide variations in the thermoelectric properties of Ag_2Se is found to be commonplace [13–16, 16, 18–20, 178–182]. Since, Ag_2Se achieves its high- zT near the room temperature, a synthesis method that does not involve high temperatures processing can solve this issue. The question, however, is how should one get high density, preferably nanostructured, without resorting to the SPS, hot-pressing or melting techniques?

Interestingly, Ag_2Se also has some very unique properties, which, if exploited well, can help overcome the issue mentioned above. First, the phase Ag_2Se forms readily when Ag and Se powders are mechanically processed [19]. And, second is the metal-like malleability and ductility of Ag_2Se [163, 183–185], which was pointed out as early as in 1963 by Simon et al. [183]. Here, we combine these properties to fabricate highly dense and chemically homogeneous $\text{Ag}_2\text{Se}_{1+\delta}$ pellets. We investigate the effect of stoichiometry δ on the thermoelectric properties, and establish the excellent reproducibility, thermal stability, and chemical homogeneity along with high zT in our samples.

4.2 Sample Synthesis and Nomenclature

The $\text{Ag}_2\text{Se}_{1+\delta}$ samples studied here are listed in Table 4.1. We have mainly used two synthesis routs to fabricate the samples mentioned in the table. The details are as follows:

Table 4.1: Details of $\text{Ag}_2\text{Se}_{1+\delta}$ samples studied in this work.

Name	δ	ρ_m (%)	Extra Phase
AS1	0	~100	Nil
AS2	0.005	~100	Nil
AS3	0.025	~100	Minor Se
AS4	0.025	~100	Minor Se
AS5	0.05	~100	Se
AS6	-0.01	~100	Ag
SSM	0	~100	Nil

Ball-milling (BM): Ag (Sigma Aldrich, 99.9% purity) and Se (Alpha Aesar, 99.999% purity) powders were taken in the desired ratio to prepare pristine Ag_2Se , Ag excess, and Se excess samples. Powders were filled in stainless steel (SS) capsule along with SS beads under Ar-atmosphere. The SS capsule was then loaded in a vertical vibratory ball mill which operates at 2 Hz frequency for 600 min. The samples, named AS1, AS2, ..., AS6, were prepared by ball-milling under Ar atmosphere followed by cold-pressing under 55 MPa pressure using KBr press. The cold-pressed pellets were hard with densities reaching 100% of the theoretically calculated density. These pellets were glued to a aluminum platform using a cold mounting epoxy and cut into desired shapes using a low-speed diamond saw. No chipping-off or breaking could be observed. The cuts were neat, and the resulting bar shaped samples were dense and shiny. The density was estimated from the spatial dimensions and mass of the samples. The high density of our samples without SPS or SSM can be attributed to the metal-like ductility of Ag_2Se , which allows the powder particles to pack closely under applied pressure in order to achieve 100% space filling.

Solid state melting (SSM): SSM sample was prepared by taking the elemental silver beads (Sigma Aldrich >99% purity) and Se pieces (Sigma Aldrich, >99% purity) according to the stoichiometric ratio (2:1) in a preheated quartz tube. The quartz tube was loaded in an Ar filled glove box and thereafter vacuum sealed under a pressure of 10^{-5} Torr and heated to 350 °C with the heating rate of 50 °C/h. After waiting at this temperature for 10 h, the temperature was raised to 920 °C at the rate of 100 °C/h where it was kept for 24 h before

cooling back to the room temperature at a cooling rate of $100\text{ }^\circ\text{C/h}$.

4.3 Characterization and Measurement Details

The phase purity was checked using the x-ray powder diffraction (XRD) technique (Bruker, D8 Advance). The lattice parameters were obtained using the Rietveld refinement. The microstructure was assessed using the field-effect Scanning Electron Microscope (FESEM) (Ultra Zeiss plus) equipped with an energy dispersive x-ray (EDS) analysis attachment (Oxford Instruments). The high-resolution electron micrographs were obtained using a transmission electron microscope (JEOL JEM 2200FS 200 keV). The simultaneous Seebeck coefficient and resistivity measurements were done on bar shaped samples using LSR3 setup (Linseis). The maximum uncertainty in these measurements is $\leq 5\%$. The temperature dependent Hall measurements were done on a home-built setup by sweeping the field between $\pm 1\text{ T}$. The thermal conductivity κ was estimated by measuring the thermal diffusivity using the Laser Flash method (LFA 1000, Linseis). The maximum uncertainty in our thermal conductivity measurement is less than 6% .

4.4 Results and Discussion

The powder x-ray diffraction (XRD) patterns are shown in Fig. 4.1. All samples formed in the previously reported orthorhombic structure (space group $P2_12_12_1$) [186]. The stoichiometric (AS1) and 0.5% Se excess samples (AS2) are found to be phase pure. However, in Ag-excess sample (AS6) and in the higher Se excess ($\delta \geq 0.025$) samples, small extra peaks are observed. These are due to unreacted Ag in the Ag-excess, and unreacted Se in the Se-excess samples. The Rietveld refinement for a representative sample (AS1) is shown in Fig. 4.2. The lattice parameters given in Table 4.4, are in good agreement with previous literature [36, 179, 187]. The Se off-stoichiometry did not show any appreciable effect on the lattice parameters.

The chemical maps for our samples are shown in Fig. 4.3. In stoichiometric (AS1) and 0.5% Se excess (AS2) samples, a uniform distribution of Ag and Se is seen. In AS6, Ag

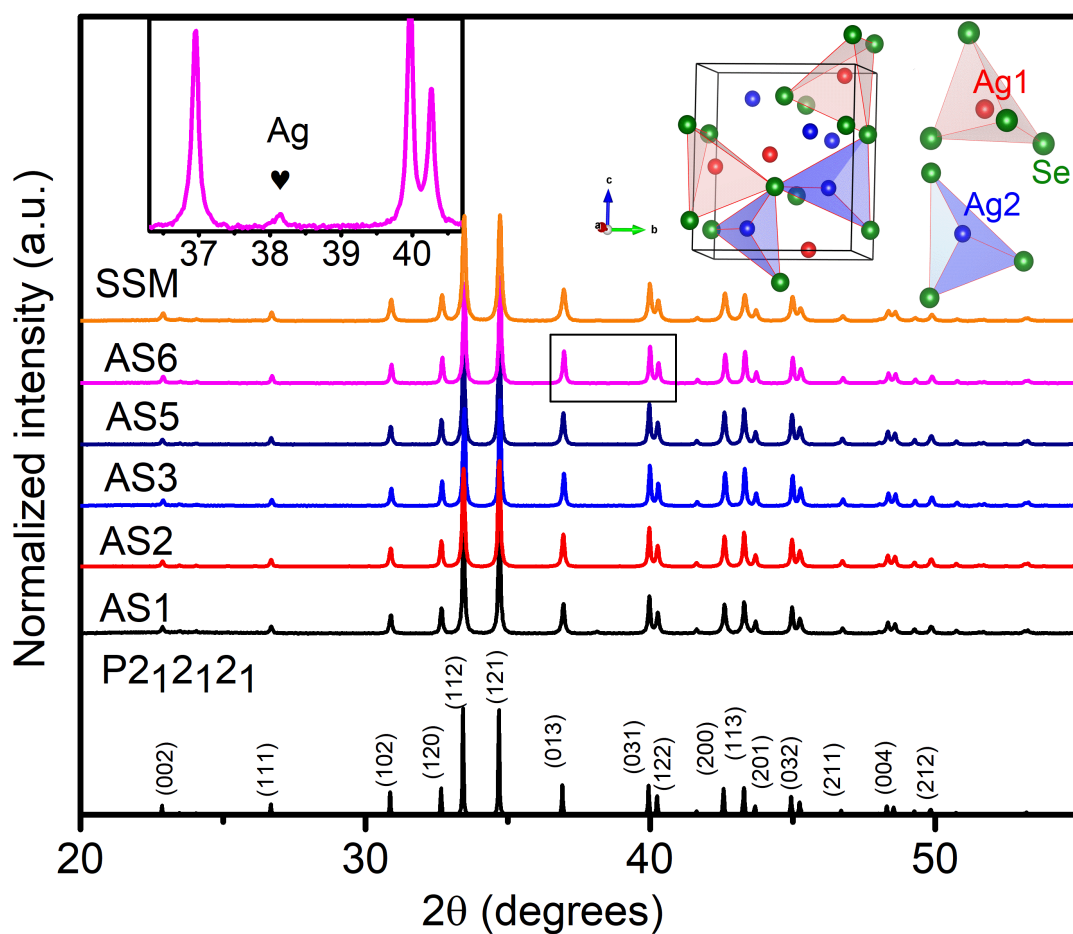


Figure 4.1: Powder x-ray diffraction patterns for samples AS1, AS2, ..., AS6. Data for a SSM sample is also shown. The simulated pattern for the space group $P2_12_12_1$ is shown at the bottom. Inset (right) shows the crystal structure of Ag_2Se . Inset (left) shows a zoomed-in view of the diffraction pattern for 1%Ag excess sample.

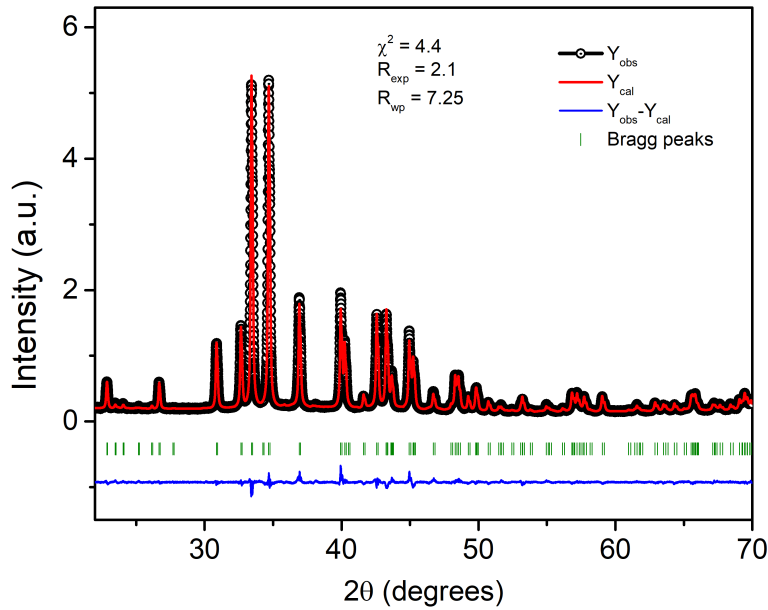


Figure 4.2: The Rietveld refinement for a representative sample AS1.

metal precipitates are visible, and in AS5, Se precipitation is observed. In AS3 and AS4, small Se precipitation is seen occasionally. These observations corroborate the XRD results. This suggests that the homogeneity field δ is extremely narrow in the Ag-rich side ($\delta \ll 0.01$), but in the Se-rich side, the solubility limit is higher than 0.005 but less than 0.025. These observations are in agreement with previous studies where δ in the Se rich side was estimated to be ~ 0.01 [16, 183], and in the Ag-rich side the solubility limit is reported to be practically nil [188]. In Fig. 6.3(a), the FESEM micrographs for a representative cold-pressed sample (AS1) is shown. For comparison the corresponding microstructure for a SSM sample is shown in and Fig. 6.3(b). While both the methods yield $\sim 100\%$ sample density, in SSM the grains are macroscopic with lateral dimensions exceeding $1 \mu\text{m}$, but in AS1, large number grains varying in size from a few nm to several hundreds of nm can be seen. This is also depicted in the inset. The AS1 sample was reexamined after heating it up to 380 K, but this has no detectable effect on the morphology, see Fig. 4.4. A representative high-resolution TEM micrograph of sample AS1 showing highly crystalline grains with well-resolved atomic

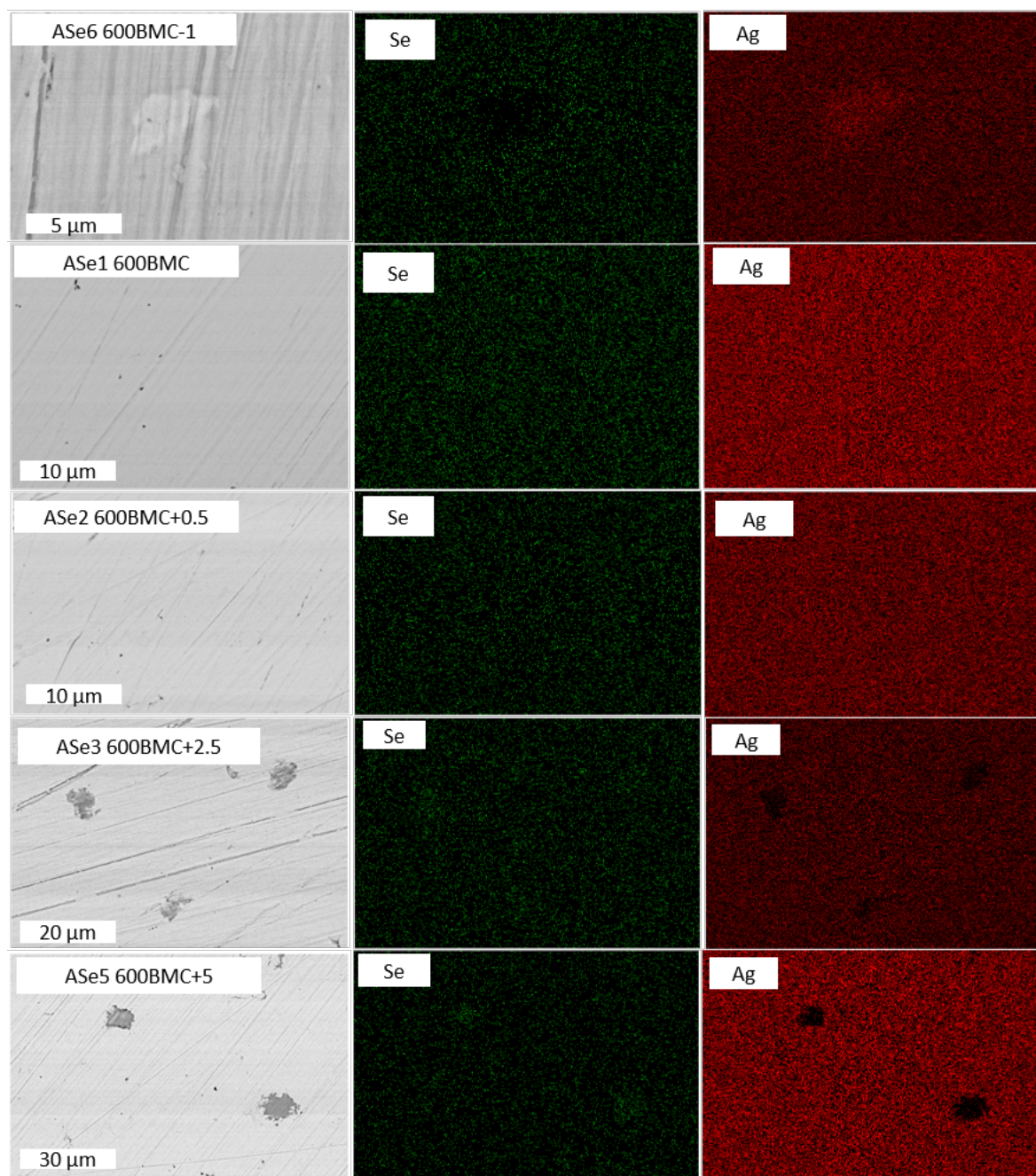


Figure 4.3: Chemical mapping of Ag₂Se samples studied in this chapter.

Table 4.2: Lattice parameters of all the samples and compared with reported values by J. Yu et al. [36]

Samples	Nominal composition	a(Å)	b(Å)	c(Å)
AS1	Ag_2Se	4.33	7.06	7.77
AS2	$\text{Ag}_2\text{Se}_{1.005}$	4.33	7.06	7.76
AS3	$\text{Ag}_2\text{Se}_{1.025}$	4.33	7.06	7.76
AS4	$\text{Ag}_2\text{Se}_{1.025}$	4.33	7.06	7.76
AS5	$\text{Ag}_2\text{Se}_{1.05}$	4.33	7.06	7.77
AS6	$\text{Ag}_2\text{Se}_{0.99}$	4.34	7.06	7.77
SSM	Ag_2Se	4.33	7.06	7.77
J. Yu et al.	Ag_2Se	4.34	7.07	7.77

planes is shown in Fig. 6.3(c). The inverse fast Fourier transform (IFFT) image of the area enclosed within the white box is shown in panel (d). The interplanar spacing for the 112 family of planes is also shown.

The temperature dependent DSC scans for various samples are shown in Fig. 4.6. In the stoichiometric Ag_2Se sample (AS1), this combined structural/superionic transition takes place at 407 K while heating and at 387 K during cooling indicating the first-order nature of the phase transition. The small Se offstoichiometry as in AS2 (0.5% excess) and AS6 (<1% deficient) appears to have no measurable effect on the transition temperature. Interestingly, in 2.5% and 5% Se excess samples the transition temperature decreases by about 10 K, but only in the cooling run. The late onset of this transition in the cooling run in these samples can be attributed to the increased concentration of Ag vacancies in the Se excess samples, which leaves more room for the mobile Ag ions to diffuse around requiring therefore an extra bit of cooling for stabilizing the room temperature phase.

4.5 Thermoelectric Properties

The thermoelectric properties of our samples are shown in Fig. 4.7. The highest temperature was kept low (~ 380 K), well below the superionic transition temperature to prevent possible changes in the microstructure due to Ag migration in the superionic phase. Also, the zT of Ag_2Se decreases significantly in the superionic phase, the normal phase around room temperature is therefore of primary interest. As shown in Fig. 4.7(a), in all the studied

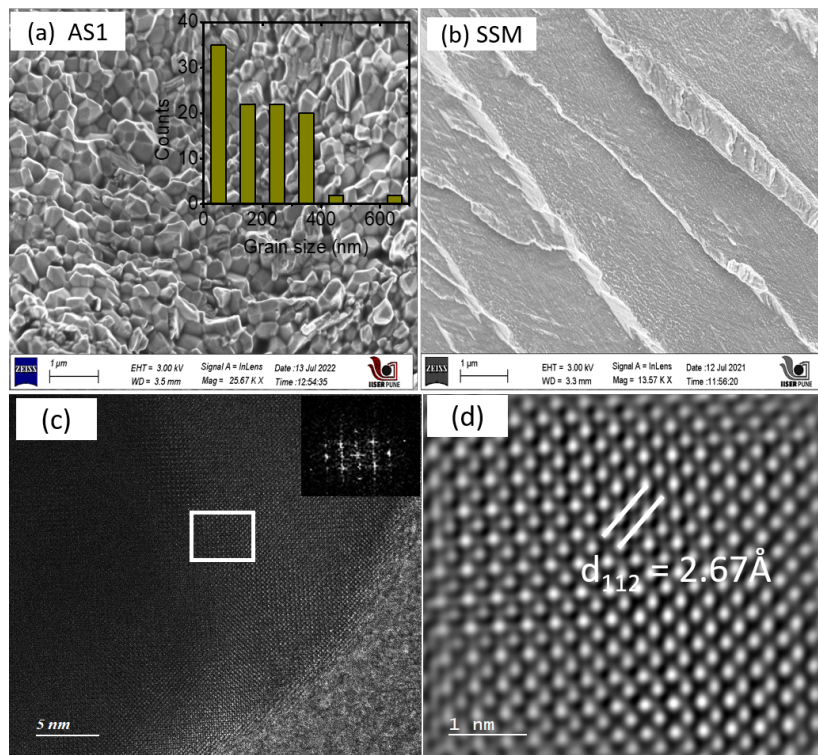


Figure 4.4: Morphology of bulk (a) ball-milled, cold pressed sample, the grain size distribution is shown in the inset, and (b) solid-state melted sample (c) shows the high resolution TEM image at 5 nm and inset is showing the FFT taken over marked rectangular area, (d) IFFT image of rectangular area marked in (c) showing [112] planes.

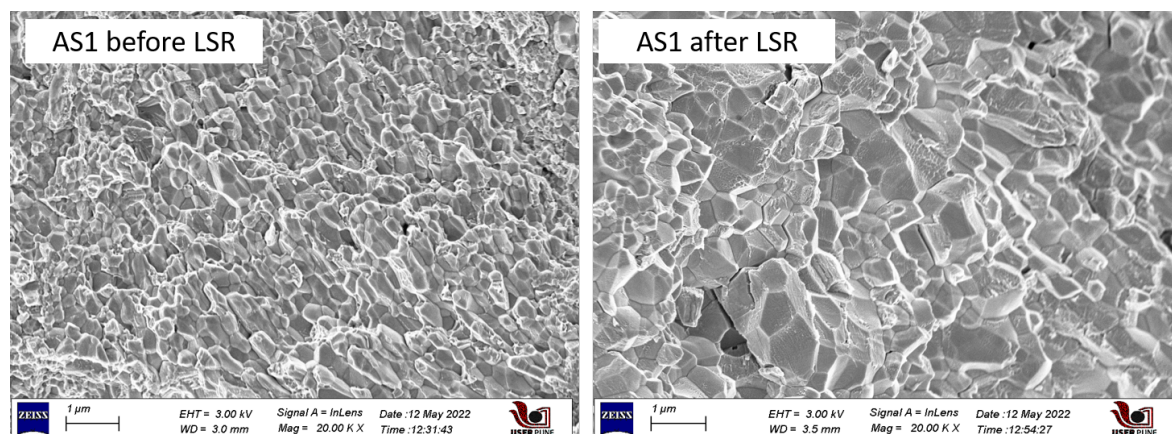


Figure 4.5: Morphology of AS1 sample before and after the LSR measurements.

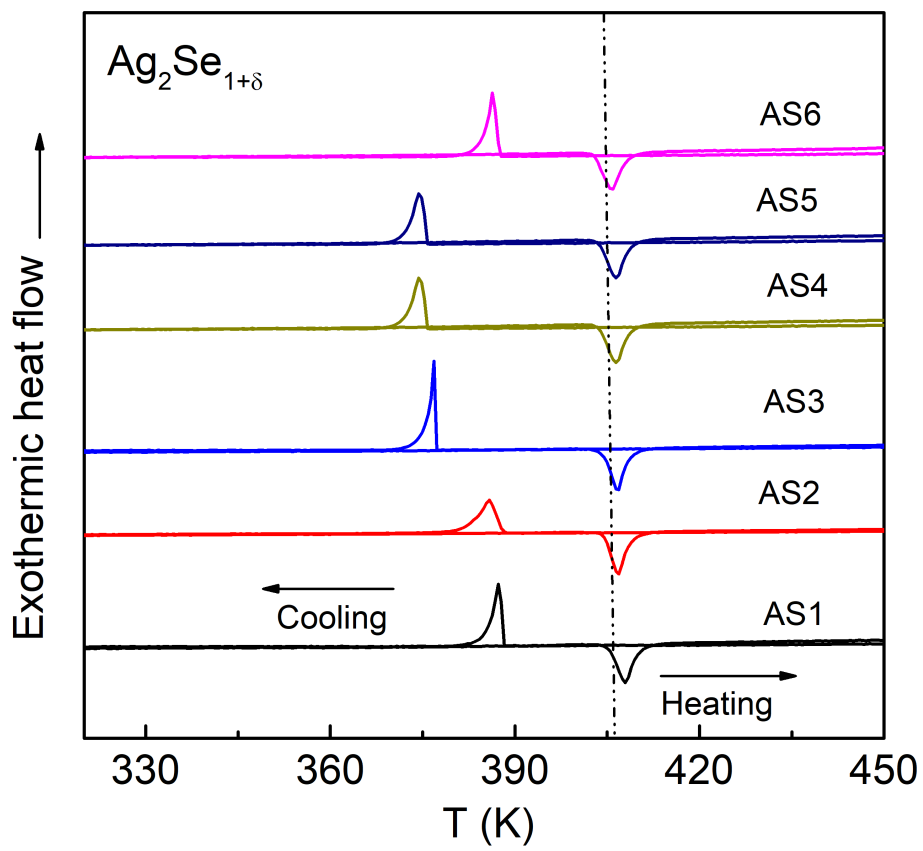


Figure 4.6: DSC measurements for all synthesized samples.

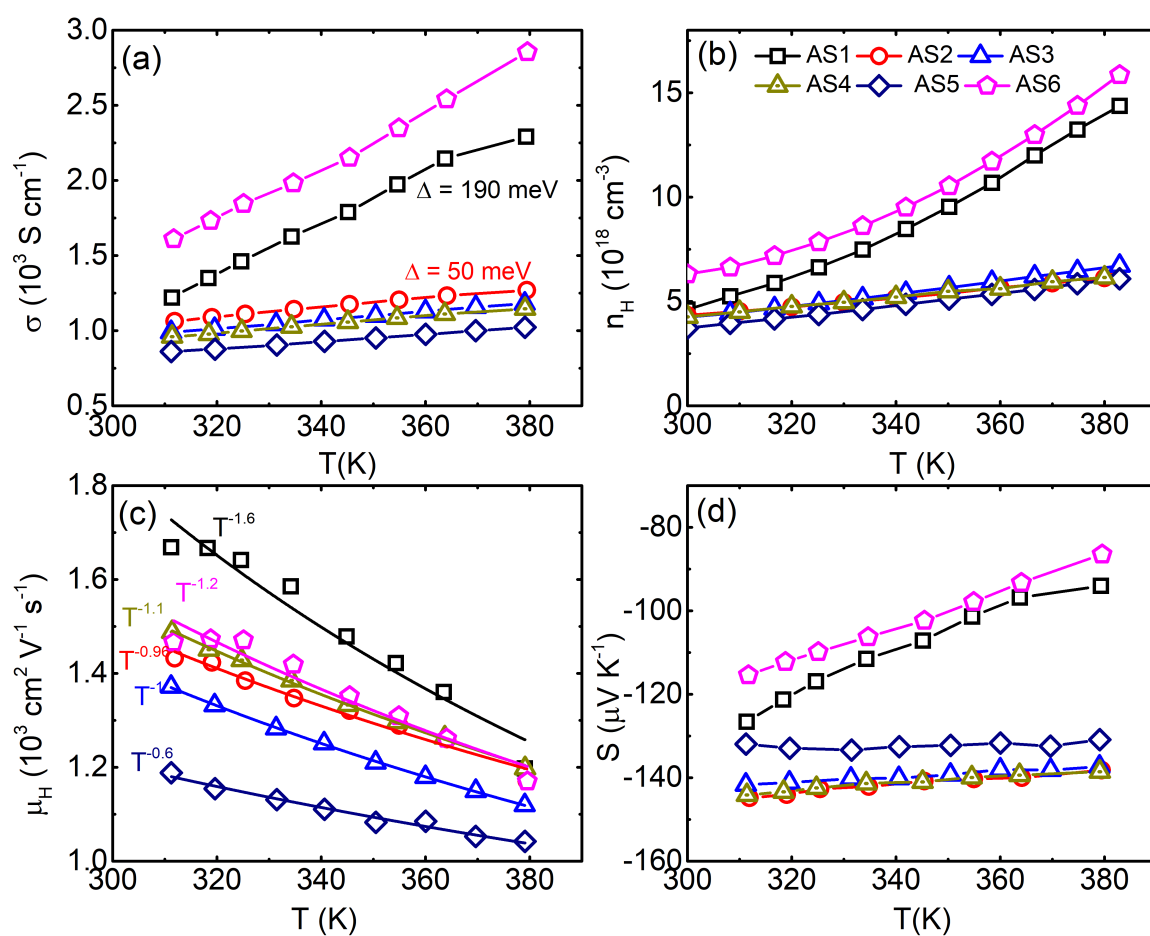


Figure 4.7: Temperature variation of (a) electrical conductivity (σ), (b) Hall carrier concentration (n_H), and (c) Hall mobility (μ_H), and (d) Seebeck coefficient (S) for the Ag_2Se samples studied in this paper.

samples, σ shows an increasing trend upon heating but significant variations are observed due to Se excess. Depending on the slope $d\sigma/dT$, we can group our samples as: X = {AS1 and AS6} (i.e., stoichiometric and slightly Ag excess), and Y = {AS2, AS3, AS4, and AS5} (Se excess samples). For group X, both σ and $d\sigma/dT$ are higher than for Y. In AS1, for example, σ ranges from $\sim 1600 \text{ S cm}^{-1}$ at 310 K to $\sim 2850 \text{ S cm}^{-1}$ at 370 K whereas in AS2 the corresponding values are $\sim 1000 \text{ S cm}^{-1}$ (310 K) and $\sim 1300 \text{ S cm}^{-1}$ (380 K). Same behavior, i.e., higher σ , $d\sigma/dT$ for stoichiometric and slightly Ag doped samples compared to the anion excess sample, has been found in some previous studies (see, for example, Ref. 16). This is due to the presence of a larger concentration of Ag interstitials in samples of group X as compared to Y. Upon Se doping, Ag interstitials (Ag^*) decrease, resulting in a decrease in the carrier concentration, and hence σ decreases [183]. The increasing behavior of σ is due to the minority carrier excitations. Fits using the Arrhenius relation, $\sigma \propto e^{-\Delta/2k_B T}$, where k_B is Boltzmann constant and Δ is the activation energy, yields $\Delta \approx 0.19 \text{ eV}$ for AS1 (representing X), and 0.05 eV for AS2 (representing Y). These values are in good agreement with previous reports [16, 189]. Due to a small band gap ($E_g \approx 0.025 \text{ eV}$ [20]) and high self-doping ($\sim 10^{18} \text{ cm}^{-3}$), the activation energy Δ in these samples is essentially $\Delta = E_g + \epsilon_F$, where ϵ_F is the Fermi energy measured from the bottom of the conduction band. The number density of Ag^* determines ϵ_F . ϵ_F (hence Δ) is accordingly higher for the samples in group X compared to the samples in Y, which explains why $d\sigma/dT$ is higher for X compared to Y. A naive estimation of ϵ_F using the Free electron model: $\epsilon_F = (3\pi\hbar^2 n)^{2/3}/2m^*$ (where symbols have their usual meaning) gives correct order of magnitude by taking the experimentally observed carrier densities and $m^* = 0.18m_e$ (vide infra). Before moving on, we note that σ of our two different 2.5% Se excess samples (AS3 and AS4) exhibit a good overlap over the whole temperature range. The temperature variation of Hall carrier concentration (n_H) is shown in Fig. 4.7(b). The sign of Hall coefficient is negative in all cases indicating n -type behavior. For samples in group X, n_H and dn_H/dT are higher than for the samples in group Y. In AS2, for example, n_H at 370 K is $\sim 6 \times 10^{18} \text{ cm}^{-3}$, but it is as high as $\sim 14 \times 10^{18} \text{ cm}^{-3}$ for AS1. Due to its small bandgap, the intrinsic regime (i.e., carrier excitation across the band

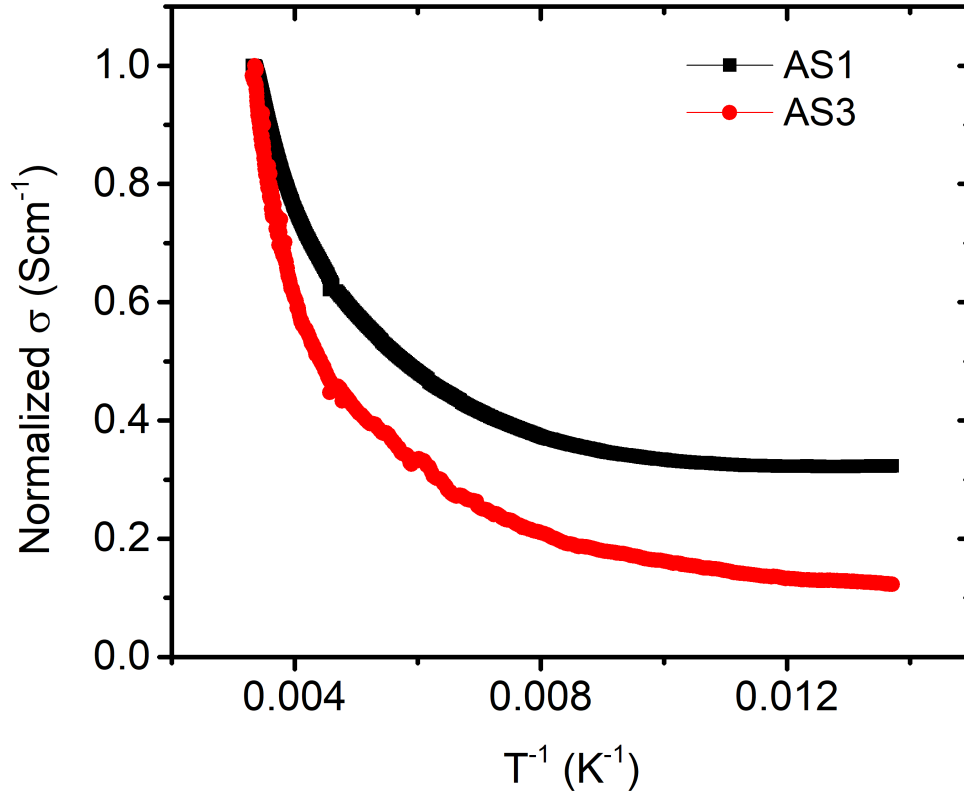


Figure 4.8: Temperature dependent electrical conductivity for two representative cold-pressed samples AS1 and AS3 from 77 K to 300 K.

gap) in Ag_2Se sets in well below 300 K [20], resulting in an increasing $n_{\text{H}}(T)$ above room temperature. To confirm this, we measured σ for two representative samples, AS1 (higher Δ) and AS3 (lower Δ) down to 77 K. The results are shown in Fig. 4.8. Upon heating above 77 K, for AS1 σ remains nearly constant up to about 100 K, above which it increases slowly due to the onset of intrinsic regime. On the other hand, in AS3, due to its low activation energy, σ starts increasing upon heating above 77 K itself.

The temperature dependence of Hall mobility (μ_{H}) is shown in Fig. 4.7(c). AS1 has a mobility of $\sim 1690 \text{ cm}^2 \text{ V}^{-1} \text{ s}^{-1}$ at 310 K, which is highest among all the cold-pressed samples investigated here. Upon heating, μ_{H} decreases following approximately a $T^{-\alpha}$ dependence with $\alpha \rightarrow 1.6$, suggesting that the electron-phonon scattering is dominant in the pristine

Ag_2Se . This temperature dependence, however, gradually weakens as the off-stoichiometric increases with $\alpha \rightarrow 0.6$ in AS5, indicating the role of increasing defect scattering contribution. Interestingly, while n_{H} is highest for the sample AS6, μ_{H} is highest for AS1. The decrease in μ_{H} on both side of $\delta = 0$ suggests that Ag or Se doping introduces additional scattering centers (point defects) leading to a mixed scattering decreasing α below the electron-phonon limit. In a recent paper by Jood et al., a similar behaviour is reported but with μ_{H} peaking at 1% Se doping and n_{H} at 0% [16]. They argued that the lower mobility of their stoichiometric sample is due to the presence of a minor metastable monoclinic phase which coexists with the main orthorhombic phase and contributes to the electron scattering. They further claimed that the metastable phase can be completely suppressed by 1% Se doping, which therefore has the highest mobility. In our samples, however, we do not evidence any metastable phase. This may be due to the different synthesis procedures used in the two studies. The temperature variation of S is shown in Fig. 4.7(d). Near 300 K, S varies from $-108 \mu\text{V K}^{-1}$ (AS6) to $-144 \mu\text{V K}^{-1}$ (AS2). With further increase in Se doping, S decreases to $-132 \mu\text{V K}^{-1}$ in AS5. This decrease can be attributed to the presence of Se precipitates in the higher doped sample. The elemental Se is a p -type semiconductor with very low mobility ($0.12 \text{ cm}^2 \text{ V}^{-1} \text{ s}^{-1}$) and high value of S ($\sim 10^3 \mu\text{V K}^{-1}$ at 300 K) [190]. The thermal excitation of minority holes may also contribute to decrease in S upon heating above 300 K. Overall, the temperature variation of S follows the expected inverse correlation with the temperature variation of n_{H} . The plot S versus n_{H} is shown in Fig. 4.9. The data from several previous studies are also included. The Pisarenko plots fits the (n_{H}, S) data points for m^* (effective mass) between $0.18m_{\text{e}}$ and $0.23m_{\text{e}}$, where m_{e} is the free electron mass in good agreement with literature [15]. This shows that excess Se does not affect either the band structure or the carrier effective mass significantly, confirming that the higher activation energy for samples AS1 and AS6 is not due to the band gap widening but rather due to self-doping from interstitial Ag. Noteworthy is the fact that m^* for Ag_2Se is considerably low compared to, for example, Bi_2Te_3 ($m^* = 1.8m_{\text{e}}$) [48]. This, in turn, explains the relatively high carrier mobility of Ag_2Se as compared to the other well investigated thermo-

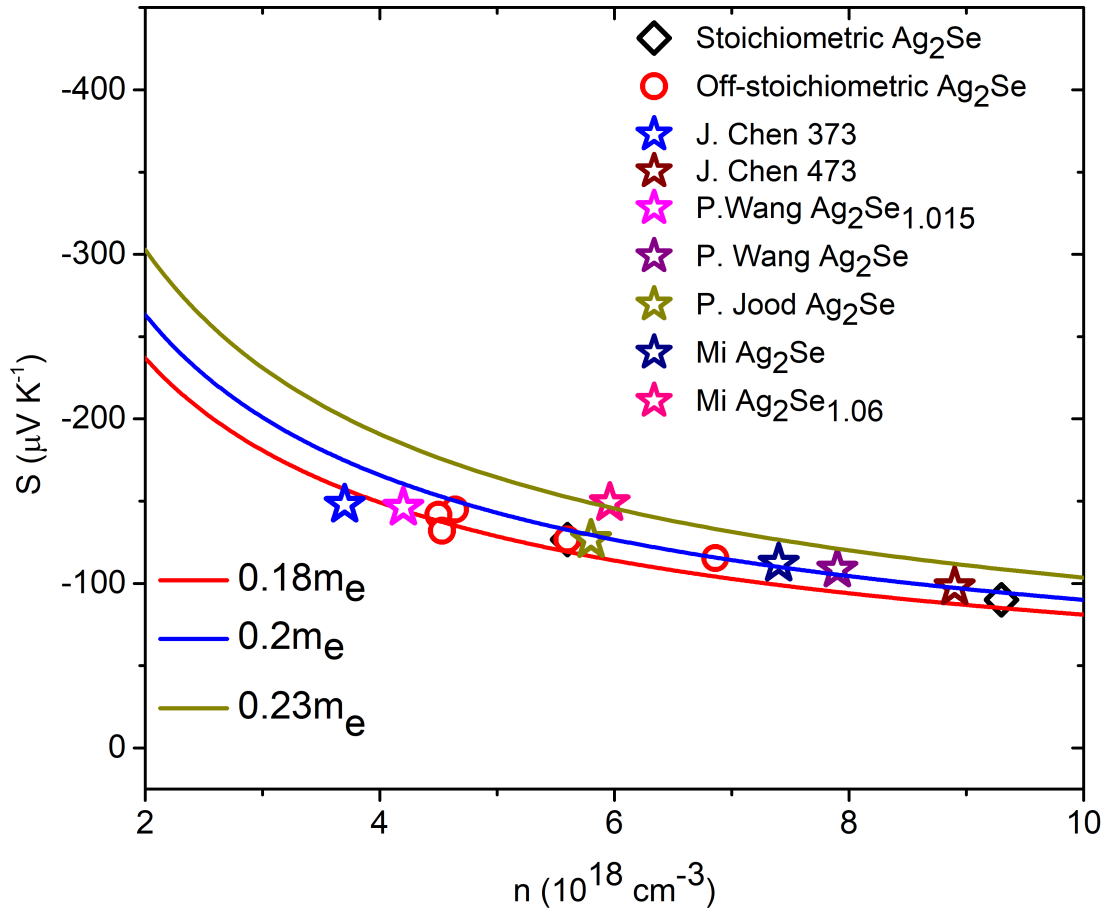


Figure 4.9: Pisarenko plots showing experimental S versus n_H data from our study and several previous reported data [13–16]. The solid lines are calculated within the single parabolic band approximation for carrier effective mass $0.18m_e$, $0.20m_e$ and $0.23m_e$.

electrics [6,47,48,191]. The combination of high σ and S results in high power factor (PF). The highest PF is recorded for AS2. The PF for this sample ranges from $22.2 \mu\text{W cm}^{-1} \text{ K}^{-2}$ (310 K) to $24.3 \mu\text{W cm}^{-1} \text{ K}^{-2}$ (370 K), see Fig. 4.10. Comparable values of PF are reported in previous studies: for example, $26.6 \mu\text{W cm}^{-1} \text{ K}^{-2}$ at 380 K in a recent study on a very well characterized, zone-melted Ag_2Se sample [20].

Temperature dependence of κ is shown in Fig. 4.11(a). κ near 300 K decreases from $\sim 1.4 \text{ W m}^{-1} \text{ K}^{-1}$ (AS1) to $0.8 \text{ W m}^{-1} \text{ K}^{-1}$ (AS3 and AS4). Overall, a good agreement is seen with previous literature [13, 16, 18, 19, 192]. κ for the two 2.5% Se excess samples (AS3

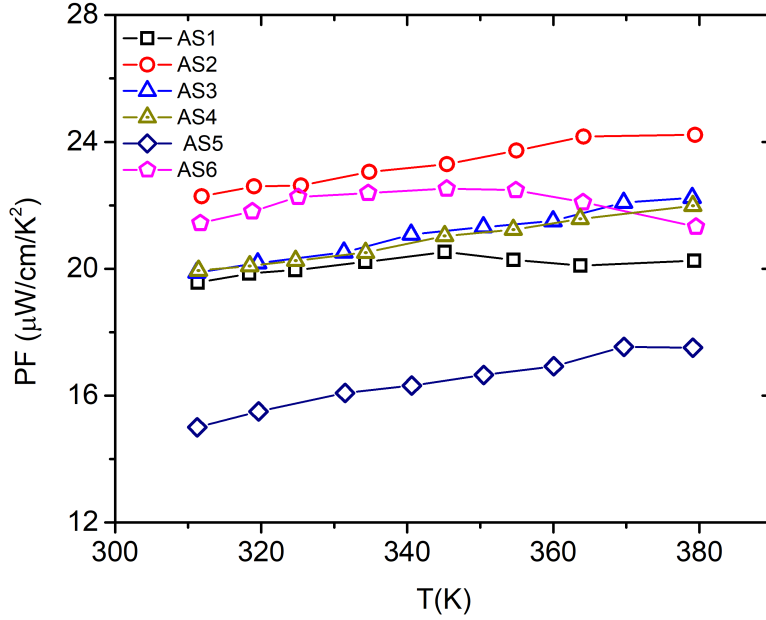


Figure 4.10: Temperature dependent power factor (PF) for Ag₂Se samples.

and AS4) overlap over the whole temperature range. It is apparent from the manner in which T-dependence of κ exhibits itself that the electronic contribution (κ_e) is rather significant. The lattice contribution (κ_l) is obtained using the relation: $\kappa_l = \kappa - L\sigma T$, where L is the Lorenz number, which is estimated using the Single Kane Band (SKB) model [193]. The generalized expression for L in SKB is:

$$L = \left(\frac{k_B}{e}\right)^2 \left[\frac{{}^2F_{-2}^1(\eta, \alpha)}{{}^0F_{-2}^1(\eta, \alpha)} - \left(\frac{{}^1F_{-2}^1(\eta, \alpha)}{{}^0F_{-2}^1(\eta, \alpha)}\right)^2 \right], \quad (4.1)$$

here, ${}^nF_k^m(\eta, \alpha)$ are the Fermi-Dirac integrals defined as,

$${}^nF_k^m(\eta, \alpha) = \int_0^\infty \left(\frac{\partial f}{\partial \epsilon}\right) \epsilon^n (\epsilon + \alpha\epsilon^2)^m (1 + 2\alpha\epsilon)^k d\epsilon \quad (4.2)$$

where the indices n, m and k take integral values that depend on the transport property and carrier scattering mechanism being considered, factor $\alpha = k_B T / E_g$ (where k_B and E_g

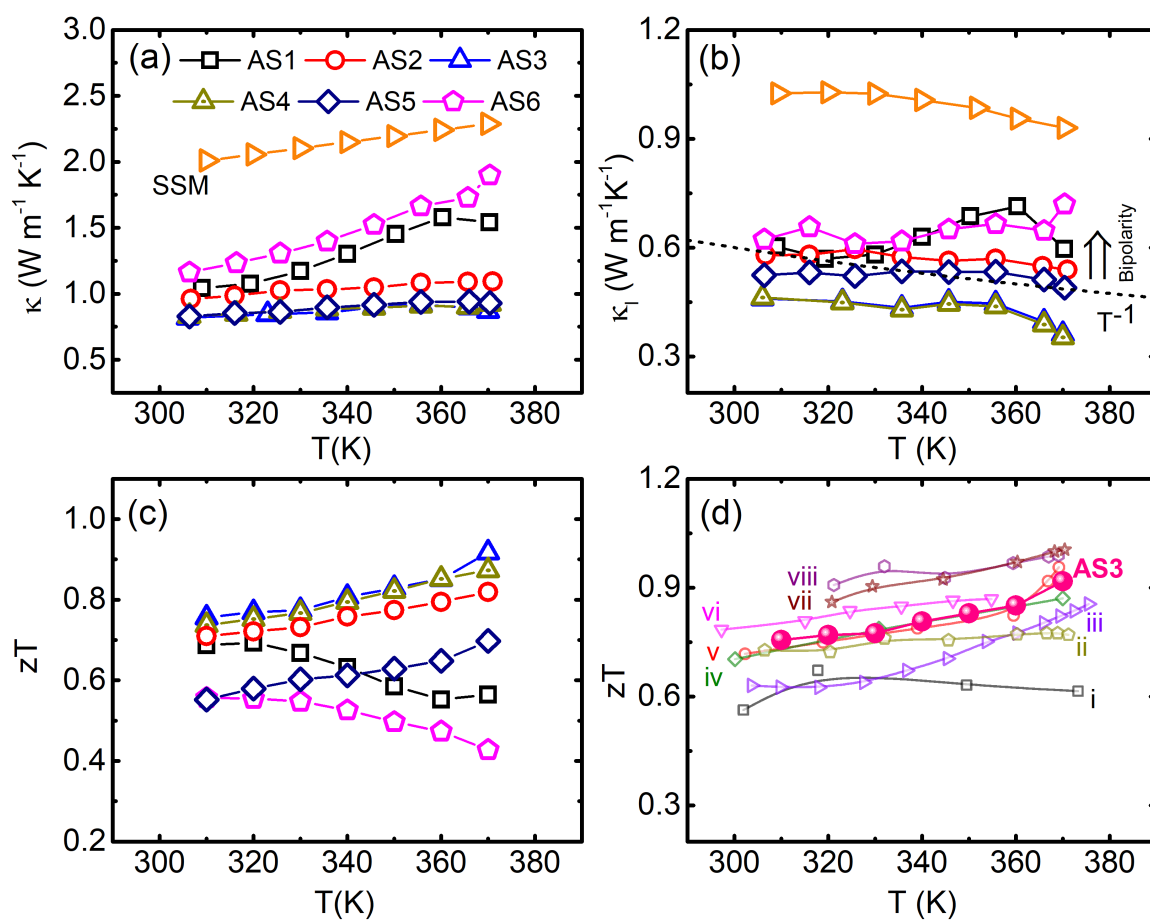


Figure 4.11: Temperature dependence of (a) thermal conductivity (κ), (b) lattice thermal conductivity (κ_l), and (c) figure-of-merit (zT). In (d) zT from literature [i] Li et al. [17], [ii] Huang et al. [18], [iii] Mi et al. [13], [iv] Chen et al. [14], [v] Yang et al. [19], [vi] Jin et al. [20], [vii] Jood et al. [16], [viii] Wang et al. [15] are plotted along with the zT of our 2.5% Se-excess sample.

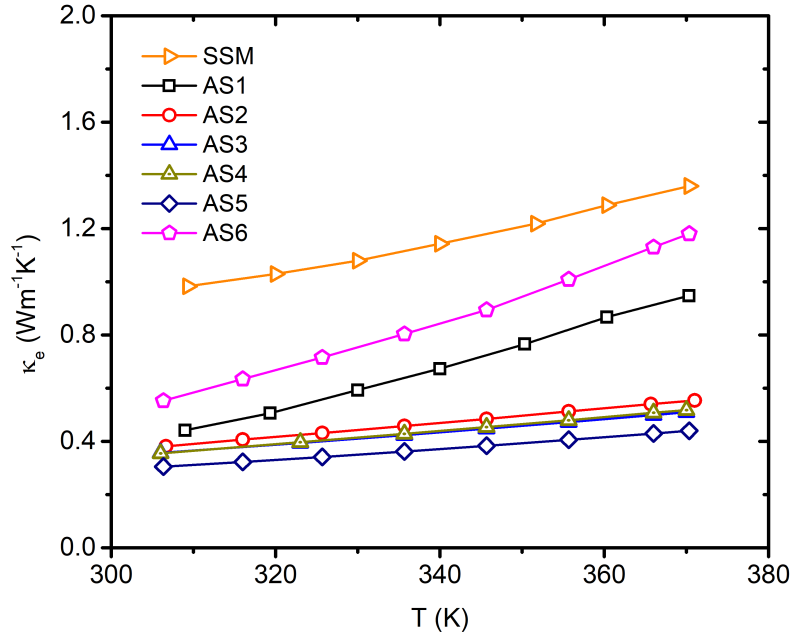


Figure 4.12: Temperature dependent electronic thermal conductivity estimated using Weidemann Franz law $\kappa_e = LT\sigma$ where L calculated using single kane band (SKB) model.

are Boltzmann constant and band gap respectively) accounts for the band nonparabolicity, and η is the reduced Fermi energy, which is estimated from the experimental value of S by assuming acoustic phonon scattering by using equation (4.3). Our analysis is done by taking $E_g = 0.05$ eV, and by assuming that the acoustic phonon scattering is the dominant form of scattering at high temperatures.

$$S = \frac{k_B}{e} \left[\frac{{}^1F_{-2}^1(\eta)}{{}^0F_{-2}^1(\eta)} - \eta \right] \quad (4.3)$$

As anticipated, $\kappa_e = L\sigma T$, shown in Fig. 4.12, constitutes almost 60% of the total measured κ . The variation of κ_l with temperature is shown in Fig. 4.11(b). Near 300 K, κ_l ranges from $0.6 \text{ W m}^{-1} \text{ K}^{-1}$ (AS1) to $0.4 \text{ W m}^{-1} \text{ K}^{-1}$ (AS3 and AS4). For comparison, κ_l for SSM sample ($1 \text{ W m}^{-1} \text{ K}^{-1}$ near 300 K) is also shown, which is significantly high compared to the cold-pressed samples, making apparent the role of grain boundary scattering in the ball-milled samples. κ_l for the SSM sample shows a T^{-1} dependence at high temperatures

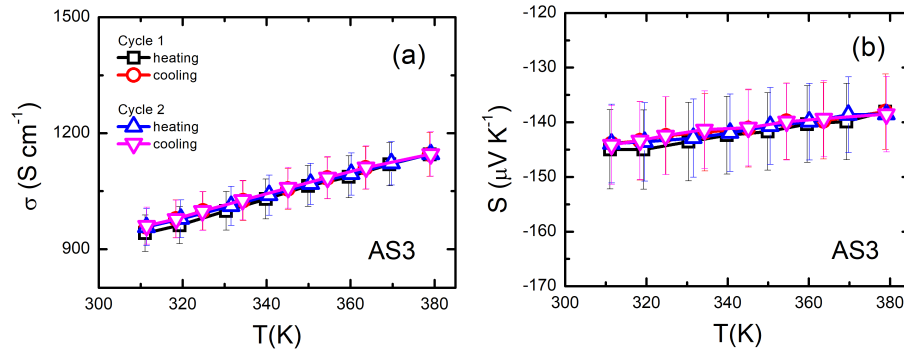


Figure 4.13: Temperature dependence of electrical conductivity and thermopower in two successive cycles.

($T > 340$ K), indicating that the acoustic phonon scattering mechanism dominates at high temperatures.

The temperature variation of zT in our samples is shown in Fig. 4.11(c). The highest zT of 0.92 is obtained for sample AS3 at 370 K, which can be attributed to its lowest thermal conductivity. It should be noted that the zT for our two independently prepared 2.5% Se excess samples (namely, AS3 and AS4) overlap satisfactorily over the whole temperature range. The 0.5% Se doped sample (AS2) with highest PF comes next with a slightly reduced zT value of 0.82 at 370 K.

In Fig. 4.11(d), the zT of our 2.5% Se excess sample (AS3) is compared with some previous studies where high zT was reported. We see that zT in our samples is comparable to some of the highest zT values previously reported for Ag_2Se . We also show that the thermoelectric properties of $\text{Ag}_2\text{Se}_{1+\delta}$ samples do not deteriorate in successive thermal cycles as shown in Fig. 4.13

4.6 Summary and Conclusion

In conclusion, we show here that it is possible to prepare highly dense $\text{Ag}_2\text{Se}_{1+\delta}$ samples at room temperature with very high and reproducible zT without employing any of the elaborate methods used in previous studies, including spark plasma sintering, solid state melting, high-temperature annealing, or zone-melting. As our method does not involve SPS for den-

sification it can readily be scaled up for higher sample yields. Further improvement via optimization of Se-doping, and by finding ways to further lower κ_e can be possible future research direction on this material. Altogether, high zT, excellent reproducibility and thermal stability, ease of preparation, and ductile nature of Ag_2Se makes it an excellent candidate for further considerations as a replacement material for Bi_2Te_3 based alloys.

Chapter 5

A facile room temperature synthesis method to prepare an inorganic ductile superionic sulphide with high figure of merit

5.1 Introduction and Motivation

Many TE materials known today can be efficiently used for power generation applications due to their superior TE properties. For instance, materials such as Bi_2Te_3 [50], PbTe [194], GeTe [195], and SiGe [196] are known for their high zT values and are used in commercial applications for power generation and solid-state coolers. However, the aforementioned bulk materials are brittle, which limits their application in scenarios where flexible TE materials are required. Moreover, synthesizing their flexible thin films often require complex techniques and instruments [71, 197]. Additionally, their hazardous and costly components do not allow their usage at a larger scale, and they can only be used in niche applications such as deep space mission programs and laser cooling.

Despite these challenges, flexible TE devices can be made out of organic TE materi-

als. However, their poor electrical transport leads to low zT values [197]. Recently, an environment-friendly inorganic compound, Ag_2S , has regained interest due to its metal-like ductility with high plastic deformation [163]. The crystal structure of room temperature phase of Ag_2S is shown in Figure 5.1(a). Ag_2S has three polymorphic crystal structures: monoclinic acanthite ($\beta\text{-Ag}_2\text{S}$), which is stable below 450 K; BCC also called argentite ($\alpha\text{-Ag}_2\text{S}$), which is stable above 450 K; and the FCC phase ($\gamma\text{-Ag}_2\text{S}$), which is stable above 860 K. In literature, the names " α " and " β " phases for Ag_2S have been used interchangeably [163, 198]. Here, in this study, we will proceed with notions used by Junod et al. [198]. The $\beta\text{-Ag}_2\text{S}$ is a ductile semiconductor having a band gap of 1 eV [198] and low carrier concentration ($1.6 \times 10^{14} \text{ cm}^{-3}$), which results in poor electrical conductivity [103]. Moreover, $\alpha\text{-Ag}_2\text{S}$ exhibits superionic conductivity, where Ag^+ ions move like a liquid through the BCC skeleton formed by S ions. The band gap of the BCC phase is reported to be around 0.3 eV from high-temperature optical studies, and the high-temperature electrical resistivity reports confirm its metal-like behavior [198]. According to the high-temperature electrical transport properties reported by Junod et al. [198], the electrical conductivity of $\alpha\text{-Ag}_2\text{S}$ depends on the thermal history of polycrystalline ingots. Their reported ingot samples showed metal-like behavior, except for one that exhibited exceptional semiconducting behavior in terms of electrical conductivity. However, the explicit reason for this distinct behavior of electrical conductivity between ingots having similar compositions is still unknown. Despite this puzzle, $\alpha\text{-Ag}_2\text{S}$ has been reported as a potential TE material in mid-temperature range due to its low band gap and lower lattice thermal conductivity in superionic phase [103, 123, 199]. In fact, the ingot sample of $\alpha\text{-Ag}_2\text{S}$ prepared by solid-state melting method has shown decent TE figure-of-merit of 0.55 at 570 K, where the samples exhibited semiconductor-like temperature-dependent electrical conductivity [123]. Since the field of environment friendly superionic TE material has recently garnered significant attention primarily due to the discovery of high zT values in Cu-based material, Cu_2S . Hence, exploring the TE properties of superionic Ag_2S and understanding its electrical transport behavior is of great interest. However, there are not many reports on the detailed TE study

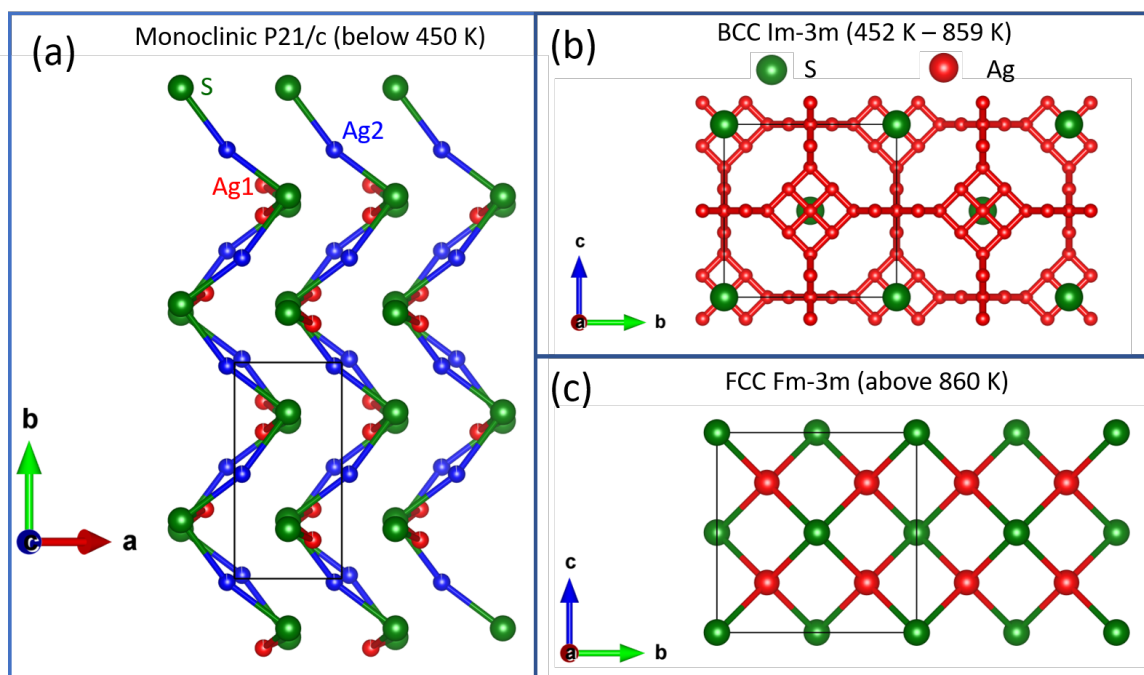


Figure 5.1: Crystal structure of Ag_2S , (a) monoclinic also known acanthite (or β -phase) stable below 450 K, (b) superionic BCC (or α -phase) phase also known as argentite stable below 859 K, and (c) superionic FCC stable above 860 K. In both β and α phases, the S atoms are arranged on a body centered cubic lattice. While in β -phase Ag atoms form a regular lattice, in α -phase the four Ag atoms are randomly distributed on the 42 crystallographic positions.

of Ag_2S , unlike the Cu_2S thermoelectric material, where high zT values of 1.7 and 2.1 have been achieved by materials engineering, creating small cation vacancies, and optimizing the synthesis method, respectively [23, 200].

There are only a few sulfide TE materials known to possess high figure-of-merit, and most of them are p-type [171]. PbS is the only lead-based sulfide that exhibits n-type conduction and a high zT value of around 1.1 at 923 K [201]. But the toxicity of lead limits its application. Therefore, further research is required to discover new, environmentally friendly, n-type sulfide TE materials, and Ag_2S could be one of the options worth exploring. The ductility of Ag_2S is one of the reasons that motivated us to investigate its TE properties for flexible TE applications, which is absent in the existing superionic copper chalcogenide compounds.

Hence, focusing on Ag_2S superionic as a TE material, in recent years, several derivatives

of Ag_2S heavily doped with Te or Se have been discovered to stabilize the superionic phase at room temperature. These superionic compounds exhibit moderate PF and low thermal conductivity, resulting in high zT values, such as 0.8 at 600 K in $\text{Ag}_{20}\text{Te}_3\text{S}_7$ [102], 0.7 at 600 K in $\text{Ag}_2\text{Te}_{0.6}\text{S}_{0.4}$ [202], and 0.8 at 600 K in $\text{Ag}_2\text{S}_{0.7}\text{Te}_{0.3}$ [203]. These ternary Ag_2S based derivatives are being well investigated now a days. However, there is a lack of detailed reports on the TE properties of binary superionic silver sulfide, Ag_2S .

To address this, we conducted a study on the TE properties of stoichiometric Ag_2S samples synthesized by both conventional solid-state melting method (SSM) and a facile room temperature powder synthesis followed by cold pressing (CP). Our results showed a significant improvement in zT from 0.49 in the SSM sample to 0.58 in the CP sample, due to the largely suppressed thermal conductivity in the latter. Additionally, we show that by adding a slight excess of sulfur (S), leading to a further decrease in thermal conductivity from $0.75 \text{ W m}^{-1} \text{ K}^{-1}$ in the stoichiometric CP sample to $0.52 \text{ W m}^{-1} \text{ K}^{-1}$ in the 1% S excess CP sample, the zT of Ag_2S can be enhanced to a value as high as 0.9. We have also tried to understand the reason behind the lower thermal conductivity in the S excess sample by using the DSC measurements.

5.2 Experimental Details

5.2.1 Sample Synthesis Using Hand Grinding and cold pressing (HCP)

We synthesized $\text{Ag}_2\text{S}_{1+x}$ ($x = 0, 0.01, 0.015, 0.02, \text{ and } 0.05$) powder samples by mixing and grinding the stoichiometric amounts of elemental Ag (sigma Alrich, 99.99% purity) powder and S (sigma Alrich, 99.999% purity) flakes. The mixing and grinding was done for 100 min and then samples were collected in plastic vials and kept for 24 hours under ambient condition for Ag and S to react completely. The powder x-ray diffraction of Ag_2S sample is shown in Figure 5.2 at intermediate stages of synthesis. For transport property measurements, the powder sample was cold pressed into 8 mm pellets using a KBr press die set. Since Ag_2S sample was also prepared by solid-state melting, we named these samples

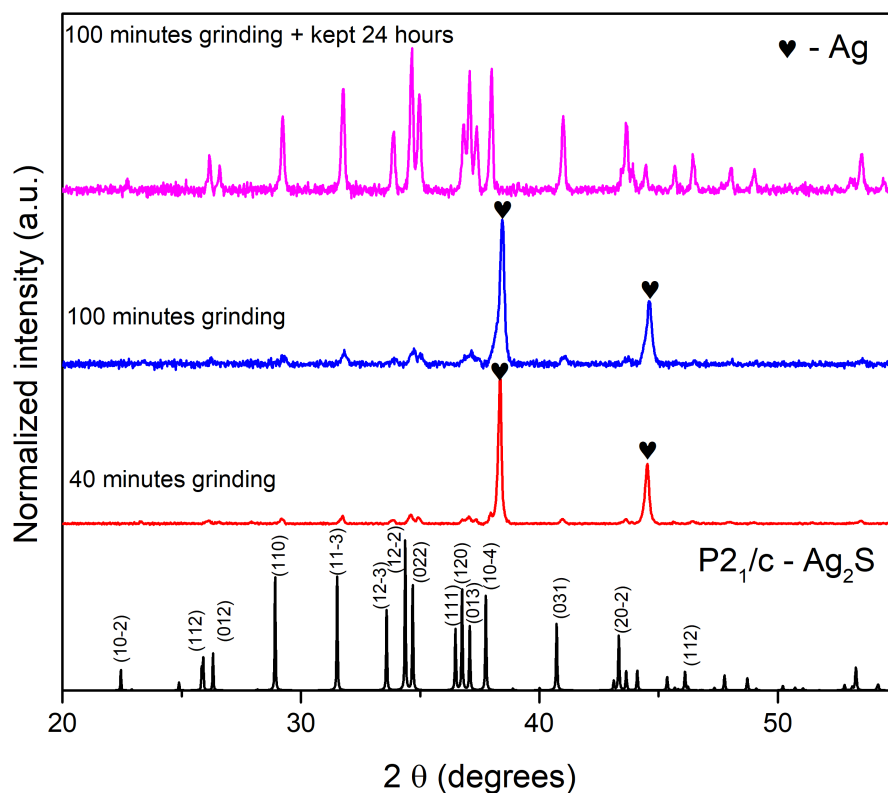


Figure 5.2: Powder x-ray diffraction of Ag_2S at different synthesis stages in ambient condition.

cold-pressed (CP) in further discussion. Unless otherwise stated, Ag_2S refers to the sample prepared by hand grinding followed by cold-pressing.

5.2.2 Sample Synthesis Using Melting Method

For the sake of comparison, we have also synthesized a pristine Ag_2S sample using the solid-state melting method (SSM). For this purpose, elemental powder of Ag (sigma Alrich, 99.99% purity) and S flakes (Sigma Aldrich, 99.999% purity) were taken in a stoichiometric ratio and vacuum sealed in a preheated quartz ampule. The ampule was heated to 1173 K with a heating rate of 50 K h^{-1} and stayed at this temperature for 24 h, after which the furnace was turned off to allow it to cool down to room temperature.

5.2.3 Characterization Techniques

For x-ray diffraction, a small section was cut from the ingot and grounded using mortar-pestle dipped in liquid nitrogen. The phase identification of powder samples at room temperature as well as at high temperature (by using an additional inbuilt heater sample stage arrangement) is performed using the powder x-ray diffraction on Bruker D8 Advance, with Cu K_{α} source. A transmission electron microscope (JEM - 2200FS) is used to examine the particle size distribution and to analyze the morphology of synthesized samples. The microstructure of bulk samples and their compositions are analyzed by scanning electron microscopy (SEM) and energy dispersive X-ray spectroscopy using Zeiss Ultra Plus. To examine the structural phase transition in our samples we have used Differential Scanning Calorimeter DSC7000 Series (Hitachi, Japan).

Electronic transport property measurements are performed on cold pressed pellets and ingot samples on rectangular bar shape sample geometries. The Seebeck and resistivity are measured simultaneously by four probe method using thermoelectric measurement setup LSR3 (Linseis). The maximum uncertainty in the resistivity and seebeck measurement is about 5%. Thermal conductivity κ is estimated using formula, $\kappa = \rho_m DC_p$ where ρ_m , C_p and D are sample density, specific heat and thermal diffusivity. Thermal diffusivity is measured on 8 mm diameter pellets using the laser flash analyzer (LFA 1000, Linseis) . The sample density is calculated by taking the weight and dimensions of bar-shaped or pellet samples. The maximum uncertainty in the thermal conductivity measurement are not more than 6%.

5.3 Results and Discussion

Figure 5.3(a) illustrates the powder x-ray diffraction (PXRD) pattern obtained at room temperature. All the peaks in the observed pattern can be assigned to the monoclinic space group $P2_1/c$ for all the synthesized samples. We observed negligible shifts in the (12-2) and (022) peaks in the S excess samples, indicating minimal changes in the lattice parameters.

The Rietveld refinement of the Ag_2S PXRD data, is shown in Figure 5.4 where two slightly different theoretical models that correspond to two sets of lattice parameters and

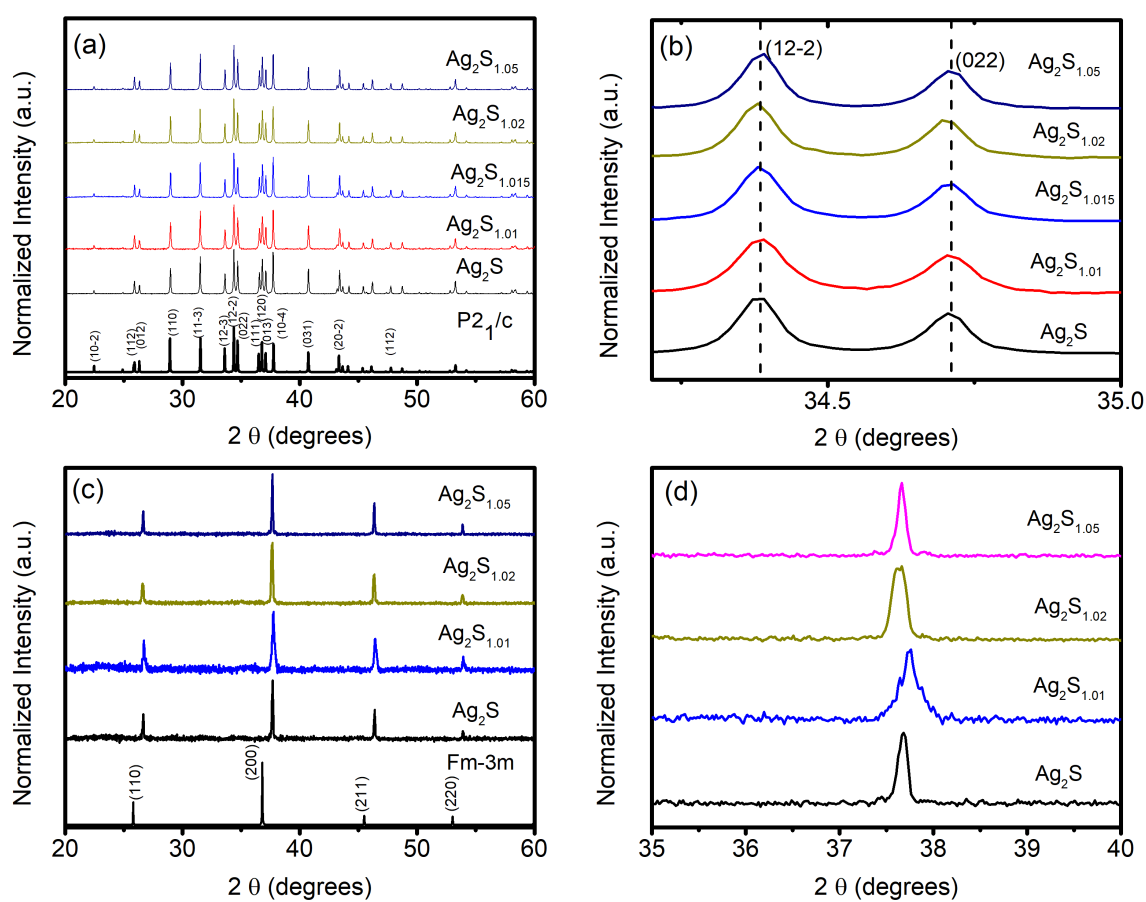


Figure 5.3: (a) Powder x-ray diffraction at room temperature, (b) (12-2) and (022) peaks showing negligible peak shift with S excess for the monoclinic phase, (c) shows the powder x-ray diffraction of the BCC superionic phase, and (d) shows a zoomed-in view of the (200) peak in different samples.

Wyckoff positions previously reported in studies by Blanton et al. (2011) and Frueh et al. (1958) are tried [21, 22]. Both models demonstrated similar goodness of fit with our experimental data. The structural parameters obtained from these two different theoretical models are given in the table 5.1.

Table 5.1: Room temperature crystal structure (Monoclinic, P2₁/c) details obtained from Rietveld refinement analysis using two different previously reported models. [21, 22]

Parameters	Using Blanton et al. model	Using Frueh et al. model
a (Å)	4.222	4.224
b (Å)	6.9186	6.921
c (Å)	8.2703	7.8574
β	110.559	99.658
Density (g cm ⁻³)	7.28	7.37
x (Ag1)	0.0458	0.7613
x (Ag2)	0.64335	0.29364
x (S)	0.26766	0.3636
y (Ag1)	0.0157	0.0166
y (Ag2)	0.3214	0.3231
y (S)	0.2312	0.2294
z (Ag1)	0.3075	0.3059
z (Ag2)	0.4362	0.4375
z (S)	0.1332	0.1337
χ^2	24.2	23.6
R _p	12.5	12.3
R _{wp}	12.4	11.9

The Rietveld analysis of the lab based data did not help to identify the better of the two models as both the models yield roughly the same values of the goodness of-fit parameters (χ^2 , R_p and R_{wp}). The main differences between the two models are: (a) the lattice parameter along the c-axis, (b) the monoclinic angle β , and (c) the x-coordinates of S, Ag1 and Ag2.

The powder x-ray diffraction pattern for the superionic body-centered cubic (BCC) phase in the Im-3m space group is shown in Figure 5.3(c) at an approximate temperature value of 550 K. It is worth noting the broadening of peaks in the Ag₂S_{1.01} composition, and this effect is magnified in Figure 5.3(d) for the (200) peak. Such xrd peak broadening can be expected either due to small particle size or due to the presence of strain.

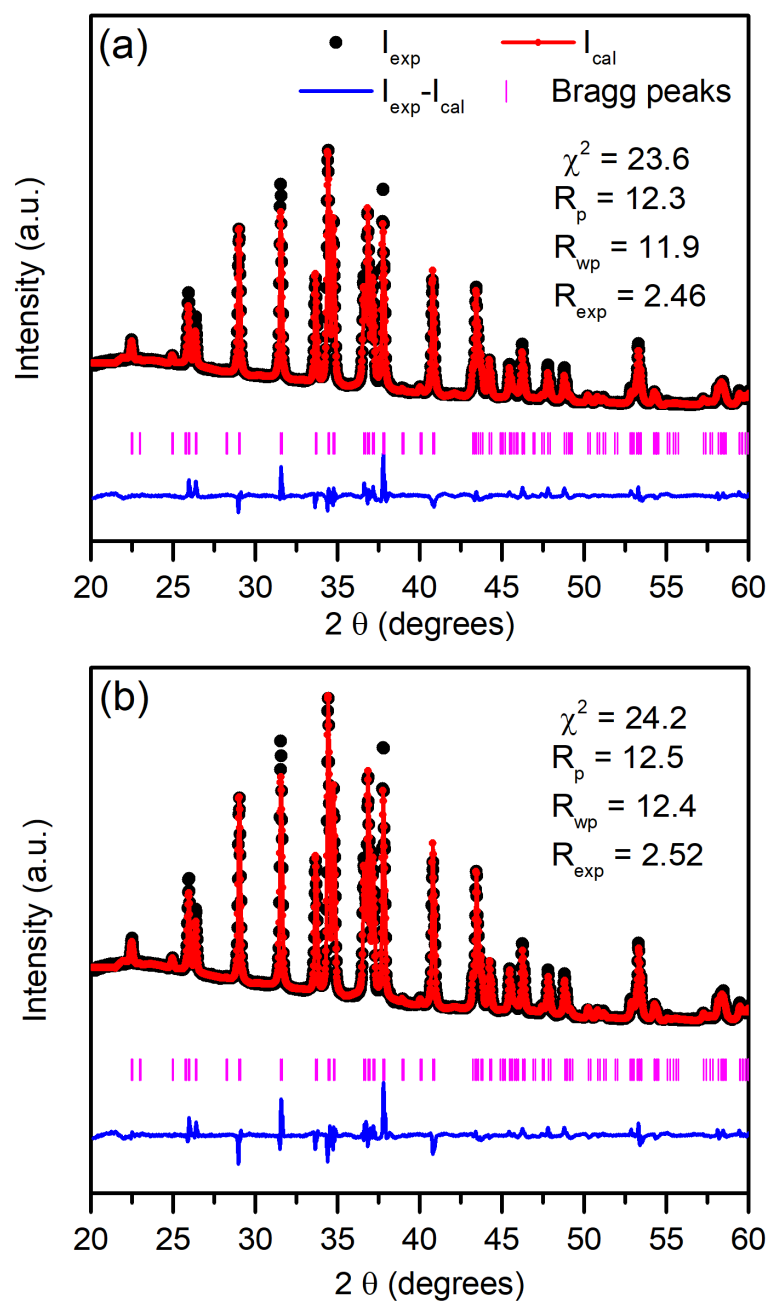


Figure 5.4: Retfield Refinement of Ag_2S (a) by using theoretical model proposed by Blanton et al. [21], and (b) using structure parameters reported by Frueh et al. [22].

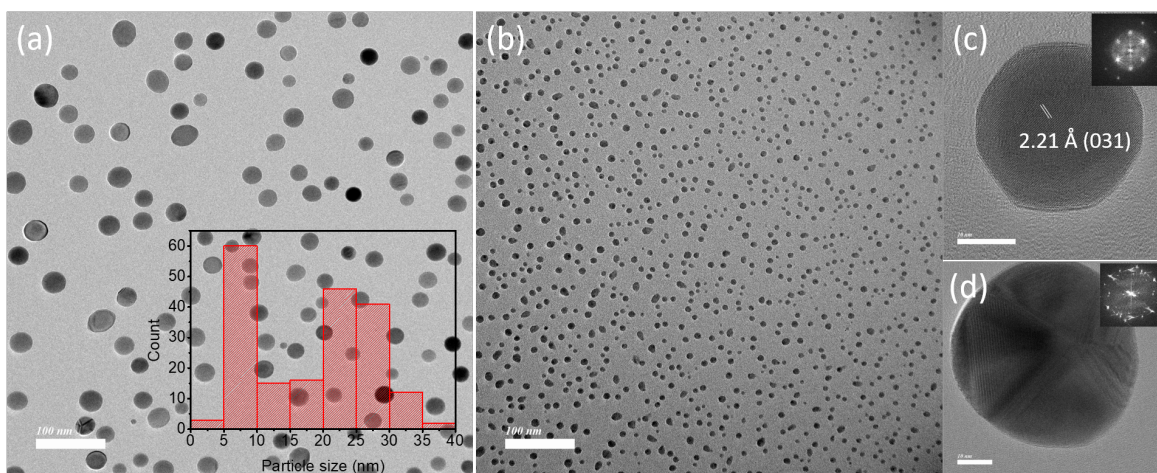


Figure 5.5: TEM analysis of Ag_2S powder sample where (a, and b) showing the TEM image at 100 nm with different nano-particle size (inset in (a) is the histogram showing particle size distribution), (c, and d) are HRTEM image at 10 nm showing two nano-particles having single crystalline and polycrystalline morphology respectively.

To get the information about morphology of our synthesized powder samples we performed the TEM analysis by dispersing them in ethanol and drop cast on amorphous carbon coated TEM grid. Interestingly, our hand grinded powder samples consisted of nanoparticles. We found a large variation in the nanoparticle size varying from 5 nm to 35 nm, see Figure 5.5 where inset in (a) shows the particle size histogram. In panel (c), we show a nanoparticle having a single crystalline arrangement of atomic planes, and in (d) we show a particle with polycrystalline-like arrangement of the atomic planes. Insets shown in (c) and (d) confirms the single crystalline and polycrystalline nature of different nanoparticles through FFT pattern. Thus, by simple hand-grinding procedure, we not only get Ag_2S nanoparticles but also a diversity in size and degree of crystallinity.

To gain further insights into the room temperature phase, a more detailed HRTEM analysis of the nanoparticle shown in Figure 5.5(d) is presented in Figure 5.6. As shown in Figure 5.6(a), the regions close to the top and bottom of the nanoparticle shown actually confirm to two distinct set of FFT patterns. Interestingly, the DSC of this sample shows the presence of two peaks during heating and cooling (Figure 5.6(b)). While heating the peaks are more closely spaced than while cooling, where these peaks are narrower and well sep-

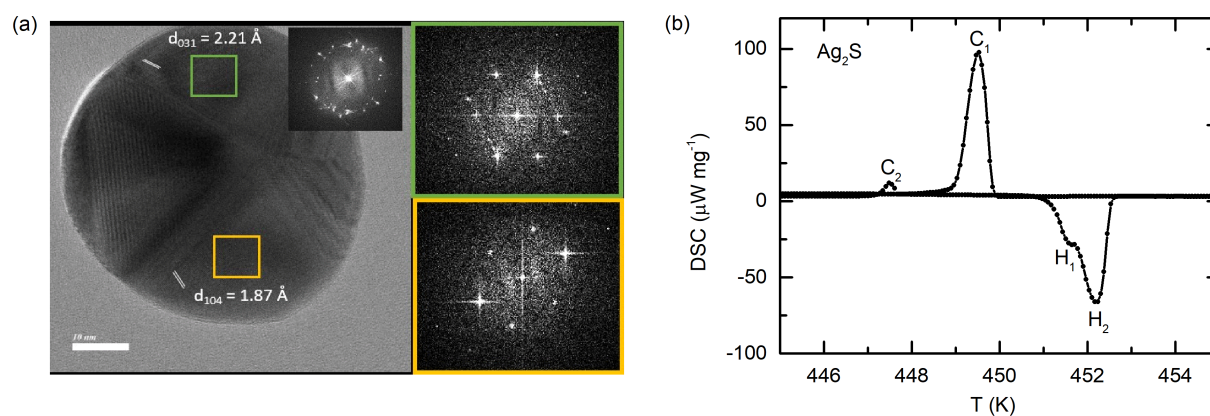


Figure 5.6: (a) HRTEM image a nanoparticle comprising of two different phases, insets shows the FFT of green and yellow marked rectangular boxes, and (b) Differential scanning calorimetry (DSC) of Ag_2S sample showing two transitions while heating (H_1 and H_2) as well as in cooling (C_1 and C_2)

arated. Since in the PXRD there are no signs of a secondary Ag_2S phase, the presence of double peak DSC signal is due to presence of a metastable Ag_2S phase which has the same monoclinic symmetry but slightly different atomic arrangement. This distinct FFT patterns observed in Figure 5.6(a) can also be attributed to the presence of the metastable phase. Presence of such metastable phases have been also observed in Ag_2Se superionic compound by Liang et al. [204] and Jood et al. [16] using detailed HRTEM studies. This hypothesis is further supported by the high-resolution transmission electron microscopy image of a different nanoparticle in Figure 5.7. Upon visual inspection, the particle appears to consist of two distinct regions, which is further supported by the distinct fast Fourier transform (FFT) patterns obtained from two separate areas of the particle. These distinct FFT patterns are attributed to the presence of metastable phase as discussed above.

To gather further evidence for metastability, we conducted detailed DSC measurements with multiple thermal cycles, and the results are presented in Figure 5.8. With consecutive thermal cycling, the peaks corresponding to two distinct transitions evolved. In the 10th run, we observed a sharp peak at 450.5 K with an elongated tail towards higher temperatures up to 451.5 K during heating. While cooling, two peaks were observed at 448.4 K and 447.6 K. However, the appearance of this doublet of peaks during cooling began from the 3rd run

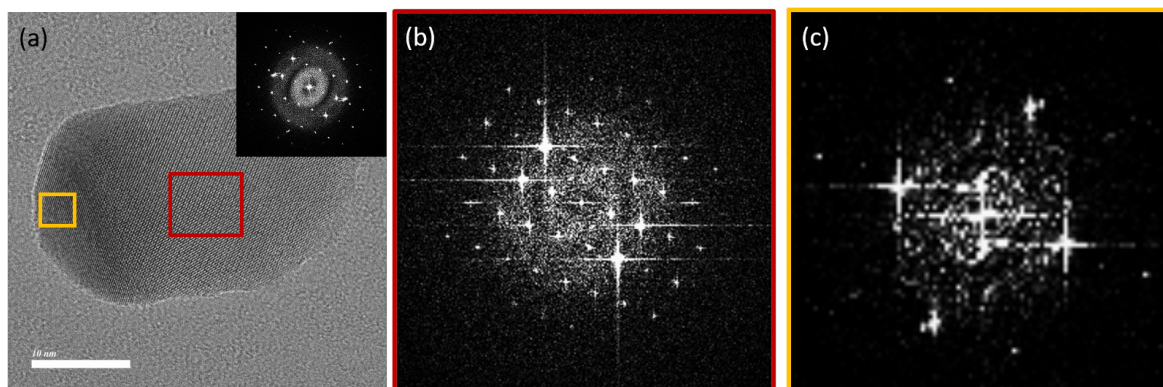


Figure 5.7: HRTEM analysis of Ag_2S powder sample where (a) shows rod like nanoparticle composed of two family of planes (-121) and (-123) forming coherent boundary (inset shows the FFT of particle), (b, and c) are the FFT of red and yellow marked rectangular areas in (a).

itself, and their peak shapes changed in subsequent thermal cycling runs, finally stabilizing after the 8th run.

Through analysis of the DSC peaks, we found that the final peaks observed during cooling were a re-adjustment of the C_1 and C_2 peaks observed in the very first run. The sharp peak with an elongated tail during heating corresponds to the H_1 and H_2 peaks observed in the initial run, which evolved with thermal cycling and stabilized by the 10th run. It can be hypothesized that the H_1 and C_1 peaks correspond to a metastable phase that undergoes changes during thermal cycling. Our observation of finding an additional two DSC peaks, along with the superionic transition from the α to β Ag_2S phase, is similar to the twinning effect as discussed by Sadanaga et al. [205], which evolves significantly with thermal cycling. Such twinning effect can also explain the intensity mismatch of PXRD peaks in Rietveld refinement, which was predominantly reported to occur along the (-104) plane [205]. Sadanaga et al. investigated the crystal structure of single crystals of Ag_2S , which inherently possess twinning. They studied the heating effect and found that the twinning effect increases while cooling the samples from the superionic phase to the room temperature phase, making the transition more complex. They observed the existence of multiple domains of the superionic phase along with the monoclinic phase.

The DSC data of $\text{Ag}_2\text{S}_{1.01}$ samples is shown in Figure 5.8(b), where a similar phase/peak

evolution near the transition temperature is observed. However, by the tenth run, the anion-excess sample seems to stabilize with broad peaks, both while heating and cooling. It shows that the shoulder peak present in case of Ag_2S , merges with the primary peak in $\text{Ag}_2\text{S}_{1.01}$ making it broad.

To understand the effect of the metastable phase on electronic transport, we performed high-temperature resistivity measurements following a similar heating profile as for the first three runs of the DSC.

The temperature-dependent resistivity, as depicted in Figure 5.9(a), exhibit significant variations between the first heating run and subsequent cooling-heating runs. During the initial heating run, the resistivity shows a sharp drop when cooled below 455 K. The resistivity continued to drop at the same rate up to 473 K, and above this temperature a very slow decrease is observed. However, during cooling, the resistivity shows a decreasing behavior ($d\rho/dT > 0$) until 450 K and increases sharply as the temperature is further decreased. Notably, a distinct kink around 450 K was observed during cooling, which was absent in the heating data and likely corresponds to the C_2 peak in the DSC scan. A similar kink also appear in the second cooling run, which is in line with the observation of C_2 peak in the second cooling DSC scan also. In the third heating run, we observed the same kink at the same temperature as in the second heating run but it disappeared in the cooling data, when measurement extended up to 673 K. This could be attributed to the reduced difference between temperatures corresponding to the C_2 and C_1 transitions observed in the DSC cooling data. Interestingly, it was noted that the resistivity magnitude decreases with each heating and cooling cycle. For a clearer visualization, refer to Figure 5.9(c). In the third run, the temperature-dependent resistivity initially exhibited behavior akin to a semiconductor during heating, but shifted towards metal like upon undergoing the structural transition while cooling till transition temperature, ultimately returning to a semiconductor state below 450 K in monoclinic phase. Therefore, our temperature-dependent electrical resistivity exhibits anomalies corresponding to those observed in the DSC data and confirms that the phase evolution with thermal cycling also affect the electronic transport significantly.

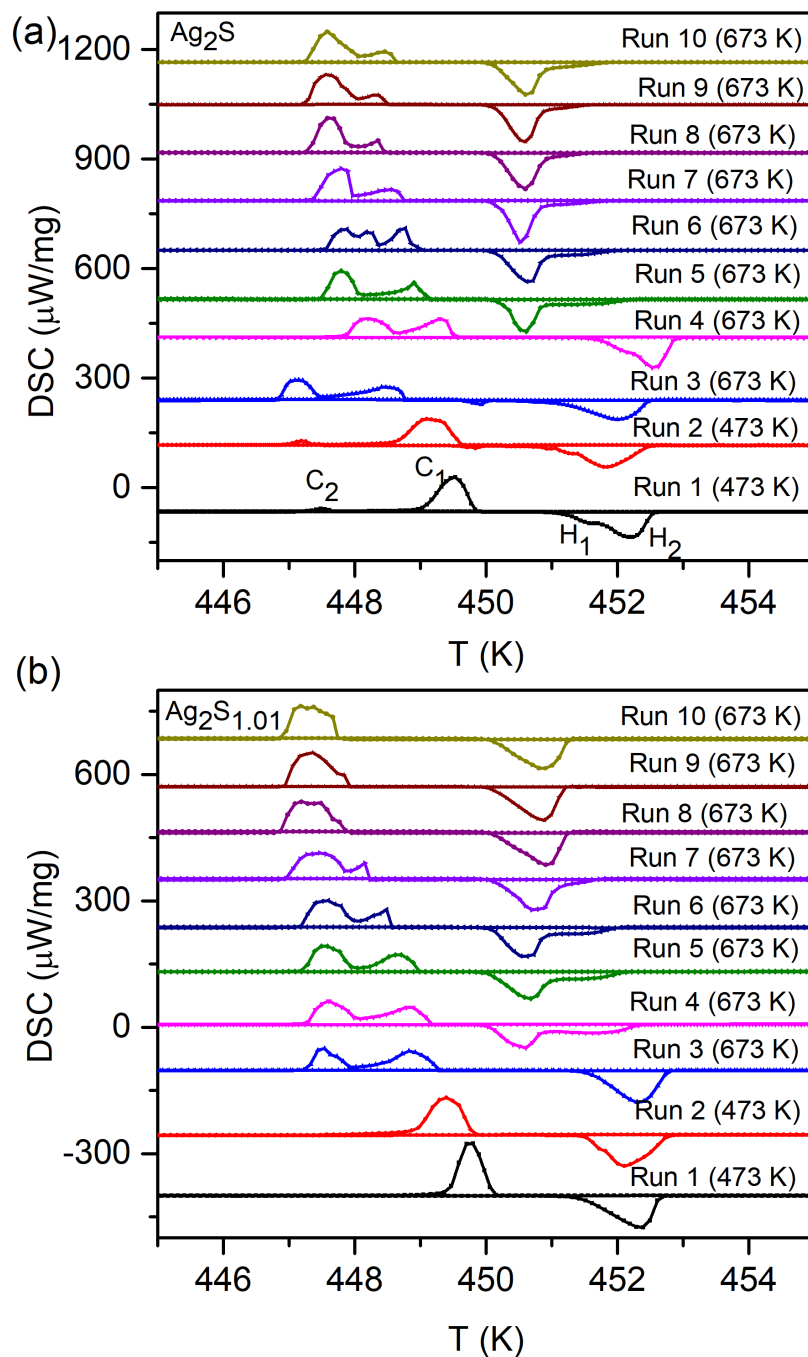


Figure 5.8: (a, and b) Shows the effect of thermal cycling on DSC of Ag_2S , and $\text{Ag}_2\text{S}_{1.01}$ cold-pressed pellet samples respectively.

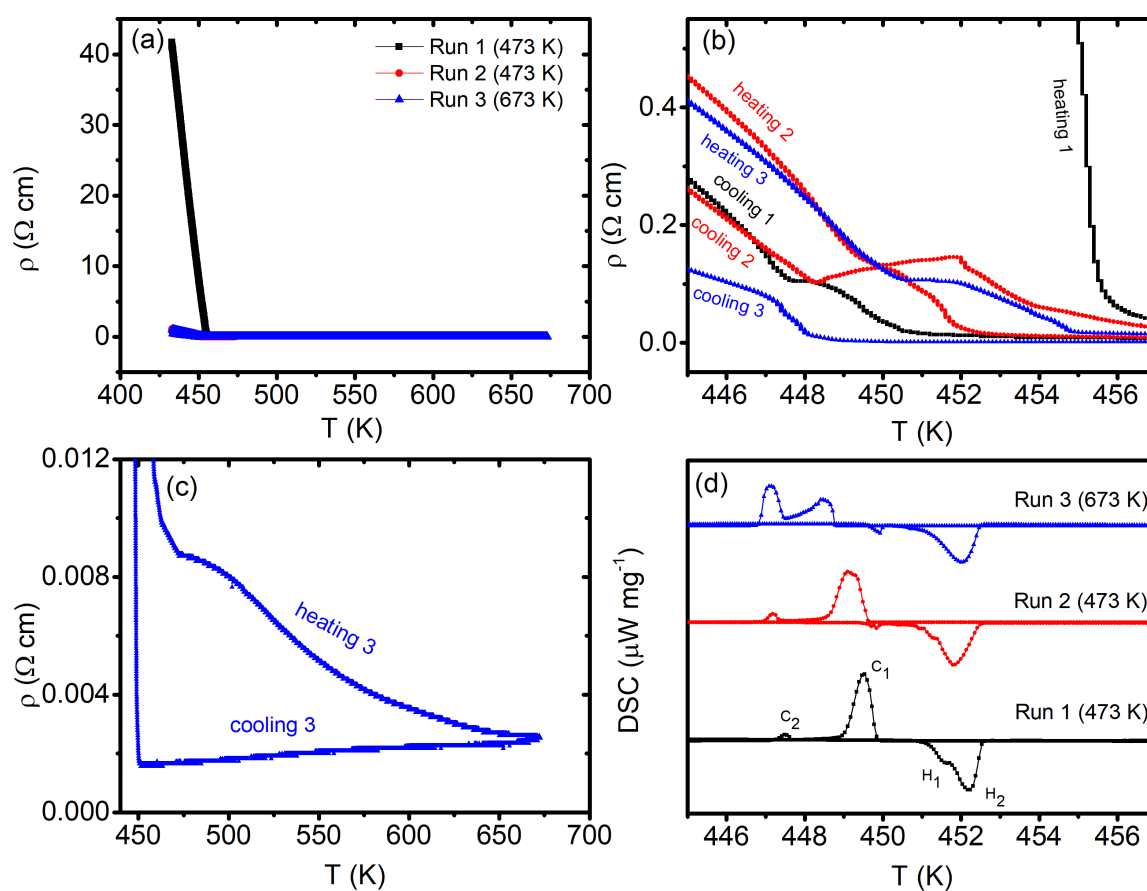


Figure 5.9: (a) Temperature dependent resistivity with three consecutive runs, (b) a zoomed-in view of the resistivity vs temperature plots around the β | α transition, (c) variation of resistivity with temperature during run 3, and (d) DSC runs with three heating and cooling cycles.

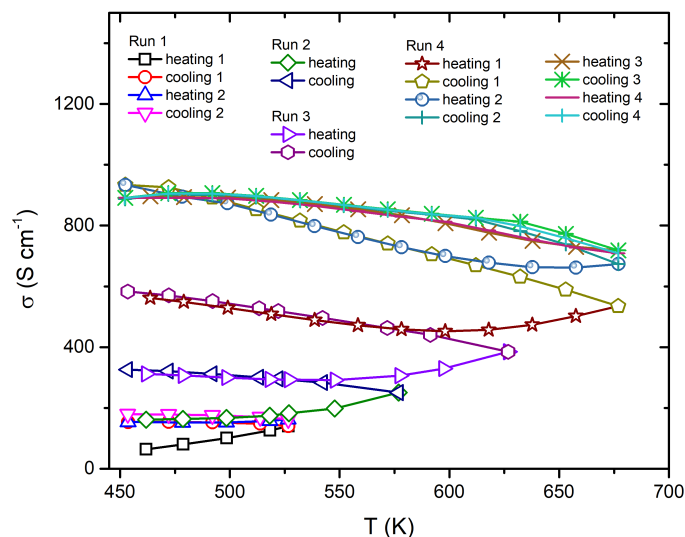


Figure 5.10: Temperature dependent electrical conductivity of Ag_2S with multiple heating and cooling cycles.

Memory Effect in Ag_2S

The metastability in Ag_2S is manifested nicely in the form of a memory effect during the resistivity measurements. To show this, in Figure 5.10, we have plotted the electrical conductivity of an Ag_2S sample as a function of temperature during successive thermal cycles, recording data during both the heating and the cooling run in each cycle. The measurements are performed only in the superionic α -phase, i.e., for $T > 450$ K, as the β -phase of Ag_2S is highly resistive as shown in the previous section. In the very first run, while heating, sample showed semiconducting behavior ($d\sigma/dT > 0$), which becomes metal-like ($d\sigma/dT < 0$) during cooling. In the next heating run $\sigma(T)$ follows the cooling curve during run 1 up to the highest temperature to which the sample was heated during run 1, but on increasing the temperature further (i.e., beyond the highest temperature employed during run 1), σ starts to increase ($d\sigma/dT < 0$) and this increasing behaviour persists up to the highest temperature during run 2. Interestingly, if the increasing part of the heating curve during run 2 is extrapolated back to the lower temperature it overlaps the heating curve during run 1. In the subsequent

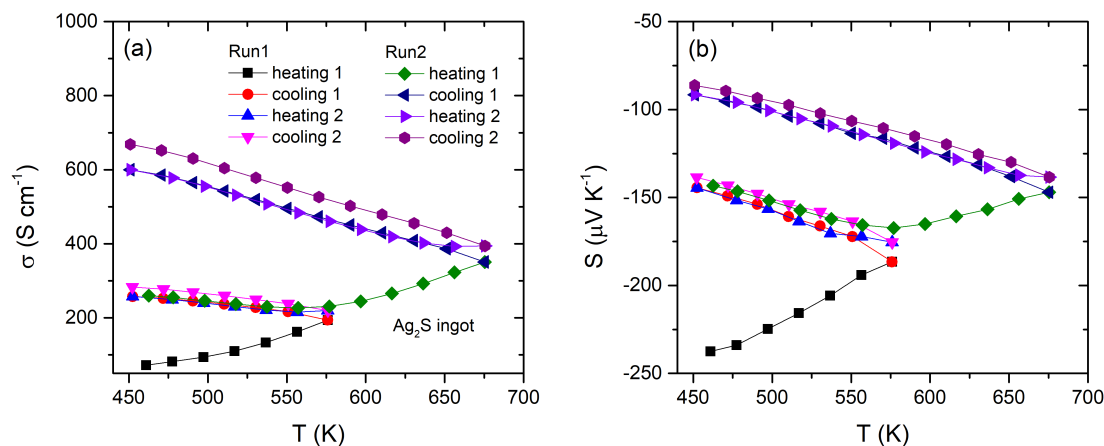


Figure 5.11: Thermal cycling effect on temperature dependent (a) electrical conductivity (σ), and (b) Seebeck coefficient (S) of Ag_2S ingot sample.

thermal cycles, the same phenomena persists. To see what would happen if the highest temperature during the successive thermal cycles is not changed, during run 4, we performed a second heating/cooling cycle. Interestingly, the heating - 2 curve followed the cooling - 1 up to the same temperature as during run 3. However, in the 3rd and 4th heating/cooling cycles during run 4, no further changes could be seen - i.e., the heating/cooling curves overlapped as expected. The temperature dependent σ data for the Ag_2S ingot sample is shown in Figure 5.11 which also show the similar memory effect upon multiple heating-cooling cycles. Seebeck coefficient of Ag_2S ingot sample is shown in Figure 5.11(b), demonstrating decreasing values with subsequent heating/cooling runs before attaining saturation. The correlation seen between the thermal history effect in σ and DSC scans suggested that this phenomenon is related to the presence of the metastable phase. In further discussions regarding the transport properties of Ag_2S samples, we will only present the final repeatable data from the end runs.

The back-scattered electron FESEM images of the ingot and cold-pressed bulk pellets are shown in Figure 5.12. As depicted by the red circled area, the secondary impurity phase is embedded in the matrix. Furthermore, the chemical mapping displayed in Figure 5.13 confirms that the impurity phase is primarily unreacted sulfur. This suggests that there is a

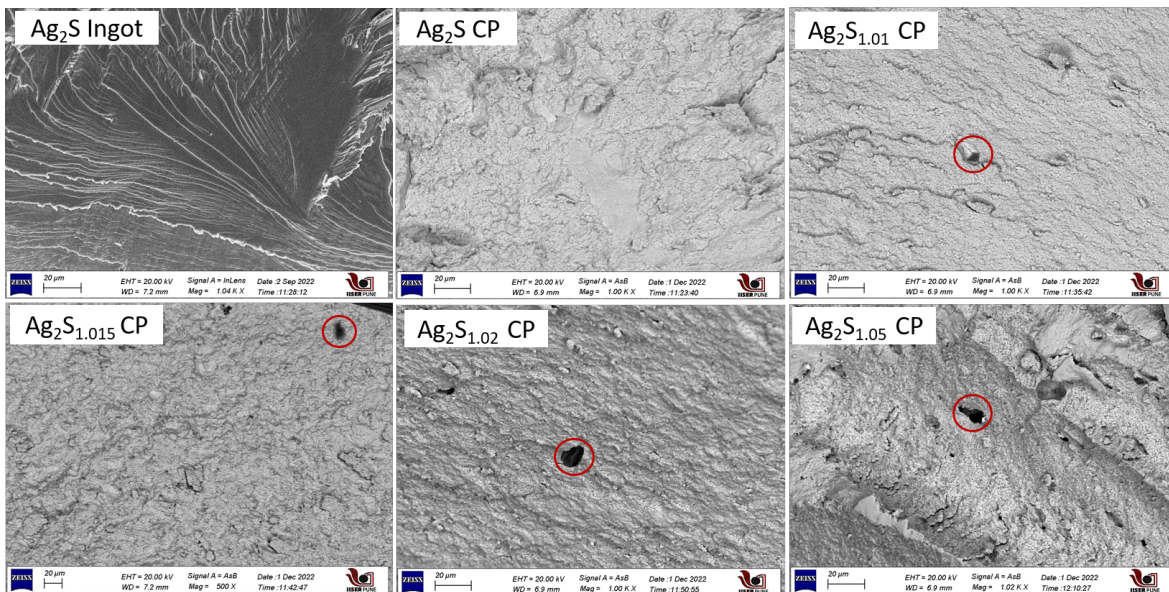


Figure 5.12: Morphology of freshly fractured piece from ingot and cold pressed pellets in back scattered electron detector mode.

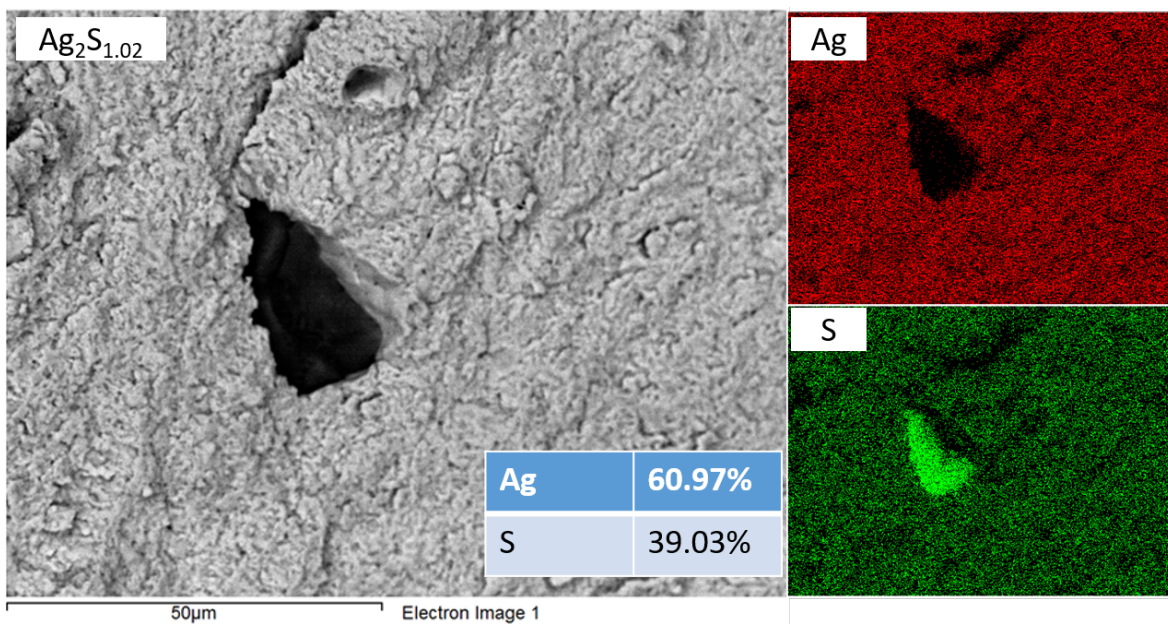


Figure 5.13: Chemical mapping of $\text{Ag}_2\text{S}_{1.02}$ CP pellet.

very low solubility limit of excess sulfur which is in agreement with the phase diagram of binary Ag_2S reported by Sharma et al. [206].

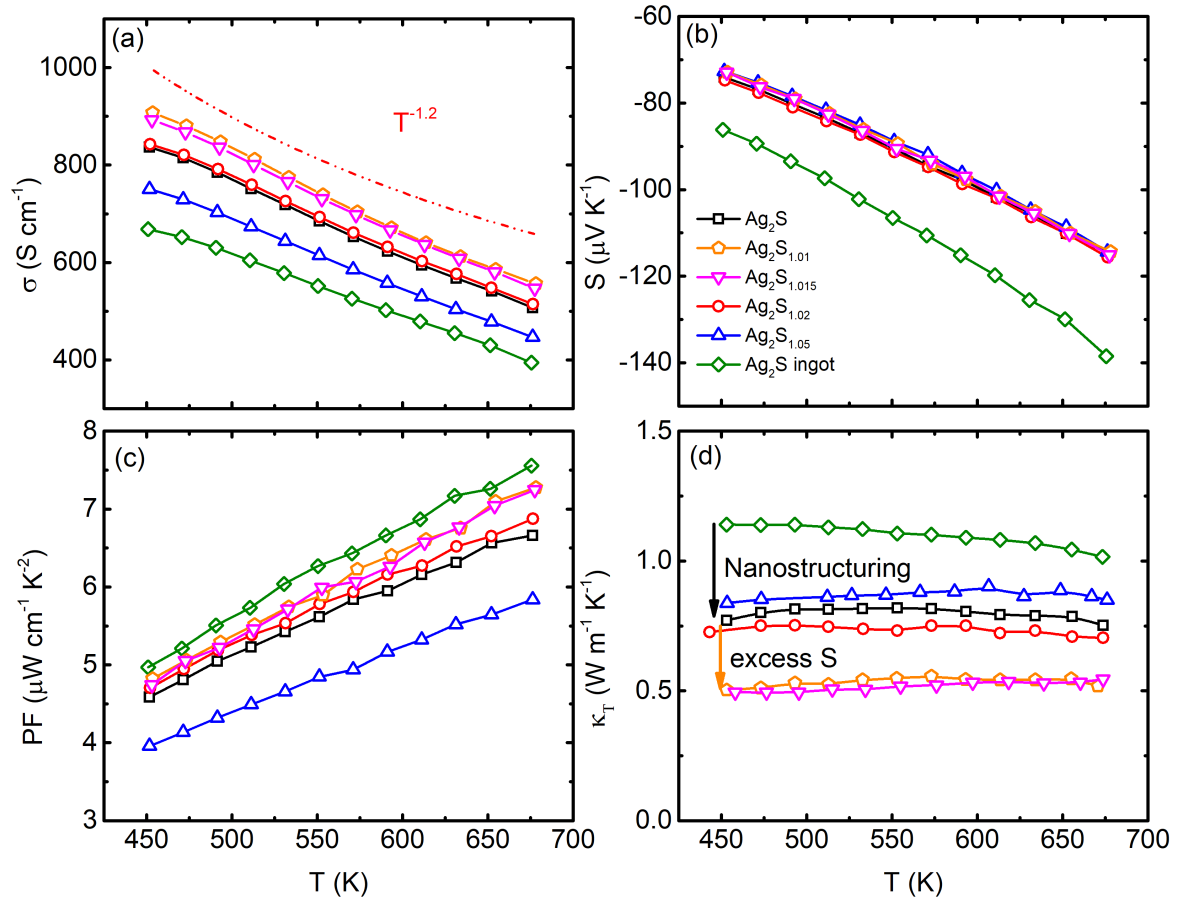


Figure 5.14: Temperature dependent (a) electrical conductivity (σ), (b) Seebeck coefficient (S), (c) power factor (PF), and (d) total thermal conductivity (κ_T).

5.4 Transport properties

The TE properties of all the samples investigated in this study are depicted in Figure 5.14, which displays the final repeatable runs between 450 K and 675 K. For comparison, the ingot samples data are also included. All samples exhibited a metal-like variation in electrical conductivity i.e., $d\sigma/dT < 0$ over the whole temperature range. The temperature dependence of σ indicates a mixed scattering mechanism of charge carriers with σ varying approximately as $T^{-1.2}$. There is negligible temperature dependence of the carrier concentration, as shown in Figure 5.15. The n_H value of approximately $2.5 \times 10^{19} \text{ cm}^{-3}$ in the α -phase is in good agreement with previous report [198]. Initially, the electrical conductivity increased from

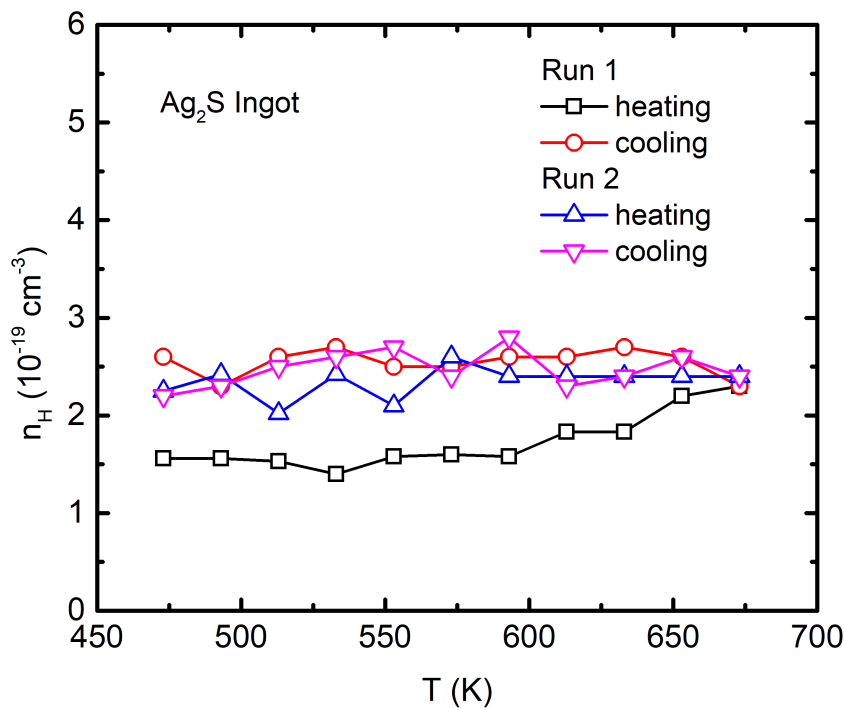


Figure 5.15: Temperature dependent carrier concentration of Ag_2S ingot sample.

840 S cm^{-1} to 900 S cm^{-1} at 450 K with a slight anion excess of up to 1.5%. However, as the anion concentration further increased, larger S precipitates formed and subsequently evaporated during heating (while measurement), resulting in the formation of pores that may have led to a decrease in σ . Moreover, it is worth mentioning that the Seebeck remain unaffected by anion excess, as evidenced from the overlapping Seebeck values observed for all the cold-pressed samples. Notably, the ingot sample exhibits the lowest electrical conductivity and consequently highest Seebeck coefficient, which can be attributed to its lower carrier concentration compared to the Ag_2S CP sample.

The ingot sample exhibited the highest PF values, ranging from $5 \mu\text{W cm}^{-1} \text{K}^{-2}$ at 450 K to $7.5 \mu\text{W cm}^{-1} \text{K}^{-2}$ at 670 K. With the exception of the 5% sulfur (S) excess sample, all CP samples displayed similar PF values, varying from $4.6 \mu\text{W cm}^{-1} \text{K}^{-2}$ at 450 K to $7 \mu\text{W cm}^{-1} \text{K}^{-2}$ at 670 K. The presence of excess sulfur (5% S) led to reduced PF values

due to poor electrical conductivity.

The total thermal conductivity (κ_T) depicted in Figure 5.14(d) demonstrates a glass-like temperature dependence. The CP samples exhibited a significant reduction in κ_T compared to the ingot, attributable to phonon scattering at the grain boundaries in our nanostructured cold-pressed pellets. Additionally, a slight excess of approximately 1% S resulted in a substantial suppression of κ_T from $0.76 \text{ W m}^{-1} \text{ K}^{-1}$ to approximately $0.5 \text{ W m}^{-1} \text{ K}^{-1}$ across the entire temperature range. The lowest κ_T values obtained in this study for slightly anion excess samples (1% and 1.5% sulfur excess) are comparable to those previously reported by Peng et al. [203] and Tuo et al. [123] in their ingot samples, which also exhibit similar temperature dependence. However, their ingot samples exhibited much lower electrical conductivity compared to samples in our study with a semiconducting temperature dependence which could be resulting from their first heating run where nearly 50% lower κ_T to its true value is observed. For example, see thermal cycling effect on thermal conductivity of our sample shown in Figure 5.16. Further, in our study, as the anion excess increased to 2% and 5%, κ_T increased and became comparable to that of the pristine sample. The exact reason behind this increase is not very clear but according to our HTXRD scans, there is no peak broadening observed in 2% and 5% S excess sample unlike 1% S excess sample.

The observed decrease in κ_T of 1% S excess sample can be understood from the broad peaks in HTXRD and broadened DSC transition peak due to the presence of equally high intensity of metastable phase. The presence of this metastable phase can result strain giving rise to peak broadening in HTXRD. Additionally, from HRTEM analysis of sample $\text{Ag}_2\text{S}_{1.01}$, we have found the multiple dislocation and stacking faults present along (014) plane which helps in reducing the κ_T , see Figure 5.17(d).

The temperature-dependent variation of zT is illustrated in Figure 5.18(a). Due to the combination of consistently high PF values and significantly reduced κ_T , the samples with slight anion excess (1% and 1.5%) exhibited elevated zT values: 0.4 at 450 K and 0.9 at 670 K. For comparison, we have included the zT variation reported by Peng et al. [203] in their Ag_2S ingot sample, which revealed an overall 80% increase in the highest zT value.

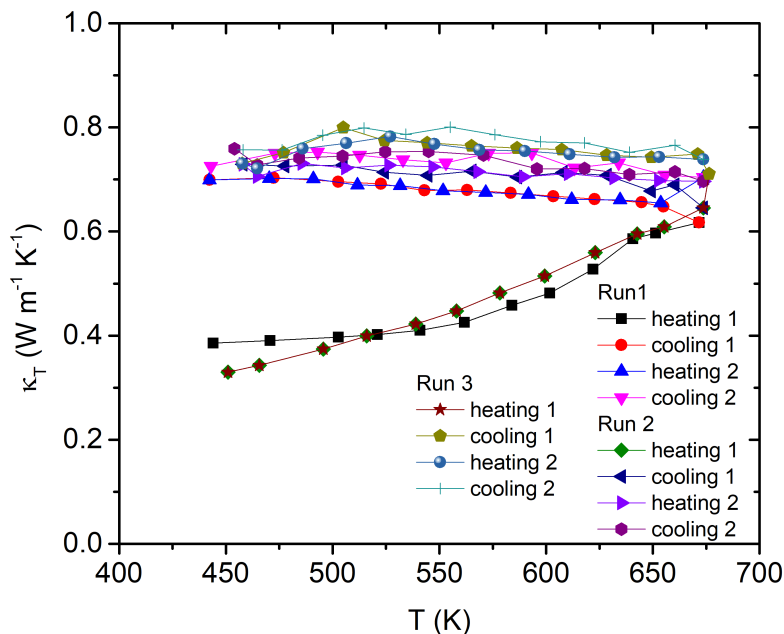


Figure 5.16: Effect of thermal cycling on thermal conductivity (κ_T) of $\text{Ag}_2\text{S}_{1.02}$ sample.

The comparative zT plot clearly indicates that the $\text{Ag}_2\text{S}_{1.01}$ sample outperforms others within the temperature range of 450 K to 670 K. Its superior thermoelectric performance, coupled with its environmentally friendly characteristics, makes it an excellent candidate for thermoelectric applications. Furthermore, the zT value can be further enhanced through appropriate doping, similar to other sulfide materials based on Pb and Cu.

We have checked the sample's stability under a unidirectional electric field for 200 minutes, as shown in Figure 5.19. Unlike Ag_2Te , which was discussed in Chapter 3, there are stability issues associated with the superionic Ag_2S thermoelectric material. The resistivity keeps decreasing with an increase in the measurement time. It is possible that the easy migration of Ag ions in Ag_2S occurs due to its larger ionic character of bonding compared to Ag_2Te . Therefore, additional efforts may be required to achieve stability under the applied field, such as using ion barriers around the grains or introducing appropriate doping elements, like Fe in the case of Cu_2S , to increase the critical voltage. [167]

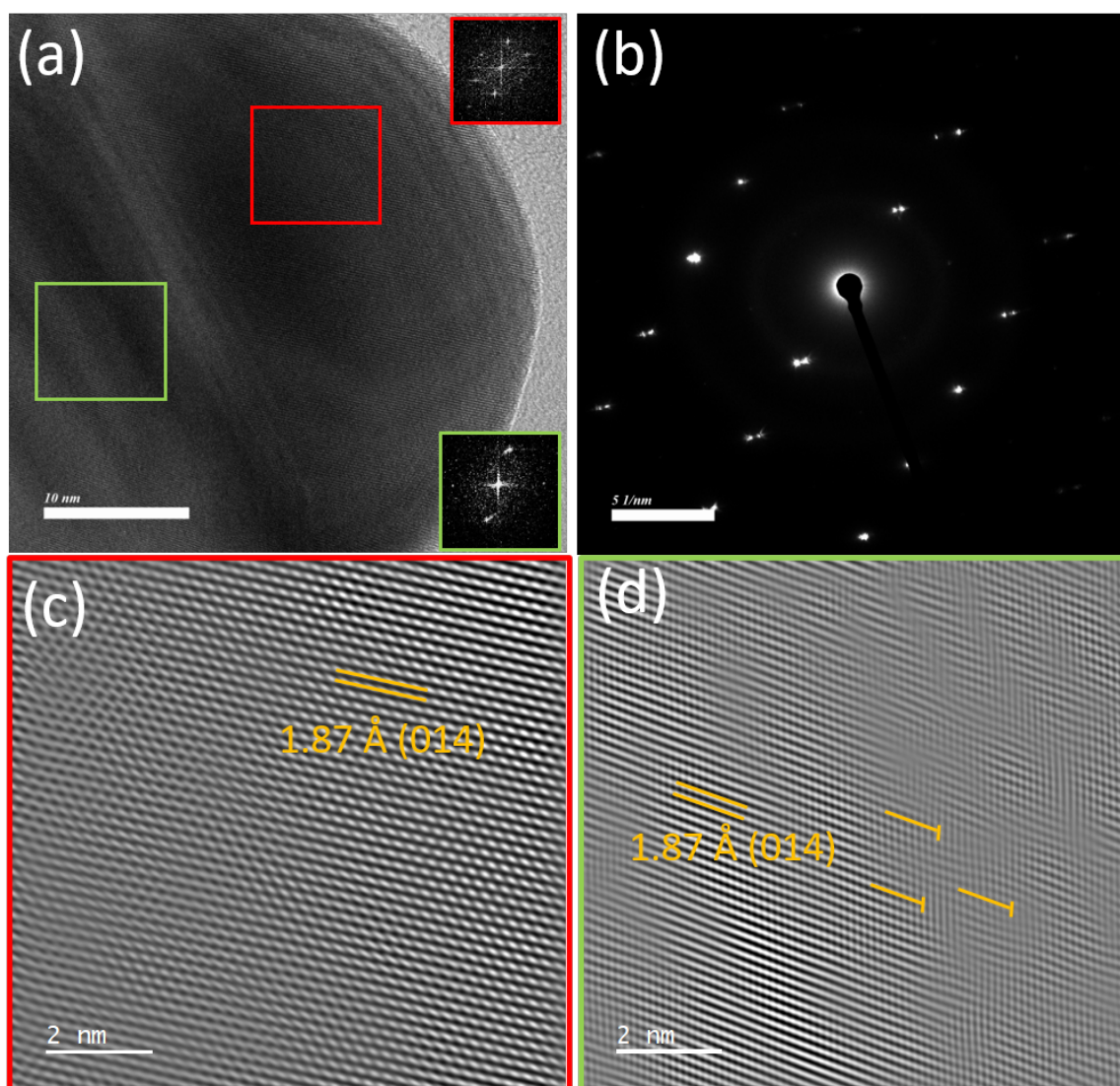


Figure 5.17: (a) HRTEM image at 10 nm and insets are showing the FFT taken over red and green marked rectangular areas, (b) shows the selected area electron diffraction (SAED) of HRTEM image shown (a) depicting presence of twinning in nanoparticle, (c) is IFFT image of red rectangular area marked in (a) and (d) shows the IFFT image on green marked rectangular area of (a).

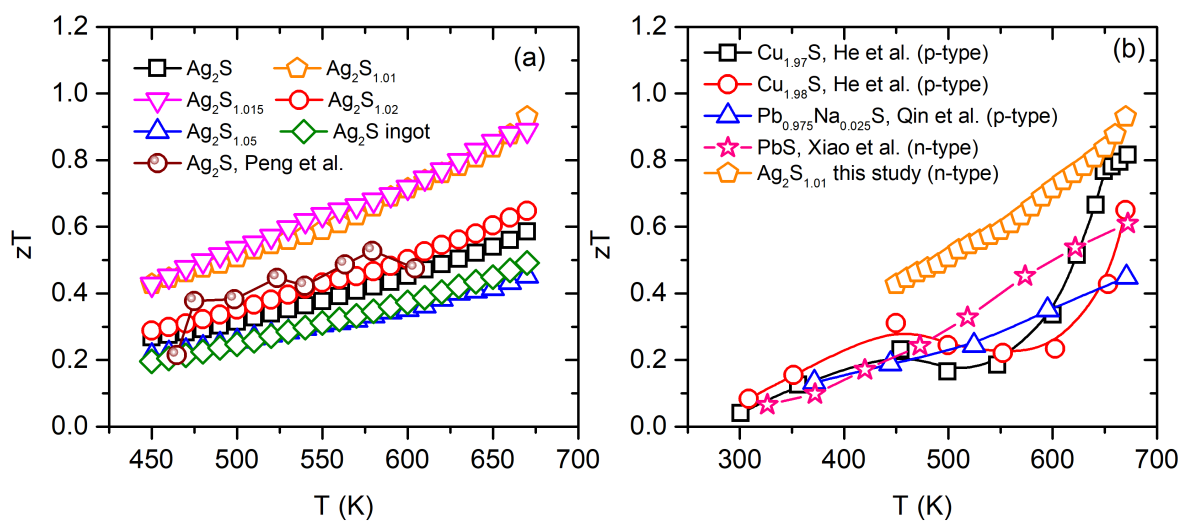


Figure 5.18: (a) Temperature dependent zT of $Ag_2S_{1+\delta}$ samples, and (b) comparison of zT of our outperforming Ag_2S sample and some reported n and p-type sulfides in previous studies by He et al. [23], Qin et al. [24] and Xiao et al. [25].

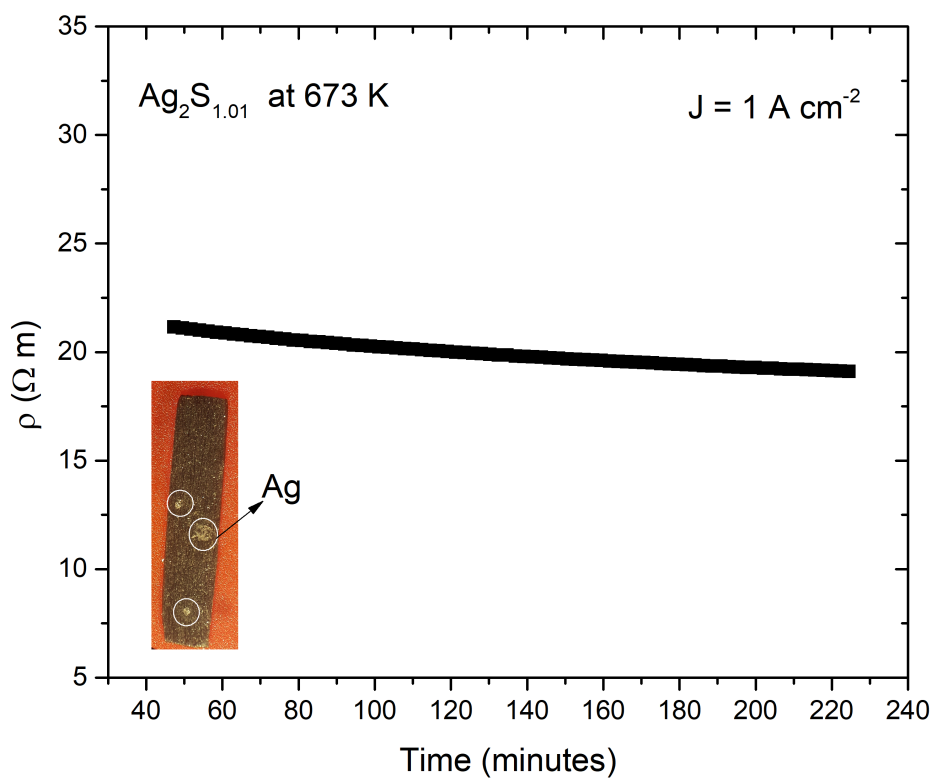


Figure 5.19: Electrical resistivity under $1 A cm^{-2}$ current density measured for continuous 200 minutes.

5.5 Summary and Conclusion

We have synthesized a series of $\text{Ag}_2\text{S}_{1+x}$ ($x = 0, 0.01, 0.015, 0.02, \text{ and } 0.05$) samples by using an all room temperature synthesis method for the first time. Our detailed DSC analysis and resistivity thermal cycling effect, sheds light on puzzling metallic and semiconducting behavior of Ag_2S . We have obtained the substantially low thermal conductivity values in our hand grinded and cold-pressed sample of pristine Ag_2S compared to the ingot sample. Our CP sample showed 30% decrement compared to the ingot sample due to nanostructuring which was further 35% decreased in anion excess sample. However, there was no significant decrease observed in PF values for both CP and ingot samples. From our detailed DSC thermal cycling study, we expect the ultra-low thermal conductivity in S excess samples (1%, and 1.5%) is attributed to the stabilization of metastable phase in equally high proportion to that of main semiconducting phase creating large strain at their interfaces. Our high temperature XRD confirmed the peak broadening in 1% S excess sample. Hence, as a consequence of largely suppressed κ and maintained high PF values, our 1% and 1.5% S excess samples showed the high zT value of 0.9 at 670 K which is highest reported in this range of temperature for any sulfide material.

Chapter 6

Development of nanostructured bulk SnTe with enhanced thermoelectric properties

6.1 Introduction and Motivation

The PbTe-derived thermoelectric materials are known for their high zT and dependable performance in the med-temperature range from 600 K to 900 K [75, 201, 207, 208]. PbTe has a cubic NaCl-type structure. The valence band of PbTe consists of a 4-fold degenerate light-hole (lh) band at the L-point where the valence band maxima (VBM) is located, and a 12-fold degenerate heavy-hole (hh) band at the Σ -point of the Brillouin zone, a few $k_B T$ below the VBM. The bands at L and Σ points tend to converge, i.e., the energy difference, $\Delta E_{L\Sigma}$, between them tend to decrease with increasing temperature giving rise to a high thermopower [75, 142, 209]. Due to heavy constituent elements and resulting large lattice anharmonicity, PbTe and its alloys also show an intrinsically low lattice thermal conductivity [75]. All these factors are highly conducive to obtaining a high zT . Indeed, in PbTe-based alloys, high zT values, surpassing 1, are reported in the mid-temperature range [26]. However, the toxicity of Pb severely limits the commercial usage of Pb-based alloys. Thus, a lead-free substitute

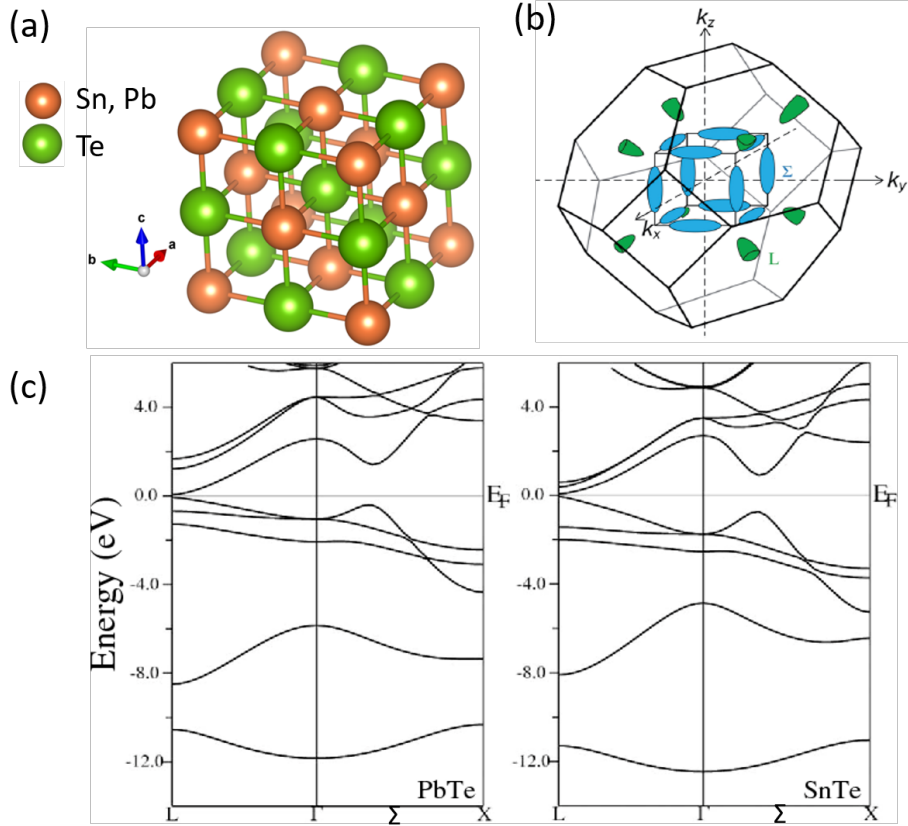


Figure 6.1: (a) Crystal structure of SnTe/PbTe, (b) Brillouin zone for cubic SnTe or PbTe showing 8 half hole pockets at low symmetry L point resulting 4-fold band degeneracy and 12 hole pockets along Σ direction giving rise to 12-fold band degeneracy (adapted from Ref [26]), (c) electronic band structure of PbTe and SnTe (adapted from Ref. [27]).

of PbTe with a comparably high zT is required.

In this regard, the environmentally friendly SnTe with an analogous crystal structure has garnered a great deal of interest recently (Figure 6.1). The valence band structure of SnTe [209] is similar to that of PbTe; however, the band gap (E_g) of SnTe (0.18 eV) is smaller than for PbTe (0.32 eV), and the energy offset between the lh and hh bands higher ($\Delta E_{L\Sigma} = 0.35$ eV as opposed to 0.15 eV in PbTe). While the smaller band gap induces bipolarity, the higher offset ($\Delta E_{L\Sigma}$) prevents the hh carriers from participating in the transport. Moreover, SnTe has an intrinsically high concentration of Sn vacancies, resulting in p -type carriers with carrier density ($n \sim 10^{20} - 10^{21} \text{ cm}^{-3}$), about an order of magnitude or so higher than what is desired. This not only affects the Seebeck coefficient of SnTe adversely but also enhances

the κ_e contribution, which is undesirable given that κ_l of SnTe is already high compared to that of PbTe. The intense research efforts of the last decade have made remarkable progress in ironing out many of these issues as summarized in the next paragraph. To get more insight into these issues and the progress made until the year 2020, the readers can refer to the excellent reviews by Li *et al.* [210] and Chen *et al.* [26].

In some previous studies, it has been shown that a slight Sn excess, i.e., using Sn:Te $\equiv 1+\delta : 1$ instead of $1 : 1$, can help in suppress the formation of Sn vacancies [211]. The optimized value of δ has been shown to be around 0.03. The composition $\text{Sn}_{1.03}\text{Te}$ is accordingly called the ‘self-compensated’ SnTe, which has a high zT value of 0.6 at 873 [211]. In recent years, to achieve further higher values of zT, a diverse range of doping experiments have been tried successfully. These include doping with Cd [211], Hg [212], Ca [213], Mn [214,215], Mg [216], Pb [217], Ag [34,218], Ga [219], In [139,211], Yb [220], Gd [221], etc.; or co-doping SnTe with Mn–Sb [222], V–Sb [223], Cu–Sb [224], Re–Sb [225], Ge–Sb [226], Mn–Bi [227], Cd–Bi [228], Ge–As [229], Ag–Cu [230], Ag–Cd [231], Ag–Gd [232], Ag–La [231], Ag–In–I [233], Ag–Y [33], Li–Ce [234], Cd–Se [235,236], In–Bi [237], Ca–I (via CaI_2) [238], Cd–Se [236], Cd–In [239,240], Mn–In [241], Mg–In [242], Pd–In [243], Y–Cu [244], Sb–Se [126], Se–S [245], etc.; or via alloying with AgSbTe_2 [211], AgSbSe_2 [246], AgInTe_2 [29], and AgBiTe_2 [247], etc.; or with AgBiTe_2 and Mn [248], AgSnSe_2 –PbTe [249], BiBr_3 and Mn [250], $\text{Ag}_{0.5}\text{Bi}_{0.5}\text{Se}$ and ZnO [251], AgCl and In [252]; or doping with $\text{Cu}_{1.5}\text{Te}$ to form SnTe– Cu_2SnTe_3 nanocomposites [253]; or through Te-deficiency which results in the formation of Te–nanoinclusions [254]. While chemical doping has proven useful in controlling n , E_g and $\Delta E_{L\Sigma}$, which improves the PF; concerted efforts on simultaneously lowering the thermal conductivity are scarce. strategies to lower κ_l of SnTe includes introduction of nano-scale features, such as endotaxial nanodots, point defect scattering, grain boundary engineering employing CdTe coating, and nanoprecipitation of secondary phases or nanoinclusions [29,254–257]. Nanoprecipitation involves the formation of nanometer-sized particles within the host matrix which scatters phonons with long mean free path, leading to a reduction in thermal conductivity. A very

significant effect of nanoprecipitation was observed in reducing the lattice thermal conductivity of SnTe samples containing CdS and Cu₂Te precipitates [211, 258]. In a recent paper, CdTe-coated (Sn, In)Te grains, where In-doping creates resonant levels while the CdTe coating enhances the phonon scattering cross-section by several orders of magnitude through the acoustic impedance matching between the SnTe (grain) and CdTe (grain-boundary). This enhances the PF and lowers κ substantially leading to a very high zT of 1.9 near 900 K [257]. While this is really state-of-the-art, due to the use of Cd the toxicity issue remains; additionally, the method used in the sample processing is relatively complex from the point of view of scalability.

In this study, we report a simpler and very effective grain-boundary engineering technique leading to a substantial reduction in the thermal conductivity of SnTe. We demonstrate the growth of SnTe nanoparticles at the grain boundaries of SnTe cold-pressed pellets upon sintering at 700°C. The cold-pressed pellets are obtained simply by hand-grinding the solid-state melted SnTe ingots using an agate-mortar pestle. Due to the nanoprecipitation of SnTe at the grain boundaries, the thermal conductivity of our furnace sintered SnTe samples is among the lowest ever reported to the best of our knowledge, more specifically $6 \pm 0.5 \text{ W m}^{-1} \text{ K}^{-1}$ at 300 K and between 2 to 3 $\text{W m}^{-1} \text{ K}^{-1}$ near 825 K. This is almost 15% lower compared to the thermal conductivity of as-melted SnTe at 300 K despite their overlapping electrical conductivities. Not only is the thermal conductivity low, the thermopower of our sintered sample also surpassed the thermopower of the ingot SnTe quite substantially due to its higher mobility and lower carrier concentration. As a result, the zT of our sintered SnTe samples (0.7 near 850 K) exceeds that of the ingot SnTe by almost 75%. Next, we extend this strategy to Ag-doped SnTe as in some previous studies, Ag-doping has been shown to enhance the zT of SnTe through band convergence, carrier optimization, and suppression of bipolarity [34, 218]. We show that in the SnAg_{0.03}Te, κ further decreases to $4.2 \pm 0.5 \text{ W m}^{-1} \text{ K}^{-1}$ at 300 K and $< 2 \text{ W m}^{-1} \text{ K}^{-1}$ near 825 K. These values are reduced by $\sim 30\% - 40\%$ over the whole temperature range with respect to the samples of the same composition prepared by solid-state melting. The resulting improvement in zT with respect to the

best Ag-doped samples in literature is about 35%. The ease with which bulk-nanostructured SnTe pellets can be fabricated in our method marks a significant development and should pave the way for bulk-nanostructured SnTe production. This strategy when combined with other dopants, such as, In or Mn may further improve the zT of bulk-naonstructured SnTe.

6.2 Experimental Details

Samples $\text{Sn}_{1.03-x}\text{Ag}_x\text{Te}$ ($x = 0, 0.03, 0.06, \text{ and } 0.09$) were prepared using Sn (Sigma Aldrich, 99.999%), Te (Alfa Aesar, 99.99%), and Ag (Sigma Aldrich, >99.9%) shots, taken in stoichiometric ratio in an alumina crucible that was flame sealed under high a vacuum in a preheated quartz tube. The precursor elements were weighed inside an Ar-filled glove box to avoid oxidation. The sealed ampoule was placed vertically in a box furnace and heated to 1173 K in 13 h and held at this temperature for 12 h. The furnace was then cooled to room temperature over a period of 13 h. This resulted in the ingots. Before grounding these ingots, they were cut using a low-speed diamond-coated cutter to prepare 6×6 square and $8 \times 3 \times 2$ rectangular samples for measuring thermal and electronic transport properties respectively. The remaining pieces of these ingots were ground to fine powders using an agate mortar-pestle. Subsequently, 8mm pellets were prepared by cold-pressing these powders using a KBr press die set. These pellets were then vacuum-sealed in preheated quartz ampoules and sintered in a box furnace that was heated to 973 K over a period of 7 h and held at this temperature for 24 h. The furnace was then cooled to room temperature over a period of 7 h. The sample with the highest Ag doping ($x = 0.09$) was sintered at 823 K. The sintered pellets were then well characterized and their thermoelectric properties investigated. We also prepared a bulk $\text{Sn}_{1.03}\text{Te}$ sample by hot press sintering (HPS). The HPS was performed on the powder obtained from grounding the leftover pieces of ingot at 773 K under 45MPa pressure for 5 minutes, resulting in a sample density of 99%. These details along with sample density for other samples are summarized in table 6.2.

For phase identification and characterization, powder x-ray diffraction was performed using a Bruker D8 Advance with a Cu K_α source. The microstructure of the bulk samples

Table 6.1: Synthesis details and sample density (ρ_{exp}/ρ_{th}) in % for samples $\text{Sn}_{1.03-x}\text{Ag}_x\text{Te}$ ($x = 0, 0.03, 0.06, \text{ and } 0.09$).

Ingot Samples (I)			
x	synthesis temperature (K)	sintering temperature (K)	density (%)
0	1173	-	93
0.03	1173	-	92
0.06	1173	-	92
0.09	1173	-	93
Hot Press Sintering (HPS)			
0	1173	773	99
Furnace Sintered (FS) Pellets			
0	1173	973	93
0.03	1173	973	93
0.06	1173	973	94
0.09	1173	823	94

was analyzed using a field-effect scanning electron microscope (FESEM) (Ultra Zeiss Plus) equipped with an energy-dispersive spectroscopy (EDS) detector for compositional analysis. Transmission electron microscopy (JEOL JEM 2200FS 200 keV) was performed on the dispersed powders obtained by grinding the ingot or sintered pellet, after drop-casting on an amorphous carbon coated support Cu-mesh grid.

To measure the transport properties of the synthesized samples, an LSR3 setup was used for the simultaneous measurement of electrical conductivity (σ) and thermopower (S). High-temperature Hall measurements were performed using an automated home-built setup by sweeping the magnetic field from +1T to -1T to estimate the temperature-dependent carrier concentration in our samples. Linseis LFA1000 set-up was used to measure the thermal diffusivity (D) of the samples. The thermal conductivity was estimated using the equation $\kappa = \rho DC_P$, where ρ and C_P stand for sample density and specific heat at constant pressure. The sample density was estimated using the formula $\rho = W/V$, by taking the weight (W) and volume (V) of the specimen. A constant value from Dulong Petit's limit of $C_P = 3nR$ was used for the specific heat.

6.3 Results and Discussion

6.3.1 Characterization

Figure 6.2(a) displays the powder x-ray diffraction of various $\text{Sn}_{1.03}\text{Te}$ samples prepared here, namely, ingot (I), HPS, and furnace sintered (FS). All three samples exhibit XRD peaks that are well-indexed using the Fm-3m space group reported in the literature [259]. However, significant peak broadening was observed for the FS sample as compared to the HPS or I samples. To understand the reason behind this, we analyzed the microstructure of our samples using the FESEM. As shown in Figure 6.2 (c), the morphology of the FS sample differed significantly from those of the ingot and HPS samples. The FS bulk sample contained grains decorated with numerous nanoparticles, whereas only a few nanoparticles were observed at the grain boundary of the HPS sample and none in the case of the ingot

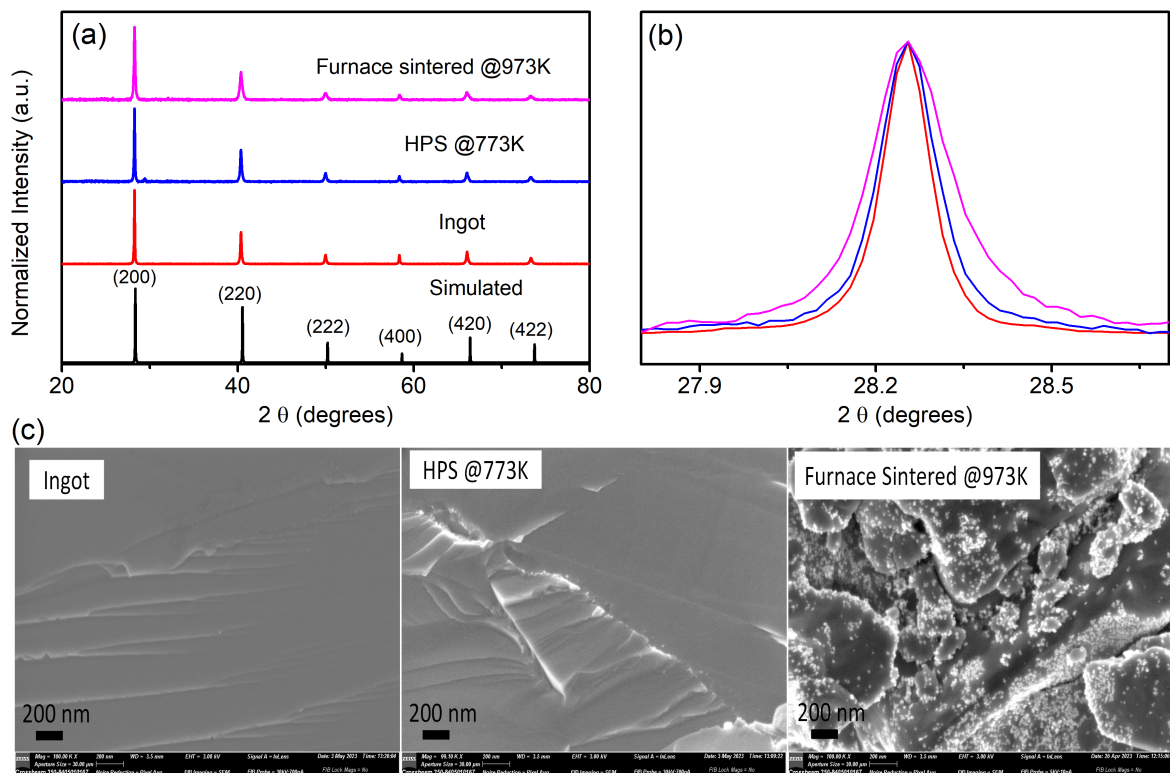


Figure 6.2: (a) Powder x-ray diffraction patterns for Sn_{1.03}Te I, HPS and FS samples, (b) shows the broadening of 200 peak after sintering the ingot powder using HPS at 773 K and furnace at 973 K, and (c) shows the morphology variation at 200 nm for three I, HPS and FS Sn_{1.03}Te samples.

sample. The formation of the nanoparticles during sintering is presumably the reason behind XRD peak broadening in the case of sample FS.

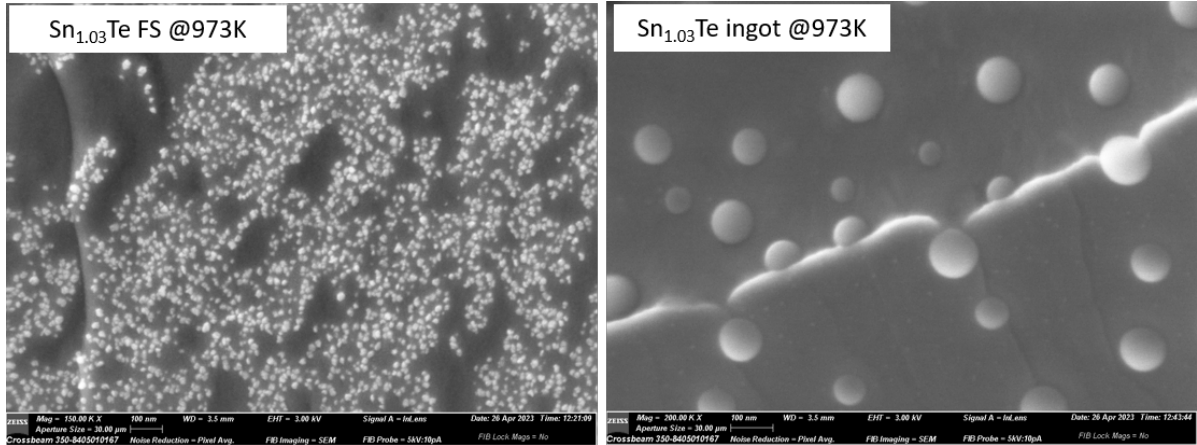


Figure 6.3: Microstructure comparison of sintered pellet and ingot Sn_{1.03}Te sample.

To confirm whether the formation of nanoparticles was solely due to furnace sintering at 973 K, we sintered an ingot piece using a similar temperature profile. The morphological comparison of both samples after sintering is presented in Figure 6.3. Interestingly, prolonged sintering of the ingot also resulted in the appearance of nanoparticles, albeit fewer in numbers compared to the FS sample. This indicates that the nanoparticles at the grain boundaries appear during the sintering process. Since, the FS sample was well grounded prior to cold pressing and sintering, it has smaller grains resulting into the appearance of a larger number of nanoparticles compared to the ingot sample where the grain-size ranges from 1 μm to 10 μm . Thus, a possible reason behind this unique morphology of FS sample appears to be the sintering process. In some cases, it is thermodynamically favorable for the vacancies to migrate towards the surface of the grains, forming nanoparticles that decorate the micro-grains, resulting in the formation of nanoparticle-decorated micro-grains. This phenomenon is well-known to occur in GeTe, where morphology can be easily manipulated by varying the percentage of vacancies at the Ge site and changing the sintering temperature [260]. However, its appearance in SnTe is reported here for the first time. This makes SnTe an interesting material to study the phenomenon of vacancy migration in addition to

the known GeTe. However, due to the exorbitant cost of Ge, the discovery of SnTe showing vacancy migration is important.

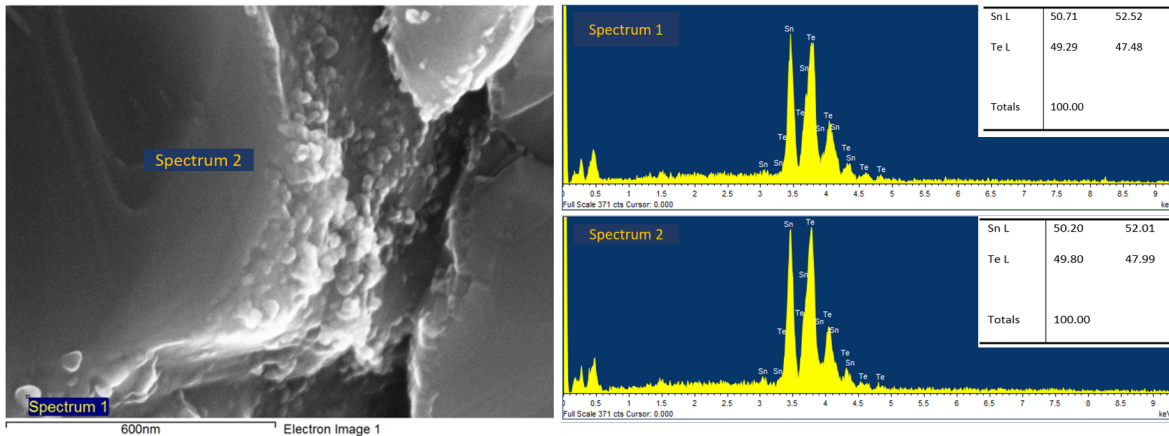


Figure 6.4: EDX analysis for determining the chemical composition of nanoparticles and bigger micrometer grains in Sn_{1.03}Te FS sample.

The chemical composition of nanoparticles and the underlying matrix was analyzed and is shown in Figure 6.4. The EDX result show similar composition for the two. The absence of any extra peak in the XRD and similarity of the EDX results confirm that the nanoparticles have the same structure and composition as bulk SnTe.

Figure 6.5 (a) displays the powder x-ray diffraction results of Sn_{1.03}Te ingot and FS samples. A zoomed-in view of the region between 30° to 33° (inset) indicates the presence of extra peaks of unreacted Sn at approximately 30.5° and 32°. Figure 6.5 (b) depicts the presence of slight Sn excess (marked with red circles) in the self-compensated SnTe sintered pellet. This was further confirmed by chemical mapping. Interestingly, upon 3% Ag doping, the Sn peaks disappeared. The powder XRD of the Ag doped is also shown in Figure 6.5(a).

Figure 6.6 (a and b) shows the x-ray powder diffraction results of all the synthesized samples with varying Ag doping. Again, the most striking difference between the x-ray diffraction patterns of the ingot [Figure 6.6(a)] and FS [Figure 6.6(a)] samples is the peak broadening discussed earlier. As shown in Figure 6.6 (c), the FWHM of the 200 peak is significantly higher for the FS samples compared to the ingots. This broadening of the diffraction is due to the nanoparticle formation as discussed earlier for the undoped Sn_{1.03}Te

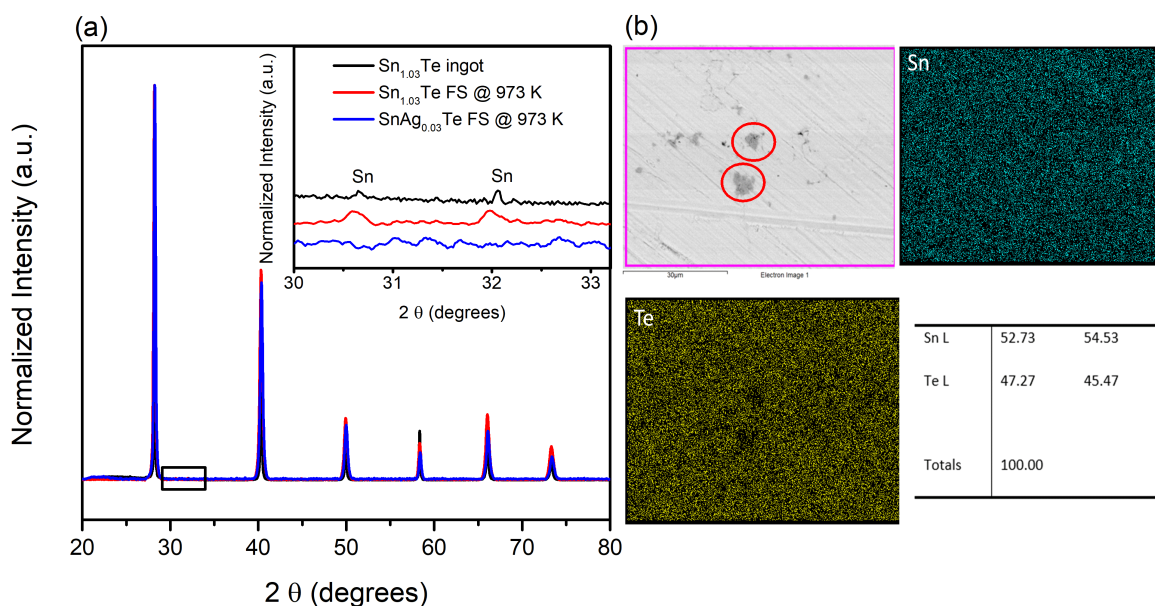


Figure 6.5: (a) Powder x-ray diffraction patterns for Sn_{1.03}Te ingot and sintered pellet samples, (b) the chemical mapping .

samples. The only exception to this is $x = 0.09$ sample where the FWHM of the FS sample is comparable to its ingot counterpart. This may suggest that incorporation of Ag beyond a certain level ($x = 0.06$) prevents the nanoparticle formation.

The variation of lattice parameters with Ag doping is shown in Figure 6.6 (d). The lattice parameter decreased with increasing Ag doping due to the smaller cation radius of Ag⁺ compared to Sn²⁺ [261]. In literature, it has been argued that Ag doping increases the Sn vacancies, resulting in a reduced lattice constant [31, 34]. However, the size mismatch between Ag⁺ and Sn²⁺ provides a natural explanation for the observed decreasing trend with increasing Ag-doping.

Figure 6.7 shows the morphology of freshly fractured surfaces from two representative ingot samples. These images indicate a highly crystalline morphology with micrometer-sized grains. In contrast, the morphology of FS samples in Fig 6.8 has changed significantly due to the presence of a large number of nanoparticles around the micron sized grains. From a visual inspection it is evident that the number of nanoparticles decreases and their size increases with increasing x . Nanoparticles of much larger size are found in the $x=0.09$ sample which

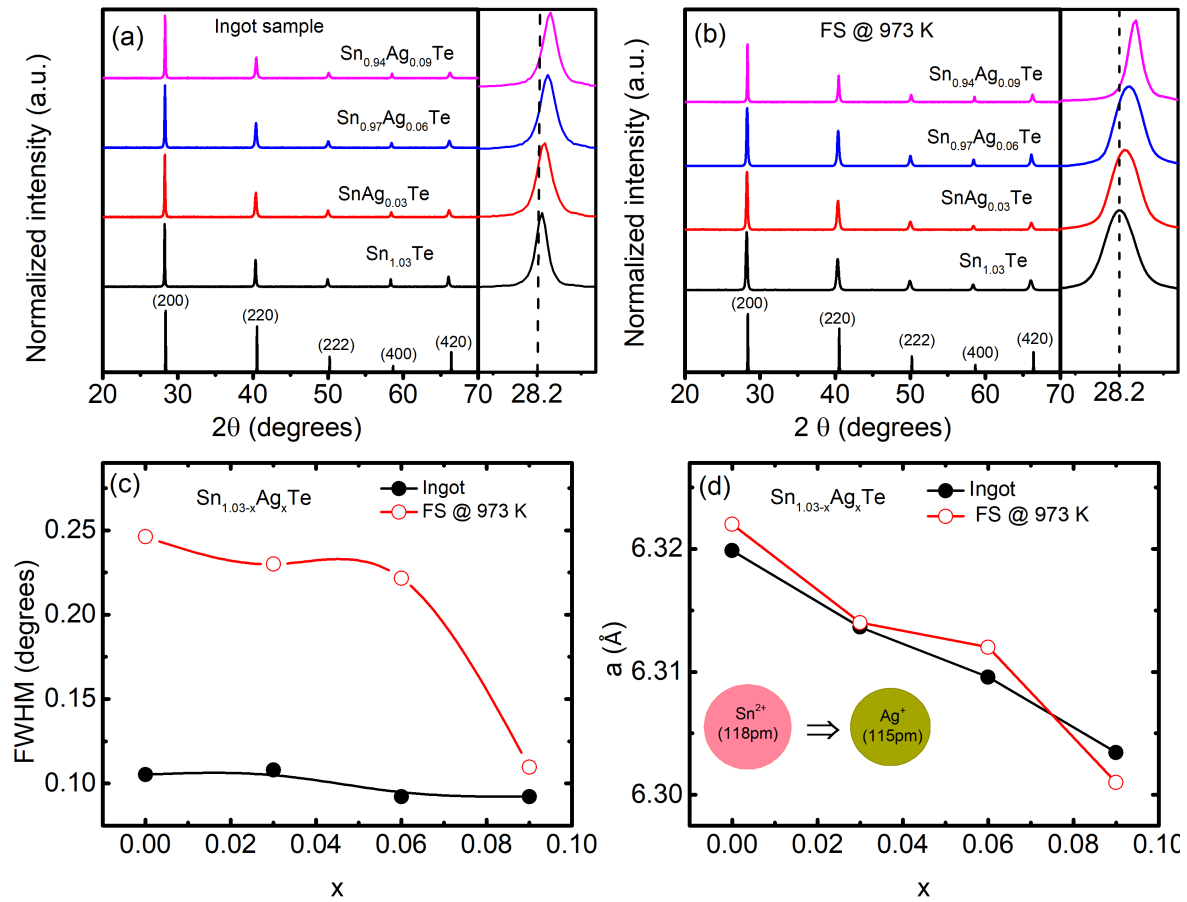


Figure 6.6: (a) Powder x-ray diffraction patterns for ingots, and (b) for sintered pellets (c, and d) represents the variation of full width at half maxima (FWHM) and lattice parameters of $\text{Sn}_{1.03-x}\text{Ag}_x\text{Te}$ ($x = 0, 0.03, 0.06$ and 0.09) ingot and sintered pellet samples.

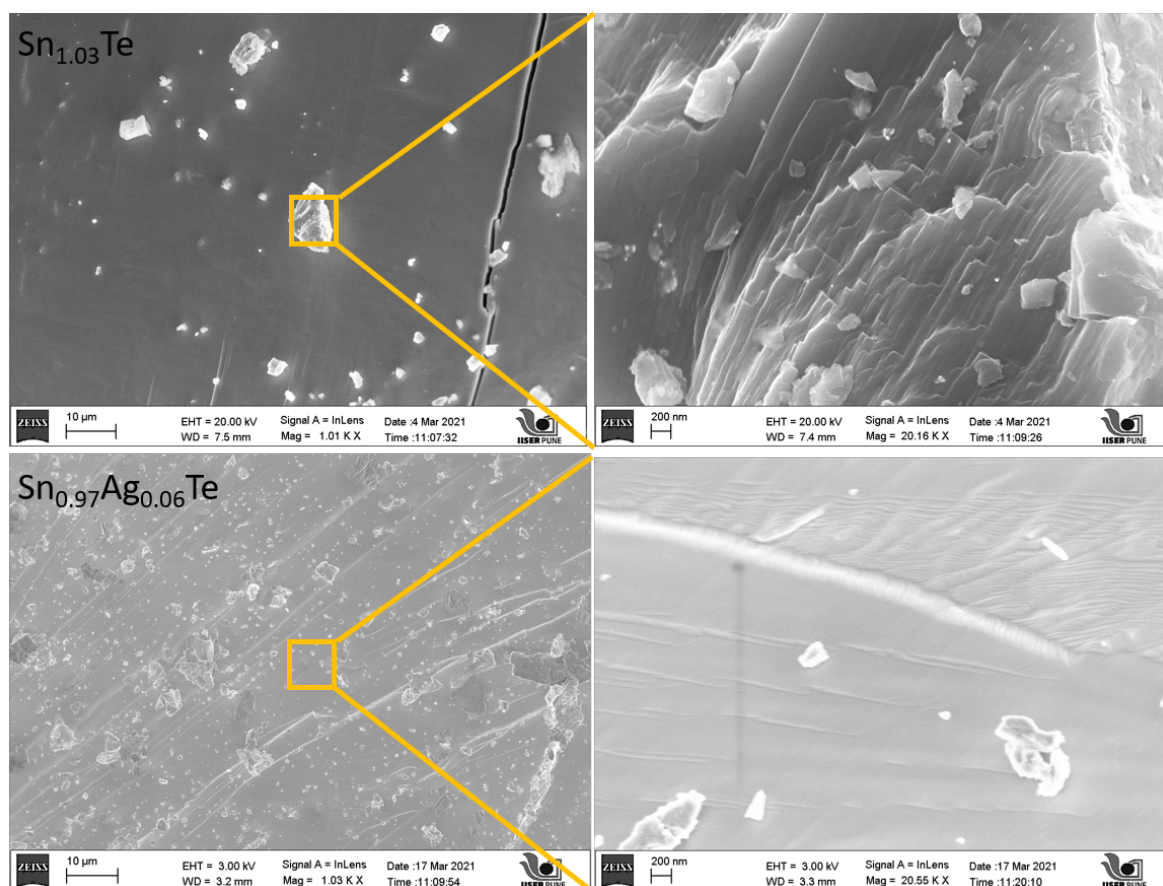


Figure 6.7: Morphology of freshly broken surfaces from $\text{Sn}_{1.03-x}\text{Ag}_x\text{Te}$ ($x = 0, 0.03, 0.06$ and 0.09) ingot samples.

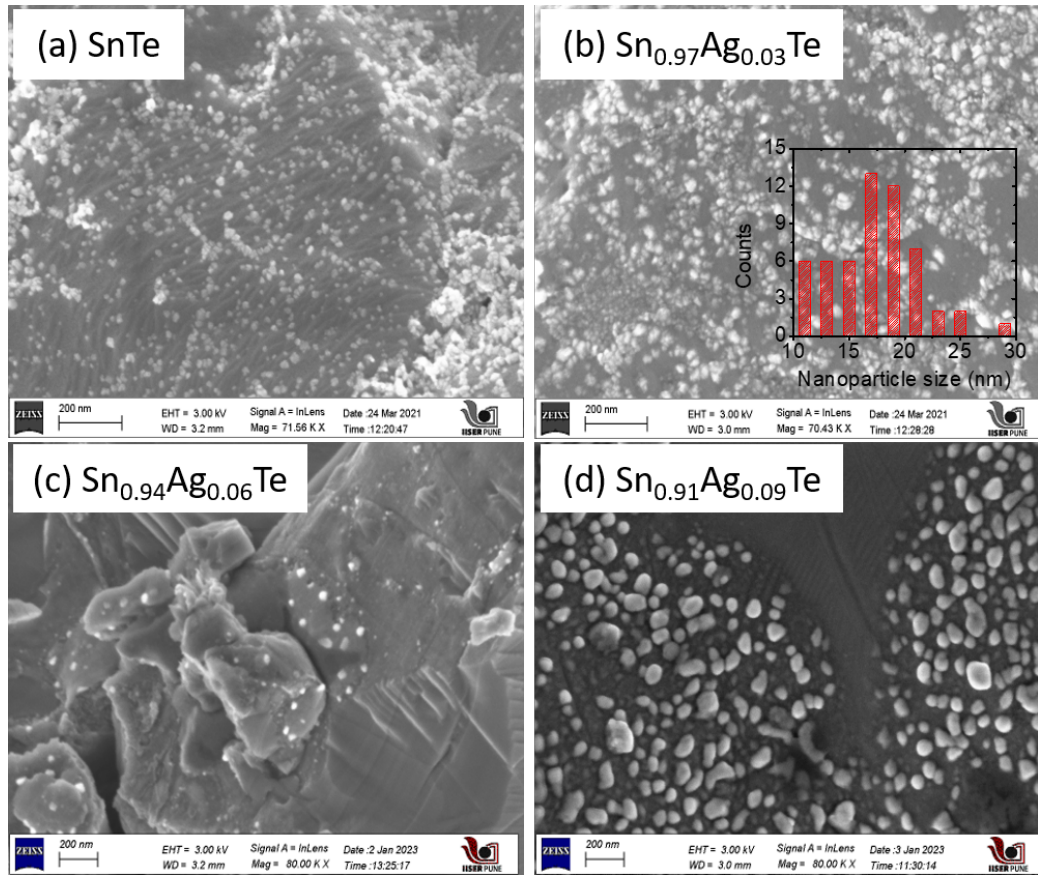


Figure 6.8: Morphology of freshly broken surfaces from $\text{Sn}_{1.03-x}\text{Ag}_x\text{Te}$ ($x = 0, 0.03, 0.06$ and 0.09) sintered pellet samples.

explains the variation of FWHM FS samples in Figure 6.6(c).

The chemical mapping of one of the representative FS samples, $\text{Sn}_{0.97}\text{Ag}_{0.06}\text{Te}$, shown in Figure 6.9, confirms the absence of Sn precipitation of any impurity phase.

6.3.2 TE properties of $\text{Sn}_{1.03}\text{Te}$

Figure 6.10 illustrates the thermoelectric properties of our $\text{Sn}_{1.03}\text{Te}$ I, HPS, and FS samples, which are compared with the previously reported results for $\text{Sn}_{1.03}\text{Te}$ ingot samples by Pathak et al [28]. Remarkably, all samples exhibited equally high electrical conductivity (σ), close to $6 \times 10^3 \text{ S cm}^{-1}$ at 300 K. In comparison, PbTe has a conductivity of 200 S cm^{-1} [6]. The higher conductivity of SnTe can be attributed to the high carrier concentration generated by the intrinsic Sn vacancies.

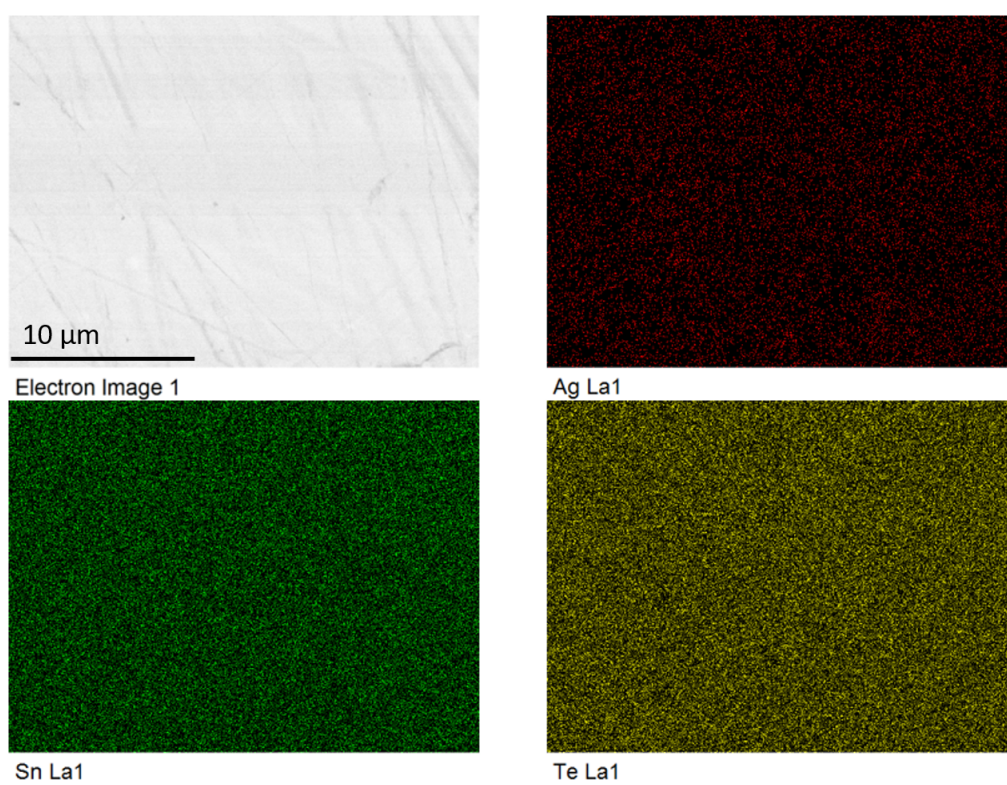


Figure 6.9: Chemical mapping of $\text{Sn}_{0.97}\text{Ag}_{0.06}\text{Te}$ sample.

Despite being a semiconductor, the electrical conductivity (σ) of SnTe decreases with increasing temperature, exhibiting metal-like behavior, as previously reported. Wu et al. [255] attributed this to the combined effect of decrease in the hole carrier concentration and mobility with temperature. Our high-temperature Hall measurements (shown in Figure 6.12) also revealed a similar variation in carrier concentration (n_H) and mobility (μ_H). Interestingly, the FS and HPS samples showed significantly improved carrier mobility compared to the I sample, as evidenced by n_H and μ_H measurements. This improvement can be attributed to the decrease in Sn vacancies, which simultaneously reduced the hole carrier concentration and improved the charge carrier transport in the FS and HPS samples.

In the complete measured range of temperature, the ingot sample exhibited lower Seebeck values due to its high hole carrier concentration of $2.6 \times 10^{20} \text{ cm}^{-3}$, which reduced to $0.48 \times 10^{20} \text{ cm}^{-3}$ and $0.62 \times 10^{20} \text{ cm}^{-3}$ after hot press sintering and furnace sintering, respectively. Our ingot sample showed good agreement with the previously reported values for ingot samples by Pathak et al [28] and other literature [29, 31, 33]. The Seebeck coefficient increased with increasing temperature, which agree well with the decreasing trend of σ .

The power factor of our samples is shown in Figure 6.10 (d). The HPS sample exhibited the highest power factor (PF) values among all samples, with a maximum value of $17.7 \text{ W cm}^{-1}\text{K}^{-1}$ at 830 K. The PF of the FS samples is slightly reduced compared to the HPS sample, but it is significantly higher than the ingot sample over the whole temperature range.

The total thermal conductivity (κ_T) of our FS sample has reduced significantly compared to the HPS and ingot samples. This remarkable reduction in κ_T can be attributed to the nanostructured morphology for this sample as discussed earlier. Since all three sample have comparable σ over the whole temperature range, the reduction in κ_T is due to reduced κ_l ($\kappa_l = \kappa_T - \kappa_e = \kappa_T - LT\sigma$). The κ_e and κ_l at 340 K in different samples is shown in Fig 6.11. The largest κ_e in the ingot sample from the study of Pathak et al. can be attributed to its high electrical conductivity. On the other hand, due to their overlapping conductivities (σ), all three samples, I, HPS and FS, show similar values of κ_e . In contrast to this, κ_L variation

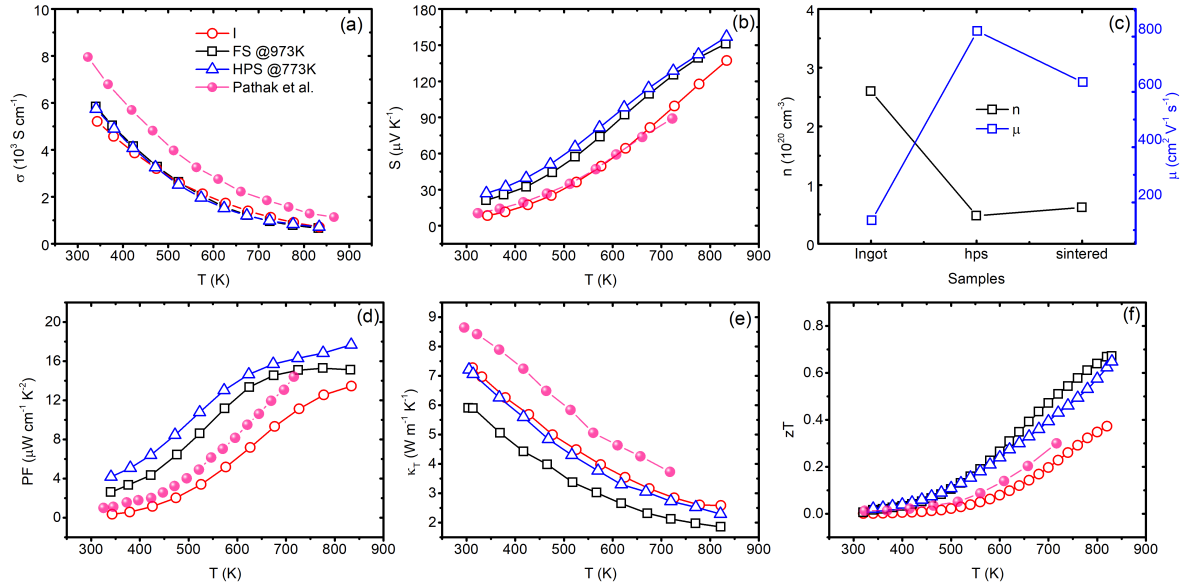


Figure 6.10: TE properties of $\text{Sn}_{1.03}\text{Te}$ I, FS @ 973 K and HPS @ 773 K, (a, and b) represents the temperature dependent σ and S , (c) shows the hole carrier concentration and mobility in different samples, (d,e, and f) represents the temperature dependent PF, total thermal conductivity (κ_T) and zT . Inset in (f) shows the zT_{max} and zT_{avg} obtained in three different samples.

between these samples is rather significant with FS sample showing the lowest κ_L among all samples. As a consequence of the largely suppressed κ_T in the FS sample, it exhibited the highest zT value of 0.68 at 830 K. The HPS sample also exhibited comparable high zT values of 0.65 due to its highest PF. The zT value of our ingot sample is in agreement with the highest zT of previously reported for an ingot sample [28].

We can see that the electronic transport of HPS is in agreement with the FS sample due to their very similar carrier concentrations. However the thermal transport of HPS followed the ingot sample due to similarity in their microstructure. After analyzing the overall TE properties of $\text{Sn}_{1.03}\text{Te}$ samples, we found that the FS sample shows superior zT_{max} and zT_{avg} , as shown in Figure 6.11(b). Having discovered and optimized the method for obtaining high zT in SnTe, our further study will focus on examining the effect of Ag doping in samples prepared analogously to the FS $\text{Sn}_{1.03}\text{Te}$ sample.

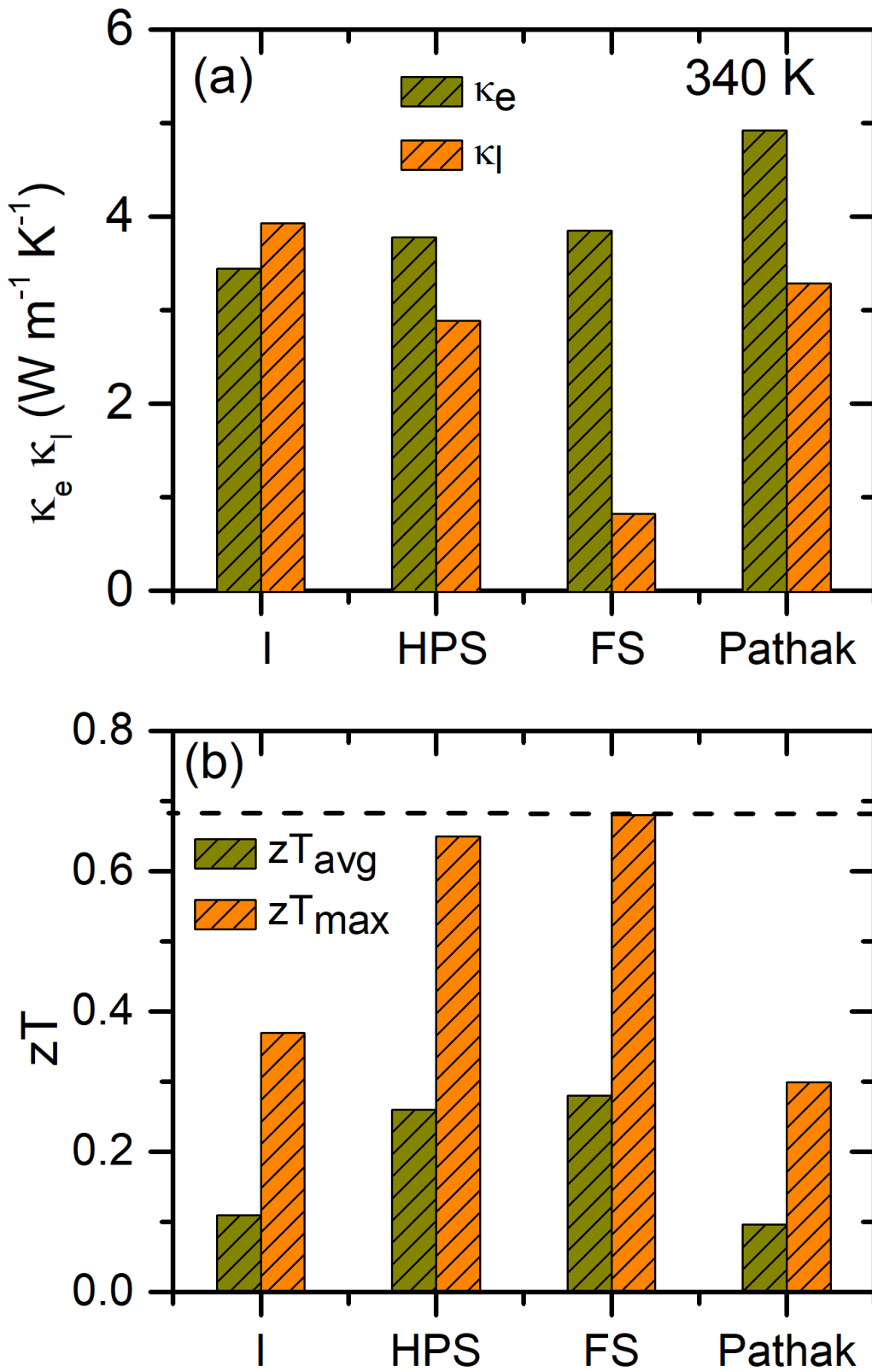


Figure 6.11: (a) κ_e and κ_l at 340 K, (b) shows zT_{max} and zT_{avg} for $\text{Sn}_{1.03}\text{Te}$ I, HPS, and FS samples from this work compared with their values from Ref [28].

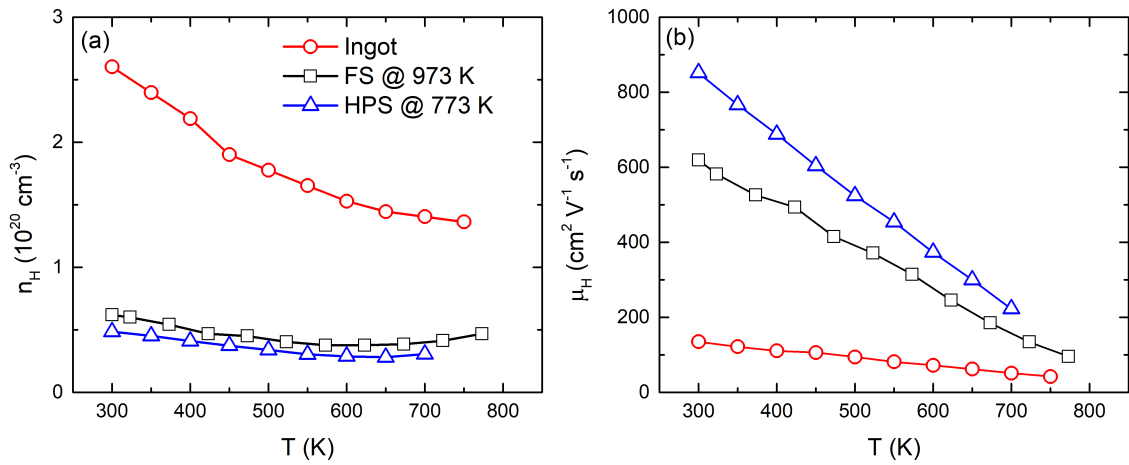


Figure 6.12: Temperature dependent (a) Hall carrier concentration, and (b) mobility variation of Sn_{1.03}Te I, HPS, and FS samples.

6.3.3 Electronic Transport Properties of Sn_{1.03-x}Ag_xTe ($x = 0, 0.03, 0.06, \text{ and } 0.09$)

Figure 6.13 shows the temperature-dependent electronic transport properties of Ag-doped FS samples. It can be observed that near room temperature the electrical conductivity decreases for Ag-doped samples. One can understand this through the combined effect of increased carrier concentration and decreased carrier mobility due to Ag doping. Ag⁺ acts as an acceptor when doped at the Sn²⁺ site, pushing the Fermi level deep into the valence band where the heavy hole band, Σ with low carrier mobility also starts contributing to electronic transport, consequently reducing the overall carrier mobility. Moreover, our *ab-initio* electronic band structure calculations using DFT show that with increasing Ag-doping even the light hole band at L-point flattens out a bit thus increasing the effective mass of the light holes thereby contributing to the decrease in mobility. A slight increase in σ upon increasing the Ag doping from $x = 0.03$ to 0.06 can be attributed to the increase in carrier concentration which seems to dominate the reduced carrier mobility as the amount of Ag doping increases. The variation of μ_H and n_H as a function of Ag-doping concentration at room temperature is shown in Figure 6.13 (b). At temperatures above 500 K, the σ of the Ag-doped samples exhibited enhancement compared to the undoped sample, suggesting the predominant influ-

ence of increased carrier concentration in the Ag-doped samples. Moreover, this indicates a modified temperature dependence of σ , attributed to alloy scattering in addition to electron-phonon scattering in the Ag-doped samples. Specifically, at 830 K, the conductivity nearly doubled with Ag doping, increasing from 0.66 S cm^{-1} in the undoped sample to 1.23 S cm^{-1} in the $x = 0.06$ sample.

The thermopower of our Ag-doped samples is depicted in Figure 6.13(c). The increase in the Seebeck coefficient (S) can be attributed to a combination of factors, including band convergence (as indicated by a decrease in $\Delta E_{L\Sigma}$) and an increase in n_H , leading to the participation of heavy holes. As a result of band convergence, the Seebeck coefficient of our FS samples exhibited an increase from $20.6 \mu\text{VK}^{-1}$ for $\text{Sn}_{1.03}\text{Te}$ to $44 \mu\text{VK}^{-1}$ for $\text{Sn}_{0.97}\text{Ag}_{0.06}\text{Te}$ near room temperature. Previous studies, such as those by Banik et al. and Xu et al., have also reported similar band convergence effects upon Ag doping [29,33]. Figure 6.15 presents a schematic diagram illustrating the impact of Ag doping on the electronic band structure of SnTe, which was created based on our analysis of the calculated electronic band structure. In the schematic diagram we have only shown the two valence bands namely, L and Σ , here Σ is the heavy hole band present along ΓK symmetric direction of the Brillouin zone called Σ band having 12-fold band degeneracy. The introduction of Ag doping slightly flattens the L band, increases the band gap by lowering the energy of the valence band maxima, and brings it closer to the Σ band, resulting in band convergence. This phenomenon decreases the energy gap $\Delta E_{L\Sigma}$ as the doping level increases.

For higher levels of Ag doping (i.e., above $x = 0.074$), the decrease in $\Delta E_{L\Sigma}$ becomes very small, leading to no further enhancement in the Seebeck coefficient, see DFT calculation shown in Figure 6.14. Our experimental S values for $\text{Sn}_{1.03-x}\text{Ag}_x\text{Te}$ samples (with $x = 0, 0.03, 0.06, \text{ and } 0.09$) align well with the theoretically calculated Pisarenko lines using a two-valence band model, as shown in Figure 6.13(d). More details regarding the computational methods and the two-valence band model can be found in Appendix B.

Similar to the temperature-dependent variation of conductivity (σ), there is a crossover of S values between undoped and Ag-doped samples at 500 K. However, after 500 K, the

Ag-doped samples exhibit lower S values compared to the undoped sample, primarily due to the dominant effect of increased carrier concentration.

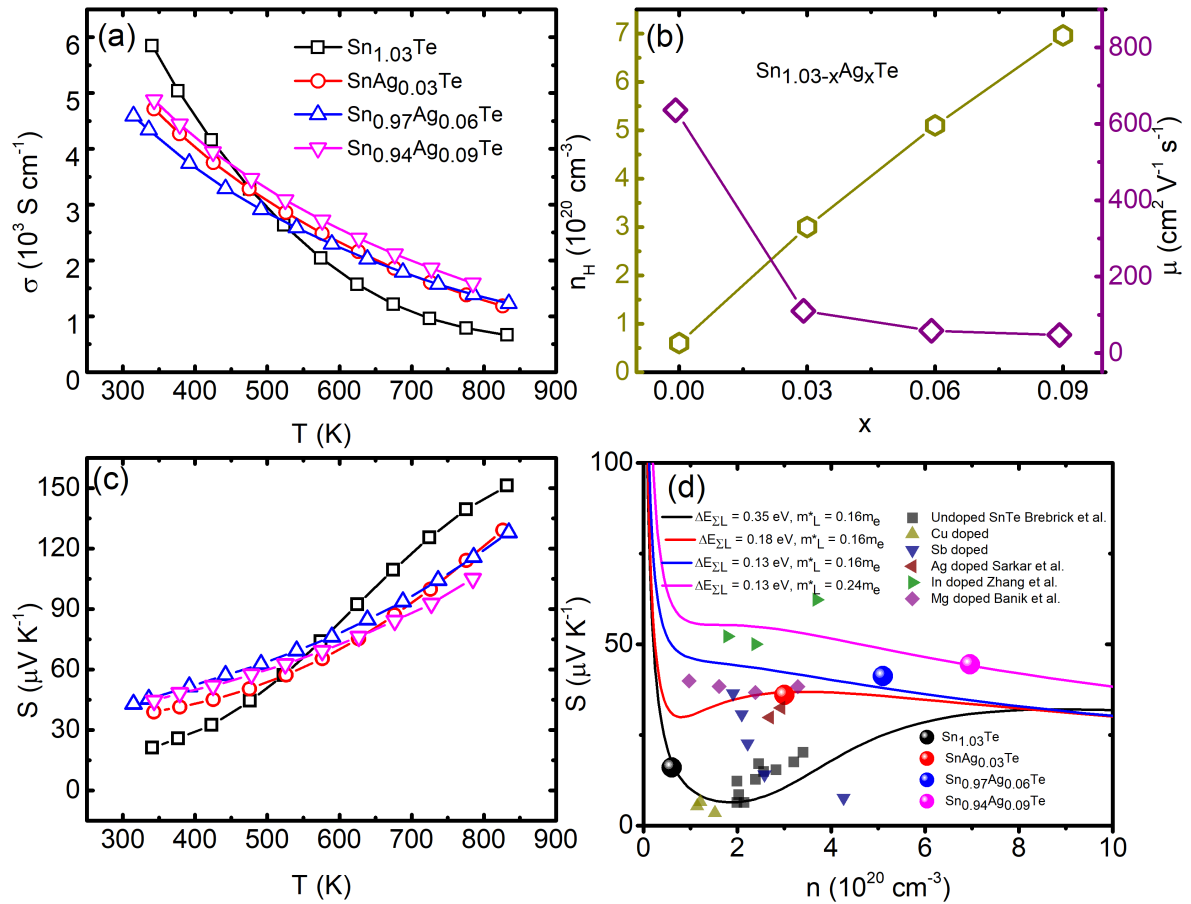


Figure 6.13: (a) Temperature dependent σ , (b) hall carrier concentration and mobility variation with Ag doping, (c) temperature dependent S , and (d) S vs n Pisarenko lines computed by using two valence band model with varying ΔE_V (heavy hole band: SPB model with $m_H^* = 0.35m_e$ and light hole band: SKB model and $m_L^* = 0.16 m_e$ and $0.24 m_e$). Literature data is also included for comparison [29–32].

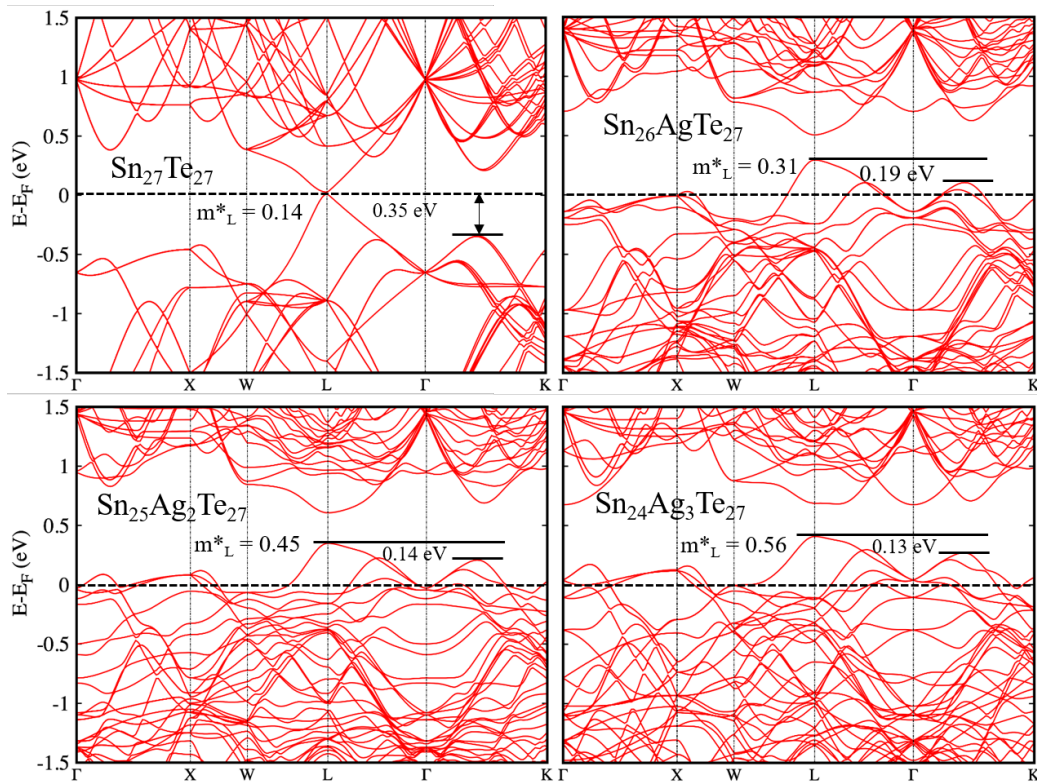


Figure 6.14: *Ab-initio* electronic band calculations for $\text{Sn}_{27}\text{Te}_{27}$, $\text{Sn}_{26}\text{AgTe}_{27}$, $\text{Sn}_{25}\text{Ag}_2\text{Te}_{27}$ and $\text{Sn}_{27}\text{Ag}_3\text{Te}_{27}$ compositions.

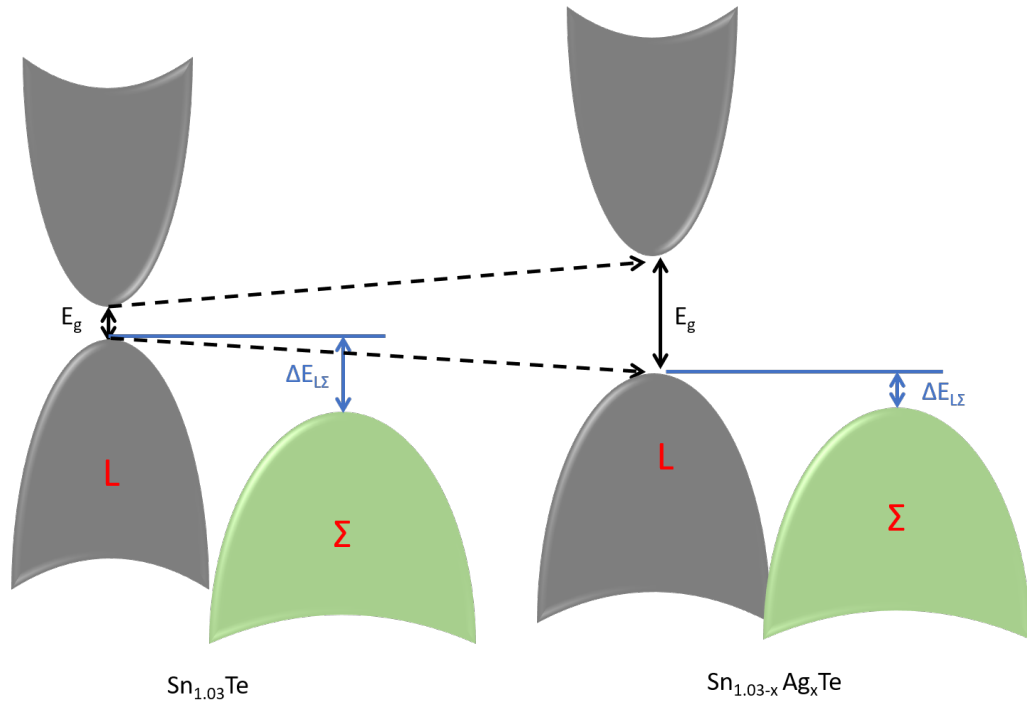


Figure 6.15: Schematic representing the electronic band structure modifications after Ag doping

The power factor as a function of temperature is depicted in Figure 6.16 (a). In the entire measured temperature range, remarkably improved PF values were obtained after Ag doping. Near room temperature, we obtained an increment of 250% in PF values with increasing Ag doping from $x = 0$ to $x = 0.09$. At 830 K, the PF value increased from $15.2 \text{ W cm}^{-2} \text{ K}^{-1}$ for the $\text{Sn}_{1.03}\text{Te}$ to $19.7 \text{ W cm}^{-2} \text{ K}^{-1}$ for $\text{SnAg}_{0.03}\text{Te}$ sample, indicating a significant enhancement due to Ag doping. Similar high values of PF (around $22 \text{ W cm}^{-2} \text{ K}^{-1}$) was reported by Pathak et al. [28] in 3% Ag doped SnTe synthesized by solid state melting method.

6.3.4 Thermal Transport and Figure of Merit of $\text{Sn}_{1.03-x}\text{Ag}_x\text{Te}$ ($x = 0, 0.03, 0.06, \text{ and } 0.09$)

Figure 6.16(b) displays the temperature-dependent total thermal conductivity (κ_T) for all Ag doped samples investigated in this study. Notably, the $x = 0.03$ sample exhibited the lowest κ_T among all the compositions investigated here over the whole temperature range. To determine κ_l , we first estimated κ_e from the Wiedemann-Franz law, $\kappa_e = LT\sigma$, where

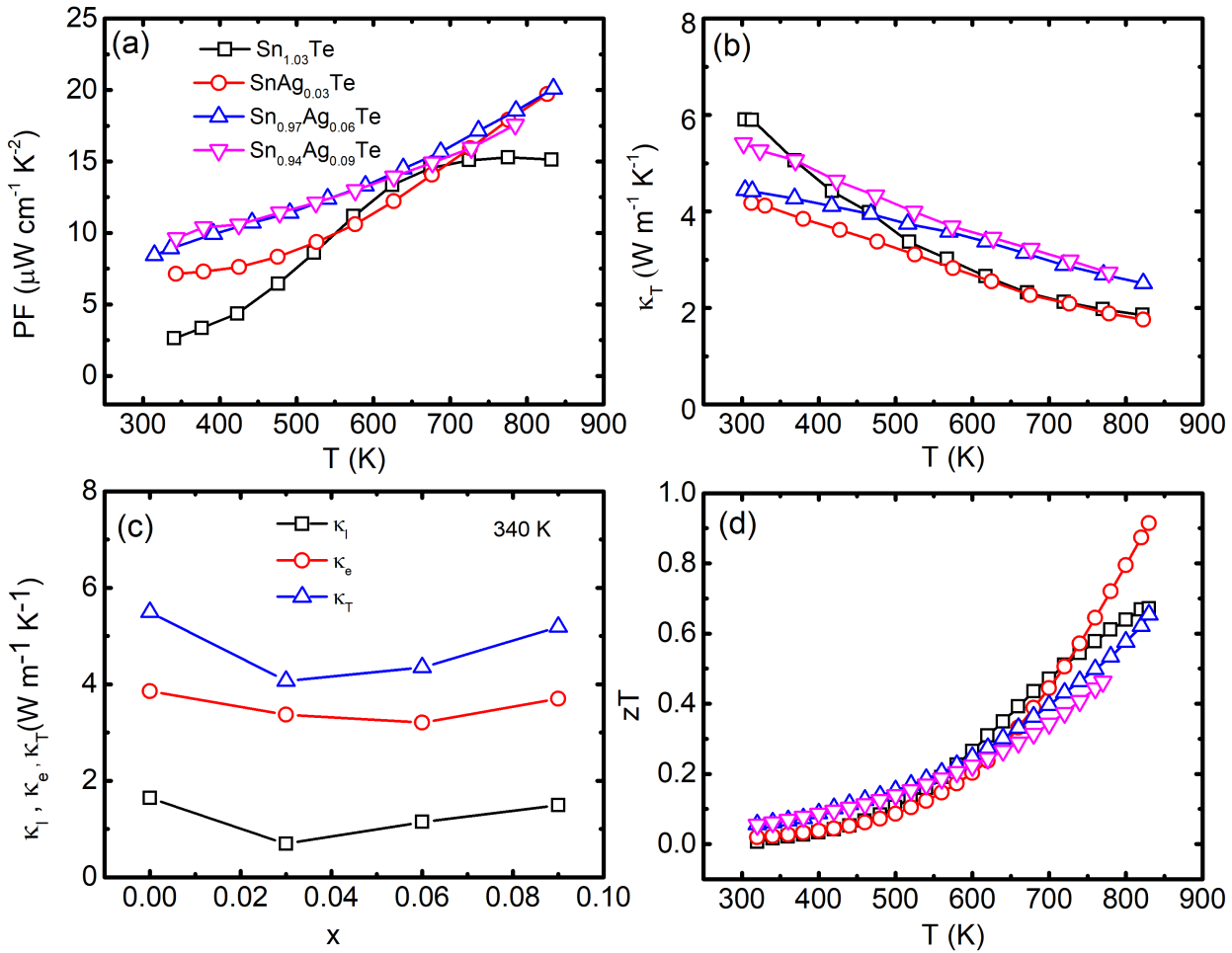


Figure 6.16: Temperature dependent (a) power factor (PF), (b) total thermal conductivity (κ_T), (c) lattice thermal conductivity (κ_l) at 340 K, and (d) zT for Sn_{1.03-x}Ag_xTe ($x = 0, 0.03, 0.06$ and 0.09) samples.

L is the Lorenz number that was calculated by simulating the experimental Seebeck data using the two-valence-band model at 340 K [153]. In Figure 6.16(c), we show κ_T , κ_e , and $\kappa_l = \kappa_T - \kappa_e$ at 340 K. κ_L initially decreases with Ag doping and then increases for $x \geq 0.03$. The enhancement in κ_l can be attributed to the increased nanoparticle size and a smaller number of particles in the $x = 0.06$ and $x = 0.09$ as depicted in Figure 6.8.

In order to understand the factors contributing to the reduced κ_l in the $x = 0.03$ sample, we conducted a thorough transmission electron microscopy (TEM) analysis. For this, a piece of the sintered pellet was grounded into a fine powder and dispersed it in ethanol to create a suspension solution, which was then drop-casted onto a Cu TEM grid coated with amorphous carbon. Our high-resolution TEM images, as depicted in Figure 6.17, reveal the presence of nano-dimensional grains, dislocations and twisted atomic planes. These defects scatter medium to small mean free path phonons, leading to the lowest lattice thermal conductivity value of $0.58 \text{ W m}^{-1} \text{ K}^{-1}$ at 340 K in $x = 0.03$ FS sample. The low κ_l values obtained in our study are slightly higher than those reported in the literature for Ge and Sb co-alloyed SnTe samples with endotaxial Cu_2Te nanostructured bulk samples [262], but are comparable to those for Cu_2Te doping along with Ge and Mn alloyed samples [263]. To mitigate any potential influence of slightly lower sample density on κ_T in our study, we conducted a comparison of our temperature dependent thermal diffusivity (D) data with existing literature data. In Figure 6.18(a), we have included data for our ingot sample for comparison. Notably, our FS sample exhibited the lowest D values throughout the entire measured temperature range, reaffirming the lower thermal conductivity obtained in this study.

Figure 6.16(d) illustrates the temperature-dependent zT . In the case of the sample doped with Ag at a concentration of $x = 0.03$, an increase in zT from 0.68 to 0.91 at 830 K is obtained, owing to the improved power factor and maintained low value of thermal conductivity. It is worth noting that previously studied ingot samples [29, 31, 33, 34] reported a maximum zT of 0.66, which is significantly surpassed by our FS sample, the comparison is shown in Figure 6.18. Notably, the high zT of our $\text{SnAg}_{0.03}\text{Te}$ ingot sample is in good agreement with that previously reported. However, in the FS sample of the same composition the

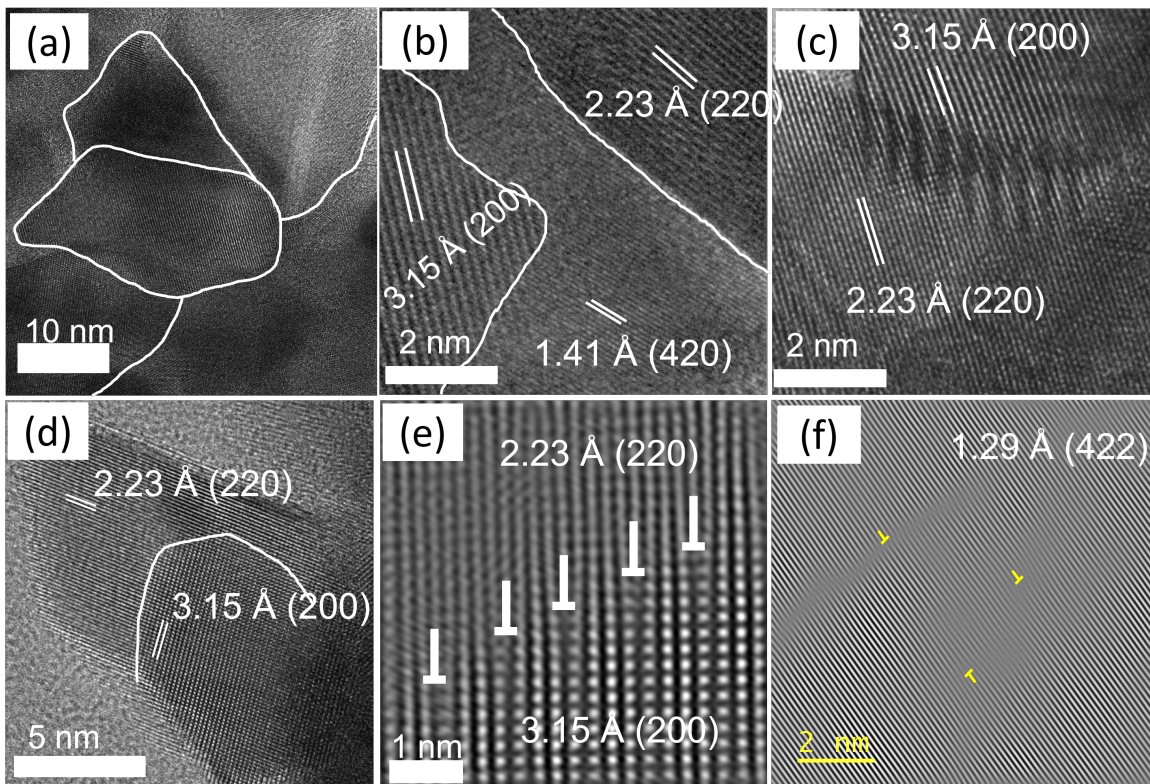


Figure 6.17: High resolution transmission electron microscopy analysis of sintered $\text{SnAg}_{0.03}\text{Te}$, (a) represents the multiple nano-size grain boundaries (b), and (c) shows the presence of semi-coherent and coherent grain boundaries, (d) shows incoherent grain boundary formed between (220) and (200) planes, (e, and f) denotes a IFFT image showing dislocation defects along (220) and (422) planes.

zT is enhanced by as much as 35% at 830 K.

To solidify the obtained results in the $\text{SnAg}_{0.03}\text{Te}$ sample, we synthesized a second sample using the same protocol. The results of the TE properties are shown in Figure 6.19. Sample 2 also showed similarly high values of zT confirming the sample reproducibility. Therefore, our synthesis method produced reproducible results establishing that sintering induced nanoparticle formation in the bulk sample indeed enhances the zT of SnTe material significantly.

Moreover, thermal stability was assessed by conducting multiple heating and cooling cycles, as depicted in Figure 6.20. Our results demonstrate excellent repeatability across consecutive heating and cooling runs, providing strong evidence for the robust thermal stability of our samples.

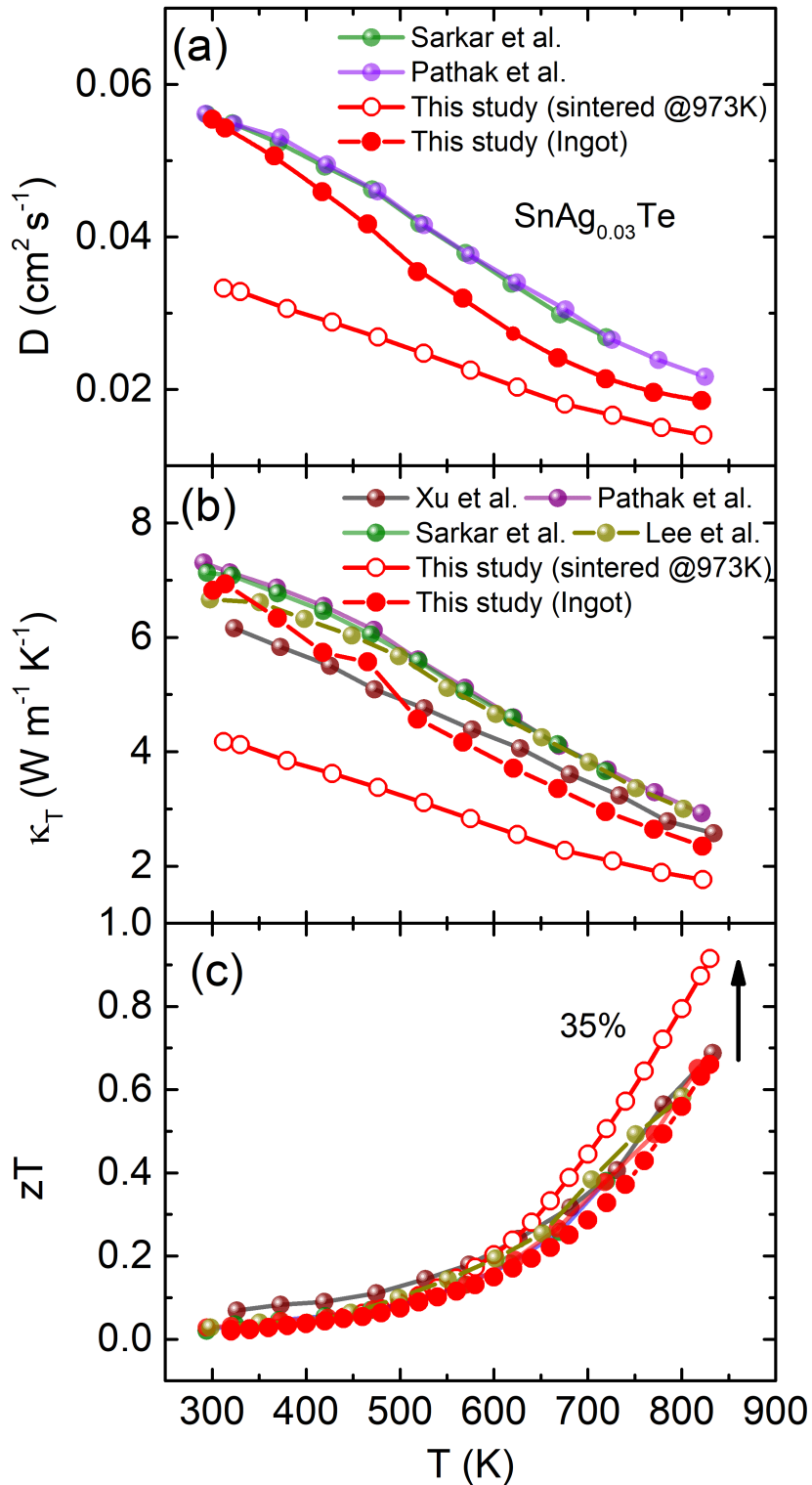


Figure 6.18: Comparison of (a) thermal diffusivity (D), (b) total thermal conductivity κ_T , and (c) zT of $\text{SnAg}_{0.03}\text{Te}$ sample from our study with the literature data from Xu et al. [33], Pathak et al. [28], Sarkar et al. [31], Lee et al. [34].

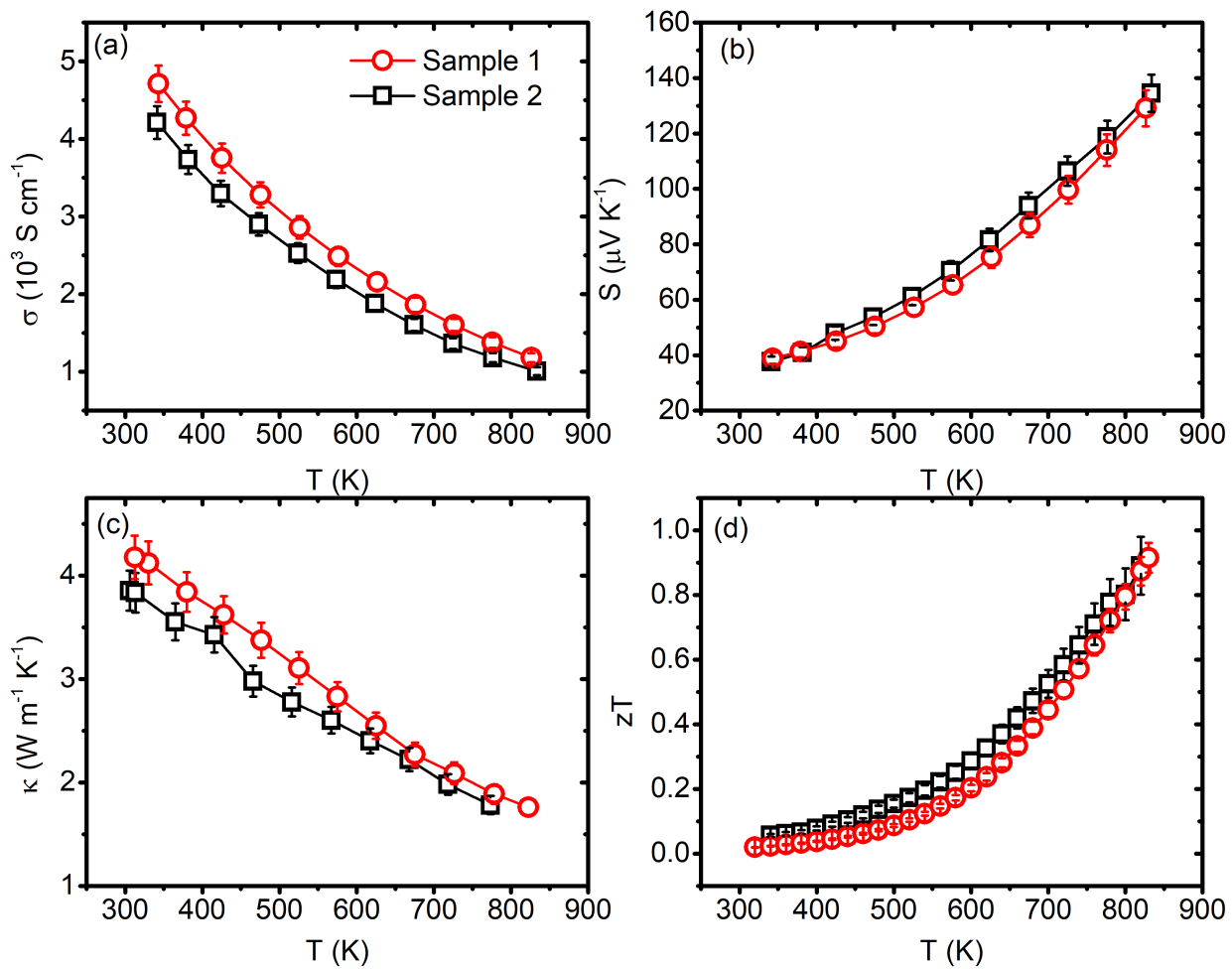


Figure 6.19: SnAg_{0.03}Te sample's comparison from our study with the literature, temperature dependent (a) thermal diffusivity (D), (b) total thermal conductivity κ_T , and (c) zT .

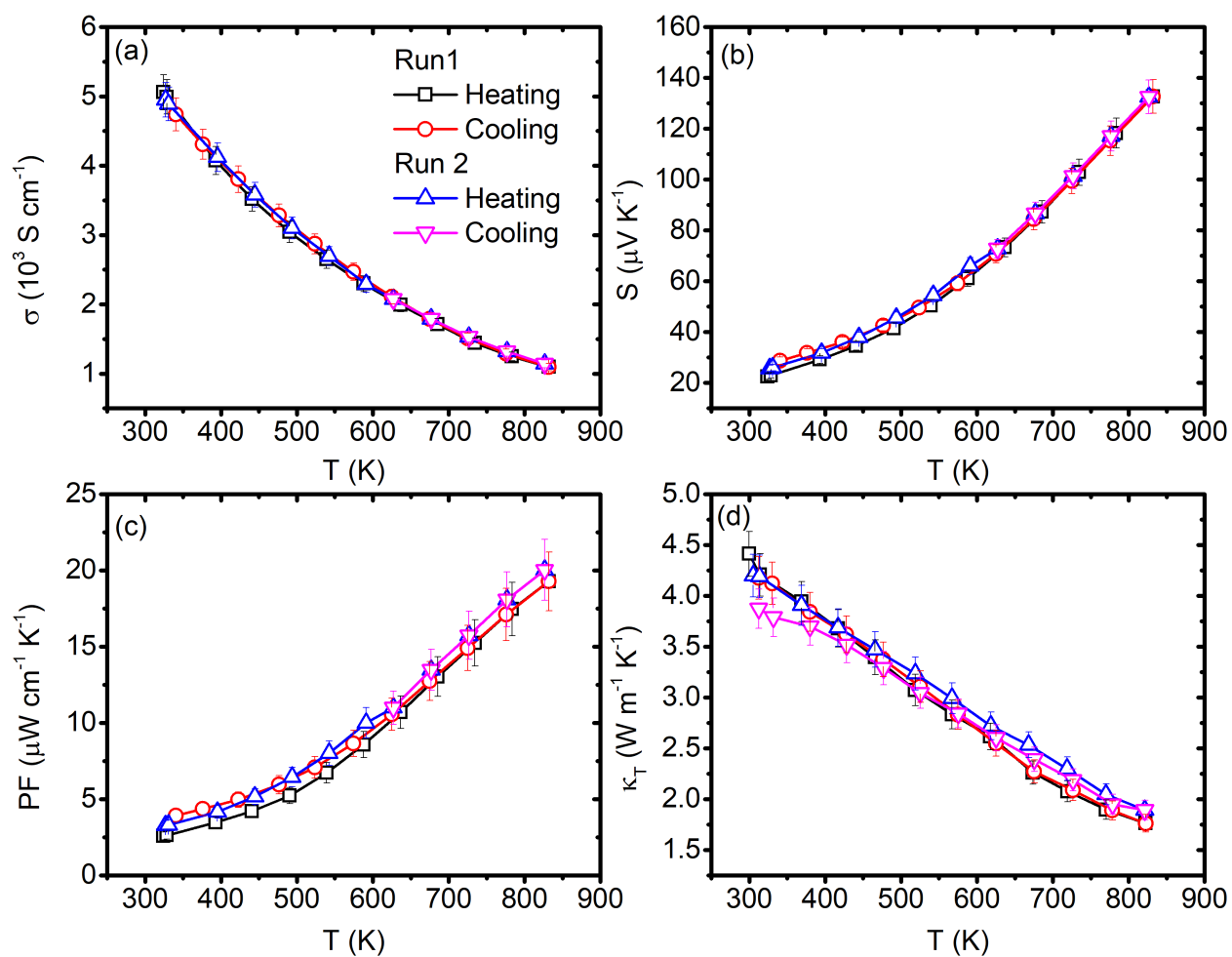


Figure 6.20: SnAg_{0.03}Te sample's comparison from our study with the literature, temperature dependent (a) thermal diffusivity (D), (b) total thermal conductivity κ_T , and (c) zT .

6.4 Summary and Conclusion

We have optimized the TE properties of self compensated SnTe by manipulating the micro structure by synthesis method involving high temperature sintering of the cold-pressed pellet obtained by grounding the ingot prepared by solid state melting. We show that this process results in formation of nanostructured bulk sample with zT values enhanced by up to 35% over the zT of the ingot sample of the same composition. The primary reason for zT enhancement is that in comparison to our ingot samples of $\text{Sn}_{1.03}\text{Te}$, we observed a significant reduction in thermal conductivity due to the nanostructuring process. Additionally, due to L - Σ bands convergence due to Ag doping, the PF has been enhanced from $15 \text{ W cm}^{-2} \text{ K}^{-1}$ for $\text{Sn}_{1.03}\text{Te}$ to $20 \text{ W cm}^{-2} \text{ K}^{-1}$ for $\text{SnAg}_{0.03}\text{Te}$. The increased PF and reduced κ_L together increase the zT from 0.67 to 0.92 at 820 K. Theoretical band calculations have corroborated our experimental findings, revealing band convergence and increased carrier effective mass with Ag doping responsible for enhanced seebeck coefficient. Therefore, our study not only provides a novel synthesis route for nanostructured bulk SnTe with improved zT , but also advances our understanding of the effects of Ag doping through DFT band calculations.

Chapter 7

Summary and Conclusion

In this thesis, we have studied the thermoelectric (TE) properties of nano-structured bulk binary silver chalcogenide superionic compounds (Ag_2X) and an environmentally friendly metavalent compound, SnTe. Ag_2X compounds exhibit stabilization in either the monoclinic or orthorhombic phase, depending on the specific X element, at room temperature. However, upon heating beyond 400 K, these compounds undergo a transformation to a liquid-like cubic superionic phase (FCC or BCC depending upon X). Superionic compounds exhibit low thermal conductivity due to the liquid-like movement of the cation sublattice within the rigid sublattice formed by anions. On the other hand, metavalent compounds demonstrate a high power factor owing to their highly symmetric crystal structure and unique electronic band structure. The superionic compounds investigated in this thesis were primarily synthesized using a novel room temperature synthesis method. However, a few samples were also synthesized using the conventional solid-state melting method for comparison purposes. Metavalent SnTe was synthesized using the conventional solid-state method followed by different sintering routes. Our focus in the superionic compound class was on sample reproducibility and stability, while simultaneously achieving an enhanced figure-of-merit. As for SnTe, we synthesized a nano-structured bulk sample for the first time without the aid of any chemical synthesis or high-frequency planetary ball milling.

In Chapter 3 of the thesis, we addressed the issue of irreproducibility in the electronic

transport properties of furnace-sintered Ag_2Te samples which was also reported in previous studies for the samples prepared by involvement of any high temperatures (>500 K). Specifically, we observed inconsistent behavior in the thermopower (S), which sometimes exhibited an n-to-n type transition and other times an n-to-p type transition at the structural and superionic transition temperature. Additionally, there was a significant variation in electrical conductivity values among the samples.

To resolve this problem, we employed a novel synthesis method that allowed us to fabricate nearly 100% dense pellets at room temperature, leveraging the ductile property of binary silver chalcogenides. By preparing stoichiometric Ag_2Te samples at room temperature, we achieved highly reproducible transport properties up to 570 K. Moreover, we successfully reduced the grain size of n-type samples, resulting in a remarkable enhancement of their thermoelectric performance. In fact, we achieved a record-high zT value of 1.2 at 570 K for the n-type Ag_2Te samples. During our investigation, we discovered that there is an upper measurement temperature limit for n-type Ag_2Te samples. Beyond this limit, we observed Ag migration, leading to a degradation of the electronic transport properties and irreproducibility. Therefore, it was crucial to carefully control the measurement temperature when characterizing these samples.

Once we obtained highly reproducible n-type Ag_2Te samples, we successfully synthesized their p-type counterparts by optimizing Ag vacancies in the composition. By introducing a 0.5% Ag deficiency in the Ag_2Te composition, we achieved a remarkable zT value of 0.64 at 570 K for the p-type sample. Overall, our study highlights the successful resolution of irreproducibility in the electronic transport properties and enhanced zT of Ag_2Te through the use of a novel room-temperature synthesis method.

In Chapter 4, we explored the thermoelectric (TE) properties of Ag_2Se . This compound is renowned for its impressive TE performance, rivaling the state-of-the-art compound Bi_2Te_3 , near room temperature. However, the industrial implementation of Ag_2Se faces a significant obstacle: sample irreproducibility. Various reports have highlighted the high zT values obtained for different compositions of $\text{Ag}_2\text{Se}_{1+x}$, where x varies from 0.01 to 0.08. The

observed variations in zT values are attributed to the inhomogeneity of the samples, arising from high-temperature synthesis methods. To address this challenge, we have employed an all-room-temperature synthesis approach, successfully achieving comparable high zT values to those reported in earlier studies. Additionally, our method ensures excellent sample reproducibility and homogeneity.

Furthermore, we have focused on comprehending the role of Se excess in the enhancement of zT in the Ag_2Se compound. We have proposed a model that incorporation of the addition of a slight anion excess suppress the Ag interstitial defects, resulting in a reduction of the carrier concentration. This allows to achieve an equally high PF compared to pristine Ag_2Se , while simultaneously lowering the total thermal conductivity. This synergistic effect contributes to the enhancement of the zT value in the anion-excess Ag_2Se compound compared to the pristine Ag_2Se .

Having established prior knowledge of obtaining highly dense pellets at room temperature, we utilized a similar approach to study the TE properties of Ag_2S . In samples with a slight anion (Sulfur, S) excess of approximately 1%, the thermal conductivity was found to be significantly reduced compared to the pristine composition, while maintaining a similar PF. Through a detailed differential scanning calorimetry (DSC) study of both pristine and anion-excess samples, we observed the formation of a metastable phase that evolved with consecutive thermal cycling. All samples exhibited two exothermic peaks during heating and two endothermic peaks during cooling, indicating the presence of two distinct types of transitions in the Ag_2S samples. Moreover, the intensity of the peak corresponding to the secondary phase was found to increase in the case of a slight anion excess sample, resulting in a significant reduction in thermal conductivity in samples with 1% and 1.15% S excess. Upon further addition of anion excess above 1.15%, the intensity of the secondary phase peak diminished during heating, approaching the thermal conductivity levels similar to those of the pristine Ag_2S sample. As a result of the decreased thermal conductivity in samples with 1% and 1.15% S excess, we achieved a remarkably high zT value of 0.9 at 670 K, which is the highest ever reported value for Ag_2S and its derivative compounds.

In Chapter 6, we conducted a study on the TE properties of an environmentally friendly metavalent compound, SnTe, which shares a similar crystal and valence band structure with PbTe. However, SnTe exhibits inferior performance compared to PbTe due to its low Seebeck coefficient and high thermal conductivity (κ) caused by a high concentration of Sn vacancies. To partially address the issue of Sn vacancies, we investigated self-compensated SnTe samples in which an additional 3% of tin was used to compensate for the vacancies. Additionally, we fabricated a nanostructured SnTe bulk sample using a novel synthesis method of furnace sintering, aiming to further reduce the κ . This is the first time we are reporting the fabrication of nanostructured bulk SnTe without aiding any chemical synthesis or high energy planetary ball mill. Our initial objective was to understand the origin of nanoparticle formation in the furnace-sintered pellets. Through our investigation, we confirmed that the presence of intrinsic vacancies led to the formation of nanoparticles on micrometer-sized grains. Furthermore, we synthesized SnTe samples using the conventional solid-state melting method and the hot press sintering (HPS) method, allowing us to compare the TE properties of the nanostructured bulk obtained from furnace sintering with those of the ingot and HPS samples. Remarkably, the furnace-sintered sample exhibited a significantly lower thermal conductivity compared to the ingot and HPS samples, resulting in a very high dimensionless figure of merit value of 0.66 at 820 K.

After successfully achieving a low thermal conductivity in SnTe through optimization of the synthesis method, we shifted our focus to improving the PF through band engineering. To simultaneously enhance the Seebeck coefficient and electrical conductivity, we chose Ag as a suitable dopant, which effectively enhanced the PF values across the entire temperature range under investigation. The introduction of Ag modified the band structure of SnTe by reducing the energy gap between the L and Σ bands. Additionally, the L band broadened, resulting in an increased effective mass of the hole carriers associated with it. These effects enhanced the Seebeck coefficient in the temperature range from room temperature to the mid-temperature range (550 K). Moreover, Ag doping increased the hole carrier concentration, leading to an increase in electrical conductivity from 550 K onwards. By combining the high Seebeck co-

efficient near room temperature and the high electrical conductivity at higher temperatures, we were able to improve the PF over the entire measured range of temperature. Specifically, it increased from $15 \mu\text{W cm}^{-1} \text{K}^{-2}$ in undoped $\text{Sn}_{1.03}\text{Te}$ to $20 \mu\text{W cm}^{-1} \text{K}^{-2}$ in the $\text{SnAg}_{0.03}\text{Te}$ sample at 820 K. Interestingly, the presence of nanoparticles in the $\text{SnAg}_{0.03}\text{Te}$ sample maintained a similarly low thermal conductivity, resulting in an improved zT value of 0.9 at 820 K.

Appendix A

Thermoelectric Properties Of $\text{Sn}_{1.03-x}\text{Ag}_x\text{Te}$ Ingot Samples

A.1

In Chapter 4, we presented the thermoelectric (TE) properties of furnace-sintered samples, $\text{Sn}_{1.03-x}\text{Ag}_x\text{Te}$ ($x = 0, 0.03, 0.06, \text{ and } 0.09$). In this appendix section, we will discuss the TE properties of their ingot samples, as shown in Figure A.1. The introduction of Ag doping resulted in a decrease in the electrical conductivity, σ , particularly near room temperature, due to the reduced carrier mobility. However, at the highest measured temperature, the effect of increased hole carrier concentration surpassed the effect of decreased carrier mobility, leading to a slight increase in σ compared to the undoped sample. Specifically, the σ values increased from $0.72 \times 10^3 \text{ S cm}^{-1}$ in the undoped sample to $1.08 \times 10^3 \text{ S cm}^{-1}$ in the Ag-doped samples.

In Figure A.1(b), we illustrate the impact of band convergence on the Seebeck coefficient (S) through Ag alloying. The Seebeck coefficient increased from $8 \mu\text{V K}^{-1}$ to $43 \mu\text{V K}^{-1}$ near room temperature. However, this increment diminished at the highest measured temperature due to the increased hole carrier concentration in the Ag-doped samples. Consequently, due to the increased S near room temperature and the enhanced σ at higher temperatures,

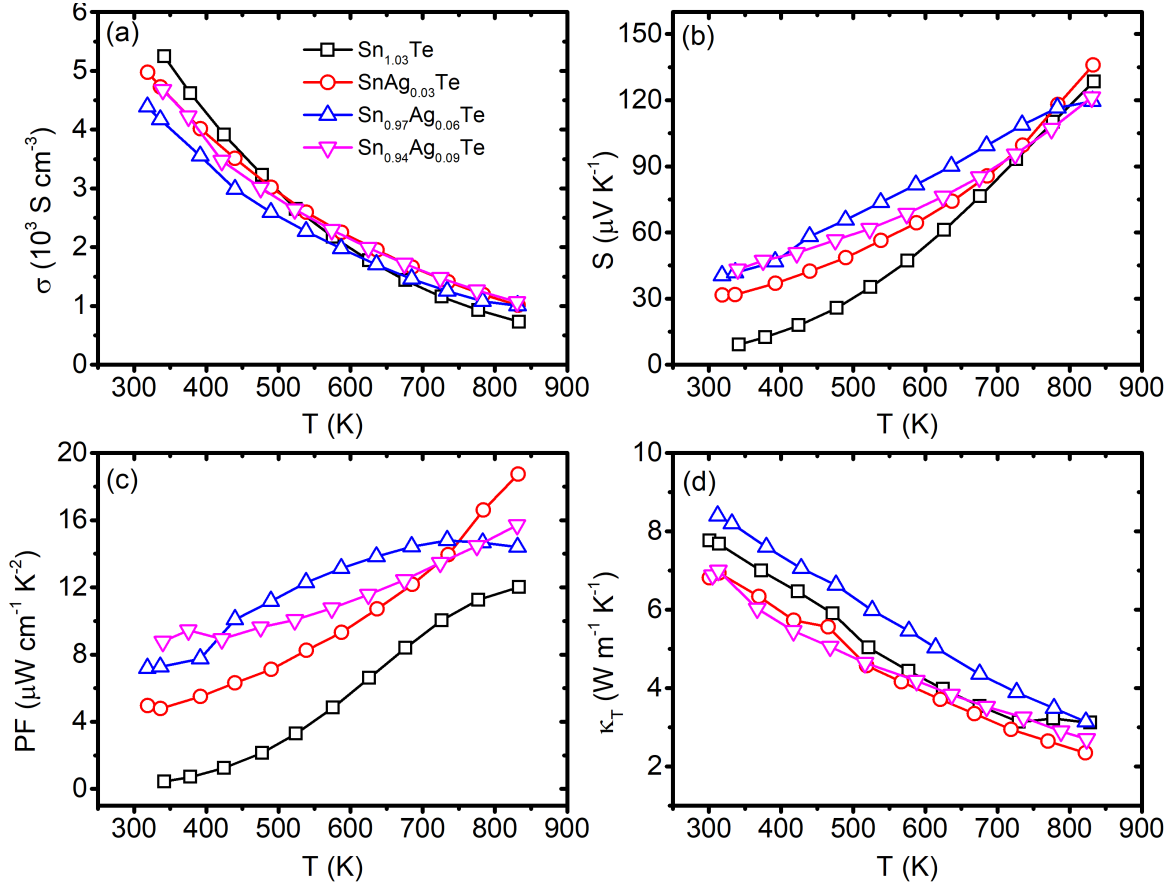


Figure A.1: Temperature dependent (a) σ , (b) Seebeck coefficient (S), (c) power factor (PF), and (d) total thermal conductivity (κ_T) for ingot $\text{Sn}_{1.03-x}\text{Ag}_x\text{Te}$ samples.

we achieved significant improvements in the power factor (PF) values of the Ag-doped ingot samples. For instance, PF increased from $0.38 \text{ W cm}^{-1} \text{ K}^{-2}$ in the undoped sample to $8.8 \text{ W cm}^{-1} \text{ K}^{-2}$ in the $x = 0.09$ sample near room temperature. Similarly, at 820 K, a substantial enhancement was observed, with PF increasing from $12.2 \text{ W cm}^{-1} \text{ K}^{-2}$ to $18.8 \text{ W cm}^{-1} \text{ K}^{-2}$ in the $x = 0.03$ ingot sample. The high PF values obtained in the ingot samples are comparable to those discussed in Chapter 6 for the furnace-sintered samples. Notably, the similar high values of PF have also been reported in previous Ag doped SnTe studies [28, 31, 33].

The total thermal conductivity (κ_T), as depicted in Figure A.1(d), exhibits a similar qualitative and quantitative behavior to that of σ , except for the $x = 0.06$ ingot sample, which

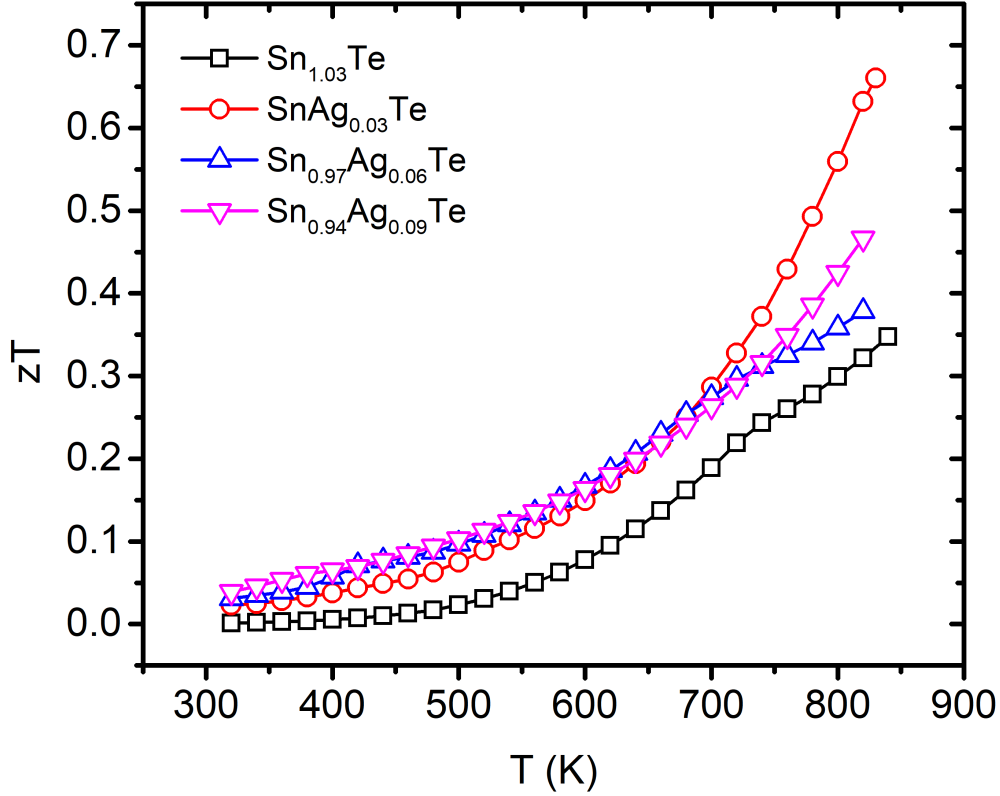


Figure A.2: Temperature dependent figure-of-merit (zT) for ingot $\text{Sn}_{1.03-x}\text{Ag}_x\text{Te}$ samples.

displayed an increased κ_T compared to the undoped sample. κ_T decreased with Ag doping due to the lowered electronic thermal conductivity (κ_e). However, the $x = 0.06$ sample demonstrated slightly higher κ_T , and the specific reason for this behavior is currently unknown to us. The temperature-dependent figure of merit, zT , is illustrated in Figure A.2. Due to the increased power factor (PF) resulting from Ag doping, along with similar total thermal conductivity (κ_T) compared to the undoped samples, the $x = 0.03$ Ag-doped sample exhibited an enhanced zT value. Specifically, the zT value increased from 0.35 to 0.66 at 820 K. The zT values of Ag doped samples are in good agreement with literature values reported for ingot samples.

Appendix B

Computational Details and Two Valence Band Model

B.1 Computational Details

The computational part of this work has been done in collaboration with Ankit Kumar who carried out the DFT calculations. Details about the calculations are given in Chapter 2.

B.2 Two Valence Band Model

We used the two-band k.p model to describe the light-hole region around the L point combined with a parabolic heavy-hole band lying $\Delta E_{L\Sigma}$ below the valence band edge [264]. We used $m_{LH}^* = 0.168 m_e$ for the effective mass of the light holes and $m_{HH}^* = 1.92 m_e$ for the effective mass of the heavy holes, and $\Delta E_{\Sigma L} = 0.35\text{eV}$ [153, 264]. The Seebeck coefficient for a non-parabolic light-hole band is given as:

$$S = \frac{k_B}{e} \left[\frac{{}_1F_{-2}^1(\eta, \alpha)}{{}_1F_{-2}^1(\eta, \alpha)} - \eta \right] \quad (\text{B.1})$$

$$\eta = \frac{E_F}{k_B T}, \alpha = \frac{k_B T}{E_g} \quad (\text{B.2})$$

where k_B is the Boltzmann constant, e is the electronic charge, η is the reduced Fermi energy and α is the nonparabolicity parameter. The function ${}^n F_k^m(\eta, \alpha)$ is the generalized form of Fermi integral given by:

$${}^n F_k^m(\eta, \alpha) = \int_0^\infty - \left(\frac{\partial f}{\partial \varepsilon} \right) \varepsilon^n (\varepsilon + \varepsilon^2)^m (1 + 2\alpha\varepsilon^2)^k \quad (\text{B.3})$$

where ε is the reduced energy $E/K_B T$, and f is the Fermi distribution function. The carrier concentration (n_p) is given as:

$$n_{pLH} = \frac{1}{3\pi^2} \left(\frac{2m_L^* k_B T}{\hbar^2} \right)^{3/2} {}^0 F_{-2}^{3/2}(\eta, \alpha) \quad (\text{B.4})$$

where \hbar is the Plank's constant and m_{LH}^* is the light-hole effective mass.

The heavy-hole band is assumed to be parabolic. The choice of $\alpha = 0$ makes the band parabolic. For this case Seebeck and carrier concentration are given as:

$$S = \frac{k_B}{e} \left[\frac{{}^1 F_{-2}^1(\eta - \Delta_v, 0)}{{}^1 F_{-2}^1(\eta - \Delta_v, 0)} - (\eta - \Delta_v) \right] \quad (\text{B.5})$$

$$n_{pHH} = \frac{1}{3\pi^2} \left(\frac{2m_H^* k_B T}{\hbar^2} \right)^{3/2} {}^0 F_{-2}^{3/2}(\eta - \Delta_v, 0) \quad (\text{B.6})$$

Here, m_{HH}^* is the heavy-hole density of state effective mass and Δ_v is $\Delta E_{L\Sigma}/k_B T$. The total effective mass from the contribution of both bands is given as:

$$S_{total} = (S_{LH}\sigma_{LH} + S_{HH}\sigma_{HH})/(\sigma_{LH} + \sigma_{HH}) \quad (\text{B.7})$$

and

$$\sigma = \frac{C}{mD^2} {}^0 F_{-2}^{3/2}(\eta, 0) \quad (\text{B.8})$$

where D is the acoustic deformation potential and C is a constant. We have taken the ratio $D_{LH}/D_{HH} = 0.5$, as used in previous study by Zhang et al. [139]. The combined Seebeck

can be obtained from equation:

$$S_{total} = (\xi S_{LH} + S_{HH})/(\xi + 1) \text{ where } \xi = m_{HH}D_{HH}^2/m_{LH}D_{LH}^2 \quad (\text{B.9})$$

The total carrier concentration is estimated as:

$$n_{total} = n_{pLH} + n_{pHH} \quad (\text{B.10})$$

Our experimental values obtained from the Hall measurements are fairly close to theoretically estimated values using equation for n_{total} . The Lorentz number is also estimated in similar manner which we have used for calculating the κ_e using Weidemann Franz law.

$$L_{total} = (\xi L_{LH} + L_{HH})/(\xi + 1) \quad (\text{B.11})$$

where

$$L_{LH} = \left(\frac{k_B}{e}\right)^2 \left[\frac{{}^2F_{-2}^1(\eta, \alpha)}{{}^0F_{-2}^1(\eta, \alpha)} - \left(\frac{{}^1F_{-2}^1(\eta, \alpha)}{{}^0F_{-2}^1(\eta, \alpha)}\right)^2 \right] \quad (\text{B.12})$$

and

$$L_{HH} = \left(\frac{k_B}{e}\right)^2 \left[\frac{{}^2F_{-2}^1(\eta - \Delta_v, 0)}{{}^0F_{-2}^1(\eta - \Delta_v, 0)} - \left(\frac{{}^1F_{-2}^1(\eta - \Delta_v, 0)}{{}^0F_{-2}^1(\eta - \Delta_v, 0)}\right)^2 \right] \quad (\text{B.13})$$

Bibliography

- [1] H. Ritchie, M. Roser, and P. Rosado, “Energy”, Our World in Data (2022).
<https://ourworldindata.org/energy>.
- [2] M. A. Zoui, S. Bentouba, J. G. Stocholm, and M. Bourouis, “A review on thermoelectric generators: Progress and applications”, Energies **13**(14), 3606 (2020).
- [3] X. Zhang and L.-D. Zhao, “Thermoelectric materials: Energy conversion between heat and electricity”, Journal of Materiomics **1**(2), 92 (2015).
- [4] I. M. Abdel-Motaleb and S. M. Qadri, “Thermoelectric devices: principles and future trends”, arXiv preprint arXiv:1704.07742 (2017).
- [5] H. Pang, X. Zhang, D. Wang, R. Huang, Z. Yang, X. Zhang, Y. Qiu, and L.-D. Zhao, “Realizing ranged performance in snite through integrating bands convergence and dos distortion”, Journal of Materiomics **8**(1), 184 (2022).
- [6] K. Biswas, J. He, I. D. Blum, C.-I. Wu, T. P. Hogan, D. N. Seidman, V. P. Dravid, and M. G. Kanatzidis, “High-performance bulk thermoelectrics with all-scale hierarchical architectures”, Nature **489**(7416), 414 (2012).
- [7] Y. Sun, L. Xi, J. Yang, L. Wu, X. Shi, L. Chen, J. Snyder, J. Yang, and W. Zhang, “The electron crystal behavior in copper chalcogenides Cu_2X ($X = Se, S$)”, Journal of Materials Chemistry A **5**(10), 5098 (2017).

- [8] K. Zhao, P. Qiu, X. Shi, and L. Chen, "Recent advances in liquid-like thermoelectric materials", Advanced Functional Materials **30**(8), 1903867 (2020).
- [9] P. Qiu, M. T. Agne, Y. Liu, Y. Zhu, H. Chen, T. Mao, J. Yang, W. Zhang, S. M. Haile, W. G. Zeier, et al., "Suppression of atom motion and metal deposition in mixed ionic electronic conductors", Nature communications **9**(1), 2910 (2018).
- [10] M. Jakob, M. Grauer, P. Ziolkowski, and O. Oeckler, "Decomposition phenomena of $\text{Zn}_{13}\text{Sb}_{10}$ under working conditions of thermoelectric generators and minimum current densities for electromigration", ACS Applied Energy Materials **3**(3), 2103 (2019).
- [11] R. Moshwan, L. Yang, J. Zou, and Z.-G. Chen, "Eco-friendly snt thermoelectric materials: progress and future challenges", Advanced Functional Materials **27**(43), 1703278 (2017).
- [12] E. Wielgosz and T. Kargul, "Differential scanning calorimetry study of peritectic steel grades", Journal of Thermal Analysis and Calorimetry **119**(3), 1547 (2015).
- [13] W. Mi, P. Qiu, T. Zhang, Y. Lv, X. Shi, and L. Chen, "Thermoelectric transport of Se -rich Ag_2Se in normal phases and phase transitions", Applied Physics Letters **104**(13), 133903 (2014).
- [14] J. Chen, Q. Sun, D. Bao, T. Liu, W.-D. Liu, C. Liu, J. Tang, D. Zhou, L. Yang, and Z.-G. Chen, "Hierarchical structures advance thermoelectric properties of porous n-type $\beta\text{-Ag}_2\text{Se}$ ", ACS Applied Materials & Interfaces **12**(46), 51523 (2020).
- [15] P. Wang, J.-L. Chen, Q. Zhou, Y. T. Liao, Y. Peng, J. S. Liang, and L. Miao, "Enhancing the thermoelectric performance of Ag_2Se by non-stoichiometric defects", Applied Physics Letters **120**(19), 193902 (2022).

- [16] P. Jood, R. Chetty, and M. Ohta, "Structural stability enables high thermoelectric performance in room temperature Ag_2Se ", Journal of Materials Chemistry A **8**(26), 13024 (2020).
- [17] D. Li, J. Zhang, J. Li, J. Zhang, and X. Qin, "High thermoelectric performance for an Ag_2Se -based material prepared by a wet chemical method", Materials Chemistry Frontiers **4**(3), 875 (2020).
- [18] S. Huang, T.-R. Wei, H. Chen, J. Xiao, M. Zhu, K. Zhao, and X. Shi, "Thermoelectric Ag_2Se : Imperfection, homogeneity, and reproducibility", ACS Applied Materials & Interfaces **13**(50), 60192 (2021).
- [19] D. Yang, X. Su, F. Meng, S. Wang, Y. Yan, J. Yang, J. He, Q. Zhang, C. Uher, M. G. Kanatzidis, et al., "Facile room temperature solventless synthesis of high thermoelectric performance Ag_2Se via a dissociative adsorption reaction", Journal of Materials Chemistry A **5**(44), 23243 (2017).
- [20] M. Jin, J. Liang, P. Qiu, H. Huang, Z. Yue, L. Zhou, R. Li, L. Chen, and X. Shi, "Investigation on low-temperature thermoelectric properties of Ag_2Se polycrystal fabricated by using zone-melting method", The Journal of Physical Chemistry Letters **12**(34), 8246 (2021).
- [21] T. Blanton, S. Misture, N. Dontula, and S. Zdziszynski, "In situ high-temperature x-ray diffraction characterization of silver sulfide, Ag_2S ", Powder Diffraction **26**(2), 114 (2011).
- [22] A. J. Frueh, "The crystallography of silver sulfide, Ag_2S ", Zeitschrift für Kristallographie-Crystalline Materials **110**(1-6), 136 (1958).
- [23] Y. He, T. Day, T. Zhang, H. Liu, X. Shi, L. Chen, and G. J. Snyder, "High thermoelectric performance in non-toxic earth-abundant copper sulfide", Advanced Materials **26**(23), 3974 (2014).

- [24] Y. Qin, Y. Xiao, D. Wang, B. Qin, Z. Huang, and L.-D. Zhao, "An approach of enhancing thermoelectric performance for p-type pbs: Decreasing electronic thermal conductivity", Journal of Alloys and Compounds **820**, 153453 (2020).
- [25] Y. Xiao, D. Wang, Y. Zhang, C. Chen, S. Zhang, K. Wang, G. Wang, S. J. Pennycook, G. J. Snyder, H. Wu, et al., "Band sharpening and band alignment enable high quality factor to enhance thermoelectric performance in n-type pbs", Journal of the American Chemical Society **142**(8), 4051 (2020).
- [26] Z. Chen, X. Guo, F. Zhang, Q. Shi, M. Tang, and R. Ang, "Routes for advancing sn te thermoelectrics", Journal of Materials Chemistry A **8**(33), 16790 (2020).
- [27] X. Gao and M. S. Daw, "Investigation of band inversion in (pb, sn) te alloys using ab initio calculations", Physical Review B **77**(3), 033103 (2008).
- [28] R. Pathak, D. Sarkar, and K. Biswas, "Enhanced band convergence and ultra-low thermal conductivity lead to high thermoelectric performance in sn te", Angewandte Chemie International Edition **60**(32), 17686 (2021).
- [29] A. Banik, U. S. Shenoy, S. Saha, U. V. Waghmare, and K. Biswas, "High power factor and enhanced thermoelectric performance of sn te-aginte₂: synergistic effect of resonance level and valence band convergence", Journal of the American Chemical Society **138**(39), 13068 (2016).
- [30] Y. Zhang, J. Sun, J. Shuai, X. Tang, and G. Tan, "Lead-free sn te-based compounds as advanced thermoelectrics", Materials Today Physics **19**, 100405 (2021).
- [31] D. Sarkar, T. Ghosh, A. Banik, S. Roychowdhury, D. Sanyal, and K. Biswas, "Highly converged valence bands and ultralow lattice thermal conductivity for high-performance sn te thermoelectrics", Angewandte Chemie International Edition **59**(27), 11115 (2020).

- [32] R. Brebrick and A. Strauss, "Anomalous thermoelectric power as evidence for two-valence bands in SnTe ", Physical Review **131**(1), 104 (1963).
- [33] W. Xu, H. Yang, C. Liu, Z. Zhang, C. Chen, Z. Ye, Z. Lu, X. Wang, J. Gao, J. Chen, et al., "Optimized electronic bands and ultralow lattice thermal conductivity in Ag and Y codoped SnTe ", ACS Applied Materials & Interfaces **13**(28), 32876 (2021).
- [34] M. H. Lee, D.-G. Byeon, J.-S. Rhyee, and B. Ryu, "Defect chemistry and enhancement of thermoelectric performance in Ag -doped $\text{Sn}_{1+\delta}\text{Ag}_x\text{Te}$ ", Journal of Materials Chemistry A **5**(5), 2235 (2017).
- [35] A. Van der Lee and J. De Boer, "Redetermination of the structure of hessite, Ag_2Te ", Acta Crystallographica Section C: Crystal Structure Communications **49**(8), 1444 (1993).
- [36] J. Yu and H. Yun, "Reinvestigation of the low-temperature form of Ag_2Se (naumannite) based on single-crystal data", Acta Crystallographica Section E: Structure Reports Online **67**(9), i45 (2011).
- [37] J. Brorsson. Unlocking the potential of a caged star: Thermoelectric quaternary clathrates (Chalmers Tekniska Hogskola (Sweden), 2021).
- [38] D. Enescu, "Thermoelectric energy harvesting: basic principles and applications", Green energy advances **1** (2019).
- [39] K. Ebrahimi, G. F. Jones, and A. S. Fleischer, "A review of data center cooling technology, operating conditions and the corresponding low-grade waste heat recovery opportunities", Renewable and Sustainable Energy Reviews **31**, 622 (2014).
- [40] H. Jouhara, N. Khordehgah, S. Almahmoud, B. Delpech, A. Chauhan, and S. A. Tassou, "Waste heat recovery technologies and applications", Thermal Science and Engineering Progress **6**, 268 (2018).

- [41] T. C. Holgate, R. Bennett, T. Hammel, T. Caillat, S. Keyser, and B. Sievers, "Increasing the efficiency of the multi-mission radioisotope thermoelectric generator", Journal of Electronic Materials **44**, 1814 (2015).
- [42] J. Ding, W. Zhao, W. Jin, C.-a. Di, and D. Zhu, "Advanced thermoelectric materials for flexible cooling application", Advanced Functional Materials **31**(20), 2010695 (2021).
- [43] F. J. DiSalvo, "Thermoelectric cooling and power generation", Science **285**(5428), 703 (1999).
- [44] A. Z. Sahin, K. G. Ismaila, B. S. Yilbas, and A. Al-Sharafi, "A review on the performance of photovoltaic/thermoelectric hybrid generators", International Journal of Energy Research **44**(5), 3365 (2020).
- [45] J. Recatala-Gomez, A. Suwardi, I. Nandhakumar, A. Abutaha, and K. Hippalgaonkar, "Toward accelerated thermoelectric materials and process discovery", ACS Applied Energy Materials **3**(3), 2240 (2020).
- [46] T. Parashchuk, B. Wiendlocha, O. Cherniushok, R. Knura, and K. T. Wojciechowski, "High thermoelectric performance of p-type pbte enabled by the synergy of resonance scattering and lattice softening", ACS Applied Materials & Interfaces **13**(41), 49027 (2021).
- [47] S. Roychowdhury, T. Ghosh, R. Arora, M. Samanta, L. Xie, N. K. Singh, A. Soni, J. He, U. V. Waghmare, and K. Biswas, "Enhanced atomic ordering leads to high thermoelectric performance in agsbte₂", Science **371**(6530), 722 (2021).
- [48] B. Zhu, X. Liu, Q. Wang, Y. Qiu, Z. Shu, Z. Guo, Y. Tong, J. Cui, M. Gu, and J. He, "Realizing record high performance in n-type bi₂te₃-based thermoelectric materials", Energy & Environmental Science **13**(7), 2106 (2020).

- [49] Y. Yu, M. Cagnoni, O. Cojocaru-Mirédin, and M. Wuttig, “Chalcogenide thermoelectrics empowered by an unconventional bonding mechanism”, Advanced Functional Materials **30**(8), 1904862 (2020).
- [50] I. T. Witting, T. C. Chasapis, F. Ricci, M. Peters, N. A. Heinz, G. Hautier, and G. J. Snyder, “The thermoelectric properties of bismuth telluride”, Advanced Electronic Materials **5**(6), 1800904 (2019).
- [51] T. J. Seebeck. Magnetische polarisation der metalle und erze durch temperatur-differenz. 70 (W. Engelmann, 1895).
- [52] N. Jaziri, A. Boughamoura, J. Müller, B. Mezghani, F. Tounsi, and M. Ismail, “A comprehensive review of thermoelectric generators: Technologies and common applications”, Energy Reports **6**, 264 (2020).
- [53] H. Goldsmid, A. Sheard, and D. Wright, “The performance of bismuth telluride thermojunctions”, British Journal of Applied Physics **9**(9), 365 (1958).
- [54] H. Ibach and H. Lüth. Solid-state physics: an introduction to principles of materials science (Springer Science & Business Media, 2009).
- [55] S. I. Kim, K. H. Lee, H. A. Mun, H. S. Kim, S. W. Hwang, J. W. Roh, D. J. Yang, W. H. Shin, X. S. Li, Y. H. Lee, et al., “Dense dislocation arrays embedded in grain boundaries for high-performance bulk thermoelectrics”, Science **348**(6230), 109 (2015).
- [56] G. Tan, F. Shi, S. Hao, L.-D. Zhao, H. Chi, X. Zhang, C. Uher, C. Wolverton, V. P. Dravid, and M. G. Kanatzidis, “Non-equilibrium processing leads to record high thermoelectric figure of merit in pbte–srte”, Nature communications **7**(1), 12167 (2016).
- [57] M. Cutler and N. F. Mott, “Observation of anderson localization in an electron gas”, Physical Review **181**(3), 1336 (1969).
- [58] X.-L. Shi, J. Zou, and Z.-G. Chen, “Advanced thermoelectric design: from materials and structures to devices”, Chemical Reviews **120**(15), 7399 (2020).

- [59] J. P. Heremans, B. Wiendlocha, and A. M. Chamoire, “Resonant levels in bulk thermoelectric semiconductors”, Energy & Environmental Science **5**(2), 5510 (2012).
- [60] Y. Pei, X. Shi, A. LaLonde, H. Wang, L. Chen, and G. J. Snyder, “Convergence of electronic bands for high performance bulk thermoelectrics”, Nature **473**(7345), 66 (2011).
- [61] X. Zianni and D. Narducci, “Parametric modeling of energy filtering by energy barriers in thermoelectric nanocomposites”, Journal of Applied Physics **117**(3), 035102 (2015).
- [62] J. P. Heremans, C. M. Thrush, and D. T. Morelli, “Thermopower enhancement in pbte with pb precipitates”, Journal of Applied Physics **98**(6), 063703 (2005).
- [63] H. Naithani and T. Dasgupta, “Critical analysis of single band modeling of thermoelectric materials”, ACS Applied Energy Materials **3**(3), 2200 (2019).
- [64] D. T. Morelli and G. A. Slack, “High lattice thermal conductivity solids”, High thermal conductivity materials pp. 37–68 (2006).
- [65] V. Q. Nguyen, J. Kim, and S. Cho, “A review of snse: Growth and thermoelectric properties”, Journal of the Korean Physical Society **72**, 841 (2018).
- [66] H. J. Goldsmid. Introduction to thermoelectricity, vol. 121 (Springer, 2016).
- [67] Y. Pei, Z. M. Gibbs, A. Gloskovskii, B. Balke, W. G. Zeier, and G. J. Snyder, “Optimum carrier concentration in n-type pbte thermoelectrics”, Advanced energy materials **4**(13), 1400486 (2014).
- [68] L. Huang, R. He, S. Chen, H. Zhang, K. Dahal, H. Zhou, H. Wang, Q. Zhang, and Z. Ren, “A new n-type half-heusler thermoelectric material nbcosb”, Materials Research Bulletin **70**, 773 (2015).

- [69] S. Wang, J. Yang, T. Toll, J. Yang, W. Zhang, and X. Tang, “Conductivity-limiting bipolar thermal conductivity in semiconductors”, Scientific reports **5**(1), 1 (2015).
- [70] K. Biswas, J. He, G. Wang, S.-H. Lo, C. Uher, V. P. Dravid, and M. G. Kanatzidis, “High thermoelectric figure of merit in nanostructured p-type pbte–mte (m= ca, ba)”, Energy & Environmental Science **4**(11), 4675 (2011).
- [71] R. Venkatasubramanian, E. Siivola, T. Colpitts, and B. O’quinn, “Thin-film thermoelectric devices with high room-temperature figures of merit”, Nature **413**(6856), 597 (2001).
- [72] N. Jakhar, N. Bisht, A. Katre, and S. Singh, “Synergistic approach toward a reproducible high zt in n-type and p-type superionic thermoelectric ag₂te”, ACS Applied Materials & Interfaces **14**(48), 53916 (2022).
- [73] J. Yu, C. Fu, Y. Liu, K. Xia, U. Aydemir, T. C. Chasapis, G. J. Snyder, X. Zhao, and T. Zhu, “Unique role of refractory ta alloying in enhancing the figure of merit of nbfesb thermoelectric materials”, Advanced Energy Materials **8**(1), 1701313 (2018).
- [74] C. Rodenkirchen, M. Cagnoni, S. Jakobs, Y. Cheng, J. Keutgen, Y. Yu, M. Wuttig, and O. Cojocaru-Mirédin, “Employing interfaces with metavalently bonded materials for phonon scattering and control of the thermal conductivity in tags-x thermoelectric materials”, Advanced Functional Materials **30**(17), 1910039 (2020).
- [75] L.-D. Zhao, H. Wu, S. Hao, C.-I. Wu, X. Zhou, K. Biswas, J. He, T. P. Hogan, C. Uher, C. Wolverton, et al., “All-scale hierarchical thermoelectrics: Mgte in pbte facilitates valence band convergence and suppresses bipolar thermal transport for high performance”, Energy & Environmental Science **6**(11), 3346 (2013).
- [76] Y. Zheng, Q. Zhang, X. Su, H. Xie, S. Shu, T. Chen, G. Tan, Y. Yan, X. Tang, C. Uher, et al., “Mechanically robust bisbte alloys with superior thermoelectric performance: a

- case study of stable hierarchical nanostructured thermoelectric materials”, Advanced Energy Materials **5**(5), 1401391 (2015).
- [77] G. Tan, S. Wang, H. Li, Y. Yan, and X. Tang, “Enhanced thermoelectric performance in zinc substituted p-type filled skutterudites $\text{CeFe}_{4-x}\text{Zn}_x\text{Sb}_{12}$ ”, Journal of Solid State Chemistry **187**, 316 (2012).
- [78] J.-L. Lan, Y. Liu, Y.-H. Lin, C.-W. Nan, Q. Cai, and X. Yang, “Enhanced thermoelectric performance of In_2O_3 -based ceramics via nanostructuring and point defect engineering”, Scientific Reports **5**(1), 7783 (2015).
- [79] T. Takabatake, K. Suekuni, T. Nakayama, and E. Kaneshita, “Phonon-glass electron-crystal thermoelectric clathrates: Experiments and theory”, Reviews of Modern Physics **86**(2), 669 (2014).
- [80] G. Dennler, R. Chmielowski, S. Jacob, F. Capet, P. Roussel, S. Zastrow, K. Nielsch, I. Opahle, and G. K. Madsen, “Are binary copper sulfides/selenides really new and promising thermoelectric materials?”, Advanced Energy Materials **4**(9), 1301581 (2014).
- [81] R. J. Quinn and J.-W. G. Bos, “Advances in half-Heusler alloys for thermoelectric power generation”, Materials Advances **2**(19), 6246 (2021).
- [82] Y. Yin, B. Tudu, and A. Tiwari, “Recent advances in oxide thermoelectric materials and modules”, Vacuum **146**, 356 (2017).
- [83] M. Ohtaki, “Recent aspects of oxide thermoelectric materials for power generation from mid-to-high temperature heat source”, Journal of the Ceramic Society of Japan **119**(1395), 770 (2011).
- [84] J. He, Y. Liu, and R. Funahashi, “Oxide thermoelectrics: The challenges, progress, and outlook”, Journal of Materials Research **26**(15), 1762 (2011).

- [85] M. Mikami, K. Chong, Y. Miyazaki, T. Kajitani, T. Inoue, S. Sodeoka, and R. Funahashi, "Bi-substitution effects on crystal structure and thermoelectric properties of $\text{Ca}_3\text{Co}_4\text{O}_9$ single crystals", Japanese journal of applied physics **45**(5R), 4131 (2006).
- [86] H. Yakabe, K. Kikuchi, I. Terasaki, Y. Sasago, and K. Uchinokura. Thermoelectric properties of transition-metal oxide NaCo_2O_4 system. In XVI ICT'97. Proceedings ICT'97. 16th International Conference on Thermoelectrics (Cat. No. 97TH8291), pp. 523–527 (IEEE, 1997).
- [87] P. Jood, R. J. Mehta, Y. Zhang, G. Peleckis, X. Wang, R. W. Siegel, T. Borca-Tasciuc, S. X. Dou, and G. Ramanath, "Al-doped zinc oxide nanocomposites with enhanced thermoelectric properties", Nano letters **11**(10), 4337 (2011).
- [88] G. Nolas, X. Lin, J. Martin, M. Beekman, and H. Wang, "Open-structured materials: Skutterudites and clathrates", Journal of electronic materials **38**, 1052 (2009).
- [89] G. A. Slack. New materials and performance limits for thermoelectric cooling. In CRC handbook of thermoelectrics, pp. 407–440 (CRC press, 2018).
- [90] A. Saramat, G. Svensson, A. Palmqvist, C. Stiewe, E. Müller, D. Platzek, S. Williams, D. Rowe, J. Bryan, and G. Stucky, "Large thermoelectric figure of merit at high temperature in czochralski-grown clathrate $\text{Ba}_8\text{Ga}_{16}\text{Ge}_{30}$ ", Journal of Applied Physics **99**(2), 023708 (2006).
- [91] X. Shi, J. Yang, J. R. Salvador, M. Chi, J. Y. Cho, H. Wang, S. Bai, J. Yang, W. Zhang, and L. Chen, "Multiple-filled skutterudites: high thermoelectric figure of merit through separately optimizing electrical and thermal transports", Journal of the American Chemical Society **133**(20), 7837 (2011).
- [92] M. Wuttig and N. Yamada, "Phase-change materials for rewriteable data storage", Nature materials **6**(11), 824 (2007).

- [93] H. Zhang, C.-X. Liu, X.-L. Qi, X. Dai, Z. Fang, and S.-C. Zhang, “Topological insulators in Bi_2Se_3 , Bi_2Te_3 and Sb_2Te_3 with a single Dirac cone on the surface”, Nature physics **5**(6), 438 (2009).
- [94] J. Mao, Z. Liu, J. Zhou, H. Zhu, Q. Zhang, G. Chen, and Z. Ren, “Advances in thermoelectrics”, Advances in Physics **67**(2), 69 (2018).
- [95] S. Abbey, H. Jang, B. Frimpong, N. Kumar, W. H. Nam, J. H. Park, C. V. Nguyen, H. Shin, J. Y. Song, S.-D. Park, et al., “Twisted grain boundary leads to high thermoelectric performance in tellurium crystals”, Energy & Environmental Science (2023).
- [96] D. An, S. Chen, X. Zhai, Y. Yu, W. Fan, T. Zhang, Y. Liu, Y. Wu, W. Wang, and G. J. Snyder, “High-performance p-type elemental Te thermoelectric materials enabled by the synergy of carrier tuning and phonon engineering”, Journal of Materials Chemistry A **8**(24), 12156 (2020).
- [97] H. Peng, N. Kioussis, and G. J. Snyder, “Elemental tellurium as a chiral p-type thermoelectric material”, Physical Review B **89**(19), 195206 (2014).
- [98] C. Zhou, Y. K. Lee, Y. Yu, S. Byun, Z.-Z. Luo, H. Lee, B. Ge, Y.-L. Lee, X. Chen, J. Y. Lee, et al., “Polycrystalline SnSe with a thermoelectric figure of merit greater than the single crystal”, Nature materials **20**(10), 1378 (2021).
- [99] R. J. Korkosz, T. C. Chasapis, S.-h. Lo, J. W. Doak, Y. J. Kim, C.-I. Wu, E. Hatzikraniotis, T. P. Hogan, D. N. Seidman, C. Wolverton, et al., “High ZT in p-type (PbTe) 1–2 x (PbSe) x (PbS) x thermoelectric materials”, Journal of the American Chemical Society **136**(8), 3225 (2014).
- [100] H. Liu, X. Shi, F. Xu, L. Zhang, W. Zhang, L. Chen, Q. Li, C. Uher, T. Day, and G. J. Snyder, “Copper ion liquid-like thermoelectrics”, Nature materials **11**(5), 422 (2012).

- [101] K. Zhao, C. Zhu, M. Zhu, H. Chen, J. Lei, Q. Ren, T.-R. Wei, P. Qiu, F. Xu, L. Chen, et al., “Structural modularization of Cu_2Te leading to high thermoelectric performance near the mott–ioffe–regel limit”, *Advanced Materials* **34**(19), 2108573 (2022).
- [102] S. Yang, Z. Gao, P. Qiu, J. Liang, T.-R. Wei, T. Deng, J. Xiao, X. Shi, and L. Chen, “Ductile $\text{Ag}_2\text{S}_7\text{Te}_3$ with excellent shape-conformability and high thermoelectric performance”, *Advanced Materials* **33**(10), 2007681 (2021).
- [103] J. Liang, T. Wang, P. Qiu, S. Yang, C. Ming, H. Chen, Q. Song, K. Zhao, T.-R. Wei, D. Ren, et al., “Flexible thermoelectrics: from silver chalcogenides to full-inorganic devices”, *Energy & Environmental Science* **12**(10), 2983 (2019).
- [104] X. Shen, C.-C. Yang, Y. Liu, G. Wang, H. Tan, Y.-H. Tung, G. Wang, X. Lu, J. He, and X. Zhou, “High-temperature structural and thermoelectric study of argyrodite $\text{Ag}_8\text{Ge}_6\text{S}_6$ ”, *ACS applied materials & interfaces* **11**(2), 2168 (2018).
- [105] K. S. Weldert, W. G. Zeier, T. W. Day, M. Panthofer, G. J. Snyder, and W. Tremel, “Thermoelectric transport in $\text{Cu}_7\text{P}_6\text{S}_6$ with high copper ionic mobility”, *Journal of the American Chemical Society* **136**(34), 12035 (2014).
- [106] D. Wu, S. Huang, D. Feng, B. Li, Y. Chen, J. Zhang, and J. He, “Revisiting Ag_2CrSe_2 as a promising thermoelectric material”, *Physical Chemistry Chemical Physics* **18**(34), 23872 (2016).
- [107] Y. Y. Gurevich and A. Ivanov-Shits. Semiconductor properties of superionic materials. In *Semiconductors and Semimetals*, vol. 26, pp. 229–372 (Elsevier, 1988).
- [108] M. Faraday. Editors: R. and J. Taylor. In *Experimental researches in electricity*, vol. 1 (University of London, 1849).
- [109] B. Jiang, P. Qiu, H. Chen, Q. Zhang, K. Zhao, D. Ren, X. Shi, and L. Chen, “An argyrodite-type $\text{Ag}_9\text{Ge}_6\text{S}_6$ liquid-like material with ultralow thermal conductivity and high thermoelectric performance”, *Chemical Communications* **53**(85), 11658 (2017).

- [110] J. P. Perdew, K. Burke, and M. Ernzerhof, “Generalized gradient approximation made simple”, Physical review letters **77**(18), 3865 (1996).
- [111] W. Qiu, P. Lu, X. Yuan, F. Xu, L. Wu, X. Ke, H. Liu, J. Yang, X. Shi, L. Chen, et al., “Structure family and polymorphous phase transition in the compounds with soft sublattice Cu_2Se as an example”, The Journal of Chemical Physics **144**(19), 194502 (2016).
- [112] S. Kashida and J. Akai, “X-ray diffraction and electron microscopy studies of the room-temperature structure of Cu_2Se ”, Journal of Physics C: Solid State Physics **21**(31), 5329 (1988).
- [113] E. Eikeland, A. B. Blichfeld, K. A. Borup, K. Zhao, J. Overgaard, X. Shi, L. Chen, and B. B. Iversen, “Crystal structure across the β to α phase transition in thermoelectric Cu_{2-x}Se ”, IUCrJ **4**(4), 476 (2017).
- [114] Q. Hu, Z. Zhu, Y. Zhang, X.-J. Li, H. Song, and Y. Zhang, “Remarkably high thermoelectric performance of $\text{Cu}_{2-x}\text{Li}_x\text{Se}$ bulks with nanopores”, Journal of materials chemistry A **6**(46), 23417 (2018).
- [115] Y. He, T. Zhang, X. Shi, S.-H. Wei, and L. Chen, “High thermoelectric performance in copper telluride”, NPG Asia Materials **7**(8), e210 (2015).
- [116] K. Zhao, A. B. Blichfeld, H. Chen, Q. Song, T. Zhang, C. Zhu, D. Ren, R. Hanus, P. Qiu, B. B. Iversen, et al., “Enhanced thermoelectric performance through tuning bonding energy in $\text{Cu}_2\text{Se}_{1-x}\text{S}_x$ liquid-like materials”, Chemistry of Materials **29**(15), 6367 (2017).
- [117] K. Zhao, P. Qiu, Q. Song, A. B. Blichfeld, E. Eikeland, D. Ren, B. Ge, B. B. Iversen, X. Shi, and L. Chen, “Ultrahigh thermoelectric performance in $\text{Cu}_{2-y}\text{Se}_{0.5}\text{S}_{0.5}$ liquid-like materials”, Materials Today Physics **1**, 14 (2017).

- [118] S. Kashida, N. Watanabe, T. Hasegawa, H. Iida, M. Mori, and S. Savrasov, "Electronic structure of ag_2s , band calculation and photoelectron spectroscopy", Solid State Ionics **158**(1-2), 167 (2003).
- [119] Z. Jahangirli, O. Alekperov, and Q. Eyyubov, "Ab-initio investigation of the electronic structure, optical properties, and lattice dynamics of $\beta\text{-ag}_2\text{te}$ ", physica status solidi (b) **255**(12), 1800344 (2018).
- [120] A. Hasegawa, "On the electronic structure of ag chalcogenides", Solid State Ionics **15**(1), 81 (1985).
- [121] Y. Pei, N. A. Heinz, and G. J. Snyder, "Alloying to increase the band gap for improving thermoelectric properties of ag_2te ", Journal of Materials Chemistry **21**(45), 18256 (2011).
- [122] H. Zhu, J. Luo, H. Zhao, and J. Liang, "Enhanced thermoelectric properties of p-type ag_2te by cu substitution", Journal of Materials Chemistry A **3**(19), 10303 (2015).
- [123] W. Tuo, C. Hong-Yi, Q. Peng-Fei, S. Xun, C. Li-Dong, et al., "Thermoelectric properties of ag_2s superionic conductor with intrinsically low lattice thermal conductivity" (2019).
- [124] F. Aliev, E. Kerimova, and S. Aliev, "Electrical and thermoelectric properties of p- ag_2te ", Semiconductors **36**, 869 (2002).
- [125] W. Kuhs, R. Nitsche, and K. Scheunemann, "The argyrodites a new family of tetrahedrally close-packed structures", Materials Research Bulletin **14**(2), 241 (1979).
- [126] J. Liu, P. Wang, M. Wang, R. Xu, J. Zhang, J. Liu, D. Li, N. Liang, Y. Du, G. Chen, et al., "Achieving high thermoelectric performance with pb and zn codoped polycrystalline snse via phase separation and nanostructuring strategies", Nano Energy **53**, 683 (2018).

- [127] R. Chen, P. Qiu, B. Jiang, P. Hu, Y. Zhang, J. Yang, D. Ren, X. Shi, and L. Chen, “Significantly optimized thermoelectric properties in high-symmetry cubic Cu_7PSe_6 compounds via entropy engineering”, *Journal of Materials Chemistry A* **6**(15), 6493 (2018).
- [128] S. Schwarzmüller, D. Souchay, D. Günther, A. Gocke, I. Dovgaliuk, S. A. Miller, G. J. Snyder, and O. Oeckler, “Argyrodite type Cu_8GeSe_6 -type temperature dependent crystal structure and thermoelectric properties”, *Zeitschrift für anorganische und allgemeine Chemie* **644**(24), 1915 (2018).
- [129] W. Li, S. Lin, B. Ge, J. Yang, W. Zhang, and Y. Pei, “Low sound velocity contributing to the high thermoelectric performance of Ag_8SbSe_6 ”, *Advanced science* **3**(11), 1600196 (2016).
- [130] S. Lin, W. Li, S. Li, X. Zhang, Z. Chen, Y. Xu, Y. Chen, and Y. Pei, “High thermoelectric performance of Ag_9GeSe_6 enabled by low cutoff frequency of acoustic phonons”, *Joule* **1**(4), 816 (2017).
- [131] G. J. Snyder and E. S. Toberer, “Complex thermoelectric materials”, *Nature materials* **7**(2), 105 (2008).
- [132] Y. Yu, D.-S. He, S. Zhang, O. Cojocaru-Mirédin, T. Schwarz, A. Stoffers, X.-Y. Wang, S. Zheng, B. Zhu, C. Scheu, *et al.*, “Simultaneous optimization of electrical and thermal transport properties of $\text{Bi}_0.5\text{Sb}_{1.5}\text{Te}_3$ thermoelectric alloy by twin boundary engineering”, *Nano Energy* **37**, 203 (2017).
- [133] C. Chang, M. Wu, D. He, Y. Pei, C.-F. Wu, X. Wu, H. Yu, F. Zhu, K. Wang, Y. Chen, *et al.*, “3d charge and 2d phonon transports leading to high out-of-plane z_t in n-type SbSe crystals”, *Science* **360**(6390), 778 (2018).

- [134] L.-D. Zhao, S.-H. Lo, Y. Zhang, H. Sun, G. Tan, C. Uher, C. Wolverton, V. P. Dravid, and M. G. Kanatzidis, “Ultralow thermal conductivity and high thermoelectric figure of merit in sntse crystals”, nature **508**(7496), 373 (2014).
- [135] J. Li, X. Zhang, Z. Chen, S. Lin, W. Li, J. Shen, I. T. Witting, A. Faghaninia, Y. Chen, A. Jain, et al., “Low-symmetry rhombohedral gete thermoelectrics”, Joule **2**(5), 976 (2018).
- [136] Y. Wu, Z. Chen, P. Nan, F. Xiong, S. Lin, X. Zhang, Y. Chen, L. Chen, B. Ge, and Y. Pei, “Lattice strain advances thermoelectrics”, Joule **3**(5), 1276 (2019).
- [137] X. Tan, H. Shao, J. He, G. Liu, J. Xu, J. Jiang, and H. Jiang, “Band engineering and improved thermoelectric performance in m-doped snte (m= mg, mn, cd, and hg)”, Physical Chemistry Chemical Physics **18**(10), 7141 (2016).
- [138] J. He, X. Tan, J. Xu, G.-Q. Liu, H. Shao, Y. Fu, X. Wang, Z. Liu, J. Xu, H. Jiang, et al., “Valence band engineering and thermoelectric performance optimization in snte by mn-alloying via a zone-melting method”, Journal of Materials Chemistry A **3**(39), 19974 (2015).
- [139] Q. Zhang, B. Liao, Y. Lan, K. Lukas, W. Liu, K. Esfarjani, C. Opeil, D. Broido, G. Chen, and Z. Ren, “High thermoelectric performance by resonant dopant indium in nanostructured snte”, Proceedings of the National Academy of Sciences **110**(33), 13261 (2013).
- [140] M. Aminzare, Y.-C. Tseng, A. Ramakrishnan, K.-H. Chen, and Y. Mozharivskyj, “Effect of single metal doping on the thermoelectric properties of snte”, Sustainable Energy & Fuels **3**(1), 251 (2019).
- [141] Y. Liu, X. Zhang, P. Nan, B. Zou, Q. Zhang, Y. Hou, S. Li, Y. Gong, Q. Liu, B. Ge, et al., “Improved solubility in metavalently bonded solid leads to band alignment, ul-

- tralow thermal conductivity, and high thermoelectric performance in snte”, Advanced Functional Materials **32**(47), 2209980 (2022).
- [142] W. Li, L. Zheng, B. Ge, S. Lin, X. Zhang, Z. Chen, Y. Chang, and Y. Pei, “Promoting snte as an eco-friendly solution for p-pbte thermoelectric via band convergence and interstitial defects”, Advanced Materials **29**(17), 1605887 (2017).
- [143] J. S. Benjamin, “Dispersion strengthened superalloys by mechanical alloying”, Metallurgical transactions **1**(10), 2943 (1970).
- [144] J. Capps, F. Drymiotis, S. Lindsey, and T. Tritt, “Significant enhancement of the dimensionless thermoelectric figure of merit of the binary ag₂te”, Philosophical magazine letters **90**(9), 677 (2010).
- [145] R. D. Cowan, “Pulse method of measuring thermal diffusivity at high temperatures”, Journal of Applied Physics **34**(4), 926 (1963).
- [146] L. Dusza, “Combined solution of the simultaneous heat loss and finite pulse corrections with the laser flash method”, High Temperatures. High Pressures (Print) **27**(5), 467 (1995).
- [147] P. Giannozzi, S. Baroni, N. Bonini, M. Calandra, R. Car, C. Cavazzoni, D. Ceresoli, G. L. Chiarotti, M. Cococcioni, I. Dabo, et al., “Quantum espresso: a modular and open-source software project for quantum simulations of materials”, Journal of physics: Condensed matter **21**(39), 395502 (2009).
- [148] W. Zhang, R. Yu, W. Feng, Y. Yao, H. Weng, X. Dai, and Z. Fang, “Topological aspect and quantum magnetoresistance of β - ag₂ te”, Physical review letters **106**(15), 156808 (2011).
- [149] A. Togo and I. Tanaka, “First principles phonon calculations in materials science”, Scripta Materialia **108**, 1 (2015).

- [150] P. Giannozzi, O. Andreussi, T. Brumme, O. Bunau, M. B. Nardelli, M. Calandra, R. Car, C. Cavazzoni, D. Ceresoli, M. Cococcioni, et al., “Advanced capabilities for materials modelling with quantum espresso”, Journal of physics: Condensed matter **29**(46), 465901 (2017).
- [151] D. Vanderbilt, “Soft self-consistent pseudopotentials in a generalized eigenvalue formalism”, Physical review B **41**(11), 7892 (1990).
- [152] H. J. Monkhorst and J. D. Pack, “Special points for brillouin-zone integrations”, Physical review B **13**(12), 5188 (1976).
- [153] L. Rogers, “Valence band structure of snte”, Journal of Physics D: Applied Physics **1**(7), 845 (1968).
- [154] P. Taylor and C. Wood, “Thermoelectric properties of ag₂te”, Journal of Applied Physics **32**(1), 1 (1961).
- [155] D. Cadavid, M. Ib, A. Shavel, O. J. Dura, M. L. De La Torre, and A. Cabot, “Organic ligand displacement by metal salts to enhance nanoparticle functionality: thermoelectric properties of ag₂te”, Journal of Materials Chemistry A **1**(15), 4864 (2013).
- [156] F. Aliev, “Electrical and thermoelectric properties of p-ag₂te in the β phase”, Semiconductors **37**(9), 1057 (2003).
- [157] R. Dalven and R. Gill, “Energy gap in β - ag₂te”, Physical Review **143**(2), 666 (1966).
- [158] C. Wood, V. Harrap, and W. Kane, “Degeneracy in ag₂te”, Physical Review **121**(4), 978 (1961).
- [159] Y. Chang, J. Guo, Y.-Q. Tang, Y.-X. Zhang, J. Feng, and Z.-H. Ge, “Facile synthesis of ag₂te nanowires and thermoelectric properties of ag₂te polycrystals sintered by spark plasma sintering”, CrystEngComm **21**(11), 1718 (2019).

- [160] D.-y. Jung, K. Kurosaki, Y. Ohishi, H. Muta, and S. Yamanaka, “Effect of phase transition on the thermoelectric properties of ag_2te ”, Materials Transactions pp. E-M2012815 (2012).
- [161] M. Fujikane, K. Kurosaki, H. Muta, and S. Yamanaka, “Thermoelectric properties of α - and β - ag_2te ”, Journal of alloys and compounds **393**(1-2), 299 (2005).
- [162] F. Aliev and V. Eminova, “Dependence of the spectra of charge carriers on the concentration of defects in silver telluride”, Physics of the Solid State **57**(7), 1325 (2015).
- [163] X. Shi, H. Chen, F. Hao, R. Liu, T. Wang, P. Qiu, U. Burkhardt, Y. Grin, and L. Chen, “Room-temperature ductile inorganic semiconductor”, Nature Materials **17**(5), 421 (2018).
- [164] I. Malik, T. Srivastava, K. K. Surthi, C. Gayner, and K. K. Kar, “Enhanced thermoelectric performance of n-type bi_2te_3 alloyed with low cost and highly abundant sulfur”, Materials Chemistry and Physics **255**, 123598 (2020).
- [165] D.-H. Kim and T. Mitani, “Thermoelectric properties of fine-grained bi_2te_3 alloys”, Journal of Alloys and Compounds **399**(1-2), 14 (2005).
- [166] X. Shi, C. Sun, Z. Bu, X. Zhang, Y. Wu, S. Lin, W. Li, A. Faghaninia, A. Jain, and Y. Pei, “Revelation of inherently high mobility enables mg_3sb_2 as a sustainable alternative to n- bi_2te_3 thermoelectrics”, Advanced Science **6**(16), 1802286 (2019).
- [167] T. Mao, P. Qiu, P. Hu, X. Du, K. Zhao, T.-R. Wei, J. Xiao, X. Shi, and L. Chen, “Decoupling thermoelectric performance and stability in liquid-like thermoelectric materials”, Advanced Science **7**(1), 1901598 (2020).
- [168] T. Mao, P. Qiu, X. Du, P. Hu, K. Zhao, J. Xiao, X. Shi, and L. Chen, “Enhanced thermoelectric performance and service stability of cu_2se via tailoring chemical compositions at multiple atomic positions”, Advanced Functional Materials **30**(6), 1908315 (2020).

- [169] T. P. Bailey and C. Uher, “Potential for superionic conductors in thermoelectric applications”, Current Opinion in Green and Sustainable Chemistry **4**, 58 (2017).
- [170] B. Wu, Y. Zhou, and M. Hu, “Two-channel thermal transport in ordered–disordered superionic Ag_2Te and its traditionally contradictory enhancement by nanotwin boundary”, The Journal of Physical Chemistry Letters **9**(19), 5704 (2018).
- [171] Z.-H. Ge, X. Liu, D. Feng, J. Lin, and J. He, “High-performance thermoelectricity in nanostructured earth-abundant copper sulfides bulk materials”, Advanced Energy Materials **6**(16), 1600607 (2016).
- [172] G. K. Madsen, A. Katre, and C. Bera, “Calculating the thermal conductivity of the silicon clathrates using the quasi-harmonic approximation”, physica status solidi (a) **213**(3), 802 (2016).
- [173] A. Katre, J. Carrete, B. Dongre, G. K. Madsen, and N. Mingo, “Exceptionally strong phonon scattering by b substitution in cubic sic”, Physical review letters **119**(7), 075902 (2017).
- [174] R. Xu, A. Husmann, T. Rosenbaum, M.-L. Saboungi, J. Enderby, and P. Littlewood, “Large magnetoresistance in non-magnetic silver chalcogenides”, Nature **390**(6655), 57 (1997).
- [175] F. Yang, S. Xiong, Z. Xia, F. Liu, C. Han, and D. Zhang, “Two-step synthesis of silver selenide semiconductor with a linear magnetoresistance effect”, Semiconductor Science and Technology **27**(12), 125017 (2012).
- [176] M. Jafarov, “On the nature of charge carrier scattering in Ag_2Se at low temperatures”, Semiconductors **44**(10), 1280 (2010).
- [177] P. Qiu, X. Shi, and L. Chen, “Cu-based thermoelectric materials”, Energy Storage Materials **3**, 85 (2016).

- [178] J. Conn and R. Taylor, "Thermoelectric and crystallographic properties of Ag₂Se", Journal of The Electrochemical Society **107**(12), 977 (1960).
- [179] M. Ferhat and J. Nagao, "Thermoelectric and transport properties of β -Ag₂Se compounds", Journal of Applied Physics **88**(2), 813 (2000).
- [180] F. Aliev, M. Jafarov, and V. Eminova, "Thermoelectric figure of merit of Ag₂Se with Ag and Se excess", Semiconductors **43**(8), 977 (2009).
- [181] H. Duan, Y. Li, K. Zhao, P. Qiu, X. Shi, and L. Chen, "Ultra-fast synthesis for Ag₂Se and CuAgSe thermoelectric materials", Jom **68**(10), 2659 (2016).
- [182] K. H. Lim, K. W. Wong, Y. Liu, Y. Zhang, D. Cadavid, A. Cabot, and K. M. Ng, "Critical role of nanoinclusions in silver selenide nanocomposites as a promising room temperature thermoelectric material", Journal of Materials Chemistry C **7**(9), 2646 (2019).
- [183] R. Simon, R. Bourke, and E. Lougher, "Preparation and thermoelectric properties of β -Ag₂Se", Advanced Energy Conversion **3**(2), 481 (1963).
- [184] H. Hu, Y. Wang, C. Fu, X. Zhao, and T. Zhu, "Achieving metal-like malleability and ductility in Ag₂Te_{1-x}S_x inorganic thermoelectric semiconductors with high mobility", The Innovation **3**(6), 100341 (2022).
- [185] H. Chen, T.-R. Wei, K. Zhao, P. Qiu, L. Chen, J. He, and X. Shi, "Room-temperature plastic inorganic semiconductors for flexible and deformable electronics", InfoMat **3**(1), 22 (2021).
- [186] R. Dalven and R. Gill, "Energy gap in β -Ag₂Se", Physical Review **159**(3), 645 (1967).
- [187] H. Billetter and U. Ruschewitz, "Structural phase transitions in Ag₂Se (naumannite)", Zeitschrift für anorganische und allgemeine Chemie **634**(2), 241 (2008).

- [188] F. Grønvold, S. Stølen, and Y. Semenov, “Heat capacity and thermodynamic properties of silver (i) selenide, *op*-Ag₂Se from 300 to 406 k and of *ci*-Ag₂Se from 406 to 900 k: transitional behavior and formation properties”, Thermochimica acta **399**(1-2), 213 (2003).
- [189] A. Epstein, S. Kulifay, and R. Stearns, “Energy gap of β silver selenide”, Nature **203**(4947), 856 (1964).
- [190] H. W. Henkels, “Thermoelectric power and mobility of carriers in selenium”, Physical Review **77**(5), 734 (1950).
- [191] M. Saleemi, M. S. Toprak, S. Li, M. Johnsson, and M. Muhammed, “Synthesis, processing, and thermoelectric properties of bulk nanostructured bismuth telluride (Bi₂Te₃)”, Journal of Materials Chemistry **22**(2), 725 (2012).
- [192] T. Day, F. Drymiotis, T. Zhang, D. Rhodes, X. Shi, L. Chen, and G. J. Snyder, “Evaluating the potential for high thermoelectric efficiency of silver selenide”, Journal of Materials Chemistry C **1**(45), 7568 (2013).
- [193] H. Naithani and T. Dasgupta, “Critical analysis of single band modeling of thermoelectric materials”, ACS Applied Energy Materials **3**(3), 2200 (2020). <https://doi.org/10.1021/acsaem.9b02015>, URL <https://doi.org/10.1021/acsaem.9b02015>.
- [194] Y. Zhong, J. Tang, H. Liu, Z. Chen, L. Lin, D. Ren, B. Liu, and R. Ang, “Optimized strategies for advancing n-type pbte thermoelectrics: A review”, ACS Applied Materials & Interfaces **12**(44), 49323 (2020).
- [195] X. Zhang, Z. Bu, S. Lin, Z. Chen, W. Li, and Y. Pei, “Gete thermoelectrics”, Joule **4**(5), 986 (2020).
- [196] J. Yang and T. Caillat, “Thermoelectric materials for space and automotive power generation”, MRS bulletin **31**(3), 224 (2006).

- [197] L. Zhang, X.-L. Shi, Y.-L. Yang, and Z.-G. Chen, “Flexible thermoelectric materials and devices: From materials to applications”, Materials Today **46**, 62 (2021).
- [198] P. Junod, H. Hediger, B. Kilchör, and J. Wullschleger, “Metal-non-metal transition in silver chalcogenides”, Philosophical Magazine **36**(4), 941 (1977).
- [199] C. Xiao, J. Xu, K. Li, J. Feng, J. Yang, and Y. Xie, “Superionic phase transition in silver chalcogenide nanocrystals realizing optimized thermoelectric performance”, Journal of the American Chemical Society **134**(9), 4287 (2012).
- [200] X. Li, Y. Lou, K. Jin, L. Fu, P. Xu, Z. Shi, T. Feng, and B. Xu, “Realizing $zT > 2$ in environment-friendly monoclinic Cu_2S –tetragonal Cu_3S_4 nano-phase junctions for thermoelectrics”, Angewandte Chemie International Edition (2022).
- [201] L.-D. Zhao, S.-H. Lo, J. He, H. Li, K. Biswas, J. Androulakis, C.-I. Wu, T. P. Hogan, D.-Y. Chung, V. P. Dravid, et al., “High performance thermoelectrics from earth-abundant materials: enhanced figure of merit in PbTe by second phase nanostructures”, Journal of the American Chemical Society **133**(50), 20476 (2011).
- [202] S. He, Y. Li, L. Liu, Y. Jiang, J. Feng, W. Zhu, J. Zhang, Z. Dong, Y. Deng, J. Luo, et al., “Semiconductor glass with superior flexibility and high room temperature thermoelectric performance”, Science advances **6**(15), eaaz8423 (2020).
- [203] L. Peng, S. Yang, T.-R. Wei, P. Qiu, J. Yang, Z. Zhang, X. Shi, and L. Chen, “Phase-modulated mechanical and thermoelectric properties of $\text{Ag}_2\text{S}_1\text{-xTe}_x$ ductile semiconductors”, Journal of Materiomics **8**(3), 656 (2022).
- [204] Q. Liang, D. Yang, F. Xia, H. Bai, H. Peng, R. Yu, Y. Yan, D. He, S. Cao, G. Van Tendeloo, et al., “Phase-transformation-induced giant deformation in thermoelectric Ag_2Se semiconductor”, Advanced Functional Materials **31**(50), 2106938 (2021).

- [205] R. Sadanaga and S. Sueno, "X-ray study on the α - β transition of Ag_2S ", Mineralogical Journal **5**(2), 124 (1967).
- [206] R. Sharma and Y. Chang, "The Ag-S (silver-sulfur) system", Bulletin of Alloy Phase Diagrams **7**(3), 263 (1986).
- [207] K. Biswas, J. He, Q. Zhang, G. Wang, C. Uher, V. P. Dravid, and M. G. Kanatzidis, "Strained endotaxial nanostructures with high thermoelectric figure of merit", Nature chemistry **3**(2), 160 (2011).
- [208] H. Wang, Z. M. Gibbs, Y. Takagiwa, and G. J. Snyder, "Tuning bands of PbSe for better thermoelectric efficiency", Energy & Environmental Science **7**(2), 804 (2014).
- [209] Y. Tsang and M. L. Cohen, "Calculation of the temperature dependence of the energy gaps in PbTe and SnTe ", Physical Review B **3**(4), 1254 (1971).
- [210] W. Li, Y. Wu, S. Lin, Z. Chen, J. Li, X. Zhang, L. Zheng, and Y. Pei, "Advances in environment-friendly SnTe thermoelectrics", ACS Energy Letters **2**(10), 2349 (2017).
- [211] G. Tan, L.-D. Zhao, F. Shi, J. W. Doak, S.-H. Lo, H. Sun, C. Wolverton, V. P. Dravid, C. Uher, and M. G. Kanatzidis, "High thermoelectric performance of p-type SnTe via a synergistic band engineering and nanostructuring approach", Journal of the American Chemical Society **136**(19), 7006 (2014).
- [212] G. Tan, F. Shi, J. W. Doak, H. Sun, L.-D. Zhao, P. Wang, C. Uher, C. Wolverton, V. P. Dravid, and M. G. Kanatzidis, "Extraordinary role of Hg in enhancing the thermoelectric performance of p-type SnTe ", Energy & Environmental Science **8**(1), 267 (2015).
- [213] R. Al Rahal Al Orabi, N. A. Mecholsky, J. Hwang, W. Kim, J.-S. Rhyee, D. Wee, and M. Fornari, "Band degeneracy, low thermal conductivity, and high thermoelectric figure of merit in SnTe - CdTe alloys", Chemistry of Materials **28**(1), 376 (2016).

- [214] G. Tan, F. Shi, S. Hao, H. Chi, T. P. Bailey, L.-D. Zhao, C. Uher, C. Wolverton, V. P. Dravid, and M. G. Kanatzidis, “Valence band modification and high thermoelectric performance in snte heavily alloyed with mnte”, Journal of the American Chemical Society **137**(35), 11507 (2015).
- [215] X. Xu, J. Cui, L. Fu, Y. Huang, Y. Yu, Y. Zhou, D. Wu, and J. He, “Enhanced thermoelectric performance achieved in snte via the synergy of valence band regulation and fermi level modulation”, ACS Applied Materials & Interfaces **13**(42), 50037 (2021).
- [216] A. Banik, U. S. Shenoy, S. Anand, U. V. Waghmare, and K. Biswas, “Mg alloying in snte facilitates valence band convergence and optimizes thermoelectric properties”, Chemistry of Materials **27**(2), 581 (2015).
- [217] S. Ahmad, A. Singh, S. Bhattacharya, M. Navaneethan, R. Basu, R. Bhatt, P. Sarkar, K. Meshram, A. Debnath, K. Muthe, et al., “Band convergence and phonon scattering mediated improved thermoelectric performance of snte–pbte nanocomposites”, ACS Applied Energy Materials **3**(9), 8882 (2020).
- [218] L. Zhao, J. Wang, J. Li, J. Liu, C. Wang, J. Wang, and X. Wang, “High thermoelectric performance of ag doped snte polycrystalline bulks via the synergistic manipulation of electrical and thermal transport”, Physical Chemistry Chemical Physics **21**(32), 17978 (2019).
- [219] R. Al Rahal Al Orabi, J. Hwang, C.-C. Lin, R. Gautier, B. Fontaine, W. Kim, J.-S. Rhyee, D. Wee, and M. Fornari, “Ultralow lattice thermal conductivity and enhanced thermoelectric performance in snte: Ga materials”, Chemistry of Materials **29**(2), 612 (2017).
- [220] S. Acharya, D. Dey, T. Maitra, A. Soni, and A. Taraphder, “Rare earth doping and effective band-convergence in snte for improved thermoelectric performance”, Applied Physics Letters **113**(19) (2018).

- [221] T. Zhang, W. Pan, S. Ning, N. Qi, Z. Chen, X. Su, and X. Tang, “Vacancy manipulation induced optimal carrier concentration, band convergence and low lattice thermal conductivity in nano-crystalline snte yielding superior thermoelectric performance”, Advanced Functional Materials **33**(10), 2213761 (2023).
- [222] J. Xia, Y. Huang, X. Xu, Y. Yu, Y. Wang, K. Sun, D. Mao, Y. Jiao, H.-F. Li, and J. He, “Fine electron and phonon transports manipulation by mn compensation for high thermoelectric performance of sb₂te₃ (snte) n materials”, Materials Today Physics **33**, 101055 (2023).
- [223] C. Wang, Y. Gong, W. Xiong, X. Yang, Q. Zhang, Y. Liu, S. Li, X. Huang, D. Li, D. Zhang, et al., “Interstitial defects facilitate dense dislocations and band convergence for high thermoelectric performance in snte”, Chemistry of Materials **35**(1), 327 (2022).
- [224] S. K. Kihoi, U. S. Shenoy, J. N. Kahi, H. Kim, D. K. Bhat, and H. S. Lee, “Ultralow lattice thermal conductivity and enhanced mechanical properties of cu and sb co-doped snte thermoelectric material with a complex microstructure evolution”, ACS Sustainable Chemistry & Engineering **10**(4), 1367 (2022).
- [225] X. Xu, J. Cui, Y. Yu, B. Zhu, Y. Huang, L. Xie, D. Wu, and J. He, “Constructing van der waals gaps in cubic-structured snte-based thermoelectric materials”, Energy & Environmental Science **13**(12), 5135 (2020).
- [226] X. Xu, J. Cui, Y. Huang, J. Xia, K. Pan, L. Xie, and J. He, “Microstructural manipulation for enhanced average thermoelectric performance: A case study of tin telluride”, ACS Applied Materials & Interfaces **15**(7), 9656 (2023).
- [227] Z. Chen, Q. Sun, F. Zhang, J. Mao, Y. Chen, M. Li, Z.-G. Chen, and R. Ang, “Mechanical alloying boosted snte thermoelectrics”, Materials Today Physics **17**, 100340 (2021).

- [228] Z. Chen, X. Guo, J. Tang, F. Xiong, W. Li, Y. Chen, and R. Ang, “Extraordinary role of bi for improving thermoelectrics in low-solubility snte–cdte alloys”, ACS applied materials & interfaces **11**(29), 26093 (2019).
- [229] X. Zhang, Z. Wang, B. Zou, M. K. Brod, J. Zhu, T. Jia, G. Tang, G. J. Snyder, and Y. Zhang, “Band engineering snte via trivalent substitutions for enhanced thermoelectric performance”, Chemistry of Materials **33**(24), 9624 (2021).
- [230] G. Jamwal, A. Kumar, M. Warish, S. Chakravarty, S. Muthiah, A. Kandasami, and A. Niazi, “Structural, electronic and thermoelectric properties of snte with dilute co-doping of ag and cu”, Journal of Alloys and Compounds **954**, 170182 (2023).
- [231] W. Xu, Z. Zhang, C. Liu, J. Gao, Z. Ye, C. Chen, Y. Peng, X. Bai, and L. Miao, “Substantial thermoelectric enhancement achieved by manipulating the band structure and dislocations in ag and la co-doped snte”, Journal of Advanced Ceramics **10**(4), 860 (2021).
- [232] L. Zhang, J. Wang, Z. Cheng, Q. Sun, Z. Li, and S. Dou, “Lead-free snte-based thermoelectrics: Enhancement of thermoelectric performance by doping with gd/ag”, Journal of Materials Chemistry A **4**(20), 7936 (2016).
- [233] M. Zhou, Z. M. Gibbs, H. Wang, Y. Han, L. Li, and G. J. Snyder, “Thermoelectric performance of co-doped snte with resonant levels”, Applied Physics Letters **109**(4) (2016).
- [234] F. Guo, B. Cui, M. Guo, J. Wang, J. Cao, W. Cai, and J. Sui, “Enhanced thermoelectric performance of snte alloy with ce and li co-doping”, Materials Today Physics **11**, 100156 (2019).
- [235] L. Wang, S. Chang, S. Zheng, T. Fang, W. Cui, P.-p. Bai, L. Yue, and Z.-G. Chen, “Thermoelectric performance of se/cd codoped snte via microwave solvothermal method”, ACS Applied Materials & Interfaces **9**(27), 22612 (2017).

- [236] Y. Zhang, J. Li, W. Hu, X. Yang, X. Tang, and G. Tan, “Boosting thermoelectric performance of snTe by selective alloying and band tuning”, Materials Today Energy **25**, 100958 (2022).
- [237] H. Tan, L. Guo, G. Wang, H. Wu, X. Shen, B. Zhang, X. Lu, G. Wang, X. Zhang, and X. Zhou, “Synergistic effect of bismuth and indium codoping for high thermoelectric performance of melt spinning snTe alloys”, ACS applied materials & interfaces **11**(26), 23337 (2019).
- [238] S. Li, J. Yang, J. Xin, Q. Jiang, Z. Zhou, H. Hu, B. Sun, A. Basit, and X. Li, “Tailoring the carrier and phonon scattering to enhanced thermoelectric performance of snTe by cation–anion codoping with eco-benign Ca²⁺”, ACS Applied Energy Materials **2**(3), 1997 (2019).
- [239] G. Tan, F. Shi, S. Hao, H. Chi, L.-D. Zhao, C. Uher, C. Wolverton, V. P. Dravid, and M. G. Kanatzidis, “Codoping in snTe: enhancement of thermoelectric performance through synergy of resonance levels and band convergence”, Journal of the American Chemical Society **137**(15), 5100 (2015).
- [240] R. Moshwan, X.-L. Shi, W.-D. Liu, L. Yang, Y. Wang, M. Hong, G. Auchterlonie, J. Zou, and Z.-G. Chen, “High thermoelectric performance in sintered octahedron-shaped Sn_{1-x}(Cd_{1-x})₂Te_{1+2x} microcrystals”, ACS applied materials & interfaces **10**(45), 38944 (2018).
- [241] L. Wang, X. Tan, G. Liu, J. Xu, H. Shao, B. Yu, H. Jiang, S. Yue, and J. Jiang, “Manipulating band convergence and resonant state in thermoelectric material snTe by Mn–In codoping”, ACS Energy Letters **2**(5), 1203 (2017).
- [242] D. K. Bhat and S. Shenoy U, “High thermoelectric performance of co-doped tin telluride due to synergistic effect of magnesium and indium”, The Journal of Physical Chemistry C **121**(13), 7123 (2017).

- [243] Z. Ma, J. Lei, D. Zhang, C. Wang, J. Wang, Z. Cheng, and Y. Wang, “Enhancement of thermoelectric properties in pd–in co-doped sn₂te and its phase transition behavior”, ACS applied materials & interfaces **11**(37), 33792 (2019).
- [244] K. Lei, H. Huang, X. J. Liu, W. Wang, K. Guo, R. K. Zheng, and H. Li, “Ultra-low lattice thermal conductivity enables high thermoelectric properties in cu and y codoped sn₂te via multi-scale composite nanostructures”, ACS Sustainable Chemistry & Engineering **11**(19), 7541 (2023).
- [245] S. Roychowdhury, R. K. Biswas, M. Dutta, S. K. Pati, and K. Biswas, “Phonon localization and entropy-driven point defects lead to ultralow thermal conductivity and enhanced thermoelectric performance in (sn₂te)_{1–2} x (sn₂se)_x (sn₂s)_x”, ACS Energy Letters **4**(7), 1658 (2019).
- [246] S.-X. Lin, X. Tan, H. Shao, J. Xu, Q. Wu, G.-Q. Liu, W.-H. Zhang, and J. Jiang, “Ultralow lattice thermal conductivity in sn₂te by manipulating the electron–phonon coupling”, The Journal of Physical Chemistry C **123**(26), 15996 (2019).
- [247] C. Nie, C. Wang, Y. Xu, Y. Liu, X. Niu, S. Li, Y. Gong, Y. Hou, X. Zhang, D. Zhang, et al., “Band modification and localized lattice engineering leads to high thermoelectric performance in ge and bi codoped sn₂te–ag₂bite₂ alloys”, Small p. 2301298 (2023).
- [248] Z. Guo, G. Wu, X. Tan, R. Wang, Z. Yan, Q. Zhang, K. Song, P. Sun, H. Hu, C. Cui, et al., “Synergistic manipulation of interdependent thermoelectric parameters in sn₂te–ag₂bite₂ alloys by mn doping”, ACS Applied Materials & Interfaces **14**(25), 29032 (2022).
- [249] S. Song, Y.-C. Tseng, and Y. Mozharivskyj, “Optimizing thermoelectric performance of sn₂te via alloying with ag₂sn₂se₂ and pbte”, Journal of Alloys and Compounds **947**, 169415 (2023).

- [250] Q. Yang, T. Lyu, B. Nan, J. Tie, and G. Xu, "Enabling high quality factor and enhanced thermoelectric performance in bibr3-doped sn0. 93mn0. 1te via band convergence and band sharpening", ACS Applied Materials & Interfaces **14**(28), 32236 (2022).
- [251] M. Li, P. Ying, Z. Du, X. Liu, X. Li, T. Fang, and J. Cui, "Improved thermoelectric performance of p-type snte through synergistic engineering of electronic and phonon transports", ACS Applied Materials & Interfaces **14**(6), 8171 (2022).
- [252] L. Wang, M. Hong, Q. Sun, Y. Wang, L. Yue, S. Zheng, J. Zou, and Z.-G. Chen, "Hierarchical structuring to break the amorphous limit of lattice thermal conductivity in high-performance snte-based thermoelectrics", ACS applied materials & interfaces **12**(32), 36370 (2020).
- [253] B. Nan, X. Song, C. Chang, K. Xiao, Y. Zhang, L. Yang, S. Horta, J. Li, K. H. Lim, M. Ibáñez, et al., "Bottom-up synthesis of snte-based thermoelectric composites", ACS Applied Materials & Interfaces **15**(19), 23380 (2023).
- [254] S. Ahmad, A. Singh, S. Bhattacharya, M. Navaneethan, R. Basu, R. Bhatt, P. Sarkar, K. Meshram, K. Muthe, S. Vitta, et al., "Remarkable improvement of thermoelectric figure-of-merit in snte through in situ-created te nanoinclusions", ACS Applied Energy Materials **3**(7), 7113 (2020).
- [255] H. Wu, C. Chang, D. Feng, Y. Xiao, X. Zhang, Y. Pei, L. Zheng, D. Wu, S. Gong, Y. Chen, et al., "Synergistically optimized electrical and thermal transport properties of snte via alloying high-solubility mnnte", Energy & Environmental Science **8**(11), 3298 (2015).
- [256] W. Li, Z. Chen, S. Lin, Y. Chang, B. Ge, Y. Chen, and Y. Pei, "Band and scattering tuning for high performance thermoelectric sn1-xmnnxte alloys", Journal of Materiomics **1**(4), 307 (2015).

- [257] J. Hwang, H. Kim, M.-K. Han, J. Hong, J.-H. Shim, J.-Y. Tak, Y. S. Lim, Y. Jin, J. Kim, H. Park, *et al.*, “Gigantic phonon-scattering cross section to enhance thermoelectric performance in bulk crystals”, *ACS nano* **13**(7), 8347 (2019).
- [258] T. Hussain, X. Li, M. H. Danish, M. U. Rehman, J. Zhang, D. Li, G. Chen, and G. Tang, “Realizing high thermoelectric performance in eco-friendly sn₂te via synergistic resonance levels, band convergence and endotaxial nanostructuring with cu₂te”, *Nano Energy* **73**, 104832 (2020).
- [259] P. Bauer Pereira, I. Sergueev, S. Gorsse, J. Dadda, E. Müller, and R. P. Hermann, “Lattice dynamics and structure of gete, sn₂te and pbte”, *physica status solidi (b)* **250**(7), 1300 (2013).
- [260] Y. Jiang, J. Dong, H.-L. Zhuang, J. Yu, B. Su, H. Li, J. Pei, F.-H. Sun, M. Zhou, H. Hu, *et al.*, “Evolution of defect structures leading to high zt in gete-based thermoelectric materials”, *Nature Communications* **13**(1), 6087 (2022).
- [261] L. De Trizio, H. Li, A. Casu, A. Genovese, A. Sathya, G. C. Messina, and L. Manna, “Sn cation valency dependence in cation exchange reactions involving cu₂-xse nanocrystals”, *Journal of the American Chemical Society* **136**(46), 16277 (2014).
- [262] X. Li, J. Liu, S. Li, J. Zhang, D. Li, R. Xu, Q. Zhang, X. Zhang, B. Xu, Y. Zhang, *et al.*, “Synergistic band convergence and endotaxial nanostructuring: Achieving ultralow lattice thermal conductivity and high figure of merit in eco-friendly sn₂te”, *Nano Energy* **67**, 104261 (2020).
- [263] J. Tang, B. Gao, S. Lin, J. Li, Z. Chen, F. Xiong, W. Li, Y. Chen, and Y. Pei, “Manipulation of band structure and interstitial defects for improving thermoelectric sn₂te”, *Advanced Functional Materials* **28**(34), 1803586 (2018).
- [264] J. Dimmock, I. Melngailis, and A. Strauss, “Band structure and laser action in pb_{1-x}sn_{1-x}te”, *Physical Review Letters* **16**(26), 1193 (1966).